The Dissertation Committee for Bich-Thu Ngoc Nguyen certifies that this is the approved version of the following dissertation:

Amine Volatility in CO_2 Capture

Committee

Gary T. Rochelle, Supervisor

Isaac C. Sanchez

Thomas M. Truskett

Ben A. Shoulders

Jim E. Critchfield

Amine Volatility in CO_2 Capture

by

Bich-Thu Ngoc Nguyen, B.S.

Dissertation

Presented to the Faculty of the Graduate School of

The University of Texas at Austin

in Partial Fulfillment

of the Requirements

for the Degree of

Doctor of Philosophy

The University of Texas at Austin

May 2013

Dedication

To my Family

Acknowledgements

First I would like to extend my sincere gratitude and appreciation to Dr. Gary Rochelle for being my research advisor and mentor throughout my entire graduate school career. He is incredibly knowledgeable and experienced in the area of CO_2 Capture. I am always in awe of the breadth of his knowledge, and strive my best to emulate the high level Ph.D. thinking process and analytical ability that he has taught me which will undoubtedly be the most valuable tool to be utilized for the rest of my Chemical Engineering career. Furthermore, Dr. Rochelle has inspired me to always have a thirst for learning, and to maintain an inquisitive and open mind to new knowledge. Both of these elements are essential and highly beneficial to my continuing growth as a Ph.D. for years to come.

Next I want to thank the Luminant Carbon Management program for sponsoring the Rochelle group's CO_2 Capture research. Without your generous contribution and those of our other industrial sponsors, we would not have a means to pursue this exciting research area which is so vital to the fate of our lives and natural environment. In particular, I wish to acknowledge GTC Technology LLC, a first-rate technology company in gas and oil processing, for both the research sponsorship and the employment opportunity as a thermodynamic specialist – a role which has undoubtedly promoted my passion and intellectual growth in the area of chemical thermodynamics, and furthermore, has been seen to complement my CO_2 thermodynamics research very well.

Additionally, I need to thank my Ph.D. committee members, Dr. Isaac Sanchez, Tom Truskett, Ben Shoulders, and Jim Critchfield, for their valuable guidance and inputs for my work. They have always raised the bar for me to grow in my understanding of thermodynamics and applied Chemical Engineering as a whole. Also, I want to thank Maeve Cooney and others in the UT Austin Chemical Engineering staff, especially T. Stockman, Kay Swift-Costales, for their assistance throughout my graduate school career. Maeve in particular has been instrumental in editing all of my reports, presentations, as well as helping me to meet many key deadlines and appointments which would otherwise be rather stressful and overwhelming if it had not been for her assistance. Also Jim Smitherman and Butch Cunningham in the Machine Shop have been my lifeline whenever I run into hardware and/or instrumentation issues. No matter how serious the problem was, they can always take care of it properly and expediently. Also, Eddie Ibarra and Kevin Haynes had been superb in handling all procurement issues without any glitch and expediently as well.

In terms of FTIR support, I am especially appreciative of Mark Nelson, the technical sales representative of the former Gasmet Air Quality Analytical company. He is a true FTIR expert and analytical chemist in his own right – the combination of which has made him a highly valuable FTIR support resource for all instrumentation issues ranging from hardware to chemical gas analysis. Mark was also supportive and accessible in handling all of our queries and problems at all times, to which I am highly grateful. And of course, there are the Rochelle group members which I must also thank. Xi Chen for NMR support, Alex Voice for his innovative experimental inputs and

solutions, Steven Fulks and Peter Frailie for their thermodynamic insights and modeling support, respectively. Additionally, Mandana Ashouri, Lynn Li, Qing Xu, Jorge Plaza, David Van Wagener, and the rest of the Rochelle group have been a pleasure to work with and are always helpful.

Last but definitely not least, I am grateful beyond words to my loving parents who have been my strongest supporters through my Ph.D. years, actually since as far back as I can remember. They have always believed in me without fail, and are also a source of strength and solace which I constantly turn to every time the going gets tough. I owe my success, professional discipline, hard-working ethics, and sense of persistence to them because of their love and guidance since I was very young. I feel very blessed to have my parents be the people that they are in setting the good life examples, and I am proud of the fact that I can see a reflection of them every day when I look in the mirror. Also I would need to thank my four aunts and uncle in law for their unwavering love, support, and patience through the years which have also gone a long way in helping me become who I am today. Ultimately, I thank God for blessing me with the family that I have, the opportunity to pursue a once-in-a-lifetime world class education, and most importantly, for blessing me with the passion and appreciation to make the most of the opportunity I am given to benefit not only myself and my family but also society in the years to come.

Amine Volatility in CO_2 Capture

Bich-Thu Ngoc Nguyen, Ph.D.

The University of Texas at Austin, 2013

Supervisor: Gary T. Rochelle

This work investigates the volatilities of amine solvents used in post-combustion CO_2 capture from coal-fired power plants. Amine volatility is one of the key criteria used in screening an amine solvent for CO_2 capture: (1) amine losses up the stack can react in the atmosphere to form ozone and other toxic compounds; (2) volatility losses can result in greater solvent make-up costs; (3) high losses will require the use of bigger water wash units, and more water, to capture fugitive amines prior to venting - these translate to higher capital and operating costs; (4) volatilities need to be measured and modeled in order to develop more accurate and robust thermodynamic models.

In this work, volatility is measured using a hot gas FTIR which can determine amine, water, and CO_2 in the vapor headspace above a solution. The liquid solution is speciated by NMR (Nuclear Magnetic Resonance). There are two key contributions made by this research work: (1) it serves as one of the largest sources of experimental data available for amine-water volatility; (2) it provides amine volatility for loaded systems (where CO_2 is present) which is a unique measurement not previously reported in the literature.

This work studied the volatility of 20 alkanolamines in water at 0.5 – 1.1 molal (m) in water (< 1.5 mol% amine) at zero loading (no CO_2) from 40 ˚ - 70 ˚C. An empirical group contribution model was developed to correlate H_{amine} to molecular structures of both alkylamines and alkanolamines. The model incorporated additional functional groups to account for cyclic structures and to distinguish between different types of alkyl groups based on the attached neighboring groups. This model represented the experimental H_{amine}, which spanned five orders in magnitude, to well within an order of magnitude of the measured values.

The second component of this research involves upgrading the AspenPlus® v.7.3 model of MDEA-PZ-CO_2-H_2O system primarily by improving MDEA thermodynamics for MDEA-H_2O, MDEA-CO_2-H_2O, and MDEA-PZ-CO_2-H_2O. A key modification was made to include the carbonate (CO_3^{2-}) species into the model chemistry set which greatly improved the fit of CO_2 solubility for MDEA-CO_2-H_2O at ultra lean loading (α) for $0.001 < \alpha < 0.01$. With MDEA-PZ-H_2O, no MDEA-PZ cross interaction parameters were needed to match the blend volatility. Ultimately, both the blend volatility, at unloaded and loaded conditions, along with speciation were adequately represented by the upgraded model.

The final component of this research involves screening the volatilities of novel amines at unloaded and nominal lean loading condition from 40 ˚ - 70 ˚C (absorber operating conditions). The volatility of tertiary and hindered amines, such as MDEA and AMP, respectively, is not a strong function of loading because these amines are unable to form stable carbamates. Conversely, the volatility of mono-amines and of diamines

decreases by ~3 and 5-20 times, respectively, due to a much greater extent of carbamate-forming speciation. PZ or a blend having a diamine promoted by PZ would be favorable for CO_2 capture due to the low volatility of the diamines in loaded solution. . Finally, in order of increasing degree of salting out as reflected by the increasing magnitude of the system asymmetric amine activity coefficient, 7 m MDEA < 4.8 m AMP ~ 7 m MDEA/2 m PZ < 8 m PZ < 7 m MEA.

Table of Contents

List of Tables …… xiv

List of Figures ……...xvii

Chapter 1: Introduction and Scope of Work ……... 1

1.1 Overview of CO_2 Capture Technology ……. 1

1.2 The Absorption/Stripping Process …… 2

1.3 Motivation for Investigating Amine Volatility ……. 3

1.4 Scope of this Work …… 4

1.5 Contributions of this Work …… 9

1.6 Outline of Dissertation ……..10

Chapter 2: Experimental Methods ……. 12

2.1 Vapor-Liquid Equilibrium: Amine Volatility Measurements …… 12

2.2 FTIR Experimental Method Validation …….. 18

2.3 Liquid Phase Sampling: Speciation Analysis …….. 28

2.4 Liquid Speciation (NMR) Method Validation …… 30

2.5 Heat Capacity Determination ……. 32

2.6 Heat Capacity Method Validation ……... 34

2.7 Error & Data Reproducibility Analysis ……... 37

Chapter 3: Aqueous Amine Volatility in Binary Amine-Water Systems …… 41

3.1 Introduction …….. 41

3.2 Theory ……... 43

3.3 Data ……... 44

3.4 Amine Structures ……... 48

3.5 Results and Discussion …….. 50

Amine Henry's Constant Comparison to UNIFAC-DMD ……50

Amine H Constant Comparison to Hine & Mookerjee Group Contribution 52

Deviation of Experimental H Constant from Infinite Dilution …… 54

Base Case Group Contribution Model …… 55

Rigorous Group Contribution Model ……... 58

Predictive Capability of the Rigorous Model ……... 70

Correlation of Solution Thermodynamic Variables ……. 71

3.6 Conclusion …… 74

Chapter 4: MDEA-PZ-CO_2-H_2O Thermodynamic Model Upgrade …….. 76

4.1 Introduction …….. 76

4.2 Theory……... 77

4.3 Data ……...82

4.4 Results and Discussion …… 95

Fawkes Model Upgrade: Binary MDEA-H_2O System …… 95

Fawkes Model Upgrade: MDEA-CO_2-H_2O System …… 99

MDEA-CO_2-H_2O Reduced Model …….. 112

Fawkes Model Upgrade: MDEA-PZ-H_2O System …… 113

Fawkes Model Upgrade: MDEA-PZ-CO_2-H_2O System …… 115

4.5. Conclusions …… 130

Chapter 5: MDEA/PZ Behavior & Generalized Amine Screening …….. 132

5.1 Introduction …… 132

5.2 Theory ……... 133

5.3 Data ……. 134

5.4 Results and Discussion ……. 138

Amine Volatility: Empirical Modeling ……. 139

Activity Coefficient Behavior: PZ and MDEA/PZ …….. 144

Amine Screening …… 158

5.5 Conclusions …….. 160

Chapter 6: Conclusions …… 164

6.1 Summary of Research Work …… 164

6.2 Key Conclusions by Topic …….. 166

Aqueous Amine Volatility in Binary Amine-H_2O Systems …… 166

Upgrading AspenPlus® MDEA-PZ-CO_2-H_2O Model ……. 167

Detailed MDEA/PZ Solution Behavior & Amine Screening ……..... 167

6.3 Recommendations and Future Work …….. 169

Appendix A: H^1 and C^{13} NMR Analysis …….. 172

Appendix B: FTIR Operational Procedure ……... 208

Appendix C: Heat Capacity Experimental Procedure & Analysis …… 218

Appendix D: FTIR Pure Component Spectra …….. 227

Appendix E: Nomenclature …… 239

References ……... 242

Vita ……. 245

List of Tables

Table 1.4-1: Summary of 20 Alkanolamines Investigated …… 5

Table 2.7-1: An Example of Experimental Precision Analysis (8 m PZ-CO_2-H_2O) … 37

Table 3.3-1: Amine H Constants and Partial Pressures from 40 ˚– 70 ˚C …… 45

Table 3.3-2: Henry's Constants for 16 Alkylamines at 25 ˚C …….. 47

Table 3.5-1. Comparison of Experimental Amine H Constants to Calculated Values from UNIFAC-DMD at 40 ˚C …… 50

Table 3.5-2. Comparison of Experimental Amine H Constants to Calculated Values from Hine and Mookerjee (1975) at 25 ˚C …… 52

Table 3.5-3. PZ Activity Coefficient for 0.5–10 m PZ at 60 ˚C, $H_{PZ,60C}$ ~150 Pa …… 55

Table 3.5-4. Regressed Parameter Values for Base Case Group Contribution Model. 56

Table 3.5-5. Henry's Constants of Alkylamines at 298K and 313K ……... 59

Table 3.5-6. Group Parameter Values for Aqueous H Constant Estimates at 40 ˚C … 60

Table 3.5-7. Summary of Amine Enthalpies of Solution …… 65

Table 3.5-8. Functional Group Parameter Values for Amine $\Delta H_{solution}/R$ …….. 66

Table 3.5-9. Comparison of Measured versus Calculated H Constants for 1,2 AEP.. 71

Table 3.5-10.Summary of Solution Thermodynamic Variables for Aqueous Amine Systems at 40 ˚C …….. 72

Table 4.3-1. MDEA Volatility in MDEA-H_2O …… 82

Table 4.3-2. MDEA Volatility in MDEA-H_2O (Kim, 2008) …….. 83

Table 4.3-3. Pure MDEA Liquid Heat Capacity (DIPPR) …….. 85

Table 4.3-4. C_p for 1.7 m, 3.5 m, 6.2 m, and 13.9 m MDEA from 5–95 ˚C (Zhang, 2002) …… 85

Table 4.3-5. CO_2 Solubility for 2.8 m, 4.5 m, and 8.4 m MDEA from 25–120 ˚C (Jou, 1982) …… 88

Table 4.3-6. C_p for 3.6–12.6 m MDEA at Various Loadings and 25 ˚C (Weiland, 1997) …… 89

Table 4.3-7. CO_2 Solubility for 7 m MDEA/2 m PZ from 40–160 ˚C (Chen and Xu) …… 90

Table 4.3-8. CO_2 Solubility for 5 m MDEA/5 m PZ from 40–160 ˚C (Chen and Xu) …… 91

Table 4.3-9. Amine Volatility and CO_2 Solubility for 7 m MDEA/2 m PZ at 40 - 70 ˚C …… 92

Table 4.3-10. Amine Volatility and CO2 Solubility for 5 m MDEA/5 m PZ at 40 – 70 ˚C …… 93

Table 4.3-11. CO_2 Solubility for 7.7 m MDEA/1.1 m PZ at 40 and 70 ˚C (Bishnoi, 2000) …… 94

Table 4.3-12. Experimental NMR Speciation for 7 m MDEA/2 m PZ at 40 ˚C ..…. 95

Table 4.3-13. Experimental NMR Speciation for 5 m MDEA/5 m PZ at 40 ˚C …… 95

Table 4.4-1. Regressed Parameter Results for Binary MDEA-H_2O …….. 95

Table 4.4-2. Regressed Parameter Results for MDEA-CO_2-H_2O ……. 100

Table 4.4-3. Regressed Parameter Results for MDEA-CO_2-H_2O Reduced Model …. 112

Table 4.4-4. Regressed Parameter Results for MDEA-PZ-CO_2-H_2O Model …….. 116

Table 5.3-1. MEA Volatility for 7 m MEA-CO_2-H_2O (Hilliard 2008) …….. 135

Table 5.3-2. MDEA Volatility for 7 m MDEA-CO_2-H_2O ……. 135

Table 5.3-3. PZ Volatility for 8 m PZ-CO_2-H_2O …….. 135

Table 5.3-4. EDA Volatility for 8 m EDA-CO_2-H_2O …… 136

Table 5.3-5. AMP Volatility for 4.8 m AMP-CO_2-H_2O …… 136

Table 5.3-6. MDEA and PZ Volatility for 7 m MDEA-2 m PZ-CO_2-H_2O …….. 136

Table 5.3-7. MDEA and PZ Volatility for 5 m MDEA-5 m PZ-CO_2-H_2O ……. 137

Table 5.3-8. PZ and 2-MPZ Volatilities for 4 m PZ-4 m 2-MPZ-CO_2-H_2O ……. 137

Table 5.3-9. PZ and AMP Volatilities for 2.3 m AMP-5 m PZ-CO_2-H_2O …… 138

Table 5.4-1. Summary of Regressed Constants for Empirical Models of Amine Volatilities …….. 139

Table 5.4-2. Summary of Enthalpies of Amine Absorption for MDEA/PZ Systems (40 ˚C) …… 143

Table 5.4-3. Summary of the Contributions to the Enthalpy of Absorption for PZ and MDEA/PZ ……. 143

Table 5.4-4. Amine Volatilities for Various Systems Screened at 40 ˚C ……. 158

Table 5.4-5. Amine Activity Coefficients for Various Systems Screened at 40 ˚C …… 159

List of Figures

Figure 1.2-1. Absorption/Stripping Process for Post-Combustion CO_2 Capture …….. 2

Figure 2.1-1. CO_2 Gravimetric Loading Apparatus ……. 13

Figure 2.1-2. FTIR Apparatus for Amine Volatility Measurements ……15

Figure 2.1-3. Schematic of Gasmet Calibrator Mechanics ……... 17

Figure 2.2-1. Vapor Pressure of Water ……. 19

Figure 2.2-2. Vapor Pressure of pure Monoethanolamine …… 20

Figure 2.2-3. MEA-CO_2-H_2O System: CO_2 Solubility Comparison between FTIR Technique and Other Methods …… 21

Figure 2.2-4. PZ-CO_2-H_2O System: CO_2 Solubility Comparison between FTIR Technique and Other Methods …… 22

Figure 2.2-5. Vapor Pressure of pure MDEA Literature Comparison …….. 23

Figure 2.2-6. Aqueous MDEA Volatility Comparison …… 24

Figure 2.2-7. Aqueous MEA Volatility Comparison …….. 25

Figure 2.2-8. Comparison of MEA Volatility Measurements for 3.5 – 11 m MEA-CO_2-H_2O between Low vs. High Temperature Apparatus ……. 26

Figure 2.2-9. Comparison of PZ Volatility Measurements for 2 – 11 m PZ-CO_2-H_2O between Low vs. High Temperature Apparatus …….. 28

Figure 2.4-1. C^{13} NMR Liquid Phase Speciation for 7 m MEA at 27 ˚C …… 30

Figure 2.4-2. H^1 NMR Liquid Phase Speciation for 1 m PZ-CO_2-H_2O System at 27 ˚C …….. 31

Figure 2.5-1. Snapshot of DSC Sample Cell …… 32

Figure 2.5-2. A Sample of Calorimetric Profiles used to Determine the C_p of the Sample of Interest …….. 33

Figure 2.6-1. Specific Heat Capacity of Water …… 35

Figure 2.6-2. Specific Heat Capacity of MEA …….. 36

Figure 2.7-1. Reproducibility of the Specific Heat Capacity Experiments for H_2O …… 39

Figure 3.4-1. Amine Structures …….. 48

Figure 3.5-1. Behavior of Asymmetric PZ Activity Coefficient in H_2O at 60 ˚C …. 54

Figure 3.5-2. Evaluation of the Base Case Aqueous Amine Henry's Constant Model …….. 58

Figure 3.5-3. Evaluation of the Rigorous Amine H Constant Model (40 ˚C) …….. 64

Figure 3.5-4. Evaluation of Predicted Enthalpies of Amine Solution …… 67

Figure 3.5-5. Evaluation of Predicted Amine Henry's Constants from 25–70 ˚C … 69

Figure 3.5-6. Correlation between Amine Enthalpy of Solution and Entropy at 40 ˚C …….. 73

Figure 4.4-1. MDEA Volatilities in MDEA-H_2O System from 40–100 ˚C …….. 97

Figure 4.4-2. MDEA-H_2O Heat Capacity from 278–368K ……. 98

Figure 4.4-3. MDEA-H_2O Heat Capacity from 278 – 368K (mass basis) …… 99

Figure 4.4-4. Comparison of predicted pKa for MDEA protonation to experimental

values …….. 102

Figure 4.4-5. CO_2 Solubility for 8.4 m MDEA-CO_2-H_2O from 25–120 ˚C ……. 104

Figure 4.4-6. CO_2 Solubility for 4.5 m MDEA-CO_2-H_2O at 40 and 100 ˚C …… 105

Figure 4.4-7. CO_2 Solubility for 2.8 m MDEA-CO_2-H_2O from 25–120 ˚C ……. 106

Figure 4.4-8. Heat Capacity for 3.6–12.6 m MDEA-CO_2-H_2O at 25 ˚C ……. 107

Figure 4.4-9. Heat Capacity for 3.6–12.6 m MDEA-CO_2-H_2O at 25 ˚C on a CO_2-free Basis …….. 108

Figure 4.4-10. Fawkes Model Prediction of 7 m MDEA-CO_2-H_2O C_p for Ldg ~0.144 …… 109

Figure 4.4-11. MDEA Volatility for 7 m and 20 m MDEA-CO_2-H_2O at 40 ˚ and 60 ˚C …… 110

Figure 4.4-12. Species Activity Coefficients for 8.4 m MDEA-CO_2-H_2O at 40 ˚C …… 111

Figure 4.4-13. MDEA and PZ Volatility for 7 m MDEA/2 m PZ for 40–70 ˚C … 114

Figure 4.4-14. MDEA and PZ Volatility for 5 m MDEA/5 m PZ for 40–70 ˚C … 115

Figure 4.4-15. CO_2 Solubility Predictions for 7 m MDEA/2 m PZ from 40–160 ˚C ……... 118

Figure 4.4-16. CO_2 Solubility Predictions for 5 m MDEA/5 m PZ from 40–160 ˚C …….. 119

Figure 4.4-17. CO_2 Solubility Predictions for 7.7 m MDEA/1.1 m PZ at 40–70 ˚C …… 120

Figure 4.4-18. Amine Volatility Predictions for 7 m MDEA/2 m PZ at 40 ˚ and 60 ˚C ……. 121

Figure 4.4-19. Amine Volatility Predictions for 5 m MDEA/5 m PZ at 40 ˚and 60 ˚C ……. 122

Figure 4.4-20. Speciation for 7 m MDEA/2 m PZ at 40 ˚C …….. 123

Figure 4.4-21. Speciation for 5 m MDEA/5 m PZ at 40 ˚C …….. 124

Figure 4.4-22. Enthalpy of CO_2 Absorption for 7 m MDEA/2 m PZ from 60 ˚– 150 ˚C ……..... 125

Figure 4.4-23. Enthalpy of CO_2 Absorption for 5 m MDEA/5 m PZ from 60 ˚ – 150 ˚C …….. 126

Figure 4.4-24. C_p Predictions for 7 m MDEA/2m PZ from 40 ˚ – 120 ˚C …….. 128

Figure 4.4-25. C_p Predictions for 5 m MDEA/5 m PZ from 40 ˚ – 120 ˚C ……129

Figure 5.4-1. Model Representation of 8 m PZ-CO_2-H_2O Volatility: Empirical vs. Fawkes Model …… 140

Figure 5.4-2. Model Representation of PZ Volatility in 7 m MDEA/2 m PZ: Empirical vs. Fawkes Model …… 141

Figure 5.4-3. Model Representation of MDEA Volatility in 7 m MDEA/2 m PZ: Empirical vs. Fawkes Model …….. 142

Figure 5.4-4. PZ Volatility in 8 m PZ-CO_2-H_2O …… 144

Figure 5.4-5. PZ Volatility for 8 m, 10 m, 20 m PZ-CO_2-H_2O at 40 ˚C ……145

Figure 5.4-6. PZ Volatility and PZ concentration in 8 m PZ-CO_2-H_2O at 60 ˚C ……. 146

Figure 5.4-7. Activity Coefficients of PZ in 8 m and 10 m PZ-CO_2-H_2O …… 147

Figure 5.4-8. Amine Activity Coefficient in the Blend with Changing PZ Concentration ……. 148

Figure 5.4-9. Amine Activity Coefficient in the Blend with Changing MDEA Concentration ……. 149

Figure 5.4-10. PZ and H_2O Activity Coefficients in 7 m MDEA/2 m PZ ……. 151

Figure 5.4-11. MDEA Activity Coefficient in 7 m MDEA/2 m PZ ……. 152

Figure 5.4-12. Amine Concentrations and Activity Coefficients for 7 m MDEA/2 m PZ at 40 ˚C …….. 153

Figure 5.4-13. PZ Activity Coefficient as a Function of Ionic Strength at 40 ˚C...154

Figure 5.4-14. MDEA Activity Coefficient as a Function of Ionic Strength at 40 ˚C ……..... 156

Figure 5.4-15. Activity Coefficients of Electrolytes in 7 m MDEA/2 m PZ at 40 ˚C ……. 157

Figure A.1: Molecular Structure and Active Nuclei of Protons associated with PZ/PZH^+ ……. 173

Figure A.2: Molecular Structure and Active Nuclei of Protons associated with $PZ(COO)^-$ /$H^+PZ(COO)$ ……. 174

Figure A.3: Molecular Structure and Active Nuclei of Protons associated with $PZ(COO)_2^{2-}$ …… 174

Figure A.4: Molecular Structure and Active Nuclei of Protons associated with MDEA/$MDEAH^+$…… 174

Figure A.5: Molecular Structure and Active Nuclei of Carbons associated with PZ/PZH^+ ……. 175

Figure A.6: Molecular Structure and Active Nuclei of Carbons associated with $PZH^+/PZ(COO)^-$ …….. 175

Figure A.7: Molecular Structure and Active Nuclei of Carbons associated with $PZ(COO)_2^{2-}$ …….. 175

Figure A.8: Molecular Structure and Active Nuclei of Carbons associated with $MDEA/MDEAH^+$ …… 176

Figure A.9: Molecular Structure and Active Nuclei of Carbons associated with HCO_3^- $/CO_3^{2-}$ …… 176

Figure A.10: H^1 NMR Spectrum of 8 m PZ-CO_2-H_2O, α = 0.25 mol CO_2/mol total alkalinity, 40 ˚C …… 177

Figure A.11: H^1 NMR Spectrum of 8 m PZ-CO_2-H_2O, α = 0.30 mol CO_2/mol total alkalinity, 40 ˚C …… 178

Figure A.12: H^1 NMR Spectrum of 8 m PZ-CO_2-H_2O, α = 0.40 mol CO_2/mol total alkalinity, 40 ˚C …….179

Figure A.13: C^{13} NMR Spectrum of 8 m PZ-CO_2-H_2O, α = 0.25 mol CO_2/mol total alkalinity, 40 ˚C (C^{12} peaks) ……. 180

Figure A.14: C^{13} NMR Spectrum of 8 m PZ-CO_2-H_2O, α = 0.25 mol CO_2/mol total alkalinity, 40 ˚C (C^{13} peaks) ……..181

Figure A.15: C^{13} NMR Spectrum of 8 m PZ-CO_2-H_2O, α = 0.30 mol CO_2/mol total alkalinity, 40 ˚C (C^{12} peaks) ……. 182

Figure A.16: C^{13} NMR Spectrum of 8 m PZ-CO_2-H_2O, α = 0.30 mol CO_2/mol total alkalinity, 40 ˚C (C^{13} peaks) …… 183

Figure A.17: C^{13} NMR Spectrum of 8 m PZ-CO_2-H_2O, α = 0.40 mol CO_2/mol total alkalinity, 40 ˚C (C^{12} peaks) …… 184

Figure A.18: C^{13} NMR Spectrum of 8 m PZ-CO_2-H_2O, α = 0.40 mol CO_2/mol total alkalinity, 40 ˚C (C^{13} peaks) …… 185

Figure A.19: H^1 NMR Spectrum of 7 m MDEA-2 m PZ-CO_2-H_2O, α = 0.07 mol CO_2/mol total alkalinity, 40 ˚C …… 186

Figure A.20: H^1 NMR Spectrum of 7 m MDEA-2 m PZ-CO_2-H_2O, α = 0.095 mol CO_2/mol total alkalinity, 40 ˚C …… 187

Figure A.21: H^1 NMR Spectrum of 7 m MDEA-2 m PZ-CO_2-H_2O, α = 0.15 mol CO_2/mol total alkalinity, 40 ˚C …… 188

Figure A.22: H^1 NMR Spectrum of 7 m MDEA-2 m PZ-CO_2-H_2O, α = 0.16 mol CO_2/mol total alkalinity, 40 ˚C …….. 189

Figure A.23: C^{13} NMR Spectrum of 7 m MDEA-2 m PZ-CO_2-H_2O, α = 0.07 mol CO_2/mol total alkalinity, 40 ˚C (C^{12} peaks) ……. 190

Figure A.24: C^{13} NMR Spectrum of 7 m MDEA-2 m PZ-CO_2-H_2O, α = 0.07 mol CO_2/mol total alkalinity, 40 ˚C (C^{13} peaks) …… 191

Figure A.25: C^{13} NMR Spectrum of 7 m MDEA-2 m PZ-CO_2-H_2O, α = 0.095 mol CO_2/mol total alkalinity, 40 ˚C (C^{12} peaks) ……. 192

Figure A.26: C^{13} NMR Spectrum of 7 m MDEA-2 m PZ-CO_2-H_2O, α = 0.095 mol CO_2/mol total alkalinity, 40 ˚C (C^{13} peaks) ……. 193

Figure A.27: C^{13} NMR Spectrum of 7 m MDEA-2 m PZ-CO_2-H_2O, α = 0.15 mol CO_2/mol total alkalinity, 40 ˚C (C^{12} peaks) …… 194

Figure A.28: C^{13} NMR Spectrum of 7 m MDEA-2 m PZ-CO_2-H_2O, α = 0.15 mol CO_2/mol total alkalinity, 40 ˚C (C^{13} peaks) …… 195

Figure A.29: C^{13} NMR Spectrum of 7 m MDEA-2 m PZ-CO_2-H_2O, α = 0.16 mol CO_2/mol total alkalinity, 40 ˚C (C^{12} peaks) …… 196

Figure A.30: C^{13} NMR Spectrum of 7 m MDEA-2 m PZ-CO_2-H_2O, α = 0.16 mol CO_2/mol total alkalinity, 40 ˚C (C^{13} peaks) …….. 197

Figure A.31: H^1 NMR Spectrum of 5 m MDEA-5 m PZ-CO_2-H_2O, α = 0.096 mol CO_2/mol total alkalinity, 40 ˚C …….. 198

Figure A.32: H^1 NMR Spectrum of 5 m MDEA-5 m PZ-CO_2-H_2O, α = 0.18 mol CO_2/mol total alkalinity, 40 ˚C ……199

Figure A.33: H^1 NMR Spectrum of 5 m MDEA-5 m PZ-CO_2-H_2O, α = 0.36 mol CO_2/mol total alkalinity, 40 ˚C …….. 200

Figure A.34: C^{13} NMR Spectrum of 5 m MDEA-5 m PZ-CO_2-H_2O, α = 0.096 mol CO_2/mol total alkalinity, 40 ˚C (C^{12} peaks) …… 201

Figure A.35: C^{13} NMR Peaks of 5 m MDEA-5 m PZ-CO_2-H_2O, α = 0.096 mol CO_2/mol total alkalinity, 40 ˚C (C^{13} peaks) …….. 202

Figure A.36: C^{13} NMR Spectrum of 5 m MDEA-5 m PZ-CO_2-H_2O, α = 0.18 mol CO_2/mol total alkalinity, 40 ˚C (C^{12} Peaks – Part 1) …….. 203

Figure A.37: C^{13} NMR Spectrum of 5 m MDEA-5 m PZ-CO_2-H_2O, α = 0.18 mol CO_2/mol total alkalinity, 40 ˚C (C^{12} Peaks – Part 2) …….. 204

Figure A.38: C^{13} NMR Spectrum of 5 m MDEA-5 m PZ-CO_2-H_2O, α = 0.18 mol CO_2/mol total alkalinity, 40 ˚C (C^{13} peaks) ……. 205

Figure A.39: C^{13} NMR Spectrum of 5 m MDEA-5 m PZ-CO_2-H_2O, α = 0.36 mol CO_2/mol total alkalinity, 40 ˚C (C^{12} peaks) …… 206

Figure A.40: C^{13} NMR Spectrum of 5 m MDEA-5 m PZ-CO_2-H_2O, α = 0.36 mol CO_2/mol total alkalinity, 40 ˚C (C^{13} peaks) …… 207

Figure B.1: Gasmet Calibrator ……. 209

Figure B.2: Internal Gasmet Calibrator Setup …….. 210

Figure B.3: Jacketed 1000 mL Glass Reactor used for VLE Experiments …… 213

Figure C.1. Snapshot of DSC Internal Chamber …….. 221

Figure C.2. Calorimetric Scan of Indium Sample (for Calibration of Cell Constant) …….. 223

Figure C.3: Calorimetric Scan of Blank Sample …….. 223

Figure C.4: Calorimetric Scan of Al_2O_3 Sample …….. 224

Figure C.5: Calorimetric Scan of an Amine Sample ……. 225

Figure D.1: Water (H_2O) FTIR Reference Spectrum …… 227

Figure D.2: Carbon Dioxide (CO_2) FTIR Reference Spectrum ……. 228

Figure D.3: Monoethanolamine (MEA) FTIR Reference Spectrum …….. 228

Figure D.4: Piperazine (PZ) FTIR Reference Spectrum …… 229

Figure D.5: N-Methyldiethanolamine (MDEA) FTIR Reference Spectrum ……. 229

Figure D.6: 2-Amino-2-Methyl-1-Propanol (AMP) FTIR Reference Spectrum …230

Figure D.7: Diethanolamine (DEA) FTIR Reference Spectrum …….. 230

Figure D.8: Ethylenediamine (EDA) FTIR Reference Spectrum ……. 231

Figure D.9: Hexamethylenediamine (HMDA) FTIR Reference Spectrum …….. 231

Figure D.10: 2-Methyl Piperazine (2-MPZ) FTIR Reference Spectrum …….. 232

Figure D.11: 1,4-Dimethyl Piperazine (DMPZ) FTIR Reference Spectrum …… 232

Figure D.12: 2,2-Dimethylaminoethoxy Ethanol (2,2-DMAEE) FTIR Reference Spectrum…… 233

Figure D.13: Dimethylethanolamine (DMEA) FTIR Reference Spectrum …….. 233

Figure D.14: DL-Alaninol (ALA) FTIR Reference Spectrum ……. 234

Figure D.15: 2-Hydroxyethyl Piperazine (HEP) FTIR Reference Spectrum ….. 234

Figure D.16: 1-Methyl Piperazine (1-MPZ) FTIR Reference Spectrum …….. 235

Figure D.17: 1,2-Aminoethyl Piperazine (AEP) FTIR Reference Spectrum …… 235

Figure D.18: Diglycolamine® (DGA) FTIR Reference Spectrum ……. 236

Figure D.19: 3-Methylamino Propylamine (MAPA) FTIR Reference Spectrum... 236

Figure D.20: 1,2-Diaminopropane (1,2-DAP) FTIR Reference Spectrum …….. 237

Figure D.21: Morpholine (MORPH) FTIR Reference Spectrum …….. 237

Figure D.22: Dimorpholino Diethyl Ether (DMORPH) FTIR Reference Spectrum …… 238

Chapter 1: Introduction and Scope of Work

1.1. Overview of CO_2 Capture Technology

Power generation is the biggest source of CO_2 emission leading to global warming, with coal-fired power plants producing up to ~81% of the CO_2 that results from worldwide electricity generation (EIA, 2008). The leading technology proposed to capture CO_2 from coal-fired power plants is a post-combustion absorption/stripping process that makes use of aqueous amine. Post-combustion capture using aqueous amine absorption has proven advantages compared to oxycombustion and pre-combustion Integrated Gasification Combined Cycle (IGCC). These unmatched advantages include: (1) amenability to be retrofitted onto an existing power plant as a tail-end process; (2) maturity of the technology; and (3) lower capital and operating costs.

For the absorption process, 30 weight percent monoethanolamine (MEA) is considered to be the baseline industry solvent and has been used for more than 70 years. In an effort to develop solvents that are better performing, many novel amine solvents have been screened to evaluate their absorption characteristics (such as capture capacity, reaction rate, resistance to thermal/oxidative degradation, and volatility). Two of the more promising new solvents screened are 8 molal (m) Piperazine (PZ) and 7 m MDEA (n-methyldiethanolamine) / 2 m PZ blend. Based on studies from the Rochelle group, both of these solvents have been shown to have excellent capacity, competitive rates, and good resistance to degradation. It remains for this work to explore the volatilities of these two solvents along with those of many other novel solvents.

1.2. The Absorption/Stripping Process

Figure 1.2-1 illustrates the standard absorption/stripping process for post-combustion CO_2 capture.

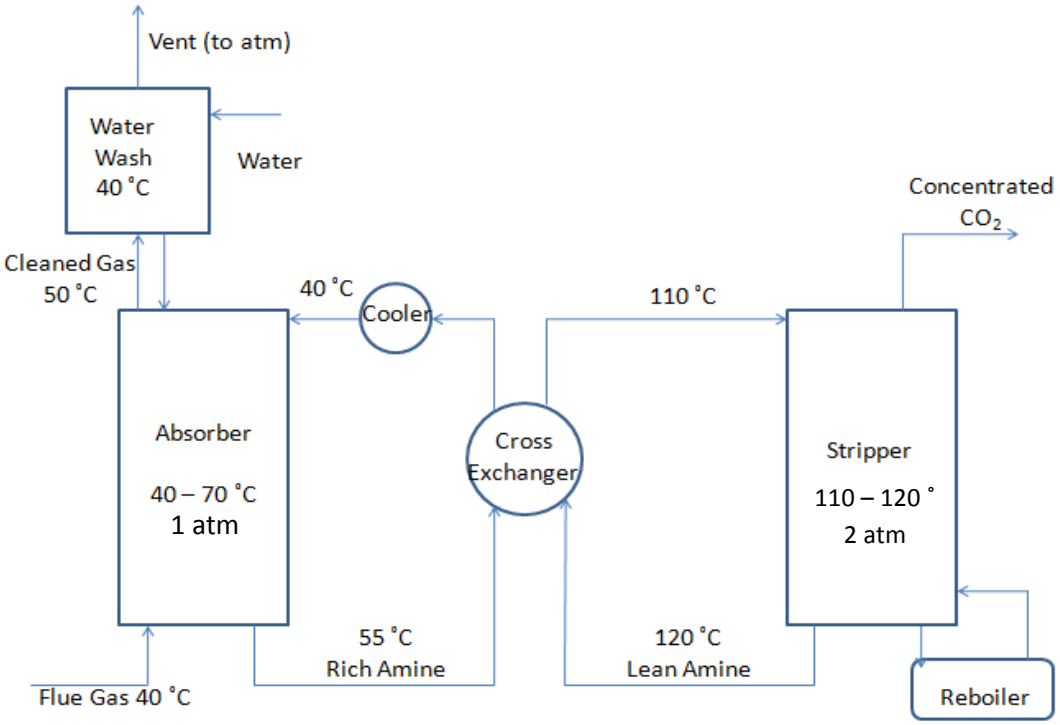

Figure 1.2-1. Absorption/Stripping Process for Post-Combustion CO_2 Capture

Flue gas from the coal-fired power plant is cooled to approximately 40 ˚C for enhanced CO_2 solubility in the absorber. This flue gas typically consists of about 7 mol% H_2O, 5 mol% O_2, and 12 mol% CO_2. It is assumed that this flue gas is already pre-treated for sulfur by a desulfurization unit before entering the absorber; thus, it is believed to have <10 ppm SO_x. Other impurities include ~30 ppm NO_x, metals (such as Cd, Zn, Hg), and fly ash particulates; however, for the scope of this work, all impurities are not considered for the sake of developing an equilibrium thermodynamic model that captures the fundamental reactions between the amine, CO_2, and H_2O.

The flue gas enters the bottom of the absorber which operates within the range from 40 ˚C – 70 ˚C throughout the length of the column and 1 atm. In a countercurrent mode, this flue gas is contacted with the amine solvent coming into the top of the absorber. The solvent comes in with a lean amount of CO_2 (~0.5 kPa P_{CO2}) due to continuous cycling throughout the capture flow process. The amine absorbs CO_2 from the flue gas by means of chemical absorption. Upon reaching the bottom of the absorber, the solvent is now loaded with a rich amount of CO_2 (~5 kPa P_{CO2}). The cleaned flue gas, now with 90% of the CO_2 removed by design, exits the top of the absorber and enters into a water wash for amine recovery prior to being vented into the atmosphere.

The rich amine stream is pumped into a cross exchanger, designed with a ±5 ˚C tempera- ture approach between its inlet and outlet streams (to ensure the optimum equivalent work for the entire process), where it is heated to ~100 ˚ - 105 ˚C. The rich stream then enters into the top of the stripper which operates between 110 ˚C – 120 ˚C and 2 atm. Steam coming from the stripper reboiler contacts the rich amine counter- currently and strips out the CO_2 by reversing the absorption reaction. The amine is now lean again as it exits the stripper and makes its way back to the absorber for continuous capture operation. The steam/CO_2 stream then exits the top of the stripper where water is then condensed out as makeup water or it can be used for the amine wash if sufficient. The CO_2 is pressurized to 150 bars in preparation for sequestration.

1.3. Motivation for Investigating Amine Volatility

Amine volatility is one of the key criteria used to evaluate the viability of an amine to be used as a solvent for CO_2 capture. Volatility is important for environmental,

economic, and research & development purposes. First, amine volatility loss up the stack can react in the atmosphere to form ozone and other toxic compounds. Currently there is no set EPA regulation for amine emissions, but most CO_2 capture processes aim to reduce amine volatility to ~1 ppm for venting purposes per conversations with CO_2 capture sponsors. From an economic standpoint, high volatility loss increases the solvent makeup cost required to replenish the amine. For the more expensive amines such as PZ, this cost can be substantial. Additionally, a large volatility loss will require the use of a bigger water wash tower and more water to treat. Both of these factors will drive up the capital and operating expenses of the CO_2 capture operation. Finally, there is a research & development need to quantify amine volatility and incorporate this type of data into the framework of a thermodynamic model in order to build a more robust model.

Amine volatility is most crucial at two places in the process: (1) at the top of the absorber (40 ˚ - 60 ˚C, 1 atm, nominal lean CO_2 loading where loading = mol CO_2/mol total alkalinity) – this is the amount of amine that would have to be treated by the water wash; (2) at the water wash (40 ˚C and 1 atm) – this is the amount of amine that will eventually be vented into the environment. The scope of this work focuses mainly on amine volatility at the top of the absorber.

1.4. Scope of this Work

There are three main areas of focus considered within the scope of this work: (1) aqueous amine volatility in binary amine-water systems; (2) rigorous thermodynamic model upgrade for MDEA-PZ-CO_2-H_2O; and (3) amine volatility screening for novel solvents that are potentially viable for CO_2 capture. The volatility of 20 amines was

measured in water. These amines were prepared at dilute concentrations ranging from 0.1 – 1.1 molal (<1.5 mol% amine) to approach the intrinsic vapor-liquid partition of the amine at infinite dilution in water. At the low amine concentrations where the aqueous volatilities were measured, these amines were considered to be diluted enough to approximate the volatility at the condition of infinite dilution to within ±10%. Aqueous amine volatilities were measured at 40 ˚- 70 ˚C and 1 atm which is representative of the standard operating conditions of the absorber. Table 1.4-1 summarizes the 20 alkanolamines studied in this work.

Table 1.4-1. Summary of 20 Alkanolamines Investigated

Amine Class	Amine Type	Amine	Acronym
Monoamines	Primary	Monoethanolamine	MEA
		Diglycolamine	DGA
		DL-Alaninol	ALA
		2-Amino-2-Methyl-1-Propanol	AMP
	Secondary	Diethanolamine	DEA
		Morpholine	MORPH
	Tertiary	N-Methyldiethanolamine	MDEA
		2,2-Dimethylethoxy Ethanol	2,2-DMAEE
		N,N-Dimethylethanolamine	DMMEA
Diamines	Primary	Hexamethylene Diamine	HMDA
		1,2-Diaminopropane	DAP
		Ethylenediamine	EDA
	Secondary	Piperazine	PZ
		2-Methyl Piperazine	2-MPZ
	Tertiary	Dimorpholino Diethyl Ether	DMORPH
		1,4-Dimethylpiperazine	1,4-DMPZ
	Mixed	Hydroxyethyl Piperazine	HEP
		3-Methylamino Propylamine	MAPA
		1-Methyl Piperazine	1-MPZ
Triamines	Mixed	1,2-Aminoethyl Piperazine	AEP

The aqueous amine volatilities were obtained experimentally as amine partial pressures. However, for purposes of analytical representation, aqueous amine volatilities will be expressed as amine Henry's constants (H) in Pa units which represent the vapor-liquid partition of the amine in terms of the ratio of the amine partial pressure to its liquid mole fraction. The Henry's constant was chosen as an intrinsic indicator of aqueous amine volatility because it is referenced to the state of infinite dilution of amine in water. By virtue of this reference state of infinite dilution, the H constant accounts for only the intrinsic amine-water interaction as opposed to accounting for both amine-water and amine-amine interactions as in the case of the amine activity coefficient.

This work also develops an empirical model to correlate the amine Henry's constants for 19 of the 20 alkanolamines studied, along with those of 16 alkylamines from the literature, to their molecular structures in a group contribution method. The model is also used to predict the experimental volatility of one of the amines (1,2-Aminoethyl Piperazine), not used in the regression, to well within ±10%. This result lends confidence that the model has excellent predictive capability for amines in addition to just being able to capture the data.

This work also focuses on upgrading the existing thermodynamic model for MDEA/PZ solvent system which was developed using the elecNRTL theory. The original model, named Guy Fawkes, was developed by Peter Frailie (a Rochelle group member) in 2010. This thermodynamic model for the quaternary system of MDEA-PZ-CO_2-H_2O was developed by means of sequential regression in which one starts by

modeling the simplest subsystems (consisting of single pure components only) then onto binary, tertiary, and ultimately the quaternary system. This work supplied various types of experimental data, including CO_2 solubility, amine volatility, heat capacity (C_p), and speciation, needed to regress the parameters of this model. The upgrading effort done in this work primarily consisted of improving the modeling of only MDEA, at all the levels within the sequential regression hierarchy, as PZ was rather well-behaved for the most part. There were two long standing issues with the original Fawkes model that were effectively resolved in this upgrade: (1) the need to be able to match experimental volatility data for MDEA/PZ blend; (2) the need to fit experimental speciation data for the blend.

VLE and rate data have previously been developed for two blends: 7 m MDEA/2 m PZ and 5 m MDEA/5 m PZ. Both of these systems are believed to be superior compared to the baseline 7 m MEA solvent for CO_2 capture. In comparison to 7 m MEA, the MDEA/PZ blends have almost twice the capture capacity (~0.8 mol CO_2/kg amine+H_2O versus 0.47 mol CO_2/kg amine+H_2O) (Closmann 2011) within the optimum operational loading range corresponding to ~0.5 and 5 kPa lean and rich CO_2 partial pressure, respectively; almost twice the rate of CO_2 reaction at (~5.1x107 mol/s*Pa*m^2 versus 3.1 mol/s*Pa*m^2) (Closmann 2011) at the nominal rich loading; much lower rate of oxidative and thermal degradation; and are also 80% - 90% less volatile (0.47 Pa P_{MDEA} and 0.30 Pa P_{PZ} versus 2.7 Pa P_{MEA} at 40 ˚C) as reported in this work. Because of these superior operating characteristics, extensive experimental work was performed to investigate MDEA/PZ along with all its binary and ternary system constituents (0.5 m –

20 m MDEA-H_2O, 0.5 m – 10 m PZ-H_2O, 7 m MDEA-CO_2-H_2O, 8 m – 10 m PZ-CO_2-H_2O, and 7 m/2 m and 5 m/5 m MDEA-PZ-H_2O). The understanding gained from performing a thorough study of MDEA/PZ will allow one to rationalize and predict the behaviors of other amine solvents of interest. This ability lends itself to the pursuit of the third objective within the scope of this work which is to analyze and generalize the behavior of other amine systems screened as potentially viable solvents for CO_2 capture.

With respect to the screening of amine solvents, this work explored a total of 9 amine systems: 7 m MEA (Hilliard 2008), 8 m PZ-CO_2-H_2O, 7 m MDEA-CO_2-H_2O, 7 m MDEA/2 m PZ and 5 m MDEA/5 m PZ-CO_2-H_2O, 4 m PZ/4 m 2-MPZ-CO_2-H_2O, 4.8 m AMP-CO_2-H_2O, 8 m EDA-CO_2-H_2O, and 2.3 m AMP / 5.0 m PZ-CO_2-H_2O. The motivation behind screening these systems for volatility stemmed from the ongoing need to formulate new solvents for CO_2 capture with promising operational characteristics which include large capture capacity, fast rates, strong resistance to oxidative and thermal degradation, and low volatility. Cost is also a factor in the use of solvent, thus, certain blends having other amines with PZ are used to reduce the high cost of using PZ alone. These novel amine systems are screened for volatility at 40 ˚ - 70 ˚C, 1 atm, and nominal lean CO_2 loading (~0.5 kPa) which are the standard operating conditions at the top of the absorber where volatility is of great concern. From the experiments, amine volatilities, in terms of partial pressures, for these systems are obtained not only for comparative purposes, but also to generalize the behavior of the system activity coefficients.

1.5. Contributions of this Work

This work is the first known investigation of amine volatility in CO_2 systems. While there had been many literature studies on amine volatility in binary amine-H_2O systems, there has not been any study of this kind for loaded CO_2 systems. The experimental method, developed by Hilliard (2008) , used to measure amine volatility is also rather original in that uses an FTIR (Fourier Transform Infrared Spectroscopy) technique, instead of the more common GC methods, to detect vapor composition down to a resolution of 5-10 ppm.

Another important contribution of this work is that it serves as one of the largest known collections of experimental data for aqueous volatility of alkanolamines used in CO_2 capture. While there are many studies to date on the volatilities of alkylamines or of only a few alkanolamines applicable to CO_2 capture, this work investigated a total of 20 alkanolamines. Furthermore, this work has successfully developed a group contribution model to correlate aqueous amine volatilities to molecular structures. This model greatly improves the predictions of aqueous volatilities for both alkanolamines (used for CO_2 capture) and alkylamines, compared to existing group contribution methods such as UNIFAC or that by Hine and Mookerjee (1979), because it is built on experimental data from both types of amines. The other two methods are not able to successfully predict the aqueous volatilities of CO_2 capture alkanolamines because they are primarily developed from the data of alkylamines not alkanolamines. The nitrogen functional group in alkylamines are thought to have different interaction with water than the nitrogen group in alkanolamines. This phenomenon is related to the type of neighboring

groups that are attached to nitrogen in alkylamines versus in alkanolamines. In alkylamines, alkyl groups are the neighbors to the nitrogen, whereas in alkanolamines the neighboring groups are often an alcohol or ether which influence how nitrogen interact with water differently than alkyl groups. Lastly, the group contribution method of Hine and Mookerjee (1975) also did not differentiate between aliphatic nitrogen and cyclic nitrogen groups. This study has found that there is a clear difference in volatility between these two nitrogen groups.

The most fundamental contribution of this research is that it truly illuminates the solution behaviors of various amines in CO_2 systems. This understanding allows for effective modeling and simulation of system thermodynamics along with process designs of the absorber.

1.6. Outline of Dissertation

The introduction chapter will be followed by the following chapters in this order: Experimental Methods, Aqueous Amine Volatility in Binary Amine-H_2O Systems, MDEA/PZ/CO_2/H_2O Model Upgrade, MDEA/PZ Detailed Investigation & Generalized Amine Screening, and Conclusions. The chapter on Experimental Methods discusses in details the techniques for amine volatility measurements using FTIR, heat capacity determination with Differential Scanning Calorimetry (DSC), and liquid speciation study using Nuclear Magnetic Resonance technique (NMR). Other supporting lab techniques, such as Total Inorganic Carbon (TIC) to verify the CO_2 loading in solution and Amine Titration to determine the amine concentration, are also covered. The body chapters are presented in order of increasing system complexity, starting with simple binary system

analysis building up to the quaternary MDEA-PZ-CO_2-H_2O system which ultimately leads to the generalization of other amine systems screened for CO2 capture.

Chapter 2: Experimental Methods

This chapter discusses the experimental methods used in this work to study (1) vapor liquid equilibrium and (2) heat capacity of multi-component systems. MDEA and PZ blends, along with their individual sub-systems, were extensively studied in both VLE and calorimetry to develop a rigorous thermodynamic model for the blend. Other amine systems were screened for their equilibrium volatility at the absorber operating condition to determine their viability for use as CO_2 capture solvents. All experiments were typically run only once, not in replicates, because the main source of experimental deviation from one run to the next lies with the precision of the instrument which does not pose significant errors. An analysis of experimental precision, or data reproducibility, will be presented in section 2.7. Accuracy of the different methods is benchmarked by measuring known systems.

2.1. Vapor-Liquid Equilibrium: Amine Volatility Measurements

Solution Preparation

Approximately 525 – 550 g of solution was prepared for each experiment. Solutions were prepared by dissolving pure, analytical-grade amine in water to achieve the desired molality (m, moles of amine/kg water). . The chemical suppliers and purity grades were: MEA (Acros Organics 99 %), PZ (Alfa Aesar 99 %), MDEA (Acros Organics 99+ %), EDA (Strem Chemicals 99 %), AMP (Acros Organics 99 %), MAPA (Acros Organics 98.5 – 100%), 2-Methyl PZ (Acros Organics 97.5 – 100%). High concentrations of PZ were heated to dissolve anhydrous solid PZ in water. The solutions

were loaded with CO_2 by sparging CO_2 in a glass cylinder on a balance to obtain a gravimetric CO_2 loading. Figure 2.1-1 shows the gravimetric loading apparatus.

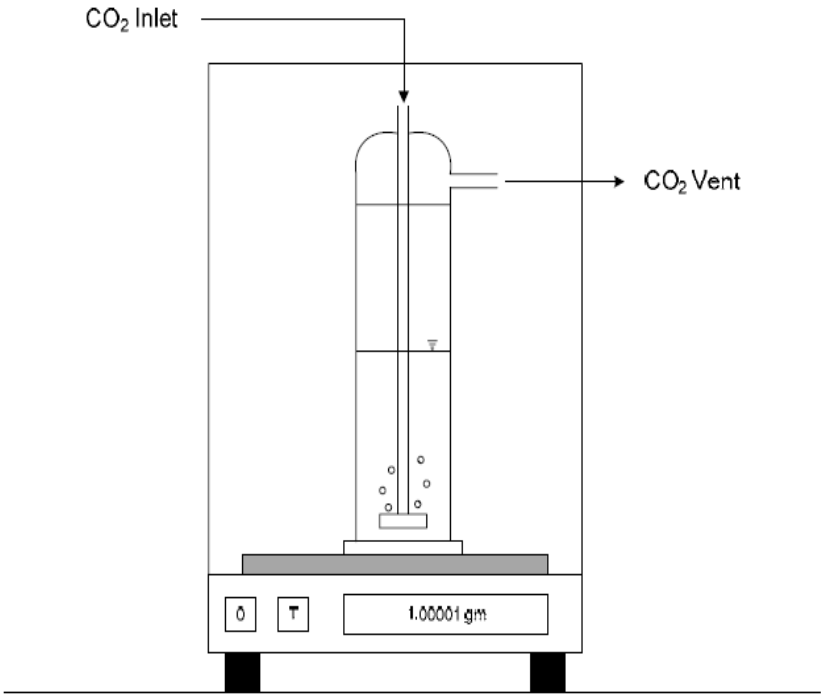

Figure 2.1-1. CO_2 Gravimetric Loading Apparatus

Amine solutions loaded with this technique produced CO_2 loading within ± 5.0 % of the target loading based on an analysis of the loaded solutions by TIC.

CO_2 Loading Verification

The CO_2 concentration in solution was verified by Total Inorganic Carbon (TIC) analysis. The samples were diluted in H_2O and injected into 30 wt % H_3PO_4 to release CO_2. The CO_2 was carried by N_2 to an infrared detector. The resulting voltage peak was integrated and calibrated with a 1000 ppm inorganic carbon standard made from a mixture of potassium carbonate and potassium bicarbonate (Ricca Chemical, Pequannock, NJ). The reproducibility of this method is about 2%.

Amine Concentration Verification

The amine concentration was determined by acid titration with an automatic Titrando series titrator with automatic equivalence point detection. A 300X diluted sample was titrated with 0.1 N H_2SO_4 to a pH of 2.4. The amount of acid needed to reach the equivalence point at a pH of 3.9 was used to calculate the total amine concentration. The reproducibility of this method is about 1%.

Vapor Headspace Sampling: Amine Volatility Measurement

Amine volatility was measured in a stirred reactor coupled with a hot gas FTIR analyzer (Fourier Transform Infrared Spectroscopy, Temet Gasmet DX-4000) as shown in Figure 2.1-2. This unit has a 10 m gas cell path length with varying detection limits between 0.1 ppm – 60 vol%+ depending on the absorption of the gas components analyzed within the range of 900 – 4200 cm^{-1} wavenumber. The FTIR apparatus and method were taken from Hilliard (2008). FTIR operation and procedure were followed exactly as prescribed by Hilliard. Details regarding FTIR operation, including clean up, are provided in Appendix B.

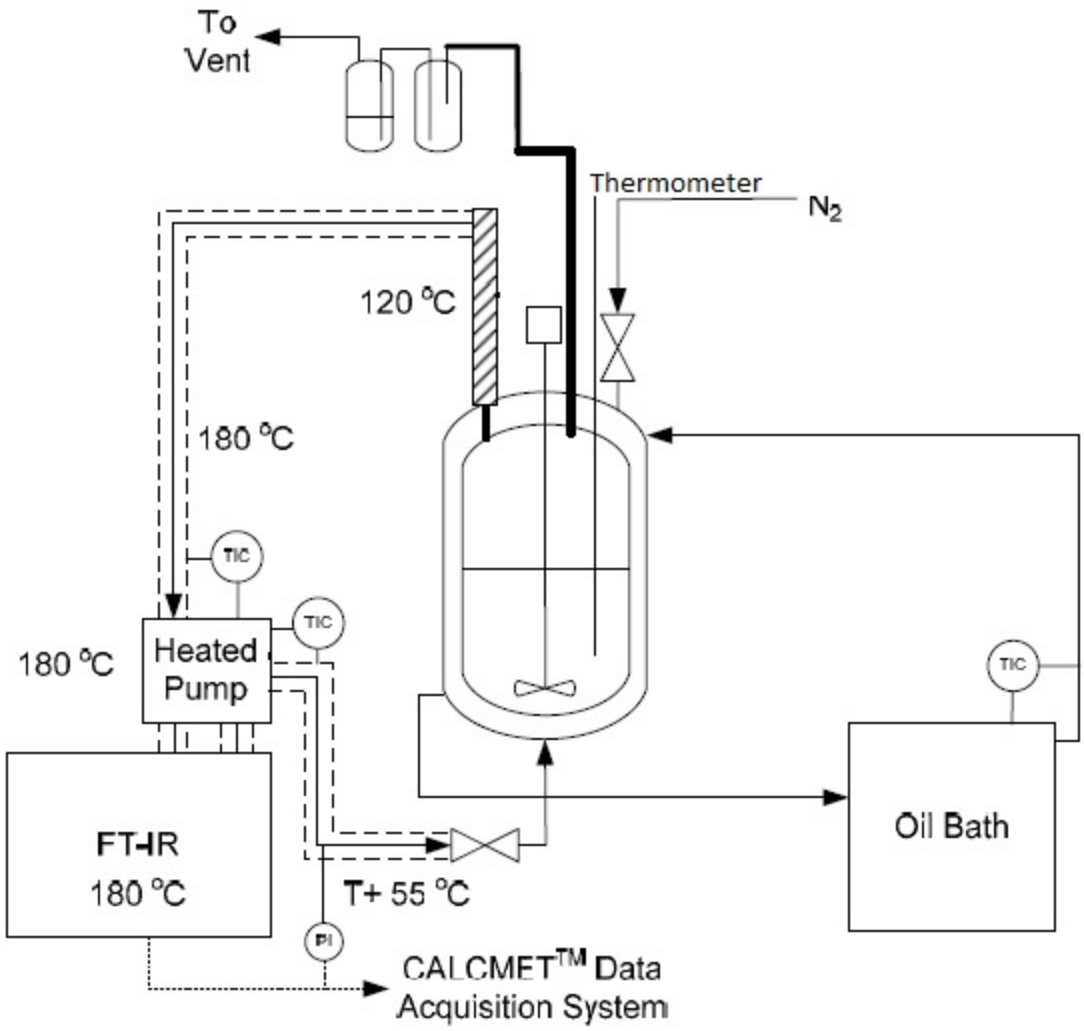

Figure 2.1-2. FTIR Apparatus for Amine Volatility Measurements

The 1L glass reactor was agitated at 350 rpm ± 5 rpm. This reactor is designed to withstand up to 45 psig at 100 ˚C; however, given the experimental needs, only low temperature experiments from 40 ˚ - 70 ˚C at atmospheric pressure are conducted as these conditions are representative of the absorber operating conditions. Temperature in the reactor was controlled to within ±0.1 °C by circulating heated dimethylsilicone oil in the outer reactor jacket to and from the oil bath. The reactor was insulated with thick

insulation material. The temperature inside the reactor was measured with a digital thermometer to within ±0.1 ˚C.

At the start of each experiment, the headspace in the reactor was swept with excess N_2. The reactor was maintained at ambient pressure by venting through a water seal. The room pressure was measured with a barometer to ±0.1 mm Hg. Vapor from the headspace of the reactor was circulated at a rate of ~5-10 L/min. by a heated sample pump to the FTIR through a heated Teflon line. Both the line and analyzer were maintained at 180 ºC to keep the material in vapor phase. The FTIR software, Calcmet, directly measures amine, CO_2, and water concentration in the gas by using a multiple least squares algorithm that is based on the work of Saarinen and Kauppinen (1991). The relative standard reproducibility in the vapor phase measurement was reported to be ±2% by Goff (2005). The margin of error in the readings, however, is expected to increase with detection of low concentration of material, and can be up to ±10% or greater for concentrations <10 ppm. After the gas passed through the FTIR, it was returned to the reactor through a heated line maintained at ~ 55 ºC hotter than the reactor ($T_{reactor}$ + 55˚C). The 55 ºC difference was necessary according to Hilliard (2008) to ensure that the return gas can thermally equilibrate with the solution in the reactor, and also to compensate for potential heat loss at the bottom of the reactor. Upon completion of an experiment, approximately 25 mL of liquid sample was taken to verify both the loading and amine concentration using TIC and amine titration, respectively.

FTIR calibration for each amine is performed using a Gasmet Calibrator. This apparatus consists of a syringe pump, a manual needle valve, and a stainless steel

injection chamber. Figure 2.1-3 displays the working mechanics of the Gasmet calibrator.

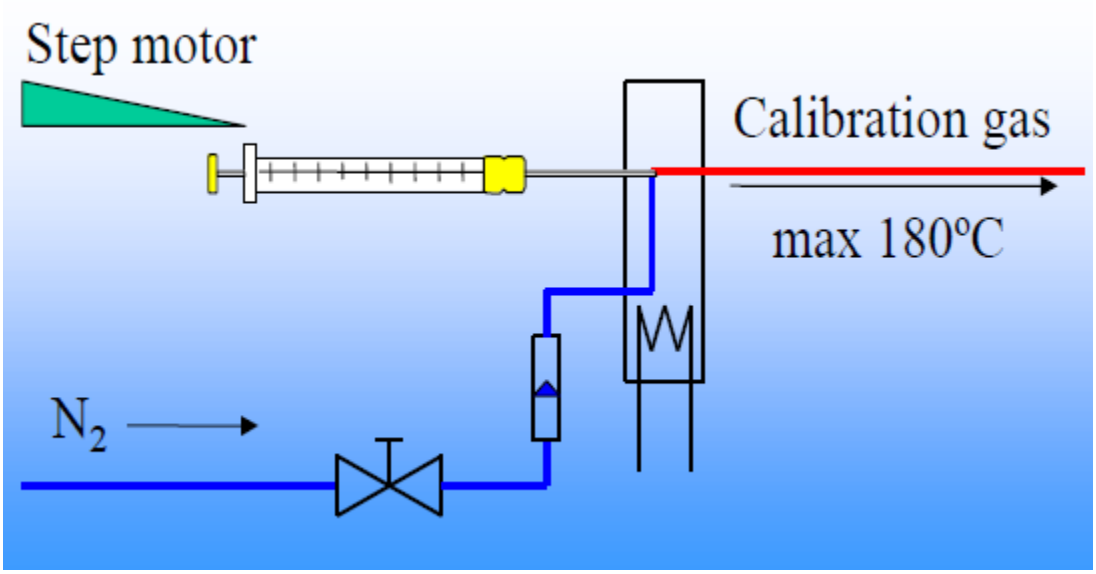

Figure 2.1-3. Schematic of Gasmet Calibrator Mechanics

A known nitrogen flow rate, typically 2 SLPM, is introduced to the calibrator at room temperature via a mass flow controller. The syringe pump injects a known and very precise flow of the target amine to be calibrated into the nitrogen flow in a heated injection chamber kept at 180 °C. This produces a continual flow of a known concentration of calibration gas that is fed into the FTIR analyzer at 180 °C. A spectrum of a known mixture of the target gas and N_2 is measured and saved as a reference calibration. A calibration must be made at each concentration of interest.

If the target amine is a solid at room temperature, it is necessary to dilute it in distilled deionized water only up to the point where it is soluble. The diluted amine-water mixture can then be injected into the heated chamber. In this case, the water component must be subtracted from the overall spectra leaving the target amine as the

remaining residual spectra. The amine residual can then be saved as a reference calibration. PZ was calibrated by this method because it is a solid at room temperature. Reference spectra for all the amines studied in this work are provided in Appendix D.

2.2. FTIR Experimental Method Validation

The FTIR experimental method was benchmarked by Hilliard (2008) by measuring pure component vapor pressure (H_2O, MEA) and CO_2 solubility of loaded amine systems (MEA-CO_2-H_2O and PZ-CO_2-H_2O). MDEA vapor pressure, MDEA-H_2O volatility, and MEA-H_2O volatility were also compared to literature values.

Pure H_2O System Benchmarking

Figure 2.2-1, taken from Hilliard (2008), shows how the water vapor pressure measurements from the FTIR method compare with accepted literature values by Kell et al.(1984) and by the DIPPR correlation.

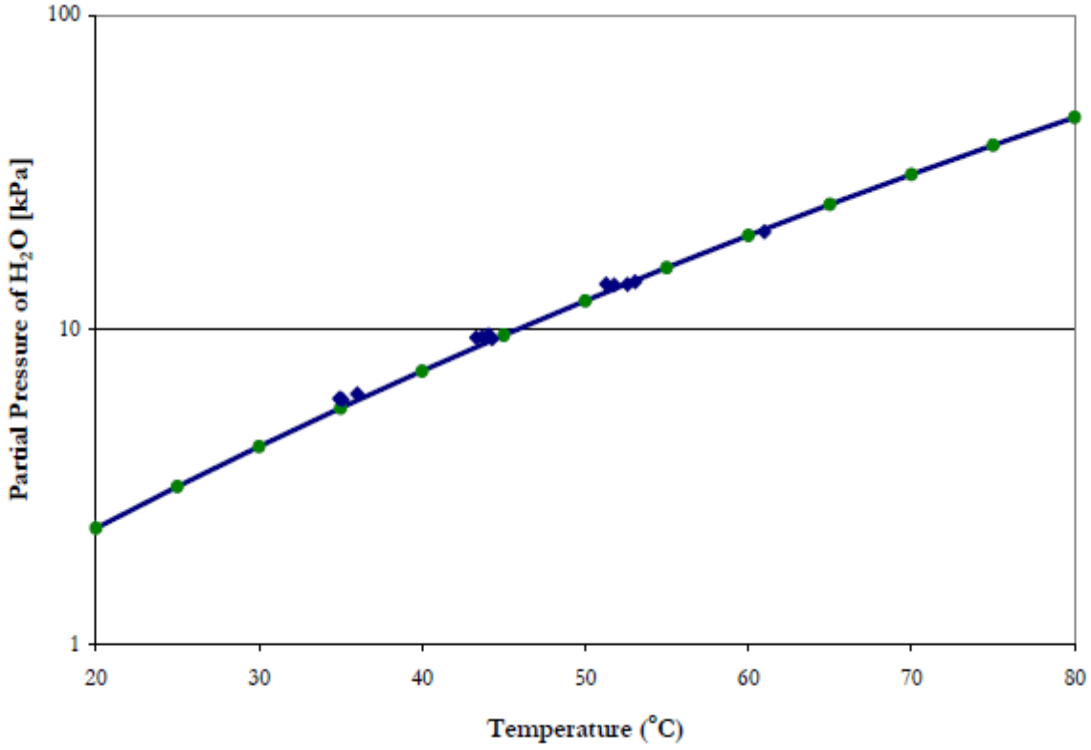

Figure 2.2-1. Vapor Pressure of Water. Points: ● Kell et al. (1984); ♦ Hilliard (2008). Line: DIPPR Correlation

Kell et al. (1984) reported a relative standard uncertainty in the measurements as < 0.2 %. Overall, measurements from the FTIR method were found to have an average absolute relative uncertainty (AARD) of ±4.4 % with the exception of a few outliers. Since the uncertainty associated with the FTIR analysis is ± 2.0 %, Hilliard (2008) considered that an experimental AARD of ± 4.40 % was acceptable as compared to estimated predictions from the DIPPR correlation based on the work of Kell et al. (1984).

Pure MEA System Benchmarking

Figure 2.2-2, taken from Hilliard (2008), illustrates how the experimental MEA vapor pressure obtained from the FTIR method compare to accepted values reported by a number of literature sources.

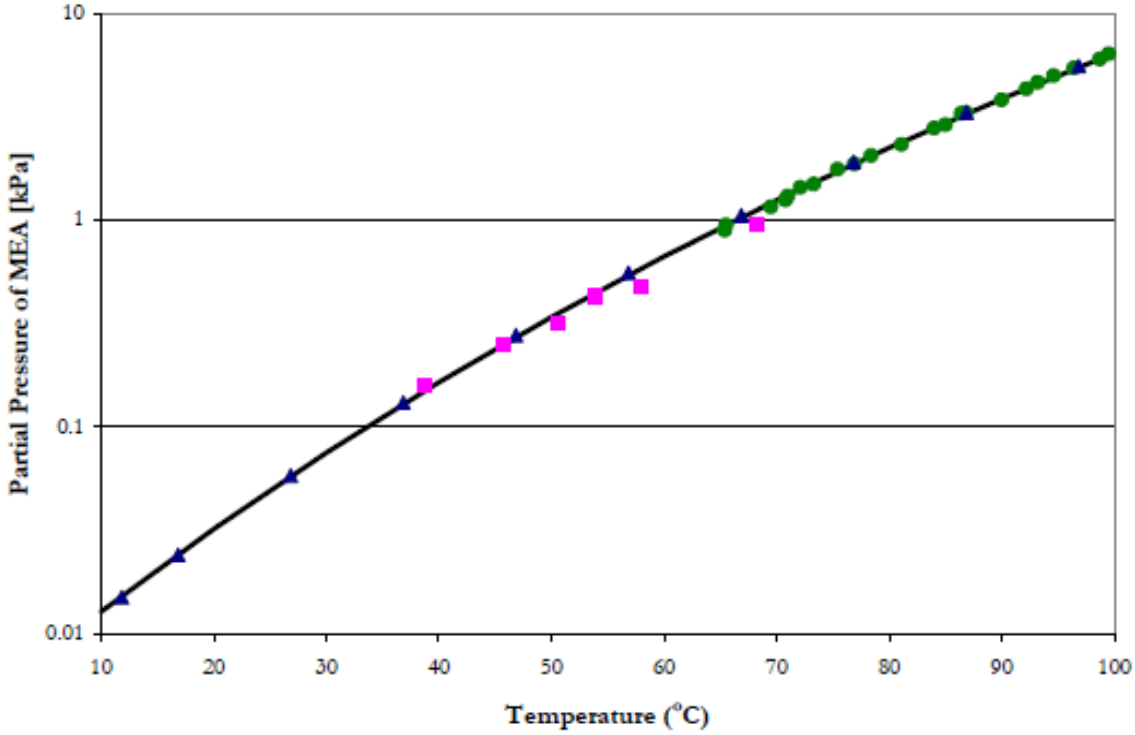

Figure 2.2-2. Vapor Pressure of pure monoethanolamine. Points: ●, Matthews et al. (1973), ♦, Engineering Sciences Data Unit (1979), ■,Hilliard (2008). Line: DIPPR Correlation

Values estimated from the DIPPR correlation were reported with a relative standard uncertainty of < 10 %. Measurements obtained from the FTIR method were found to be adequate within an AARD of ±7.3 % with the exception of a few outliers.

MEA-CO_2-H_2O Benchmarking

CO_2 solubility measurements for loaded MEA obtained from the FTIR technique are compared to those reported by Jou et al. (1995) and Dugas (2009) in Figure 2.2-3.

Jou measured the equilibrium CO_2 partial pressure with an equilibrium cell. Dugas used a wetted wall column apparatus to obtain CO_2 partial pressures.

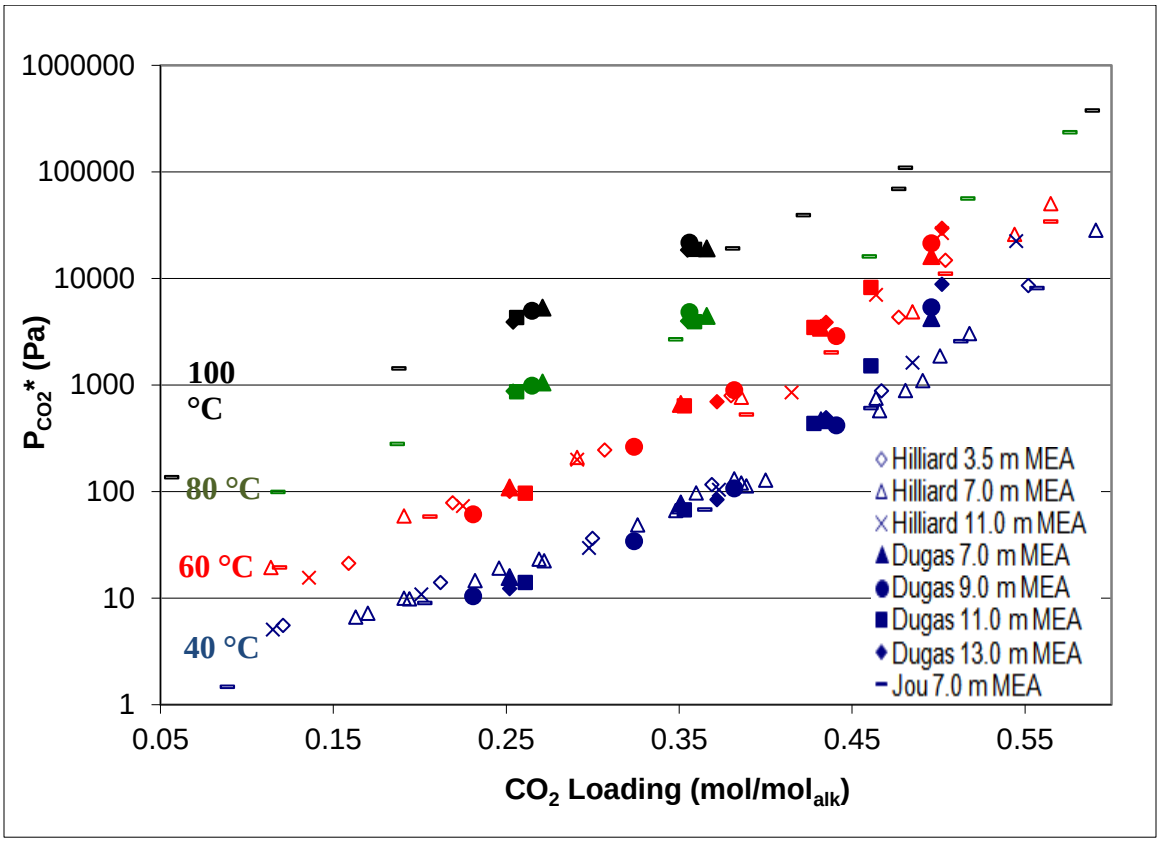

Figure 2.2-3. MEA-CO_2-H_2O: CO_2 Solubility Comparison between FTIR Technique (Hilliard 2008) and Other Methods

Figure 2.2-3, taken from Hilliard (2008), shows that experimental measurements from the FTIR technique are fairly comparable with measurements reported by Jou (1995) and Dugas (2009) with respect to the experimental loading and partial pressure of CO_2. Given that the FTIR data is consistent with those obtained via other analytical techniques, it suffices to conclude that the FTIR method is valid and accurate.

PZ-CO_2-H_2O Benchmarking

Figure 2.2-4 shows how the experimental CO_2 solubility measurements for the PZ-CO_2-H_2O system obtained using the FTIR method compare to those obtained from

other experimental techniques. Data from the current work and those of Hilliard (2008) were obtained using the FTIR analysis. Dugas (2009) measured CO_2 solubility using a wetted wall column whereas Ermatchkov (2006) measured the equilibrium partial pressure using headspace gas chromatography.

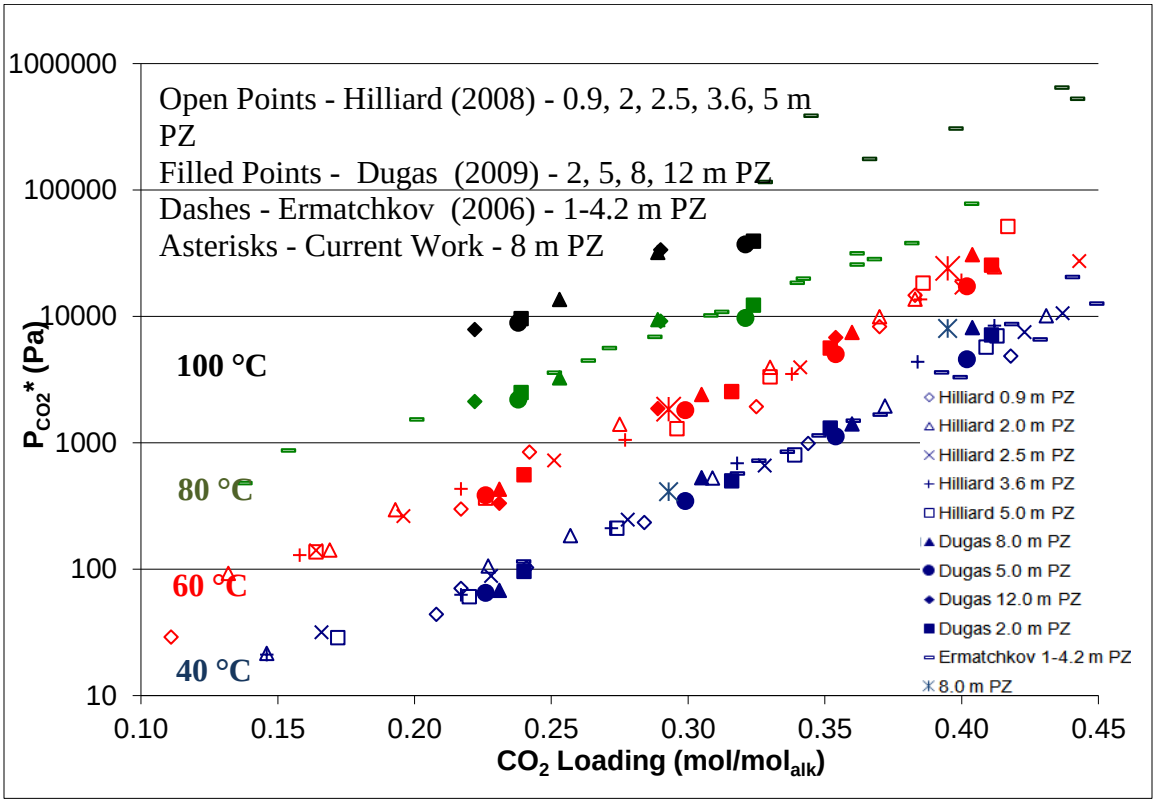

Figure 2.2-4. PZ-CO_2-H_2O: CO_2 Solubility Comparison between FTIR Technique and Other Methods

The experimental CO_2 solubility measurements obtained by both Hilliard (2008) and this work by using the FTIR method are consistent with measurements reported by the literature with respect to the experimental loading and partial pressure of CO_2.

Other Literature Comparisons

Pure MDEA Vapor Pressure

The vapor pressure of pure MDEA (N-Methyldiethanolamine) from 40 ˚ - 65 ˚C was measured and compared to reported DIPPR measurements. Figure 2.2-5 displays the experimental MDEA vapor pressure comparison.

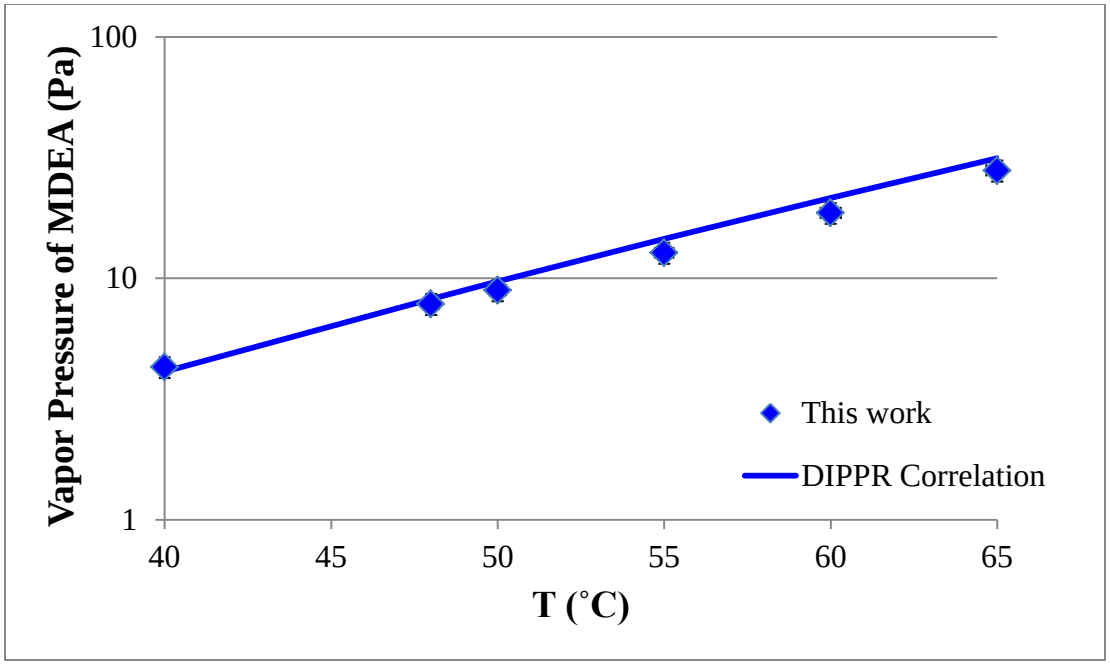

Figure 2.2-5. Vapor Pressure of pure MDEA Literature Comparison

The DIPPR correlation is reported to have a relative standard uncertainty of <5% error. Given this margin of uncertainty, the MDEA vapor pressure measurements from this work are found to be within ±10% of the DIPPR values.

MDEA-H_2O Volatility

Figure 2.2-6 shows measurements of aqueous MDEA volatility, or its partial pressure, for a range of MDEA liquid mole fraction (x_{MDEA}) in comparison to data reported by Kim et al. (2008). This investigator conducted the experiment in an

ebulliometer cell and analyzed the compositions of both the vapor condensate and liquid solution by using Gas Chromatography (GC).

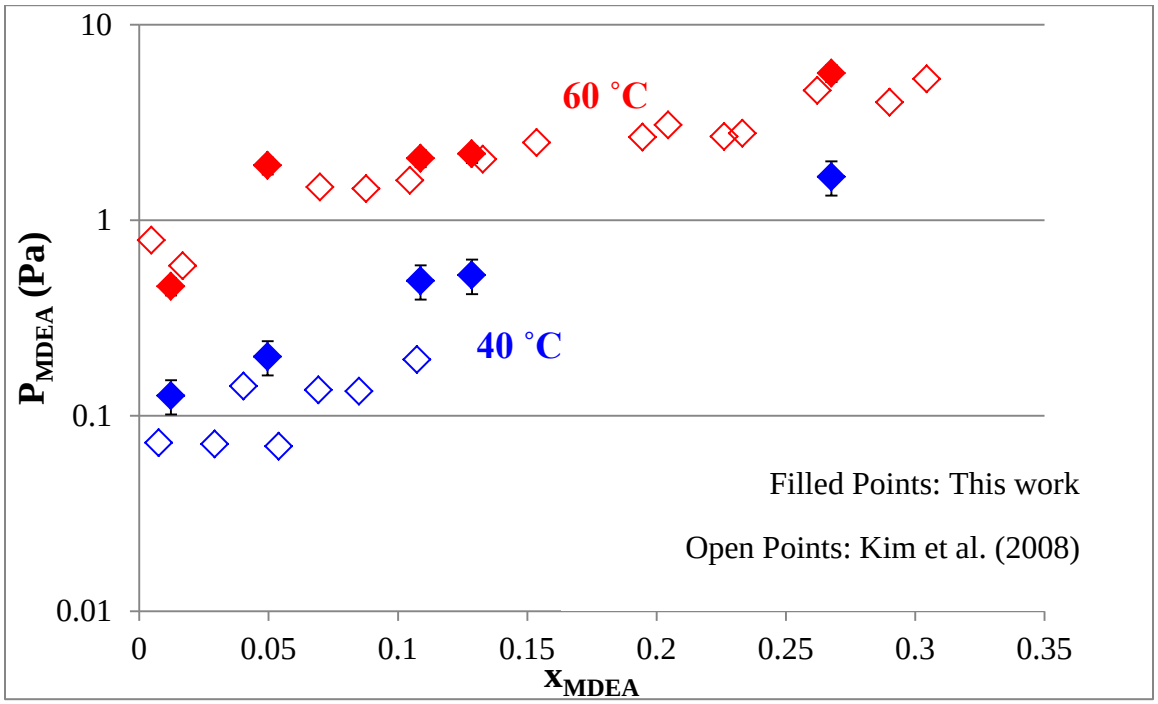

Figure 2.2-6. Aqueous MDEA Volatility Comparison

The experimental MDEA volatility measured by the two techniques agrees fairly well at both temperatures particularly at 60 ˚C. At 40 ˚C, there is a minor offset between the two sets of measurements due to there being a greater degree of experimental uncertainty to both methods as a result of extremely low MDEA volatilities being measured at low temperature. Also, it is expected for there to be greater experimental uncertainty at low temperature with the ebulliometry method which makes use of boiling the solution. At 40 ˚C and extremely low system pressure, the solution will boil but with much lower MDEA content in the overhead than water, thus making it especially challenging to analyze MDEA with good accuracy due to its sheer low quantity in comparison to all the water present.

MEA-H_2O Volatility

Figure 2.2-7 compares measured values of MEA partial pressures from Hilliard (2008) to data reported by Kim et al. (2008).

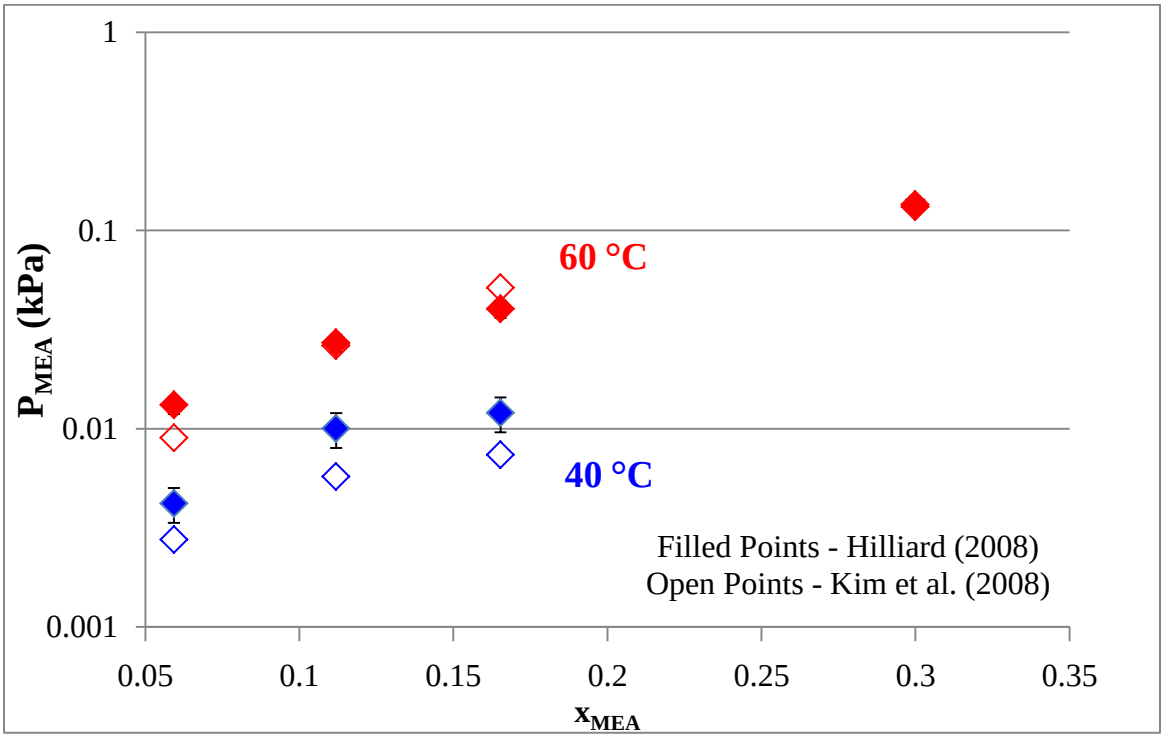

Figure 2.2-7. Aqueous MEA Volatility Comparison

As was in the case of MDEA-H_2O, the experimental MEA volatilities from both techniques agree fairly well for the most part despite a minor offset seen at 40 ˚C. This offset is potentially due to suspected systematic limitation with the ebulliometry method as discussed previously.

MEA-CO_2-H_2O Volatility

Xu (2011), a former Rochelle group member, measured the volatility of 7 m MEA-CO_2-H_2O from 80 – 140 ˚C using a 2-equilibrium cell coupled with FTIR analysis. Using the 7 m MEA volatility measurements along with those of Hilliard (2008) for 3.5 –

11 m MEA at 50 – 60 ℃, Xu (2011) developed an empirical expression which correlated MEA volatility, normalized by the total MEA liquid mole fraction, to temperature and loading. The empirical expression is as follows:

$$ln\left(\frac{P_{MEA}}{x_{MEA}}\right) = (30 \pm 0.3) + (-8153 \pm 96)\frac{1}{T} + (-2594 \pm 81)\frac{\alpha^2}{T} \qquad (2\text{-}1)$$

Figure 2.2-8 shows how the high temperature MEA volatility measurements from Xu (2011) and the low temperature measurements from Hilliard (2008) compare against the empirical model predictions.

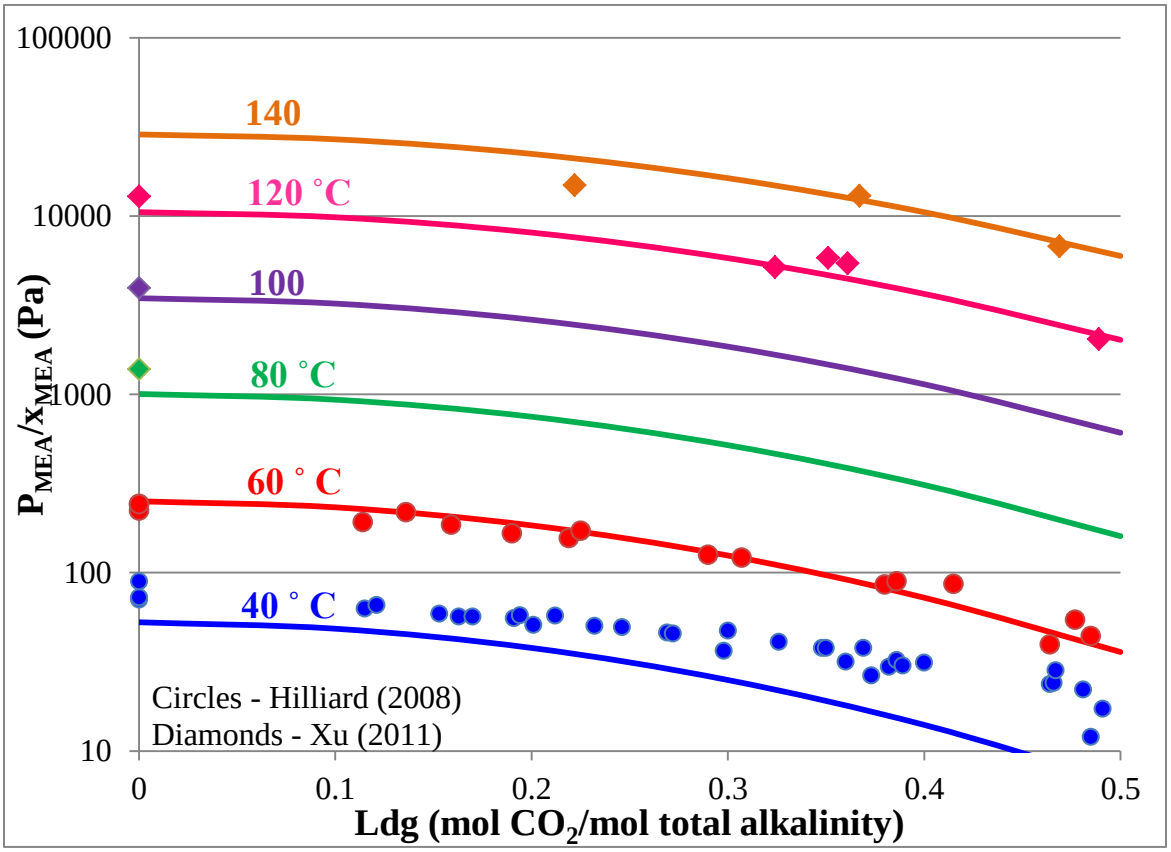

Figure 2.2-8. Comparison of MEA Volatility Measurements for 3.5 – 11 m MEA-CO_2-H_2O between Low vs. High Temperature Apparatus

The MEA volatility measurements for 3.5 – 11 m MEA-CO_2-H_2O at 40 ˚C by Hilliard (2008) are not consistent with the rest of the measurements at other temperature. Thus the 40 ˚C data were excluded from the empirical model regression. This data was later considered to be erroneous due to faulty FTIR calibrations for low MEA concentrations coupled with the fact that the low volatility measurements most likely challenged the detection limit of the instrument. Other than this issue, the rest of the data between the low and high temperature apparatus are internally consistent with each other as evident by observation and the fact that they can both be modeled together by a unifying empirical expression.

PZ-CO_2-H_2O Volatility

Xu (2011) also measured the volatility of 5 – 11 m PZ-CO2-H2O at 120 ˚ and 150 ˚C. Using the low temperature PZ volatility measurements for 2 – 10 m PZ from Nguyen (2010), Xu (2011) also developed an empirical expression to correlate PZ volatility, normalized by the total PZ liquid mole fraction, to temperature and loading. The empirical model for normalized PZ volatility is as follows:

$$ln\left(\frac{P_{PZ}}{x_{PZ}}\right) = (-123 \pm 3) + (21.6 \pm 0.6) ln\,\mathrm{T} + (20.2 \pm 3.5)\alpha + (-18174 \pm 1933)\frac{\alpha^2}{T} \quad (2\text{-}2)$$

Figure 2.2-9 shows how the high temperature PZ volatility measurements from Xu (2011) and the low temperature measurements from Nguyen (2010) compare against the empirical model predictions.

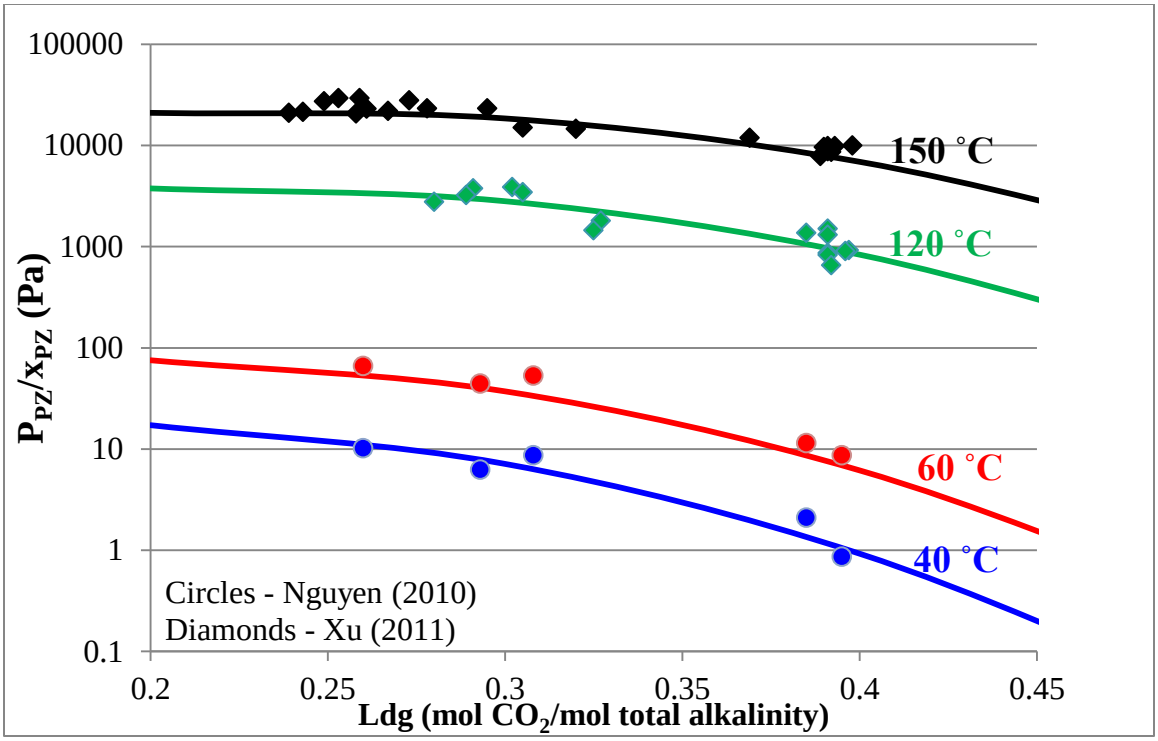

Figure 2.2 – 9. Comparison of PZ Volatility Measurements for 2 – 11 m PZ-CO_2-H_2O between Low vs. High Temperature Apparatus

PZ volatility measurements made by the low and high temperature apparatus are internally consistent with each other. Both sets of measurements show consistent temperature and loading effects on PZ volatility. In addition, the measurements can both be modeled by a unifying empirical expression, which further demonstrate internal consistency.

2.3. Liquid Phase Sampling: Speciation Analysis

In order to have a complete picture of the system VLE, the liquid solutions must also be analyzed for speciation in addition to measuring their headspace volatility. Liquid phase speciation is determined by using Nuclear Magnetic Resonance (NMR) technique. This analysis was performed by the UT Austin Chemistry NMR Department.

Loaded solutions (whose volatilities were measured with the FTIR) cannot simply be submitted for NMR analysis because they are not magnetically active. Unloaded aqueous amine solutions were charged with $^{13}CO_2$ to enhance the NMR response.

The procedure for preparing NMR samples is as follows. A batch of amine-water solution, approximately 5 – 10 g, was prepared and subsequently mixed with 1 wt % 1,4-dioxane (Fisher ≥ 99.9% pure) and 10 wt % deuterium oxide (Cambridge Isotopes, ≥ 99.9% pure). Dioxane serves as an internal reference, while the deuterium oxide acts as a resonance lock for field stabilization to prevent the NMR signal of the sample from being swamped by that of the solvent. The solution was then loaded with $^{13}CO_2$ (99% purity, Cambridge Isotopes Laboratory) using a mini glass sparging apparatus until the desired loading was achieved. Next, the loaded solution was transferred into an NMR tube (Wilmad glass, 5 mm OD x 0.77 mm ID) which was sealed thermally. The NMR analysis was performed with a Varian Inova 500 MHz NMR Spectrometer with variable temperature control. Samples at 40 °C and 60 °C were thermally conditioned by heating for at least 1 hour in a water bath at the temperature of interest prior to NMR analysis.

Both H^1 and C^{13} NMR analyses are used to determine the composition of the liquid sample. Note that with either of these NMR techniques it is not possible to distinguish a species from its protonated form (for example PZ and PZH^+) due to the fast exchange of proton between the unprotonated and protonated species. C^{13} NMR uniquely provides the concentration of bicarbonate in the system, a species which cannot be determined from H^1 NMR since it is generated from $^{13}CO_2$. For all the remaining species in the system other than bicarbonate, both H^1 and C^{13} analyses provide close

results that match well within ±10% of each other. Details regarding NMR peak assignment are provided in Appendix A.

2.4. Liquid Speciation (NMR) Method Validation

MEA-CO_2-H_2O Benchmarking

The experimental liquid speciation method used in this work was benchmarked by Hilliard (2008) for 7 m MEA-CO_2-H_2O and 1 m PZ-CO_2-H_2O systems at 27 ˚C. Figure 2.4-1 illustrates how the speciation analysis from this work compares to the literature for loaded 7 m MEA.

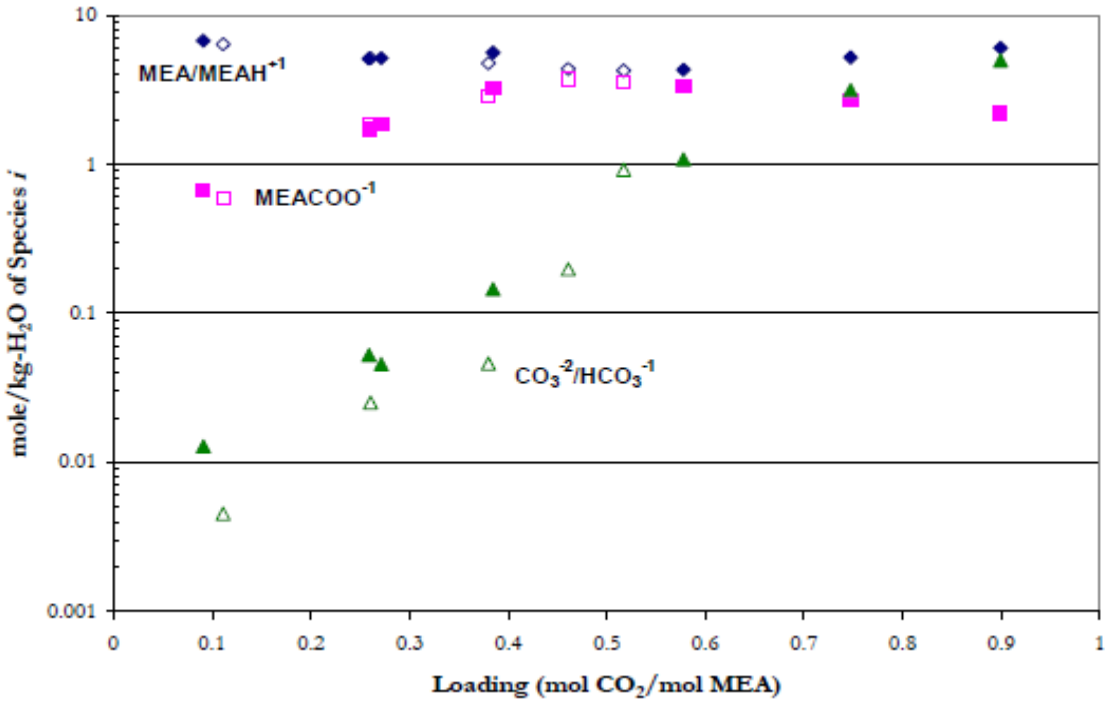

Figure 2.4-1. C^{13} NMR Liquid Phase Speciation for 7 m MEA at 27 ˚C. Closed Points: Poplsteinova (2004). Open Points: Hilliard (2008).

It appears that the experimental speciation from Hilliard (2008) benchmarking agrees well with that of Poplsteinova (2004) for loaded 7 m MEA at 27 ˚C. There is, however, a minor discrepancy in the reported CO_3^{-2}/HCO_3^{-1} concentrations between

Hilliard (2008) and the literature. This offset was potentially attributed to the difficulty of accurately measuring low concentrations at 0.01 – 0.1 mol/kg-H_2O of the species.

PZ-CO_2-H_2O Benchmarking

Hilliard (2008) also benchmarked the liquid speciation NMR method used in this work with literature data for 1 m PZ-CO_2-H_2O system at 27 ˚C. Figure 2.4-2 displays the comparison between the two sets of results.

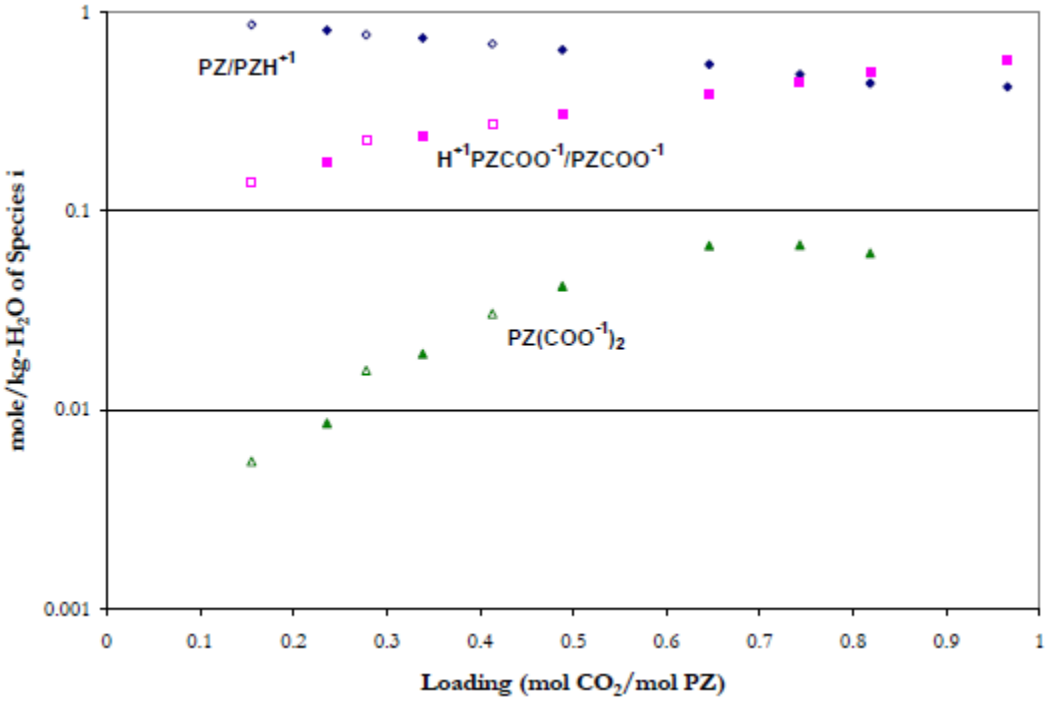

Figure 2.4-2. H^1 NMR Liquid Phase Speciation for 1 m PZ-CO_2-H_2O System at 27 ˚C. Closed Points: Ermatchkov et al. (2003). Open Points: Hilliard (2008).

The experimental speciation results from Hilliard (2008) are seen to agree very well with those of Ermatchkov et al. (2003). These results serve to validate the accuracy of the Liquid Speciation NMR analysis used in this work.

2.5. Heat Capacity Determination

A 304-stainless steel pan (Perkin Elmer #03190218) was filled to capacity with 60 μL of solution before being sealed with a lid and O-ring. When properly sealed, the entire steel cell can withstand an internal pressure up to 150 bars. A vapor headspace of roughly 5–10% in volume was estimated to exist in the sealed unit. The sample pan was then placed against an empty reference pan inside a Differential Scanning Calorimeter instrument (TA Instruments DSC-Q100) to measure the difference in the amount of heat absorbed by the two pans. This amount of heat differential was subsequently used to determine the heat capacity of the solution. Details regarding the Heat Capacity experimental procedure and data interpretation are provided in Appendix C. Below is a snapshot inside the DSC cell where the differential heat absorbed by a reference pan compared to a sample pan is measured.

Figure 2.5-1. Snapshot of DSC Sample Cell

The cell constant and temperature response of the DSC instrument have to be calibrated using Indium metal, which has a known melting point (156.6 ºC). The cell constant is an internal machine parameter that is used to adjust for subtle differences in

the calorimetric response of the unit. In addition, temperature calibration is done to ensure that the sample thermocouple is reading correctly under experimental conditions. The specific heat capacity of a sample can be determined by referencing against the heat capacity of an empty pan and that of a pan containing a known amount of Al_2O_3 which is used to determine a calorimetric sensitivity constant to be discussed later. Figure 2.5-2 shows sample calorimetric profiles of the empty baseline pan, the Al_2O_3 sample, and the sample of interest.

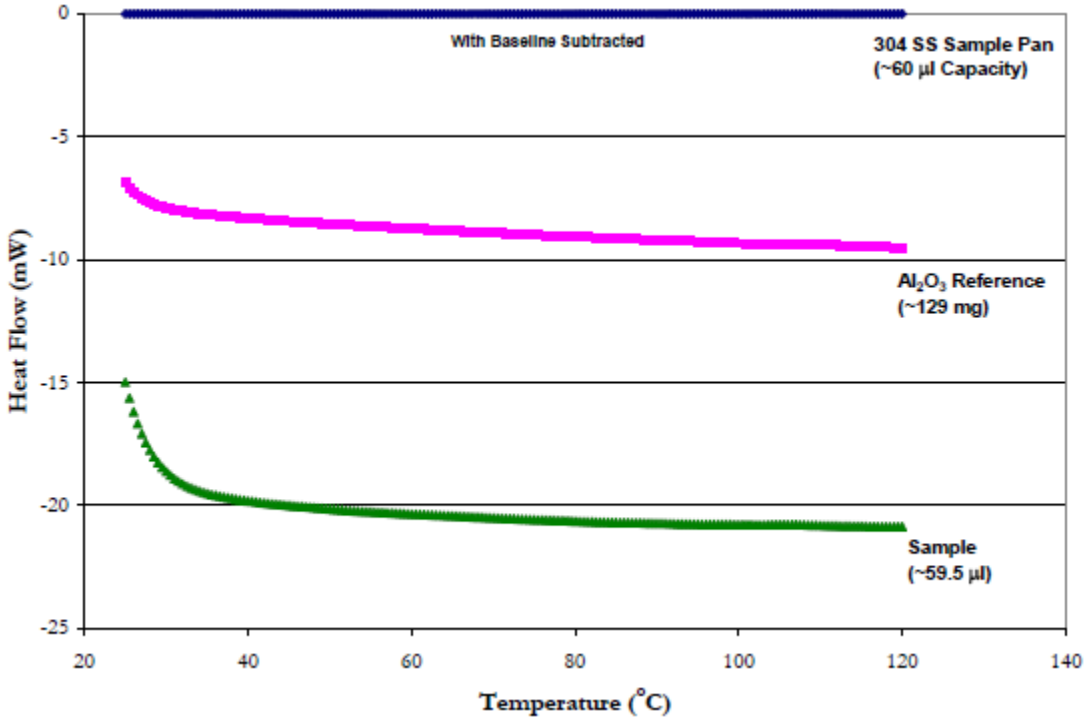

Figure 2.5-2. A Sample of Calorimetric Profiles used to Determine the C_p of the Sample of Interest

The heat capacity of the sample can be determined by the following

$$C_P(s) = \left[\frac{60 \cdot E \cdot D_s}{W_s \cdot b}\right] - \left[\frac{\Delta W \cdot C_P^{pan}}{W_s}\right] \tag{2-3}$$

where

C_p (s) is the specific heat capacity of the sample, kJ/kg-K,
E is the calorimetric sensitivity of the DSC apparatus,
b is the heat rate, 5 ^oC / min,
D_s is the vertical displacement between the empty sample pan and the sample DSC thermal
curves at a given temperature, mW,
W_s is the mass of the sample, mg,
ΔW, is the difference in mass between the reference pan and the sample pan, and
C_p^{pan} is the specific heat capacity of the 304 stainless steel pans

The calorimetric sensitivity constant E can be determined given the known heat capacity of Al_2O_3 by using the expression below:

$$E = \left[\frac{b}{60 * D_{st}}\right]\left[W_{st} \cdot C_P^{Al_2O_3} + \Delta W \cdot C_P^{pan}\right] \quad (2\text{-}4)$$

where

D_{st} is the vertical displacement between the empty sample pan and the Al_2O_3 DSC thermal
curves at a given temperature,
W_{st} the mass of Al_2O_3 sample, mg, and
C_p^{Al2O3} is the specific heat capacity of Al_2O_3

Details pertaining to the complete heat capacity procedure used in this work can be referenced to Hilliard (2008).

2.6. Heat Capacity Method Validation

The experimental heat capacity method was benchmarked by measuring the heat capacity of water, pure MEA, and that of MEA-H_2O system for comparison against literature. These benchmarking activities were performed and reported by Hilliard (2008).

Pure H_2O System Benchmarking

Figure 2.6-1, taken from Hilliard (2008), shows the experimental water heat capacity measured by Hilliard (2008) in comparison to literature values.

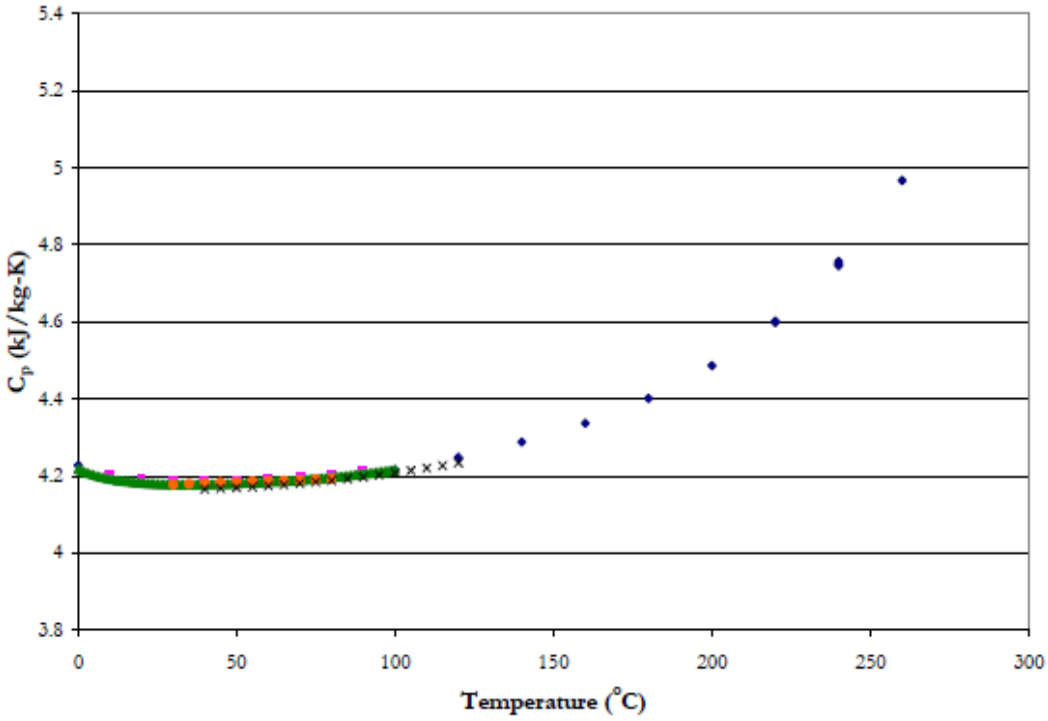

Figure 2.6-1. Specific Heat Capacity of Water . Points: ♦ Kell et al. (1984); ■ Engineering Sciences Data (1966); ▲ Osborne et al. (1939); ●Chiu et al. (1999); × Hilliard (2008)

The experimental water heat capacity measurements from this method were found to be ±0.4% of the average specific heat capacity of water reported in the literature. Since the experimental measurements from this method tend to underestimate literature data, it was estimated that the measurements would have ±2% (Hilliard 2008).

Pure MEA Benchmarking

In addition to benchmarking pure water heat capacity, the experimental heat capacity method of this work was also benchmarked by Hilliard (2008) with pure MEA

heat capacity since these measurements were commonly established in the literature. Figure 2.6-2 compares the experimental MEA C_p of this work to other sources.

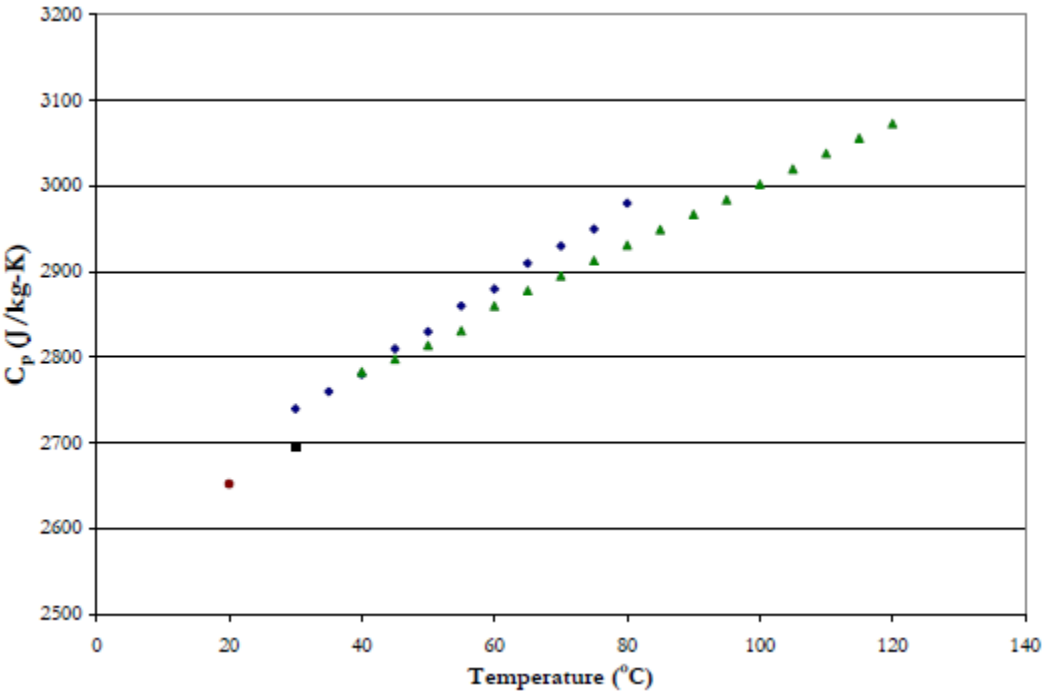

Figure 2.6-2. Specific Heat Capacity of MEA. Points: ■ The Dow Chemical Company (1981); ● Swanson and Chueh (1973); ♦ Chiu et al. (1999); ▲ Hilliard (2008).

It appears that the experimental C_p of MEA measured by Hilliard (2008) agrees well with that of the literature to within ±2%. Furthermore, the experimental C_p measurements from Hilliard (2008) also show similar temperature dependence to the literature.

MEA-H_2O Heat Capacity

The C_p of 3.5 m and 7 m MEA-H_2O at 40 ˚, 60 ˚, and 80 ˚C were also benchmarked by Hilliard (2008) to the literature. Graphs will not be shown here due to some of the original data being missing, but it was concluded that the experimental C_p for

aqueous MEA systems matched well with literature values over the entire temperature and concentration range.

2.7. Error & Data Reproducibility Analysis

Amine Volatility Measurements

In order to quantify the degree of experimental precision between runs, duplicate samples were prepared for PZ-CO_2-H_2O system and analyzed for the same experimental conditions. Table 2.7-1 shows the experimental errors, or precision, between duplicate runs for 8 m PZ-CO_2-H_2O volatility measurements at 0.3 and 0.4 loading, respectively.

Table 2.7-1. An Example of Experimental Precision Analysis (8 m PZ-CO_2-H_2O)

			40 ˚C			60 ˚ C		
	PZ (m)	Ldg (mol CO_2/mol tot alk)	P_{CO2} (Pa)	P_{PZ} (Pa)	P_{H2O} (Pa)	P_{CO2} (Pa)	P_{PZ} (Pa)	P_{H2O} (Pa)
Run A*	7.96	0.293	410	0.784	5889	1844	5.58	15572
Run C	8.19	~0.3 (gravimetric)	424	0.713	6083	1975	5.29	15157
Error			3.35%	9.01%	3.28%	7.12%	5.28%	2.66%
Run B	7.87	~0.4 (gravimetric)	9525	0.088	5903	24974	0.951	16409
Run D*	7.93	0.395	8187	0.108	5918	23968	1.09	15486
Error			16.4%	18.8%	0.2%	4.2%	13.2%	6.0%

* denotes the run that was used to report the data

Note that the loadings from runs B and C were not analyzed with TIC (only the gravimetric loadings were reported). Nevertheless, one can get a sense of how much a target CO_2 loading can vary when prepared gravimetrically and how that variation can drive the component partial pressures in duplicate runs.

For a targeted gravimetric loading, the CO_2 partial pressure can be seen to vary anywhere from 3% up to 16 - 20% in between the runs at 0.3 and 0.4 loading, respectively. The higher the target loading, the greater the difference in CO_2 partial pressure between runs. This is because CO_2 partial pressure is an exponential function

with respect to loading, therefore any small deviation in loading from one run to the next would result in a big difference in CO_2 partial pressure.

PZ partial pressures are seen to vary from 9% to 19% between the runs at 0.3 and 0.4 loading, respectively. The main source of discrepancy in PZ partial pressure between runs is attributed to the difference in loading between the runs which drive the PZ volatility accordingly. A different source for the discrepancy, which is not reflected in the error analysis in Table 2.7-1, is the inherent variation in the FTIR analysis. An analysis of the same sample can vary from 0.5% to 2%. Also the smaller the amine partial pressure, the greater the error in the measurement which can also translate into greater variation between different analyses of the same sample, or between different runs with the same targeted gravimetric loading. Small amine partial pressures are more difficult to detect than high partial pressures because the instrument is operating closer to the detection limit (<10 ppm or < ~1 Pa).

Finally, differences in water partial pressures between the runs that are targeted to have approximately the same gravimetric loading are typically much less than 10%. This is because water partial pressures are very high in these systems, thus the relative variation in these pressures among runs is relatively small. Also the FTIR is known to provide very reliable water measurements. This is because water is the most dominant species in the systems considered in this work and has the largest concentration.
The same level of experimental uncertainty between runs, along with the likely error sources discussed above, can be expected for other amine systems as well.

Heat Capacity Measurements

For any given sample, four runs are used to determine and report the averaged heat capacity of the sample. The precision, or reproducibility of the runs, was determined by Hilliard (2008) by benchmarking the measured heat capacity of water from four runs. Figure 2.7-2 shows the measurements of water heat capacity from the runs for 40 ˚ - 120 ˚C.

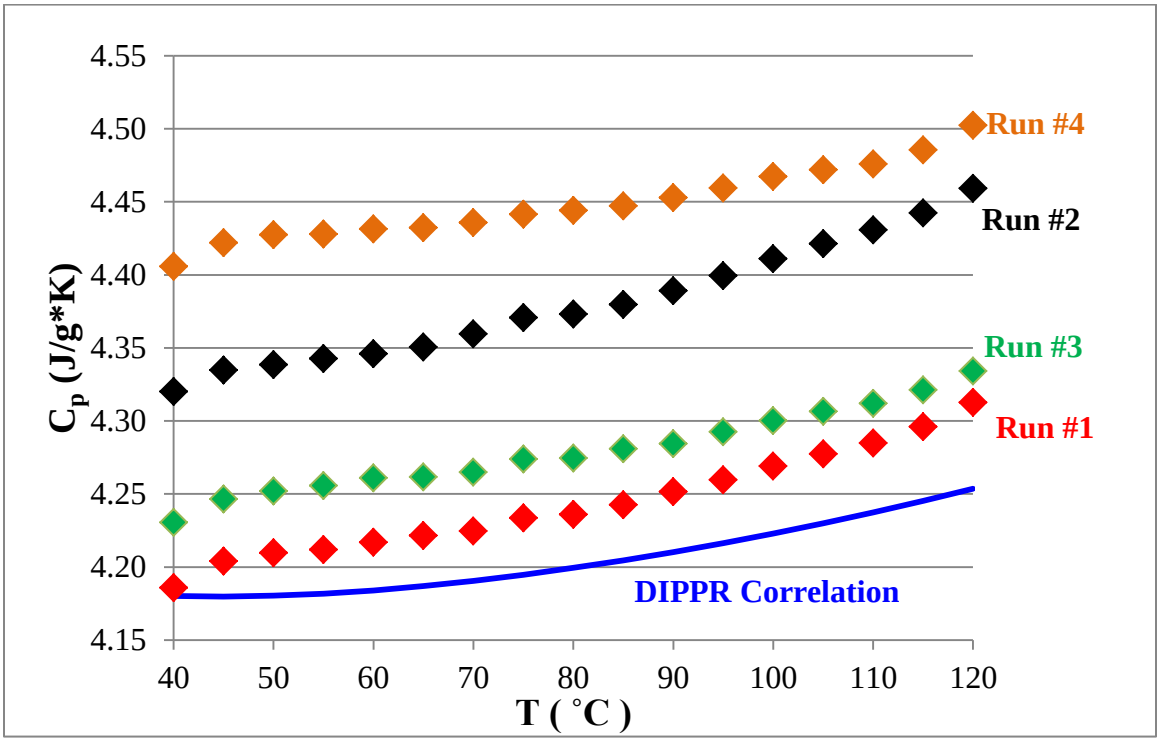

Figure 2.7-1. Reproducibility of the Specific C_p Experiments for H_2O

The standard deviation, or reproducibility, between the runs was found to be ±10%. This same level of reproducibility can be expected for other systems measured. In Figure 2.7-1 above, note that the 40 ˚C data points seem to be lower than expected, or are somewhat out of line with the rest of the series. This phenomenon is considered to be an instrumental anomaly or artifact of the DSC that is yet to be explained. Also, the

temperature behavior of Run #2 from ~90 ˚ - 120 ˚C is steeper than what is known to be according to the DIPPR water heat capacity correlation. This behavior is sometimes observed in runs for other systems as well, and is attributed to the phenomenon of CO_2, amine, and water vaporization, or even partial boiling in this case with pure water, into the small headspace above the solution. The degree of species vaporization into the headspace is a function of both the species concentrations in solution and the headspace volume, which is estimated to be anywhere from 10% - 15% of the entire sample cell. This headspace is present as a result of the part of the lid that stands above the top of the pan (filled to its maximum capacity ~ 60 μL).

In the analysis of samples, a correction has to be made to account for the phenomenon of CO_2 and H_2O vaporization into the headspace at high temperature (~90 ˚ - 120 ˚C). The analysis used to correct for species vaporization involves determining the gap space volume above the solution which would minimize the sum of squared residuals between the measured heat capacities (with vaporization) and the calculated heat capacities (estimated without vaporization). The calculated heat capacities are determined from the true enthalpy of solution, $Q_{solution}$, which is estimated by subtracting the heats associated with CO_2 and H_2O vaporization from the total measured enthalpy. Using empirical models developed for CO_2 solubility and H_2O volatility, one can calculate the partial pressure of these species above solution; subsequently the moles of each species can be determined by using the Ideal Gas Law (assuming a gap space volume) which can then be used to estimate the heats associated with the species vaporization.

Chapter 3: Aqueous Amine Volatility in Binary Amine-Water System

3.1. Introduction

The study of amine volatility in dilute amine-water systems provides key understanding that is crucial to the design of water wash units used in the CO_2 capture process. Typical water wash operations involve treating gas with only a few ppm of amine and up to 15 mole % of water. Aqueous amine volatility at the water wash condition also needs to be measured in order to quantify fugitive amine emission to the atmosphere. There is also a scientific interest in having a better understanding of amine-water interactions to generalize and predict the volatilities of a large number of amines used in CO_2 capture without the need for extensive experimentation.

While there are several published measurements on the VLE of amine-water systems, only a few of them measure the vapor phase mole fraction of the amine. This work measures the vapor composition of the amines, particularly at very dilute amine concentration, to elucidate the intrinsic amine-water interactions. Furthermore, this work is believed to provide one of the largest collections of experimental data of amine volatility in water for as many as 20 amines that are relevant to CO_2 capture.

Other work that investigated aqueous amine volatility will now be summarized. Lenard et al. (1990) measured the gas phase composition of monoethanolamine (MEA) in binary aqueous solution (343K and 363K) using gas chromatography. These data were represented using a three-parameter Redlich-Kister expansion. Pappa et al. (2006) made isobaric T-x-y measurements for the AMP-H_2O system at 66.7, 80.0, and 101.3 kPa using a modified Swietoslawski ebulliometer with sample compositions being determined using

a standard curve of refractive index for this system at 25 ˚C. Kim et al. (2008) used an ebulliometer setup to determine the total pressure with the liquid and vapor mole fractions of MEA, methyldiethanolamine (MDEA), and methylaminopropanolamine (MAPA) analyzed using gas chromatography. Cai et al. (1996) measured isobaric VLE at 101.3 kPa and 66 kPa (373K - 443K) of MEA in water using the standard curve of refraction index versus the mole fraction of the binary mixture at 20 ºC. The liquid phase activity coefficients were calculated with the UNIFAC group contribution model as published by Larsen et al. (1987).

This work investigates the aqueous volatility of 20 amines that are potentially viable for CO_2 capture, including MEA, piperazine (PZ), and MDEA. The amine partial pressure was obtained experimentally at the absorber operating conditions of 40 ˚– 70 ˚C and 1 atm using a hot gas FTIR. Given the partial pressures, the amine Henry's constants can be determined and are used as the primary indicator of amine volatility. A group contribution model is developed using experimental H constants from this work along with those of 16 alkylamines obtained from the literature.

This model is believed to be more reliable and accurate in the prediction of amine volatility for CO_2 capture amines (alkanolamines) than existing group contribution models such as UNIFAC and that of Hine and Mookerjee (1975). Although these other models are regressed using a larger database of compounds, they are not able to adequately predict the volatilities of alkanolamines since their functional group parameters were largely regressed from alkylamine data. The alkanolamines used for CO_2 capture application are much more structurally complex than alkylamines. In the

case of the alkanolamines, the presence of hydroxyl and ether groups can influence the interaction of the amine group with water differently than how the alkyl groups in alkylamines affect the interaction of the amine group with water. Thus, amine group parameters regressed from alkylamine data are not reliable in predicting the volatility of alkanolamines such as the ones used in CO_2 capture.

3. 2. Theory

Amine volatility is expressed using the amine Henry's constant (H):

$$H_{amine} = \frac{P_{amine}}{\gamma^*_{amine} * x_{amine}} \quad (3\text{-}1)$$

where:

P_{amine} is the amine partial pressure (Pa)
x_{amine} is the amine liquid phase mole fraction
γ^*_{amine} is the asymmetric amine activity coefficient defined at the reference state of infinite dilution of amine in water

At the dilute amine concentrations used in the experiments (~0.1–1.05 m amine in H_2O), the amine asymmetric activity coefficients are assumed to be 1. Extrapolating the data from the dilute experimental concentration to infinite dilution shows that the amine asymmetric activity coefficients are usually within ±10% of unity. This result will be demonstrated in the *Results and Discussion* section.

The symmetric activity coefficient for an amine infinitely diluted in water, γ^{∞}_{amine}, can be estimated by using the UNIFAC-Dortmund Modified group contribution theory (UNIFAC-DMD). Therefore the amine Henry's constant can be calculated as:

$$H_{amine} = \gamma^{\infty}_{amine} P^{sat}_{amine} \quad (3\text{-}2)$$

The amine partition coefficient, K, between the air and the solution, as defined in the group contribution model by Hine and Mookerjee (1975) is:

$$K = \frac{c_w}{c_g} \tag{3-3}$$

where:

c_w is the concentration of dilute amine in water (mol/L or M)
c_g is the concentration of amine in the vapor or air (mol/L or M)

The amine partition coefficient K can be converted into the amine Henry's constant H (Pa) using the equation below:

$$H_{amine} = \frac{RT\rho_M}{K} \tag{3-4}$$

where:

R is the universal gas constant (8.314 m^3*Pa/mol*K)
T is temperature in K
ρ_M is the molar density of water (mol/m^3)
K is the dimensionless partition coefficient from Eq. (3-3)

The temperature dependence of the amine Henry's constants is assumed to have Arrhenius behavior in accordance with the Gibbs-Helmholtz relation as follows:

$$\frac{d \ln H_{amine}}{d\left(^1/_T\right)} = \frac{-\Delta H_{solution}}{R} \tag{3-5}$$

The amine Henry's constant is estimated as a function of temperature by:

$$H_{amine}(\mathrm{T}) = H_{amine,313.15K} e^{\frac{-\Delta H_{solution}}{R}\left(\frac{1}{T(K)} - \frac{1}{313.15K}\right)} \tag{3-6}$$

3.3. Data

Table 3.3-1 gives the experimental amine partial pressure and Henry's constant for all the CO_2 capture alkanolamines investigated in this work. Amine and water partial pressure is estimated to have ±6% error. The experimental amine H constants are expected to have ±10% error in consideration of: (1) experimental uncertainty and (2) amine solutions being dilute but not infinitely diluted in water.

Table 3.3-1. Experimental Amine H Constant and Partial Pressure from 40 ˚– 70 ˚C

T (C)	P_{amine} (Pa)	P_{H2O} (kPa)	H_{amine} (Pa)		T (C)	P_{amine} (Pa)	P_{H2O} (kPa)	H_{amine} (Pa)
0.5 m MDEA (N-Methyldiethanolamine)					**0.09 m 1,4 DMPZ (1,4-Dimethyl Piperazine)**			
40	0.265	7.39	29.7		40	2.71	6.87	1510
45	0.288	9.38	32.3		45	4.44	8.63	2470
50	0.312	12.6	35.0		50	8.15	11.4	4540
55	0.369	15.9	41.4		55	12.9	14.8	7160
60	0.455	19.8	51.0		60	21.0	18.6	11700
65	0.593	25.4	66.5		65	33.8	24.1	18800
70	0.767	31.4	85.9		70	53.1	30.7	29500
0.48 m PZ (Piperazine)					**0.47 m DMAEE (2,2-Dimethylamino Ethoxy Ethanol)**			
40	0.399	7.27	46.6		40	0.504	7.05	60.0
45	0.516	9.17	60.2		45	0.614	8.74	73.2
50	0.630	12.2	73.5		50	0.803	11.5	95.8
55	0.930	15.5	109		55	1.46	14.9	174
60	1.36	19.3	159		60	2.04	18.8	243
65	2.11	25.0	246		65	3.69	24.3	440
70	3.09	31.7	361					
					0.57 m DMEA (Dimethylethanolamine)			
0.45 m DGA® (Diglycolamine®)					40	21.4	6.93	2110
40	0.153	7.06	19.1		45	31.5	8.72	3100
45	0.159	8.95	19.8		50	47.7	11.5	4700
50	0.169	11.7	21.0		55	69.7	15.0	6860
55	0.202	15.3	25.1		60	96.9	18.9	9540
60	0.261	19.0	32.5		65	139	24.4	13700
65	0.382	24.5	47.5		70	194	30.8	19200
0.49 m MAPA (3-Methylamino Propylamine)					**0.48 m MORPH (Morpholine)**			
40	1.28	9.11	147		40	8.78	7.05	1020
45.1	1.56	12.0	178		45	13.1	8.94	1530
50	2.54	16.3	291		50	19.0	11.8	2220
55	3.34	20.5	382		55	26.6	15.1	3100

60	4.96	26.3	567		60	39.6	19.2	4620
65.2	7.47	33.8	855		65	54.7	24.7	6380
					70	76.5	31.0	8930
0.5 m EDA (Ethylenediamine)					**0.28 m DMORPH (Dimorpholino Diethyl Ether)**			
40	0.892	7.29	100		40	0.254	6881	50.7
45	1.03	9.19	116		45	0.263	8675	52.5
50	1.59	12.2	179		50	0.283	11567	56.5
55	2.09	15.8	234		55	0.371	15057	74.0
60	3.05	19.7	342		60	0.394	19046	78.5
65	4.10	25.3	459		65	0.465	24730	92.7
					70	0.491	31112	97.8
0.7 m MEA (Ethanolamine) (Kim et al., 2008)					**0.13 m HEP (Hydroxyethyl Piperazine)**			
40	0.728	7.28	60.0		40	0.089	7172	38.0
60	5.87	19.6	432		45	0.168	9065	72.1
80	13.9	46.4	954		50	0.341	11854	146
100	49.8	99.5	3481		55	0.393	15341	169
					60	0.460	19226	197
0.3 m DAP (1,2-Diaminopropane)					65	0.506	24804	217
40	0.636	5.76	118		70	0.596	31279	255
45	1.21	7.54	226					
50.2	1.59	10.0	295		**0.22 m DL-ALA (DL-Alaninol)**			
55	2.13	13.1	397		40	0.680	7075	172
60.1	3.01	17.3	561		45	0.839	9068	213
65	4.03	22.1	750		50	1.12	11858	285
					55	1.67	15147	424
1.05 m 1MPZ (1-Methyl Piperazine)					60	2.55	18934	645
40	2.65	6.87	143		65	4.20	24215	1065
45	4.94	8.82	266					
50	7.51	12.3	405		**0.5 m DEA (Diethanolamine)**			
55	11.6	14.6	628		40.1	0.178	7387	19.9
60	18.7	18.6	1010		45	0.199	9283	22.3

65	29.1	23.7	1566		50	0.215	12078	24.1
					55	0.227	15771	25.4
0.44 m AMP (2-Amino-2-Methyl-1-Propanol)					60	0.240	19565	26.9
40	2.48	7.27	316		65	0.243	25154	27.2
45	3.60	9.19	458					
50	5.71	12.2	727		**0.95 m 2MPZ (2-Methyl Piperazine)**			
55	8.50	15.9	1082		40	0.811	6758	48.2
60	12.2	19.8	1547		45	1.26	8674	75.0
65	18.2	25.5	2315		50	2.13	10850	127
					55	2.87	13685	170
0.1 m HMDA (Hexamethylenediamine)					60	4.46	17798	265
40	0.265	6.98	148		65	7.24	21681	431
45	0.277	8.78	154		70	10.6	33589	630
50	0.284	11.6	158					
55	0.366	14.9	204					
60	0.530	18.7	295					
65	0.809	24.2	450					
70	0.931	29.5	518					

Table 3.3-2 displays the experimental H constants for 16 alkylamines at 25 ˚C as provided by Hine and Mookerjee (1975).

Table 3.3-2. Henry's Constants for 16 Alkylamines at 25 ˚C

Amine	H_{amine} (Pa)
Ethylamine	57,100
Propylamine	68,700
Butylamine	84,500
Pentylamine	137,000
Hexylamine	150,000
Dimethylamine	99,200
Diethylamine	143,000
Dipropylamine	286,000
Dibutylamine	509,000
Piperidine	24,900
Pyrrolidine	13,400

Hexamethyleneimine	34,400
Trimethylamine	584,000
Triethylamine	826,000
N-Methylpyrrolidine	169,000
N-Methylpiperidine	194,000

3.4. Amine Structures

Figure 3.4-1 shows the structures for all 20 amines that were investigated in this work.

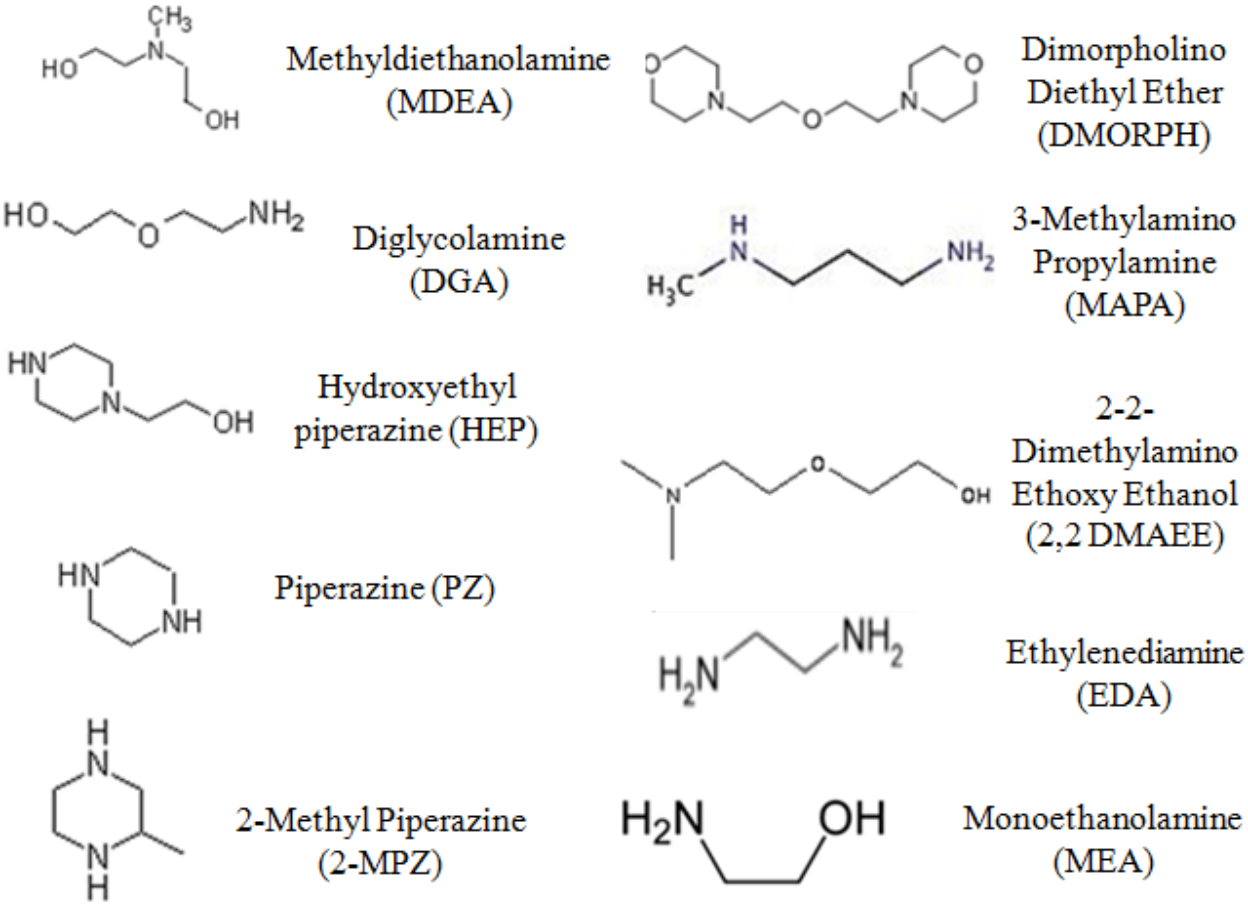

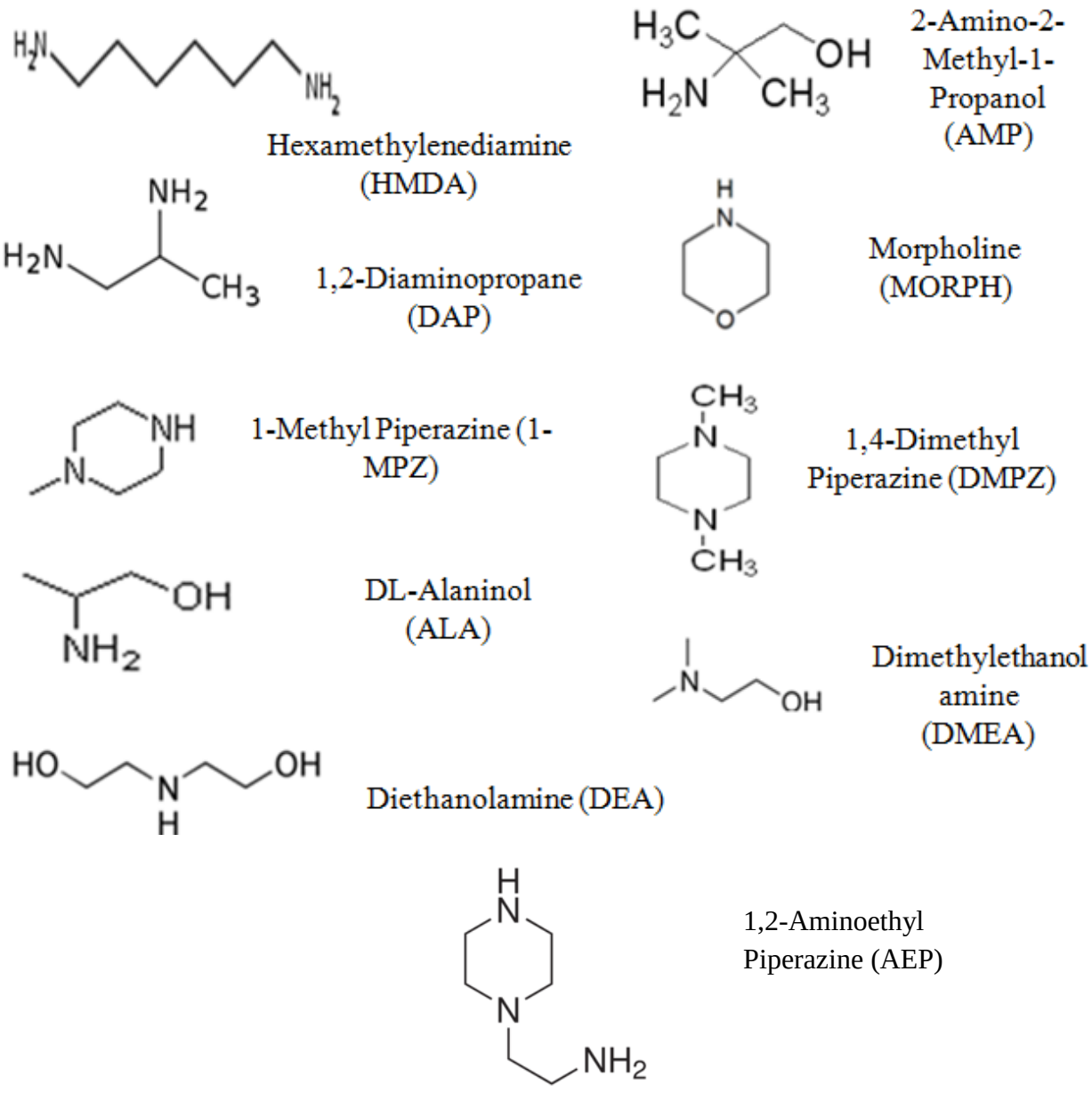

Figure 3.4-1. Amine Structures

3.5. Results and Discussion

Comparison of Amine H Constants from this Work to UNIFAC-DMD Predictions

In using Eq. (3-2) from above, the amine H constants at 40 ˚C can be computed from the infinite dilution activity coefficients of amines in water as estimated by the UNIFAC-DMD group contribution theory. Table 3.5-1 shows the estimated H constants for a number of alkanolamines from this work in comparison to experimental values at 40 ˚C.

Table 3.5-1. Comparison of Experimental Amine H Constants to Calculated Values from UNIFAC-DMD at 40 ˚C

Amine	$\gamma^{\infty UNIFAC}_{amine,}$	$P^{sat}_{amine,}$	H^{UNIFAC}_{amine}	H^{exp}_{amine}	H^{UNIFAC}/H^{exp}
MDEA	10.2	4.11 ± 0.21	41.9 ± 2.14	29.7 ± 2.97	1.41
PZ	0.776	1140 ± 57	885 ± 44.2	46.6 ± 4.66	19.0
DGA	19.8	10.9 ± 0.5	216 ± 9.90	19.1 ± 1.91	11.3
EDA	0.007	3980 ± 200	27.9 ± 1.40	100 ± 10	0.279
MEA	0.443	164 ± 8.20	72.7 ± 3.63	60.1 ± 6.01	1.21
1,2 DAP	0.086	3600 ± 180	310 ± 15.5	118 ± 11.8	2.63
HMDA	0.458	163 ± 8.10	74.4 ± 3.71	148 ± 14.8	0.503
DMEA	5.00	1210 ± 60.5	6050 ± 303	2110 ± 211	2.87
MORPH	1.41	3004 ± 150	4240 ± 211	1030 ± 103	4.12
HEP	3.71	10.8 ± 0.538	40.1 ± 2.00	38.0 ± 3.80	1.06
DEA	8.02	0.379 ± 0.019	3.04 ± 0.152	19.9 ± 1.99	0.153

The symmetric amine infinite dilution activity coefficients (defined at the reference state of pure amine), γ^{∞}_{amine}, at 40 ˚C are estimated with UNIFAC-DMD method using AspenPlus® V.7.3. The amine saturation pressures at 40 ˚C are all interpolated values based on experimental data (with stated standard deviations <5%) obtained from DIPPR Thermodynamic Database. Any potential inaccuracy in the final amine H constants estimated by UNIFAC-DMD is mainly attributed to inaccuracy in the

estimated infinite dilution activity coefficients rather than to errors in the experimental amine saturation pressures (which were stated to have low experimental uncertainties of <5%). For the majority of amines shown in Table 3.5-1, the experimental H constants from this work and those predicted by UNIFAC-DMD theory agree within an order of magnitude.

HEP (hydroxyethyl piperazine) and MEA (monoethanolamine) show the closest agreement between the experimental value and the UNIFAC-DMD prediction. This observation serves to validate the accuracy of the experimental method of this work by indicating that there is no systematic issue with the method, which could result in a gross systematic discrepancy between UNIFAC-DMD and the experimental method for all amines where one set of values is consistently higher or lower than the other.

PZ (piperazine) and DGA (diglycolamine) show the greatest discrepancy by more than an order of magnitude between experimental versus estimated H constant values. It is unexpected that DGA has a much greater estimated H constant (~216) compared to MDEA (~41.9) according to UNIFAC-DMD. This observation implies that DGA is more volatile than MDEA which seems rather counterintuitive as MDEA is believed to be more nonpolar than DGA due to the presence of the methyl group, which should increase its volatility due to unfavorable interaction with water. This hypothesis is validated by experimental measurements which show that the measured H constant of DGA is ~19.1 whereas that of MDEA is ~29.7. This translates to aqueous MDEA being more volatile than aqueous DGA experimentally. Another important conclusion that can be drawn from comparing MDEA to DGA is that aqueous amine volatility does not

necessarily correlate with pure component volatility. At 40 ˚C, although DGA has a greater saturation pressure than MDEA, the latter is believed and shown experimentally to have greater aqueous volatility. Due to the obvious discrepancy between UNIFAC-DMD and experimental measurements, it is determined that it is crucial to investigate alkanolamines extensively in order to elucidate the true interaction between amine and water, which is the main driver of amine volatility.

Comparison of Amine Henry's Constants from this Work to Hine and Mookerjee Group Contribution Methodology (1975)

Table 3.5-2 summarizes the amine Henry's constant, as determined from the partition coefficient K estimated by using the group contribution method established by Hine and Mookerjee (1975), and the experimental Henry's constants measured by this work at 25 ˚C.

Table 3.5-2. Comparison of Experimental Amine H Constants to Calculated Values from Hine and Mookerjee (1975) at 25 ˚C

	$H^{H\&M}_{amine,\ 25C}$	$H^{exp}_{amine,\ 25C}$	$H^{H\&M}/H^{exp}$
MDEA	1.38E-04	27.5	5.00E-6
PZ	37.9	40.4	9.40E-1
DGA	0.001	17.8	6.75E-5
MAPA	3.54	127	2.79E-2
EDA	9.98	87.8	1.14E-1
MEA	0.561	52.0	1.08E-2
1,2 DAP	4.16	103	4.05E-2
1-MPZ	158	118	1.34E+0
AMP	9.75	268	3.64E-2
HMDA	39.7	134	2.96E-1
1,4 DMPZ	659	1230	5.38E-1
2,2 DMAEE	0.021	50.9	4.19E-4
DMEA	9.98	1810	5.51E-3
MORPH	615	883	6.97E-1

DMORPH	8.49E-06	48.2	1.76E-7
HEP	0.002	33.6	6.50E-5
ALANINOL	2.34	148	1.58E-2
DEA	0.020	19.4	1.05E-3
2-MPZ	158	40.4	3.92E+0

The majority of amines in Table 3.5-2 show gross discrepancy between the estimated H constants by Hine and Mookerjee (1975) and the experimental H constants at 25 ˚C. In the case of almost all of the amines shown, there are functional groups in the amine structures that are not present in Hine and Mookerjee, including $CH_2(C)(OH)$, $CH_2(C)_2(N)$, $N_{cy}(C_{cy})_2(CH_3)$, $C(C)_3(N)$, $CH_3(N_{cy})$, $C_{cy}H_2(C_{cy})(O_{cy})$, $O_{cy}(C_{cy})_2$, $N_{cy}(C_{cy})_2(C)$, $CH_2(C)(N_{cy})$,$CH(N)(C)_2$, and $C_{cy}H(N_{cy})(C_{cy})(CH_3)$, where the groups denoted in parentheses designate neighboring groups that are attached to the base group not enclosed in parentheses. The cy subscript denotes a cyclic structure which is a feature not present in the Hine and Mookerjee model (1975).

In the cases of cyclic amines, aromatic groups have to be used in place of cyclic groups to make the estimates. A few of the cyclic amines show less than 50% discrepancy between calculated and experimental values, which suggest that the functionality of aromatic groups may be similar enough to those of cyclic groups to where one can perhaps be used in place of the other without incurring significant errors. As for the straight chained amines, all of them show nearly 100% error between calculated and experimental values. It appears that the amine H constants calculated by Hine and Mookerjee (1975) are most often systematically lower than the experimental values. This result is because the calculated values are derived from alkylamines which

do not possess many of the complex functional groups present in alkanolamines used for CO_2 capture; furthermore, alkylamines are orders of magnitude more volatile than alkanolamines which introduce large errors when extrapolating to the latter.

Deviation of the experimental H constant from the true H constant at infinite dilution

This work assumes that the experimental Henry's constant is within ±10% of the actual Henry's constant at infinite dilution in water. This generalized assumption is made for all amine systems studied based on an analysis of PZ-H_2O. Figure 3.5-1 shows how the experimental (asymmetric) activity coefficient of PZ in H_2O varies with PZ at 60°C.

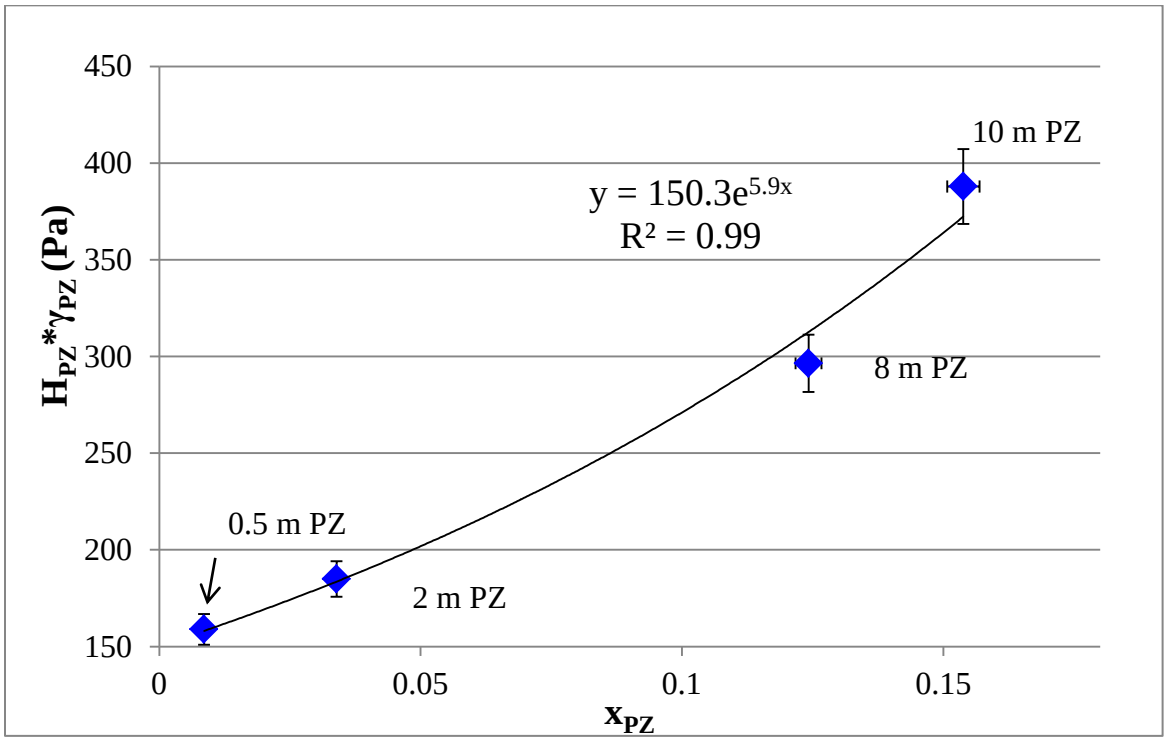

Figure 3.5-1. Behavior of Asymmetric PZ Activity Coefficient in H_2O at 60 ˚C

The true Henry's constant, determined by extrapolating this data to an infinitely diluted PZ concentration, is ~150.3 Pa. Table 3.5-3 summarizes the estimated asymmetric PZ activity coefficient at other PZ concentrations.

Table 3.5-3. PZ Activity Coefficient for 0.5–10 m PZ at 60 ˚C, $H_{PZ,60C}$ ~150 Pa

PZ (m)	x_{PZ}	$\gamma_{PZ,60C}$
0.5 m	8.57E-03	1.05
2 m	3.39E-02	1.22
8 m	1.24E-01	2.08
10 m	1.54E-01	2.48

The experimental PZ Henry's constant at 60 ˚C was determined at the most dilute PZ concentration where volatility was still detectable by the FTIR (0.5 m PZ). At this concentration, the asymmetric PZ activity coefficient is estimated to be 1.05. Therefore, the experimental PZ Henry's constant estimated, 157.8 Pa, using data for 0.5 m PZ will have an error of within ±10% compared to the true PZ Henry's constant of 150.3 Pa. For all other amine systems studied, the experimental H constants are generally assumed to have at most ±10% error as the amine concentrations were varied between 0.1 and 1.05 m amine. The exact percentage of error cannot be determined for each amine because no extensive data was taken to study amine volatility as a function of amine concentration.

Base Case Group Contribution Model

The experimental Henry's constants for 19 alkanolamines studied in this work from 40 ˚ - 70 ˚C, along with those of 16 alkylamines at 25 ˚C as reported by Hine and Mookerjee (1975), were used to regress group contribution parameters for the following base case model developed to represent amine H constant as a function of temperature:

$$ln\,H\,(Pa) = Intercept + B\left(\frac{1}{313.15K} - \frac{1}{T(K)}\right) + C\big(T(K)\big) + \sum kj * nj \tag{3-7}$$

where:

k_j is the parameter value for functional group j
n_j is the number of occurrences of group j in an amine structure

With this model form, all of the amines are assigned the same temperature dependence, which is nonlinear in reciprocal temperature with two adjustable parameters. Table 3.5-4 provides the regressed parameter values for Eq. (3-7).

Table 3.5-4. Regressed Parameter Values for Base Case Group Contribution Model

Parameter	Value	Standard Error (±)
N_{cy}	-3.90	0.38
N	-2.87	0.36
OH	-2.48	0.23
O	-1.70	0.25
CH_2, CH	0.216	0.08
C_{cy}	0.703	0.15
CH_3-(C)	0.952	0.15
CH_3-(N)	1.10	0.14
CH_3-(N_{cy})	1.60	0.19
B	-139,458	17,863
C	1.36	0.17
Intercept (Pa)	-417	54

12 parameters were used to represent both the functional group contributions and temperature dependence of 35 amines from 40 ˚ - 70 ˚C (a total of 139 data points). This model establishes two important distinctions: (1) cyclic (cy) versus non-cyclic structure – this distinction is not found in the earlier group contribution model by Hine and Mookerjee (1975) but is warranted in this work; (2) differentiation among different types of methyl groups based on the neighboring groups attached to them – in this case, the

neighboring group attached to the methyl can either be a straight chained amine (N), a cyclic amine (N_{cy}), or a straight chained carbon (C). Also, in contrast to other group contribution models, this one does not distinguish between the different types of amine group (primary, secondary, versus tertiary). Parameter N encompasses the total number of nitrogens in a given straight chained amine. The parameter N_{cy} denotes the number of nitrogens in a cyclic amine. The parameter O signifies the sum of ether groups in a given amine regardless of whether that amine is cyclic or not. The goodness of fit statistic R^2 is ~0.90 which indicates a robust fit of the experimental H. The parameter values are all statistically significant as they are large compared to their corresponding standard errors.

In Table 3.5-4, the functional group parameters are ranked from top to bottom in the order of most polar to most non-polar as given by their signed magnitudes. The presence of polar groups tends to lower the tendency to volatilize into the vapor phase; thus, polar groups are seen to have negative parameter values as they decrease the magnitudes of the H constants. The opposite is true for the case of non-polar groups.

Figure 3.5-2 illustrates how the calculated H constants, obtained from the base case model, compare to experimental values.

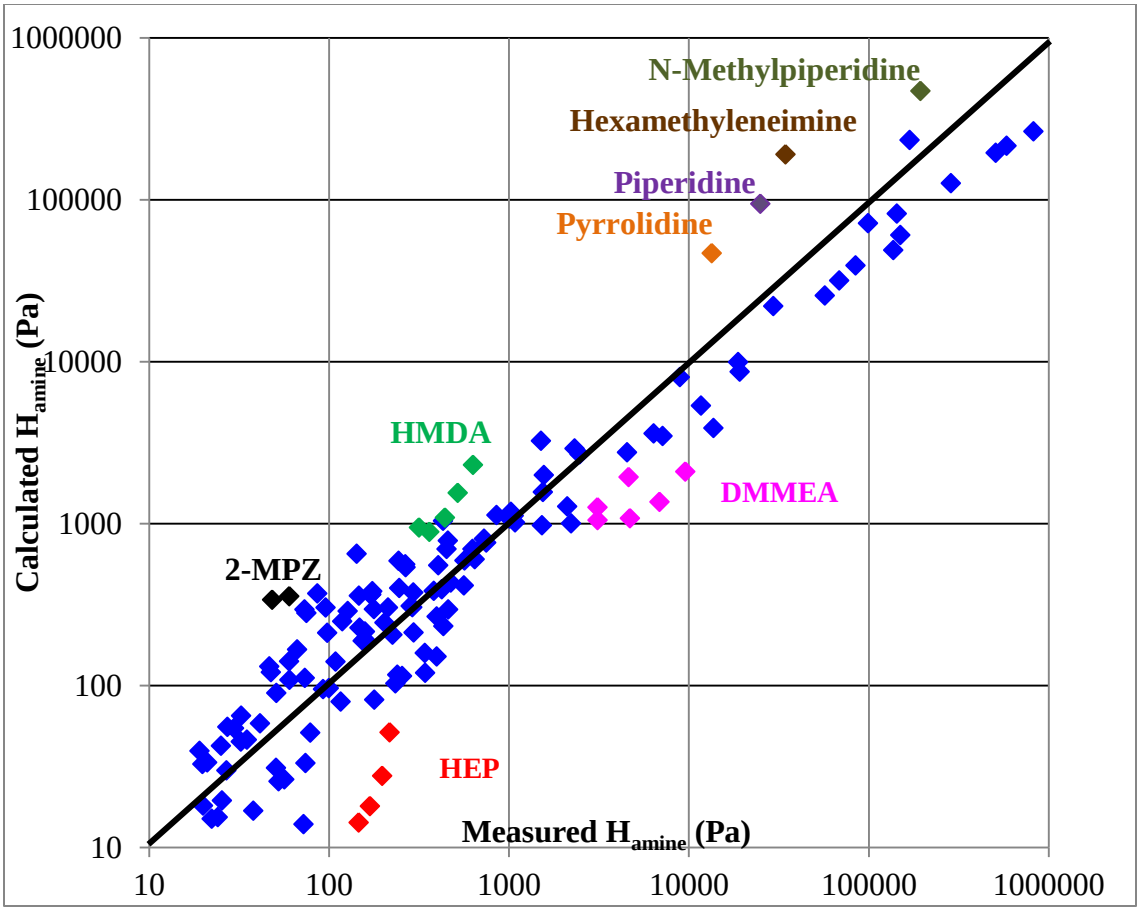

Figure 3.5-2. Evaluation of the Base Case Aqueous Amine Henry's Constant Model

The base case model under-predicts the temperature dependent volatility of low volatile alkanolamines such as HEP and DMMEA. Meanwhile, it tends to overestimate the volatilities of highly volatile alkylamines. With the exception of the outliers noted, the base case model is able to represent the H of the amines to within an order of magnitude of the experimental values over five decades of H.

Rigorous Group Contribution Model

In addition to the base case model, a rigorous model was also generated to provide a more sophisticated representation of aqueous amine H. The rigorous model

consists of three parts: (1) a correlation of H constants at 40 ˚C to molecular structures using a group contribution method; (2) a correlation of the individual enthalpies of amine solution to group contribution; (3) an extrapolation of H constants as a function of temperature using Eq. (3-6) which makes use of the estimated values of H at 40 ˚C and the enthalpies of solution.

In order to develop a correlation between the H constants, of both alkanolamines and alkylamines, at 40 ˚C and molecular structures, it was necessary to obtain estimates of the alkylamine H constants at 40 ˚C from the literature. The H constants of a number of alkylamines at 40 ˚C were obtained by using published values of H constants at 25 ˚C along with the measured enthalpies of solution of the different alkylamines. The experimental H constants for the alkylamines at 25 ˚C are from Hine and Mookerjee (1975) whereas the enthalpies of solution are obtained from the compilation by Sander (1999). The complete citation for the source of each enthalpy measurement in the Sander compilation is provided in the Reference section. The alkylamine H constants at 40 ˚C (313.15K) are then estimated using Eq. (3-6) given the values of $H_{amine,\ 25\ ^\circ C}$ and the enthalpies of solution.

Table 3.5-5. Henry's Constants of Alkylamines at 298K and 313K($H_{amine,\ 298K}$ from Hine and Mookerjee 1975; $\Delta H_{sol}/R$ from cited references in Sander 1999)

Alkylamine	H_{298K} (experimental)	ΔH_{sol}/ R (K)	H_{313K} (est.)
Pyrrolidine	13,388	7,600[c]	45,394
Piperidine	24,930	7,900[c]	88,701
Hexamethyleneimine	34,413	8,200[c]	128,487
Ethylamine	57,111	3,600[a]	101,836
Dimethylamine	99,247	4,000[a]	188,717
Diethylamine	143,456	10,000[b]	715,237
N-Methylpyrrolidine	168,546	7,600[c]	571,471

N-Methylpiperidine	193,517	7,900[c]	688,536

a: Wilhelm et al. (1977)
b: USEPA (1982)
c: Cabani et al. (1971)

The experimental H constants at 40 ˚C for 19 of the CO_2 capture amines studied in this work and for the 8 alkylamines (shown in Table 3.5-5) were correlated to molecular structures using the following semi-empirical model:

$$ln\, H_{amine,313.15K}\ (Pa) = Intercept + \sum k_j * n_j \quad (3\text{-}8)$$

where:

k_j is the parameter value for functional group j
n_j is the number of occurrences of group j in an amine structure

Group j is a group (amine, hydroxyl, or ether) that exists at a given bond juncture in a straight chained amine structure. Group j_{cy} designates a group that exists at a given bond juncture in a cyclic amine structure. Group j-(i) denotes a base group j (either a CH_2 or CH_3 in this case) at a given bond juncture that is connected to a neighboring group i at an adjacent bond juncture (either a carbon, amine, or hydroxyl neighbor) in an amine structure.

A total of 27 data points, representing the H constants of 27 amines at 40 ˚C, were regressed using XLSTAT 2012 to obtain the functional group parameter values. Table 3.5-6 summarizes the parameter results for Eq. (3-8).

Table 3.5-6. Group Parameter Values for Aqueous H Constant Estimates at 40 ˚C

Group j	Parameter Value	Standard error (±)
N	-18.9	2.2
NH	-15.0	1.7
O	-13.8	1.6

NH_2	-12.1	1.1
OH	-10.8	0.98
N_{cy}	-7.57	0.38
O_{cy}	-4.30	0.55
CH_2-(CH_2)	0.126	0.20
CH_3-(CH)	0.160	0.30
C_{cy}	0.294	0.20
CH_3-(N_{cy})	1.85	0.32
CH_3-(N)	4.48	0.69
CH_2-(OH/N)*	5.41	0.68
Intercept (ln Pa)	17.5	0.98

*****a CH_2 group that is attached to either a hydroxyl or nitrogen group on either side

This model differentiates between primary (NH_2), secondary (NH), and tertiary (N) amines. There are also two other important distinctions made among the groups: (1) cyclic (cy) versus non-cyclic – this distinction is not found in the earlier group contribution model by Hine and Mookerjee (1975) but is found to be necessary in this work to improve the fit; (2) differentiation among different types of methyl groups (CH_3) and methylene groups (CH_2) by the neighboring groups attached to them – in this case, the neighboring group attached to the methyl, or methylene group, can either be a straight chained amine (N), a cyclic amine (N_{cy}), a hydroxyl (OH), or a straight chained alkyl group.

The goodness of the fit statistic, R^2 , is ~0.985 which indicates a robust fit of the experimental H_{amine}. The majority of the parameter values are statistically significant as they are larger than their corresponding standard errors. Finally, all of the group parameters used are determined to be independent with no two groups having a

correlation greater than 0.9. The pair of parameters with the largest correlation though still acceptable, ~0.865, is N_{cy} and C_{cy}. This is expected as both the nitrogen and carbon are found to naturally exist on the same cyclic molecule side by side, thus it can be rationalized that there is an overlap in their molecular functionalities that is difficult to isolate to each individually. Other pairs of parameters showing high but acceptable correlation are the CH_2-(OH/N) with OH (~0.696), and CH_3-(N) with N(~0.738). Again the groups within each pair are adjacent neighbors thus resulting in a molecular overlap that is difficult to isolate to each group individually. Not only is there a functional overlap due to the group proximity to each other, there is also a mathematical overlap because the hydrophilic groups (OH, N) are independent groups, thus to mathematically represent the joint contribution of the polar group with an alkyl group can be confounding.

In Table 3.5-6, the functional group parameters are ranked from top to bottom in the order of most polar to most non-polar as given by their signed magnitudes. Polar groups, such as the amines and ether, are hydrophilic in nature. The presence of hydrophilic groups tends to lower the tendency of an amine to volatilize into the vapor phase; thus, hydrophilic groups are seen to have negative parameter values which decrease the magnitudes of the H constants. Conversely, non-polar groups such as the alkyl groups tend to increase the tendency of an amine to volatilize; therefore, they have positive parameter values which increase the magnitudes of the H constants. Methyl or methylene groups attached to hydrophilic groups (nitrogen or OH) appear especially more hydrophobic than those that are attached to carbons. Although there is no definitive scientific explanation for why this is the case, it can perhaps be hypothesized that

hydrophilic neighoring groups are more electronegative than carbon neighboring groups, thus withdrawing electrons from the base methyl (or methylene) group to a greater extent than the latter, which decreases the electronegativity difference between the atoms in the base methyl (or methylene) group and thereby making the base group more nonpolar than they would be otherwise.

The intercept used in the model is physically significant and has units of ln Pa. Since the ln H_{amine} modeled has units of ln Pa, it follows that the intercept must also have units and is needed to anchor the reference state of the system to infinite dilution in water. Without the use of this intercept, the signs of the polar versus nonpolar groups would be counterintuitive and consequently lose physical significance. If H_{amine} is expressed as a unitless partition coefficient K using Eq. (3-4), then the model would be ln K (unitless) = $1.24 + \sum k_j * n_j$. The values of all the group parameters would be the same as shown in Table 3.5-6. Given that K is the concentration of the amine in water divided by its concentration in the gas, the polar groups would have positive values as they increase the amine concentration in water due to favorable aqueous interactions, and vice versa.

Figure 3.5-3 shows how the amine H constants calculated from the rigorous model compare to experimental values at 40 ˚C.

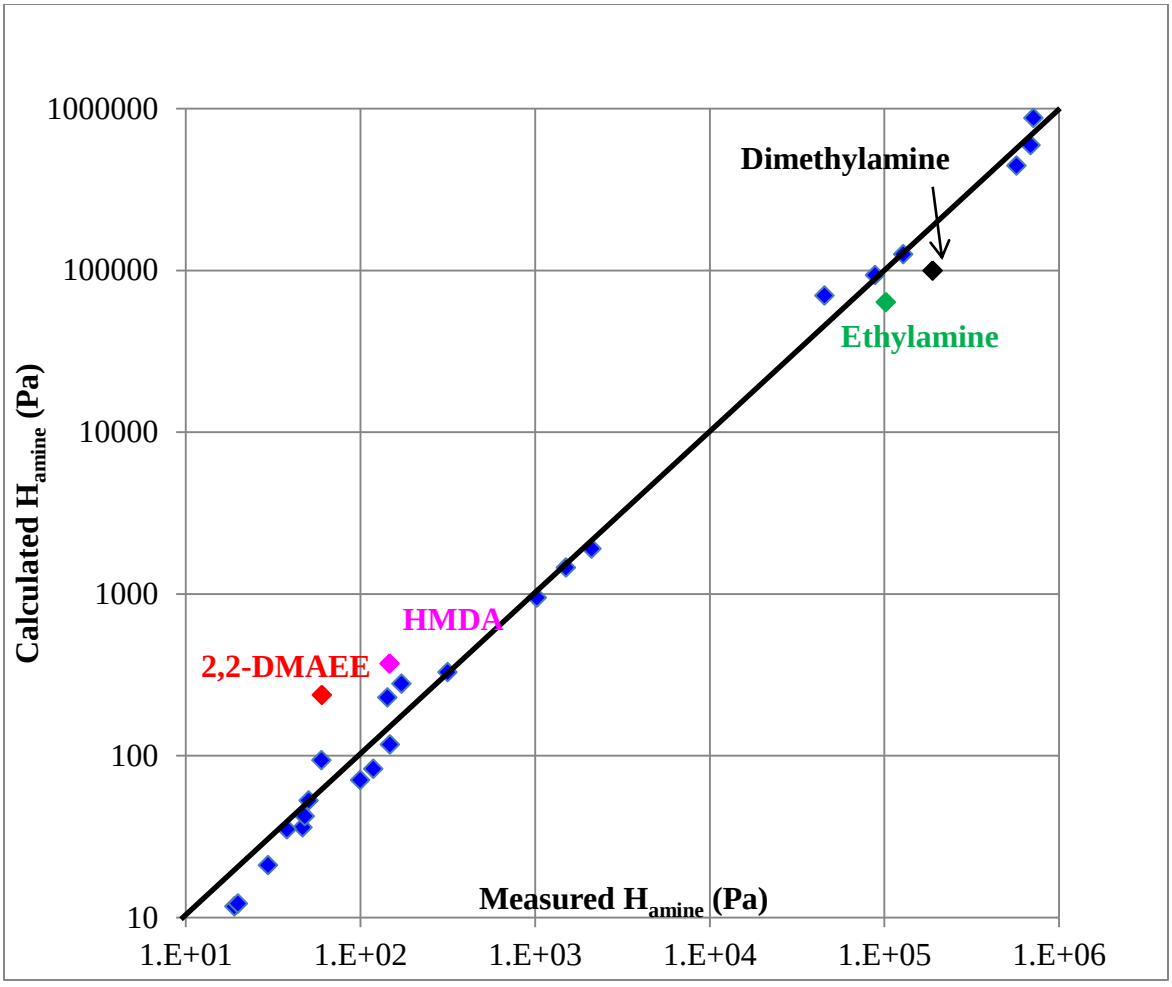

Figure 3.5-3. Evaluation of the Rigorous Amine H Constant Model (40 ˚C)

It can be seen that the rigorous model can represent the majority of the amine H constants at 40 ˚C to well within an order of magnitude of the experimental values.

The second portion of the rigorous model involves representing the temperature behavior of the amine Henry's constants between 25–70 ˚C. In theory, the model should be able to extrapolate even outside this temperature range given its form from Eq (3-6). The experimental enthalpies of solution for the 19 amines measured in this work are obtained by taking the derivative of natural log of the measured Henry's constants with respect to inverse temperature according to the Gibbs-Helmholtz relation expressed in

Eq. (3-5). The enthalpies of the remaining 8 alkylamines were measured by different authors and summarized in Sander (1999). Table 3.5-7 shows $\Delta H_{solution}/R$ for all 27 amines studied, including the alkylamines.

Table 3.5-7. Summary of Amine Enthalpies of Solution

Amine	$\Delta H_{solution}/R$ (K)
MDEA	3822
PZ	7438
DGA	3742
MAPA	7563
EDA	6730
MEA	7613
1,2 DAP	7425
1-MPZ	9941
AMP	8477
HMDA	4980
1,4 DMPZ	10697
2,2 DMAEE	8542
DMEA	7911
MORPH	7747
DMORPH	2636
HEP	6369
ALANINOL	7743
DEA	1322
2-MPZ	9169
Pyrrolidine	7600
Piperidine	7900
Hexamethyleneimine	8200
Ethylamine	3600
Dimethylamine	4000
Diethylamine	10000
N-Methylpyrrolidine	7600
N-Methylpiperidine	7900

The experimental enthalpies of solution for all 27 amines are correlated to the functional groups presented earlier according to the following form:

$$\frac{\Delta H_{solution}}{R}\ (K) = Intercept + \sum f_j{*}n_j \qquad (3\text{-}9)$$

Table 3.5-8 summarizes the functional group parameter values, f_j, for the enthalpy of solution correlation.

Table 3.5-8. Functional Group Parameter Values for Amine $\Delta H_{solution}/R$

Group j	Parameter Value	Standard error (±)
CH_2-(OH/N)	-2610	2098
CH_3-(N)	-1961	2137
O_{cy}	-720	1713
CH_2-(CH_2)	-269	618
C_{cy}	405	612
CH_3-(N_{cy})	974	988
N_{cy}	1292	1164
OH	1830	3011
CH_3-(CH)	1831	921
NH_2	3716	3262
Intercept	4236	3033
O	5116	4867
NH	5483	5303
N	10345	6906

The R^2 for the enthalpy of solution fit is only ~0.65 which indicates that the fit is not good. A number of the parameters are not statistically significant given the magnitudes of their standard errors relative to the parameter values themselves. This lack of fit suggests that there is not a strong intrinsic correlation between the enthalpy of amine solution with molecular structure as there is between structure and aqueous volatility. Nevertheless, a group contribution method must also be used to represent the enthalpies of amine solution for purposes of representation and prediction of new amines

in the future. It is also possible that the temperature dependence of H_{amine} has not been measured accurately without systematic or random error. The range of temperature in this work is only 40 to 70°C. The accuracy of FTIR measurements at low amine partial pressure (low T) may create a systematic error.

Figure 3.5-4 shows how the enthalpies of amine solution predicted using group contribution parameters from Table 3.5-8 compare to experimental values.

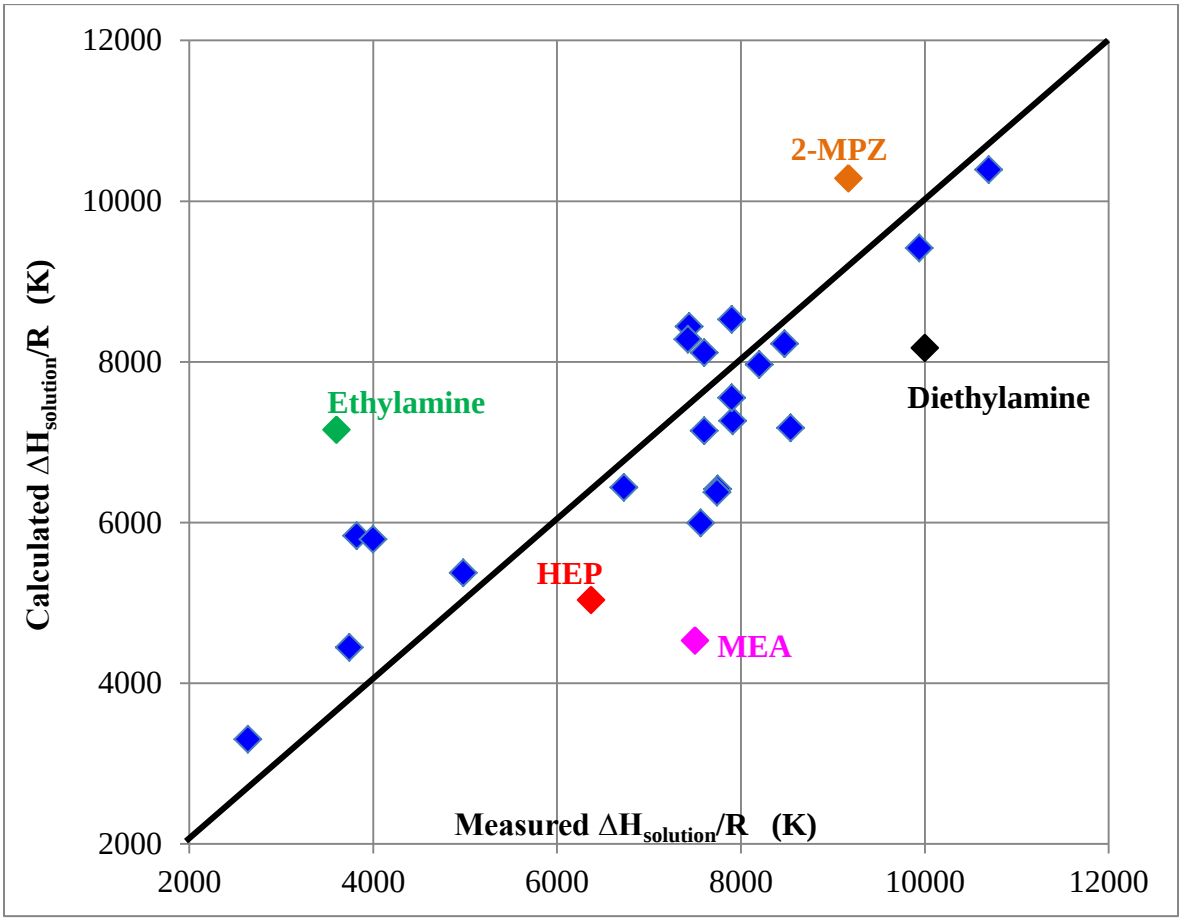

Figure 3.5-4. Evaluation of Predicted Enthalpies of Amine Solution

In Figure 3.5-4, despite the lack of a strong fit, the calculated enthalpies of solution for the majority of the amines were still well within ±35% of the experimental

values with the exception of a few outliers including MEA. A possible reason for why MEA is not fitted well is because it potentially dimerizes in solution with other MEA molecules by hydrogen bonding. If this is the case, then the model does not have a term to account for the effect of dimerization. Also, this phenomenon, if it is happening in solution, is hard to detect and quantify.

Given the calculated amine Henry's constant at 40 ˚C Eq. (3-8) and the calculated enthalpy of solution Eq. (3-9), one can predict the Henry's constant at any temperature of interest using Eq. (3-6). Figure 3.5-5 compares the experimental and predicted values of the amine Henry's constant for all 35 amines (19 alkanolamines and 16 alkylamines) considered in this work for the range of temperature from 25–70 ˚C.

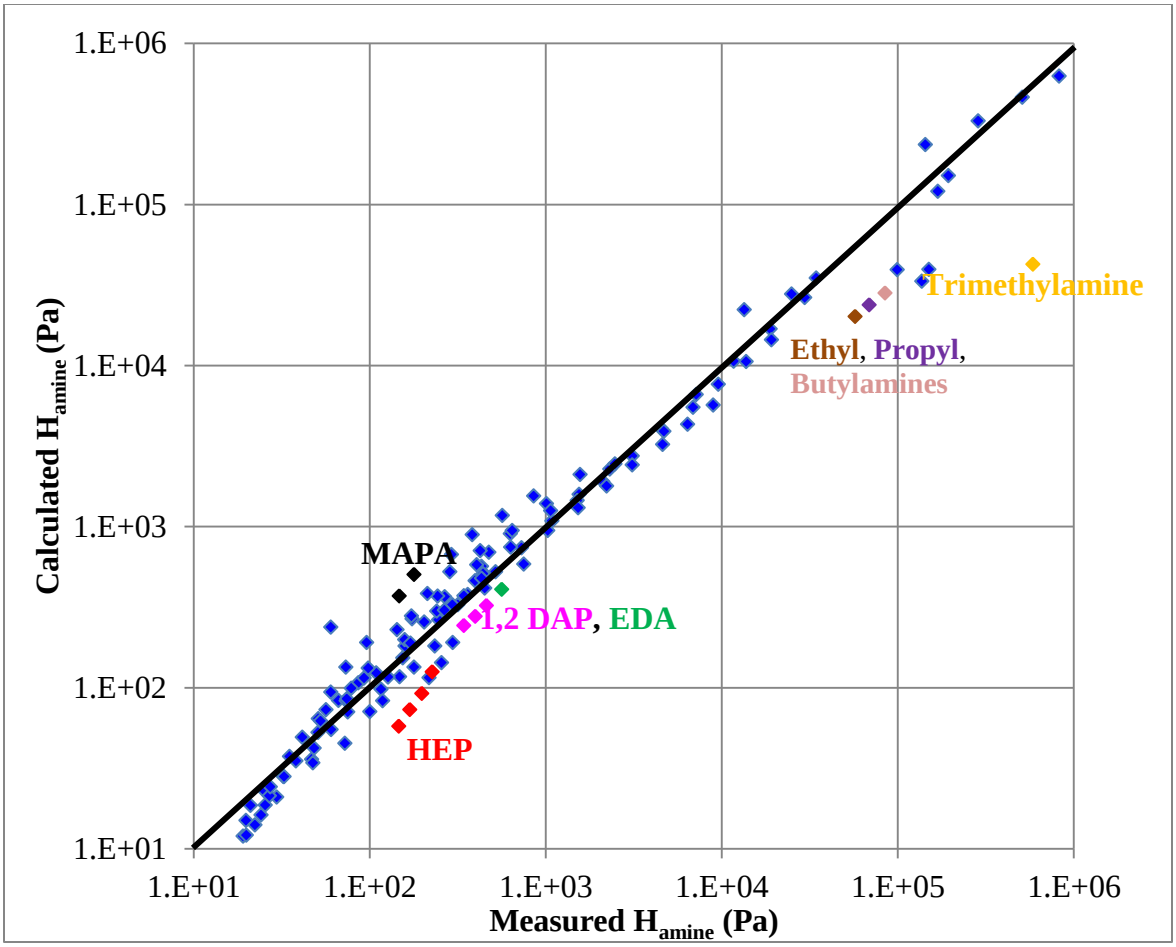

Figure 3.5-5. Evaluation of Predicted Amine Henry's Constants from 25 ˚–70 ˚C

It can be seen from Figure 3.5-5 that this rigorous model does a fair job of representing most of the 35 amines from 25 ˚ - 70 ˚C to within an order of magnitude with the exception of a few outliers as shown. Furthemore, the rigorous model appears to be more accurate than the base case model in its representation of amine H constants due to the appearance of a tighter data fit. In the region of low amine H constants, HEP stands out as an entire temperature series (40 ˚ - 70 ˚C) that is not fitted as well as the others. The inability to fit HEP mainly stems from the experimental scatter in the raw volatility data. This results in a poor linear fit of HEP enthalpy of solution to the

Arrhenius temperature behavior (R^2 ~ 0.87 only as compared to that of other amines). In the case of the other outliers, such as 1,2-Diaminopropane, EDA, and MAPA, the problem lies with not being able to fit compounds having two amino groups as well as fitting monoamines. Also the confidence for alkyl group parameters attached to carbons is not statistically significant which also contributed to a marginal fit. Nonetheless, unlike with HEP, these diamines do show good fits of the temperature dependence due to the fact that their experimental volatility data are much more linear with temperature than HEP. In the case of the alkylamines, the model underestimated the H constants of the alkylamine family, consisting of ethylamine through hexylamine, at 25 ˚C. It was challenging to estimate both the H constant at 40 ˚C and the enthalpies of solution for these alkylamines since only experimental data for ethylamine is available. To better anchor the structural contribution of the alkyl groups in this alkylamine family, there needs to be data for at least one more compound in this family such as propylamine in addition to ethylamine.

Predictive Capability of the Rigorous Model

The rigorous model was used to predict the H constant of 1,2-Aminoethyl Piperazine (AEP) from 40 ˚ - 65 ˚C. Note that this amine was not included in the model regression earlier. Table 3.5-9 shows how the rigorous model predictions compare to the experimental measurements.

Table 3.5-9. Comparison of Measured versus Calculated H Constants for 1,2 AEP

T (˚C)	H_{meas} (Pa)	H_{calc} (Pa)	Structure
40	16.7 ± 6.5	10.4	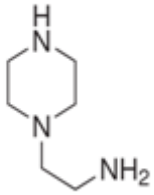
45	21.3 ±6.5	14.8	
50	31.5 ± 5.5	20.7	
55	42.2 ± 5.5	28.8	
60	49.5 ± 5.0	39.5	
65	54.7 ± 5.0	53.7	

The H constants for AEP were estimated from 40 ˚ - 65˚ C by using an estimated H constant at 40 ˚C of ~10.4, calculated from the functional group parameter values of Table 3.5-6, and an estimated $\Delta H_{solution}$ of ~6939 J/mol which was calculated by using Table 3.5-8. Given the experimental uncertainty of the measurements as shown in Table 3.5-9, it can be seen that the calculated H constants are somewhat underestimating the experimental values although the discrepancy becomes less with increasing temperature. These results indicate that the rigorous model is able to predict an amine H constant to well within an order of magnitude of the experimental values as shown earlier. Furthermore, this capability is considered satisfactory given that the model can be used to estimate the H constant of any amine in water, whether it be an alkanolamine or alkylamine whose volatilities can span over five orders of magnitude.

Correlation of Solution Thermodynamic Variables

At a given temperature, the change in Gibbs free energy of an amine going from vapor to aqueous phase is a function of the amine Henry's constant according to the following:

$$G_{amine,\ aq} - G_{amine,\ i.g.} = \Delta G_{amine} = -RT\ln H_{amine} \qquad (3\text{-}10)$$

This change in an amine Gibbs energy can be expressed in terms of changes in other thermodynamic variables as follow:

$$-RTlnH_{amine} = \Delta G_{amine} = \Delta H_{amine} - T\Delta S_{amine} \quad (3\text{-}11)$$

where

ΔH_{amine} is the enthalpy of amine solution
ΔS_{amine} is the change in entropy

The change in Gibbs energy for an amine going from vapor to aqueous state at 40 ˚C can be calculated using the H constant. The change in entropy for an amine going from vapor to aqueous state at 40 ˚C can then be calculated by taking the difference between the ΔG and the measured ΔH. For 40 ˚C, Table 3.5-10 summarizes the estimated change in entropies for 19 amines from this work and 7 alkylamines from the literature which have measured enthalpies of solution available.

Table 3.5-10. Summary of Solution Thermodynamic Variables for Aqueous Amine Systems at 40 ˚C

Amine	-ΔG (J/mol)	$\Delta H_{solution}$ (J/mol)	TΔS (J/mol)
MDEA	8825	31779	40604
PZ	10004	61837	71841
DGA	7673	31113	38786
MAPA	12989	62877	75866
EDA	11990	55949	67939
MEA	10664	62357	73021
1,2 DAP	12431	61731	74162
1-MPZ	12914	82645	95560
AMP	14984	70474	85458
HMDA	13004	41404	54408
1,4 DMPZ	19053	88937	107990
2,2 DMAEE	10661	71015	81675
DMEA	19929	65770	85699
MORPH	18049	64406	82455
DMORPH	10222	21919	32141

HEP	9469	52954	62423
ALANINOL	13406	64371	77777
DEA	7789	10988	18777
2-MPZ	10090	76231	86321
Pyrrolidine	27918	63186	91104
Piperidine	29662	65681	95343
Hexamethyleneimine	30627	68175	98802
Dimethylamine	31628	33256	64884
Diethylamine	35097	83140	118237
N-Methylpyrrolidine	34512	63186	97699
N-Methylpiperidine	34997	65681	100678

There seems to be a correlation between the aqueous enthalpy of amine solution and its entropy at 40 ˚C. Figure 3.5-6 shows the correlation between these two variables.

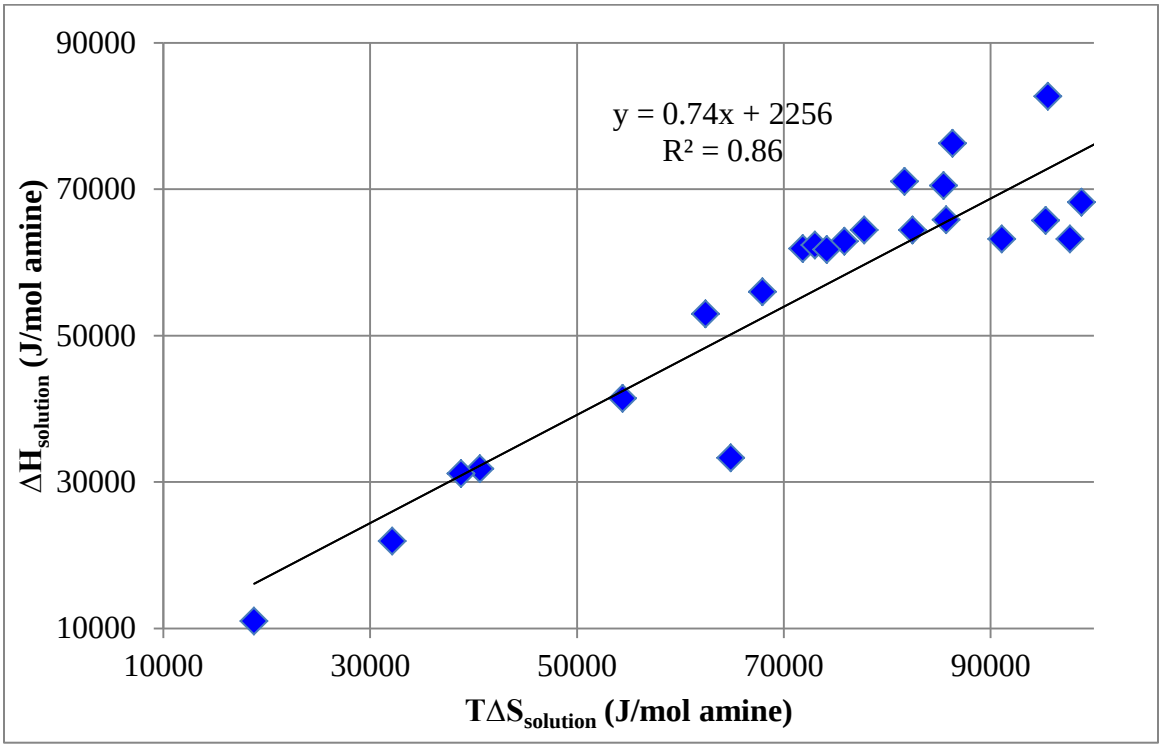

Figure 3.5-6. Correlation between Enthalpy of Amine Solution and Entropy at 40 ˚C

It can be seen that the enthalpy of amine solution is correlated to entropy for all the

amines studied at 40 ˚C. Given the expression of the linear trend fit, it can be seen that the quantity of $T\Delta S$ (x-variable) and $\Delta H_{solution}$ (y-variable) are almost 1:1.

3.6. Conclusions

The experimental H constants of alkanolamines measured in this work are compared to predictions from different group contribution theories in the literature. For the majority of the amine systems studied, both the experimental H constants from this work and those predicted by UNIFAC-DMD theory agree to within an order of magnitude with the exception of PZ and DGA. In comparing the experimental amine H constants to calculated values using the group contribution established by Hine and Mookerjee (1975), it was seen that the calculated values are systematically one to many orders of magnitude less than the experimental data.

Both the base case and rigorous models are able to estimate the H constants, for the majority of amines, to well within an order of magnitude of the experimental values, which span over five orders of magnitude in the temperature range from 25 ˚ - 70 ˚C. The rigorous model is seen to provide a tighter fit of all the experimental data than the base case model. The rigorous model was also demonstrated to have predictive capability for estimating the H constant of an amine of interest (1,2-AEP) to within the margin of experimental errors. In conclusion, the models developed in this work are more reliable than UNIFAC-DMD and the Hine and Mookerjee group contribution method for estimating H constants of alkanolamines, especially those of cyclic amines such as PZ, which are used for CO_2 capture.

Given the dilute working amine concentrations of this work, the measured amine Henry's constants are found to be ±10% from the true Henry's constants at infinite dilution of amine in water. From the base case model, it can be seen that the hydrophilic strengths of the different polar groups are as followed: $O < OH < N < N_{cy}$. The rigorous model has a similar ranking order of hydrophilic groups with further differentiation between cyclic versus non-cyclic ether and between the different types of amine groups. In order of increasing hydrophobicity, $C < C_{cy} < CH_3\text{-}(\ C\ ) < CH_3\text{-}(N) < CH_3\text{-}(N_{cy})$. The rigorous model also has similar ranking of hydrophobic groups with further differentiation between methyl versus methylene groups based on whether they are attached to a neighboring carbon or a polar group.

The enthalpies of solution of the different aqueous amine systems studied appear to be adequately represented with Arrhenius temperature behavior which assumes a constant enthalpy of solution over a range of temperature. Nonetheless, the base case model shows an improved fit of the data with the use of an additional temperature term which implies that the enthalpy of solution is a function of temperature to some extent. Finally, it is seen that there is a correlation between the enthalpy of solution and the entropy at 40 ˚C where $\Delta H_{solution} = 0.74T\Delta S_{solution} + 2256$ (J/mol).

Chapter 4: MDEA-PZ-CO_2-H_2O Thermodynamic Model Upgrade

4.1. Introduction

The MDEA-PZ-CO_2-H_2O system was modeled in AspenPlus® v.7.3. by Peter Frailie, a Rochelle group member, in 2010. The system was modeled using the liquid activity method. The vapor phase of the system was represented using the Soave-Redlich-Kwong (SRK) equation of state, whereas the liquid phase was modeled using Electrolyte NRTL (eNRTL) theory**.** This MDEA-PZ model, named the Guy Fawkes model, was built upon an earlier PZ-CO_2-H_2O model developed by Hilliard (2008) with modifications to fit high concentration PZ systems made by Van Wagener (2010). The 2010 Fawkes model, while it provided a reasonably accurate representation of loaded PZ systems, did not adequately capture MDEA thermodynamics. There were two primary issues with the model: (1) inability to fit the MDEA and PZ volatilities for the blend neither at unloaded or at loaded condition; (2) inability to match the experimental speciation data for the blend.

Thus this work focused on resolving these two issues primarily by remodeling the MDEA thermodynamics portion of the blend which includes the sub-systems: MDEA-H_2O and MDEA-CO_2-H_2O. Note that the sub-systems were modeled using a sequential regression technique which involved first regressing data for the simplest systems building on to the regression of the most complex system. In keeping with this regression concept, the first system whose data was regressed was MDEA-H_2O, followed by MDEA-CO_2-H_2O, MDEA-PZ-H_2O, and ultimately MDEA-PZ-CO_2-H_2O. The end goal of this modeling effort is to be able to properly represent all the key thermodynamic

properties of the blend which include CO_2 solubility, amine volatility, speciation, heat capacity, and enthalpy of CO_2 absorption.

4.2. Theory

NRTL Theory

The NRTL (Non-Random Two Liquid) model was developed by Renon and Prausnitz (1968). It is a model that is built on the principle of local composition where the concentrations of components in different local pockets within the mixture are different than the overall mixture composition. This is a result of the differences both in molecular size and intermolecular forces between different pairs of molecules. Essentially speaking, the NRTL model is an excess Gibbs energy model which has the following form for a binary system:

$$\frac{G^{excess}}{RT} = x_1 x_2 \left(\frac{\tau_{21} G_{21}}{x_1 + x_2 G_{21}} + \frac{\tau_{12} G_{12}}{x_2 + x_1 G_{12}}\right) \quad (4\text{-}1)$$

where

x_i is the mole fraction of component i
τ_{ij} is the binary interaction parameter between components i and j
G_{ij} is the Gibbs energy of interaction between components i and j, where $G_{ij} = e^{-\alpha_{ij}\tau_{ij}}$ and α_{ij} is the molecule-molecule non-randomness factor which characterizes the tendency of species i and j to be distributed in a non-random fashion. It is set equal to 0.2 for the amine systems in this work as this factor is considered characteristic of polar non-associated species.

The molecule to molecule binary interaction parameter τ_{ij} is temperature dependent and is expressed as the following:

$$\tau_{ij} = a_{ij} + \frac{b_{ij}}{T} + c_{ij} \ln T + d_{ij} T \quad (4\text{-}2)$$

An amine activity coefficient can be derived from the following thermodynamic relationship:

$$\ln \gamma_{amine} = \left[\frac{\delta\left(\frac{nG^{excess}}{RT}\right)}{\delta n_{amine}}\right] \tag{4-3}$$

For a binary system, such as MDEA-H_2O, the activity coefficient of one of the two species is expressed as follows:

$$\ln \gamma_i = x_j^2 \left[\tau_{ji}\left(\frac{G_{ji}}{x_i + x_j G_{ji}}\right)^2 + \frac{\tau_{ij} G_{ij}}{\left(x_j + x_i G_{ij}\right)^2}\right] \tag{4-4}$$

elecNTRL Theory

The elecNRTL theory is used to model solutions having electrolytes, or charged species, such as the amine-CO_2-H_2O solutions. With ions in an electrolyte solution, the elecNRTL theory is based on two fundamental assumptions:

(1) Like Ion Repulsion: The local composition of cations around cations is zero and the same can be said for anions. This is because of the large repulsive forces between ions of the same sign within a neighborhood.

(2) Local Electroneutrality: The distribution of cations and anions around a central molecular species is such that the net local ionic charge is zero.

Like the NRTL theory, the elecNRTL theory is also anchored upon the excess Gibbs free energy of a system. This quantity is made up of three contributions:

$$\frac{G^{*E}}{RT} = \frac{G^{*E,PDH}}{RT} + \frac{G^{*E,Born}}{RT} + \frac{G^{*E,lc}}{RT} \tag{4-5}$$

where

PDH is the Pitzer-Debye-Huckel contribution for long range ion to ion interactions
Born is the Born correction for change in mixed solvent reference state
lc is the local contribution for short range interactions

Since the activity coefficient of a species is simply the derivative of the excess Gibbs energy for a system with respect to the change in the number of moles of that species, it can also be expected that the activity coefficient would also consist of the same three contributions.

Long Range Contribution

The PDH term in Eq. (4-5) accounts for the long range ion-ion interactions that occur at low ionic strengths.

$$\frac{G^{*E,PDH}}{RT} = -\sum x_k \left(\frac{1000}{M_s}\right)^{0.5} \left(\frac{4A_\phi I_x}{\rho}\right) \ln(1 + \rho I_x^{0.5}) \qquad (4\text{-}6)$$

where:

M_s is the molecular weight of the solvent
ρ is the "closest approach" parameter
I_x is the ionic strength (mole fraction basis)
A_φ is the Debye-Huckel parameter

Note that I_x is defined per the following:

$$I_{x=}\ 0.5\ \sum_i x_i\ z_i^2 \qquad (4\text{-}7)$$

with:

x_i is the mole fraction of species i
z_i is the charge of species i

The Debye-Huckel parameter is calculated as follows:

$$A_\phi = \frac{1}{3}\left(\frac{2\pi N_o d}{1000}\right)^{0.5} \left(\frac{e^2}{D_w kT}\right)^{1.5} \qquad (4\text{-}8)$$

with:

N_o is Avogadro's number
d is the solvent's density
e is the electron charge
D_w is the dielectric constant of water
T is temperature in K
k is the Boltzmann constant

Born Correction

The Born correction is used to account for the change in reference state given by the difference in dielectric constants.

$$\frac{G^{*E,Born}}{RT} = \left(\frac{e^2}{2kT}\right)\left(\frac{1}{D_m} - \frac{1}{D_w}\right)\frac{\sum_i x_i z_i^2}{r_i}\, 10^{-2} \tag{4-9}$$

where:

r_i is the Born radius of ionic species
D_m is the dielectric constant of the mixed solvent

Local Contribution

The elecNRTL model accounts for short range interactions among different species. The local contribution to the excess Gibbs energy is given as follows (note that the subscripts m, c, and a stand for molecule, cation, and anion, respectively):

$$\frac{G_m^{*E,lc}}{RT} = \sum_m X_m \frac{\sum_j X_j G_{jm}\tau_{jm}}{\sum_k X_k G_{km}} + \sum_c X_c \sum_{a'}\left(\frac{X_{a'}}{\sum_{a''} X_{a''}}\right)\frac{\sum_j G_{jc,a'c}\tau_{jc,a'c}}{\sum_k X_k G_{kc,a'c}} + \ldots$$
$$\ldots + \sum_a X_a \sum_{c'}\left(\frac{X_{c'}}{\sum_{c''} X_{c''}}\right)\frac{\sum_j G_{ja,a'c}\tau_{ja,a'c}}{\sum_k X_k G_{ka,a'c}} \tag{4-10}$$

where:

$$G_{cm} = \frac{\sum_a X_a G_{ca,m}}{\sum_{a'} X_{a'}}, \qquad G_{am} = \frac{\sum_c X_c G_{ca,m}}{\sum_{c'} X_{c'}},$$

$$\alpha_{cm} = \frac{\sum_a X_a \alpha_{ca,m}}{\sum_{a'} X_{a'}}, \qquad \alpha_{am} = \frac{\sum_c X_c G_{ca,m}}{\sum_{c'} X_{c'}},$$

$$G_{jc,a'c} = \exp\left(-\alpha_{jc,a'c}\tau_{jc,a'c}\right), \qquad G_{ja,c'a} = \exp\left(-\alpha_{ja,c'a}\tau_{ja,c'a}\right),$$

$$G_{im} = \exp\left(-\alpha_{im}\tau_{im}\right), \qquad G_{ca,m} = \exp\left(-\alpha_{ca,m}\tau_{ca,m}\right),$$

$$\tau_{ma,ca} = \tau_{am} - \tau_{ca,m} + \tau_{m,ca}, \qquad \tau_{mc,ac} = \tau_{cm} - \tau_{ca,m} + \tau_{m,ca},$$

$X_j = x_j C_j$ with $C_j = z_j$ for ions and $C_j = 1$ for molecules
α is the non-randomness parameter
τ is the binary interaction parameter

Note that the tau interaction parameter above accounts for the interaction between a molecule to an electrolyte cation/anion pair. These interaction parameters are given by the following:

$$\tau_{m,ca} = A_{m,ca} + \frac{B_{m,ca}}{T} + C_{m,ca}\left[\frac{\left(T^{ref} - T\right)}{T} + \ln\left(\frac{T}{T^{ref}}\right)\right]$$

$$\tau_{ca,m} = A_{ca,m} + \frac{B_{ca,m}}{T} + C_{ca,m}\left[\frac{\left(T^{ref} - T\right)}{T} + \ln\left(\frac{T}{T^{ref}}\right)\right]$$

(4-11)

Once again $\tau_{m,ca} \neq \tau_{ca,m}$. The A, B, C constants in the above expression correspond to pair parameters GMELCC, GMELCD, and GMELCE, in AspenPlus® 7.3 respectively.

4.3. Data

The data sets used to regress the MDEA-H_2O, MDEA-CO_2-H_2O, and MDEA-PZ-CO_2-H_2O systems are provided in the following tables.

Binary MDEA-H_2O System

Table 4.3-1 shows MDEA volatility for 0.5 m, 7 m, and 20 m MDEA in H_2O from 40–70 ˚C. The measured temperature was assigned an experimental uncertainty of ±1% and the MDEA volatility measurements were expected to have a ±4% error.

Table 4.3-1. MDEA Volatility in MDEA-H_2O

MDEA (m)	T(˚C)	P_{MDEA} (Pa)
0.50	40	0.18
	45	0.19
	50	0.22
	55.1	0.27
	60	0.35
	65	0.43
	70	0.57
6.84	40	0.48
	45	0.69
	50	1.04
	55	1.49
	60	1.85
	65	2.72
	70	4.06
8.2	40	0.52
	45	0.91
	50	1.10
	55	1.43

	60	2.18
	65	3.24
	70	4.84
20	40	1.09
	45	1.50
	50	2.00
	55	2.89
	60	4.14
	65	6.02
	70	9.27

Table 4.3-2 gives aqueous MDEA volatility measured by Kim (2008) using an ebulliometer cell coupled with GC analysis. The measured temperature was assigned an experimental uncertainty of ±1% whereas the volatility data had a ±4% error.

Table 4.3-2. MDEA Volatility in MDEA-H_2O (Kim, 2008)

T (˚C)	x_{MDEA}	P_{MDEA} (Pa)
60	0.005	0.791
	0.017	0.584
	0.088	1.45
	0.133	2.05
	0.205	3.07
	0.290	4.01
	0.305	5.28
	0.262	4.61
	0.226	2.68
	0.233	2.79
	0.195	2.66
	0.154	2.50
	0.105	1.60
	0.070	1.48
80	0.306	23.7
	0.148	7.29
	0.104	3.83
	0.076	3.51
	0.055	3.58

	0.039	3.18
	0.006	0.470
	0.014	1.40
	0.022	1.85
	0.048	3.61
	0.074	6.58
	0.097	5.96
	0.139	8.54
	0.174	11.2
	0.220	19.5
100	0.319	76.5
	0.260	70.9
	0.228	54.3
	0.188	43.2
	0.099	27.6
	0.072	25.5
	0.053	22.1
	0.011	6.99
	0.024	12.8
	0.046	16.5
	0.090	40.8
	0.139	47.7
	0.187	57.7
	0.290	70.2
	0.357	89.8
	0.006	3.01
	0.012	6.99
	0.023	12.8
	0.054	21.2
	0.075	29.1
	0.099	42.2

Table 4.3-3 shows the liquid heat capacity of pure MDEA from 5–95 ˚C. The measured temperature was assigned a ±0.1 ˚C and C_p was assumed to have a ±1% uncertainty. The data was obtained from DIPPR thermodynamic database.

Table 4.3-3. Pure MDEA Liquid Heat Capacity (DIPPR)

T (˚C)	C_p (kJ/kmol*K)
5	256.1
10	260.1
15	263.5
20	266.6
25	269.6
30	272.3
35	275.1
40	277.7
45	280.4
50	283.1
55	285.8
60	288.6
65	291.4
70	294.3
75	297.3
80	300.4
85	303.6
90	306.9
95	310.4

Table 4.3-4 summarizes the C_p for 1.7 m, 3.5 m, 6.2 m, and 13.9 m MDEA. This data was obtained by Zhang et al. (2002). The measured temperature was assigned a ±0.1 ˚C and C_p was assumed to have a ±1% uncertainty.

Table 4.3-4. C_p for 1.7 m, 3.5 m, 6.2 m, and 13.9 m MDEA from 5 ˚– 95 ˚C (Zhang, 2002)

T (˚C)	x_{MDEA}	x_{H2O}	C_p (kJ/kmol*K)

5	0.030	0.970	83.1
5	0.060	0.940	88.4
5	0.100	0.900	95.8
5	0.200	0.800	114
10	0.030	0.970	83.2
10	0.060	0.940	89.3
10	0.100	0.900	97.2
10	0.200	0.800	116
15	0.030	0.970	83.2
15	0.060	0.940	90.0
15	0.100	0.900	98.3
15	0.200	0.800	118
20	0.030	0.970	83.5
20	0.060	0.940	90.6
20	0.100	0.900	99.4
20	0.200	0.800	119
25	0.030	0.970	83.7
25	0.060	0.940	91.2
25	0.100	0.900	100
25	0.200	0.800	121
30	0.030	0.970	83.9
30	0.060	0.940	91.7
30	0.100	0.900	101
30	0.200	0.800	122
35	0.030	0.970	84.2
35	0.060	0.940	92.2
35	0.100	0.900	102
35	0.200	0.800	124
40	0.030	0.970	84.5
40	0.060	0.940	92.5
40	0.100	0.900	103
40	0.200	0.800	125
45	0.030	0.970	84.5
45	0.060	0.940	92.9
45	0.100	0.900	103
45	0.200	0.800	127
50	0.030	0.970	84.7

50	0.060	0.940	93.2
50	0.100	0.900	104
50	0.200	0.800	128
55	0.030	0.970	84.8
55	0.060	0.940	93.5
55	0.100	0.900	104
55	0.200	0.800	129
60	0.030	0.970	85.0
60	0.060	0.940	93.8
60	0.100	0.900	105
60	0.200	0.800	131
65	0.030	0.970	85.1
65	0.060	0.940	94.1
65	0.100	0.900	106
65	0.200	0.800	132
70	0.030	0.970	85.2
70	0.060	0.940	94.4
70	0.100	0.900	106
70	0.200	0.800	133
75	0.030	0.970	85.4
75	0.060	0.940	94.8
75	0.100	0.900	107
75	0.200	0.800	134
80	0.030	0.970	85.7
80	0.060	0.940	95.3
80	0.100	0.900	108
80	0.200	0.800	136
85	0.030	0.970	86.0
85	0.060	0.940	95.9
85	0.100	0.900	108
85	0.200	0.800	137
90	0.030	0.970	86.5
90	0.060	0.940	96.5
90	0.100	0.900	109
90	0.200	0.800	138
95	0.030	0.970	87.3
95	0.060	0.940	97.3

95	0.100	0.900	110
95	0.200	0.800	139

MDEA-CO_2-H_2O

Table 4.3-5 displays the CO_2 solubility data for 2.8 m, 4.5 m, and 8.4 m MDEA at a wide range of loading for 25, 40, 70, 100, and 120 ˚C. This experimental data was obtained by Jou et al. (1982). The measured temperature was assumed to have an uncertainty of ±1% whereas the CO_2 solubility was assigned a ±4% error.

Table 4.3-5. CO_2 Solubility for 2.8 m, 4.5 m, and 8.4 m MDEA from 25–120 ˚C (Jou, 1982)

	2.8 m MDEA			4.5 m MDEA			8.4 m MDEA	
T(˚C)	Ldg	P_{CO2} (kPa)	T (˚C)	Ldg	P_{CO2} (kPa)	T (˚C)	Ldg	P_{CO2} (kPa)
25	0.638	9.26	40	0.011	0.033	25	0.784	48.1
25	0.452	4.22	40	0.013	0.040	25	0.318	5.3
25	0.334	1.55	40	0.016	0.056	25	0.072	0.384
25	0.040	0.030	40	0.017	0.069	25	0.031	0.086
25	0.033	0.022	40	0.027	0.146	25	0.019	0.034
25	0.017	0.007	40	0.039	0.224	25	0.010	0.009
25	0.005	0.001	40	0.059	0.415	25	0.006	0.004
40	0.866	101	40	0.077	0.719	40	0.700	83.4
40	0.441	11.2	40	0.106	1.10	40	0.285	13.3
40	0.224	2.38	40	0.118	1.26	40	0.136	2.67
40	0.068	0.184	40	0.166	2.16	40	0.061	0.703
40	0.012	0.013	40	0.23	3.82	40	0.010	0.030
40	0.005	0.004	40	0.249	4.43	40	0.006	0.011
40	0.004	0.003	40	0.296	5.89	40	0.004	0.008
40	0.003	0.002	40	0.336	8.29	40	0.002	0.002
70	0.841	447	40	0.394	12.0	70	0.740	705
70	0.369	40.9	40	0.519	19.1	70	0.189	40.3
70	0.044	0.951	40	0.0077	0.963	70	0.021	0.918
70	0.021	0.305	100	0.0094	1.35	70	0.008	0.17
70	0.006	0.048	100	0.013	1.72	70	0.002	0.018

70	0.001	0.003		100	0.025	5.56		70	0.001	0.010
70	0.001	0.002		100	0.027	5.02		70	0.001	0.005
100	0.564	573		100	0.034	9.84		70	0.0004	0.002
100	0.502	373		100	0.048	15.6		100	0.532	1310
100	0.130	30.8		100	0.064	19.1		100	0.256	331
100	0.004	0.128		100	0.087	36.5		100	0.095	63.1
100	0.002	0.047		100	0.107	65.9		100	0.028	7.69
120	0.689	1930		100	0.134	103		100	0.004	0.277
120	0.336	493		100	0.16	125		100	0.003	0.174
120	0.097	57.7		100	0.219	217		100	0.002	0.071
120	0.013	3.8		100	0.231	262		100	0.001	0.055
120	0.002	0.116		100	0.271	236		100	0.001	0.040
120	0.001	0.073						120	0.743	5290
								120	0.525	2920
								120	0.279	857
								120	0.128	248
								120	0.055	69.1
								120	0.019	14.3
								120	0.002	0.479
								120	0.001	0.183
								120	0.001	0.143

Table 4.3-6 shows the heat capacity for 3.6 m, 5.6 m, 8.4 m, and 12.6 m MDEA systems having various loadings at 25 ˚C. This data was obtained by Weiland et al. (1997). The measured heat capacities were assumed to have a ±5% experimental uncertainty.

Table 4.3-6. C_p for 3.6–12.6 m MDEA at Various Loadings and 25 ˚C (Weiland, 1997)

3.6 m MDEA			**8.4 m MDEA**	
Loading	**C_p (kJ/kg*K)**		**Loading**	**C_p (kJ/kg*K)**
0	3.787		0	3.407
0.05	3.761		0.05	3.366
0.1	3.703		0.1	3.342
0.15	3.684		0.15	3.298

0.2	3.684		0.2	3.294
0.25	3.636		0.25	3.208
0.3	3.607		0.3	3.163
0.35	3.545		0.35	3.136
0.4	3.496		0.4	3.132
0.45	3.436		0.45	3.12
0.5	3.436		0.5	3.094
5.6 m MDEA			**12.6 m MDEA**	
Loading	**C_p (kJ/kg*K)**		**Loading**	**C_p (kJ/kg*K)**
0	3.585		0	3.174
0.05	3.531		0.13	3.087
0.1	3.528		0.25	3.005
0.15	3.526		0.38	2.976
0.2	3.473		0.51	2.886
0.25	3.46		0.64	2.849
0.3	3.384			
0.35	3.365			
0.4	3.35			
0.45	3.287			
0.5	3.24			

MDEA-PZ-CO_2-H_2O

Table 4.3-7 shows the CO_2 solubility for 7 m MDEA/2 m PZ from 40–160 ˚C. The data from 40–100 ˚ were obtained from Chen (2010) and those from 120–160 ˚C were taken from Xu (2010). Chen measured CO_2 solubility using a wetted wall column. Xu obtained the data using a high temperature FTIR setup. The measured temperature was assigned an experimental uncertainty of ±1% and the CO_2 solubility was given a ±1% error.

Table 4.3-7. CO_2 Solubility for 7 m MDEA/2 m PZ from 40–160 ˚C (Chen and Xu)

Temperature (˚C)	Loading	P_{CO2} (kPa)	x_{MDEA}	x_{PZ}	x_{CO2}	x_{H2O}
40	0.093	0.19	0.107	0.030	0.016	0.847
40	0.166	0.95	0.105	0.030	0.028	0.837

40	0.237	2.8	0.104	0.030	0.039	0.827
40	0.286	5.3	0.103	0.030	0.046	0.821
60	0.093	1.3	0.107	0.030	0.016	0.847
60	0.166	4.4	0.105	0.030	0.028	0.837
60	0.237	13.5	0.104	0.030	0.039	0.827
60	0.273	19.6	0.104	0.030	0.044	0.822
80	0.027	1.27	0.108	0.031	0.005	0.857
80	0.093	5.62	0.107	0.030	0.016	0.847
80	0.166	17.6	0.105	0.030	0.028	0.837
100	0.027	5.21	0.108	0.031	0.005	0.857
100	0.093	19.8	0.107	0.030	0.016	0.847
120	0.132	137	0.103	0.029	0.021	0.846
120	0.226	628	0.092	0.026	0.033	0.849
140	0.125	356	0.100	0.029	0.020	0.852
140	0.206	1362	0.090	0.026	0.029	0.855
160	0.113	785	0.098	0.028	0.017	0.857
160	0.178	2452	0.088	0.025	0.025	0.862

Table 4.3-8 gives the CO_2 solubility for 5 m MDEA/5 m PZ from 40–160 ˚C. The data from 40–100 ˚ were obtained from Chen (2011) and those from 120–160 ˚C were taken from Xu (2011). The measured temperature was assigned an experimental uncertainty of ±1% and the solubility data had a ±1% error.

Table 4.3-8. CO_2 Solubility for 5 m MDEA/5 m PZ from 40–160 ˚C (Chen and Xu)

Temperature (˚C)	Loading	P_{CO2} (kPa)	x_{MDEA}	x_{PZ}	x_{CO2}	x_{H2O}
40	0.18	0.24	0.073	0.073	0.040	0.814
40	0.23	0.64	0.072	0.072	0.050	0.805
40	0.28	2.2	0.072	0.072	0.060	0.796
40	0.33	3.5	0.071	0.071	0.070	0.788
40	0.37	6.6	0.070	0.070	0.078	0.781
60	0.18	1.5	0.073	0.073	0.040	0.814
60	0.23	3.7	0.072	0.072	0.050	0.805
60	0.28	8.8	0.072	0.072	0.060	0.796
60	0.33	18.3	0.071	0.071	0.070	0.788
60	0.37	28.2	0.070	0.070	0.078	0.781

80	0.18	6.7	0.073	0.073	0.040	0.814
80	0.23	16.9	0.072	0.072	0.050	0.805
100	0.22	39.9	0.073	0.073	0.048	0.806
100	0.28	109	0.072	0.072	0.060	0.797
120	0.22	169	0.073	0.073	0.048	0.807
120	0.27	343	0.072	0.072	0.058	0.798
140	0.21	478	0.073	0.073	0.046	0.808
140	0.26	885	0.072	0.072	0.056	0.800
160	0.20	1122	0.073	0.073	0.043	0.811
160	0.24	1746	0.072	0.072	0.052	0.803

Table 4.3-9 and 4.3-10 show CO_2 solubility and amine volatility for both 7 m MDEA/2 m PZ and 5 m MDEA/5 m PZ, respectively, as obtained from this work. The measured temperature was assigned a ±1% whereas both the amine volatility and CO_2 pressure measurements were assumed to have a ±10% uncertainty.

Table 4.3-9. Amine Volatility and CO_2 Solubility for 7 m MDEA/2 m PZ at 40 ˚ - 70 ˚C

T (˚C)	Ldg	P_{PZ} (Pa)	P_{MDEA} (Pa)	P_{H2O} (Pa)	P_{CO2} (Pa)
40	0	1.07	0.46	6390	0
40	0.143	0.3	0.47	6190	524
40	0.193	0.15	0.44	6090	1430
40	0.24	0.13	0.47	6080	3560
45	0	1.61	0.81	7890	0
45	0.143	0.4	0.72	7790	750
45	0.193	0.23	0.65	7680	1930
45	0.24	0.18	0.65	7680	5740
50	0	2.5	1.15	10300	0
50	0.143	0.59	1.1	10200	1150
50	0.193	0.34	1.03	10100	3230
50	0.24	0.25	1.18	10300	9010
55	0	3.8	1.62	13200	0
55	0.143	0.99	1.63	13000	1600
55	0.193	0.57	1.66	13000	5440
55	0.24	0.33	1.65	13100	13500

60	0	5.48	1.91	16700	0
60	0.143	1.47	2.16	16200	2540
60	0.193	0.78	2.16	16300	7350
60	0.24	0.49	2.02	16700	17600
65	0	8.48	2.83	21100	0
65	0.143	2.28	3.44	20800	3590
65	0.193	1.33	3.29	20900	11700
65	0.24	0.85	3.08	21900	26600
70	0	11.73	4.23	26800	0
70	0.143	3.63	5.62	26500	6000
70	0.193	1.93	4.85	26700	16800
70	0.24	1.3	4.68	28400	33100

Table 4.3-10. Amine Volatility and CO_2 Solubility for 5 m MDEA/5 m PZ at 40 ˚ - 70 ˚C

T (˚C)	Ldg	P_{PZ} (Pa)	P_{MDEA} (Pa)	P_{H2O} (Pa)	P_{CO2} (Pa)
40	0	5.04	0.36	6300	0
40	0.221	0.51	0.45	5990	598
40	0.307	0.24	0.37	5880	6630
40	0.362	0.16	0.3	5800	19100
45	0	6.45	0.5	8000	0
45	0.221	0.72	0.61	7600	1090
45	0.307	0.27	0.52	7580	9650
45	0.362	0.2	0.41	7490	26100
50	0	8.75	0.64	10200	0
50	0.221	1.22	0.91	10100	1720
50	0.307	0.37	0.77	9970	15200
50	0.362	0.23	0.59	10300	35000
55	0	12.11	0.99	12900	0
55	0.221	1.81	1.34	12700	2660
55	0.307	0.54	1.11	13100	21800
55	0.362	0.35	0.88	13600	42200
60	0	17.78	1.45	16300	0
60	0.307	0.91	1.64	16400	29500
60	0.362	0.54	1.32	17300	53400
60.3	0.221	2.85	1.75	16200	4250
65	0	27.81	2.22	20700	0

65	0.221	4.37	2.69	20600	7320
65	0.307	1.5	2.22	21500	36400
65	0.362	1	2.13	22800	66500
70	0	44.77	2.78	26600	0
70	0.221	6.78	4.07	26500	10600
70	0.307	2.52	3.42	27500	47600

Table 4.3-11 summarizes the CO_2 solubility for the 7.7 m MDEA/1.1 m PZ system at 40 and 70 ˚C as taken from Bishnoi (2000). The loadings from Bishnoi work (mol CO_2/mol total amine) have been converted to the loading basis used in this work (mol CO_2/mol total alkalinity) as reported below. The measured temperature was assigned a ±1% and the CO_2 pressure was assumed to have a ±1% uncertainty.

Table 4.3-11. CO_2 Solubility for 7.7 m MDEA/1.1 m PZ at 40 ˚ and 70 ˚C (Bishnoi, 2000)

T (˚C)	Loading	P_{CO2} (kPa)	x_{MDEA}	x_{PZ}	x_{CO2}	x_{H2O}
40	0.02	0.033	0.119	0.017	0.004	0.860
40	0.05	0.115	0.119	0.017	0.008	0.856
40	0.06	0.236	0.118	0.017	0.010	0.855
40	0.08	0.367	0.118	0.017	0.012	0.853
40	0.12	1.1	0.117	0.017	0.019	0.847
40	0.12	1.3	0.117	0.017	0.019	0.847
40	0.17	2.6	0.117	0.017	0.025	0.842
40	0.25	7.5	0.115	0.016	0.038	0.831
70	0.01	0.034	0.120	0.017	0.001	0.863
70	0.01	0.241	0.119	0.017	0.002	0.862
70	0.02	0.491	0.119	0.017	0.003	0.861
70	0.04	0.78	0.119	0.017	0.006	0.858
70	0.08	3.6	0.118	0.017	0.013	0.852

Tables 4.3-12 and 13 show the speciation results for 7 m MDEA/2 m PZ and 5 m MDEA/5 m PZ, respectively, at 40 ˚C. The raw H^1 and C^{13} NMR spectra, along with peak identification information, are provided in Appendix A.

Table 4.3-12. Experimental NMR Speciation for 7 m MDEA/2 m PZ at 40 ˚C (Speciation Unit: Liquid Mole Fraction, x_i)

Ldg	0.07	0.095	0.15	0.16
$x_{MDEA/MDEAH+}$	0.1053	0.1066	0.1052	0.1087
$x_{PZ/PZH+}$	0.0211	0.0171	0.0138	0.0109
$x_{PZCOO-/H+}$	0.0094	0.0120	0.0157	0.0155
$x_{PZ(COO)2-}$	0.0009	0.0018	0.0044	0.0052
x_{HCO3-}	0.0005	0.0007	0.0017	0.0021

Table 4.3-13. Experimental NMR Speciation for 5 m MDEA/5 m PZ at 40 ˚C (Speciation Unit: Liquid Mole Fraction, x_i)

Ldg	0.096	0.18	0.36
$x_{MDEA/H+}$	0.0745	0.0732	0.0701
$x_{PZ/H+}$	0.0558	0.0395	0.0159
$x_{PZCOO-/H+}$	0.0185	0.0290	0.0416
$x_{PZ(COO)2-}$	0.0015	0.0052	0.0157
x_{HCO3-}	0.0005	0.0010	0.0060

4.4. Results and Discussion

Fawkes Model Upgrade: Binary MDEA-H_2O System

The following data sets were used in the regression of MDEA-H_2O parameters: (1) MDEA volatilities for MDEA liquid mole fractions up to ~0.36 at 40–100 ˚C; (2) C_p for pure liquid MDEA from 5–95 ˚C; (3) C_p for 1.7 m, 3.5 m, 6.2 m, and 13.9 m MDEA from 15–95 ˚C. Table 4.4-1 shows the regressed parameters for MDEA-H_2O.

Table 4.4-1. Regressed Parameter Results for Binary MDEA-H_2O

Parameter	Component i	Component j	Value (SI units)	Standard deviation
HENRY/1	MDEA	H_2O	-31.6	37.2

HENRY/2	MDEA	H_2O	-9862	1071
HENRY/3	MDEA	H_2O	14.3	6.44
HENRY/4	MDEA	H_2O	-0.055	0.010
HENRY/7	MDEA	H_2O	0	0
NRTL/1	H_2O	MDEA	-0.572	0.004
NRTL/1	MDEA	H_2O	-0.996	0.005
NRTL/2	H_2O	MDEA	0	0
NRTL/2	MDEA	H_2O	1629	10.8
NRTL/3	H_2O	MDEA	0.2	0
NRTL/5	H_2O	MDEA	0	0
NRTL/5	MDEA	H_2O	-0.281	0.002
NRTL/6	H_2O	MDEA	0	0
NRTL/6	MDEA	H_2O	0	0

The regressed parameters are statistically significant as the majority of them are much larger in value than the associated standard deviations. Parameters showing zero values in the table were fixed and not regressed. This set of results represents the most simplified model for this system with all the parameters shown being required to obtain adequate fits of the experimental data. Figure 4.4-1 displays the calculated MDEA volatility, as predicted by a Flash calculation using the above regressed parameters, in comparison to the experimental MDEA volatilities.

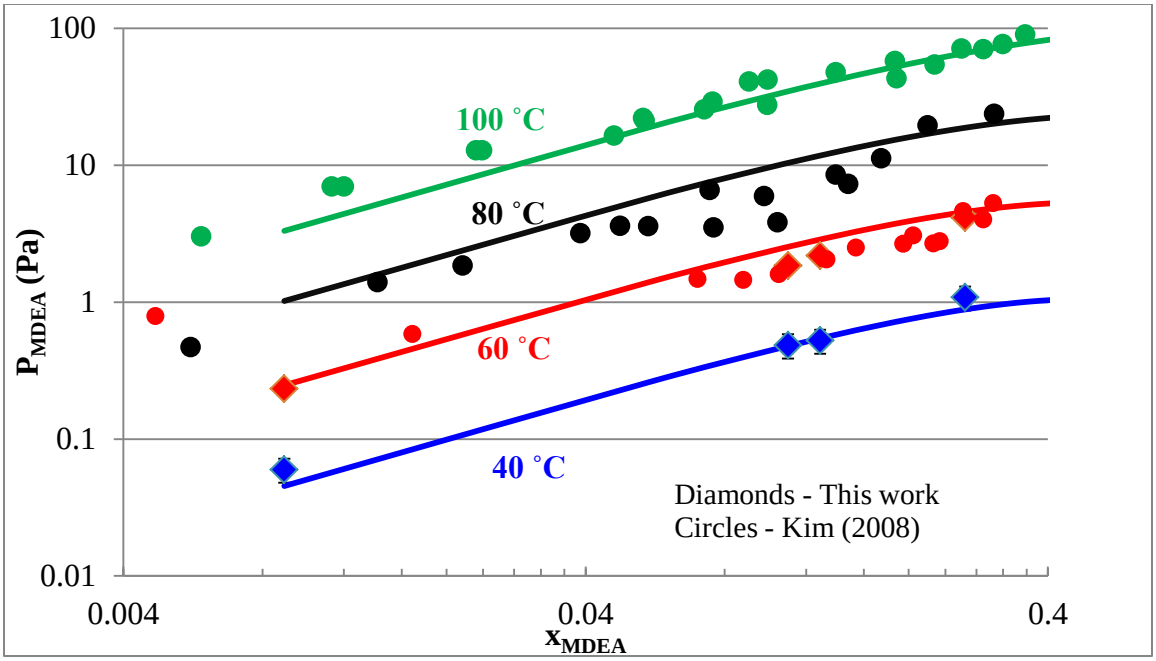

Figure 4.4-1. MDEA Volatility in MDEA-H_2O from 40–100 ˚C

The upgraded Fawkes model is able to represent both the temperature and the effect of MDEA concentration. A separate thermodynamic model may still be required to characterize MDEA volatility and related thermodynamics at very dilute amine concentration typical of water wash operation.

Figure 4.4-2 shows the prediction of MDEA-H_2O heat capacity relative to experimentally measured C_p from 278–368 K.

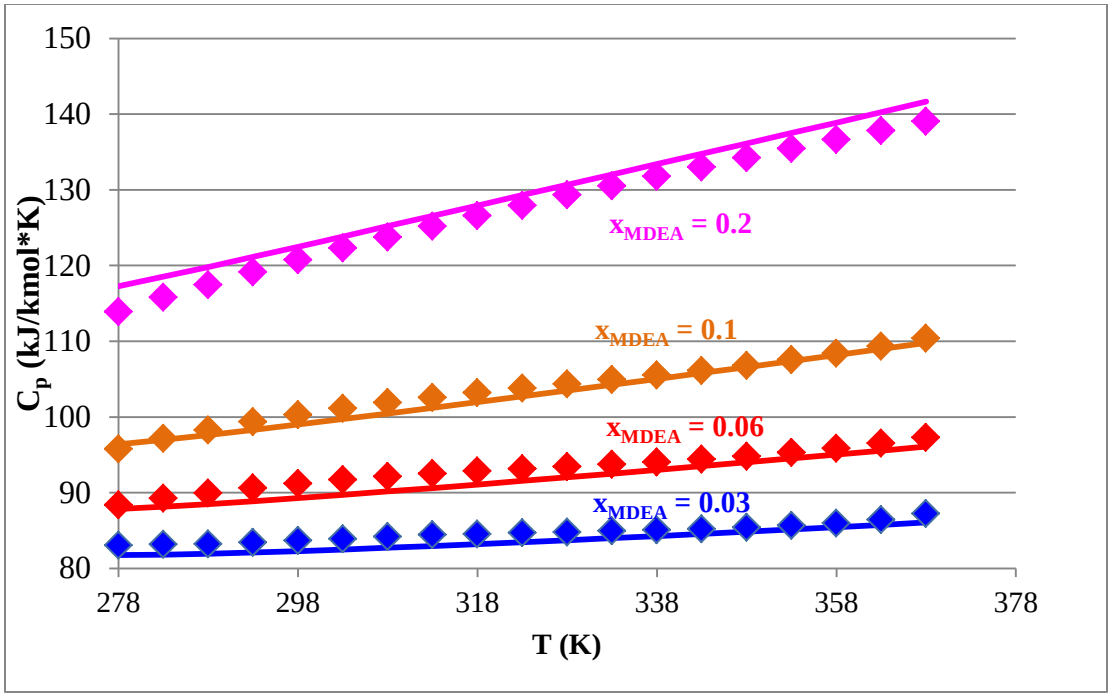

Figure 4.4-2. MDEA-H_2O Heat Capacity from 278–368K (Zhang et al., 2002)

The upgraded model predictions, as represented by solid lines, closely match the experimental C_p in capturing the effects of temperature and MDEA. The solution heat capacity increases with MDEA because MDEA as a species has a large positive contribution to the total C_p. MDEA has a greater intrinsic molar heat capacity than water because it is a bigger molecule with more degrees of freedom for motion.

Figure 4.4-3 displays the same experimental heat capacity of aqueous MDEA (Zhang 2002) in comparison to that of pure water and pure MDEA on a mass basis.

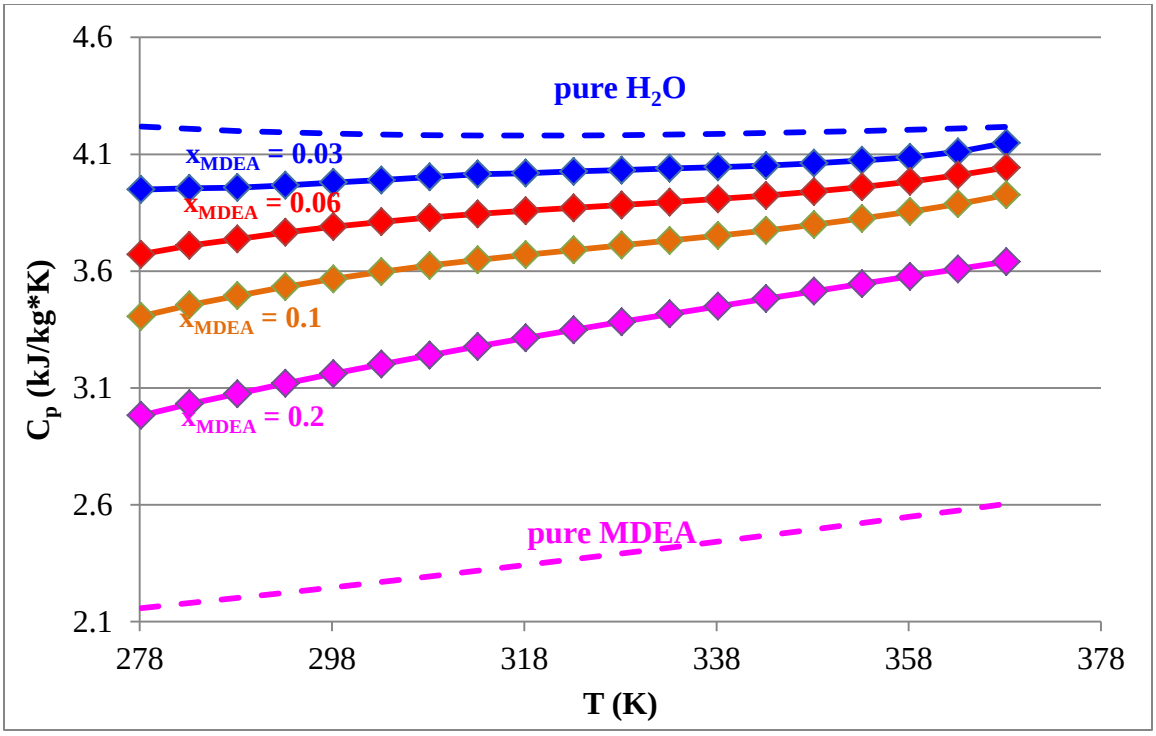

Figure 4.4-3. MDEA-H_2O Heat Capacity from 278 – 368K vs. Pure H_2O and Pure MDEA Heat Capacity (Zhang et. al, 2002)

On a mass basis, the specific heat capacity of aqueous MDEA is the summed contribution of the pure MDEA and pure H_2O heat capacities weighted by their respective fractions. The greater the MDEA fraction, the lower the specific heat capacity of aqueous MDEA as it approaches the limit of pure MDEA heat capacity, and vice-versa.

Fawkes Model Upgrade: MDEA-CO_2-H_2O

The parameters for MDEA-CO_2-H_2O were regressed using the following data sets: (1) CO_2 solubility for 2.8 m, 4.5 m, and 8.4 m loaded MDEA; (2) C_p for 3.6 m, 5.6 m, 8.4 m, and 12.6 m loaded MDEA. All data sets were weighted equally. Table 4.4-2 summarizes the regressed parameter results for MDEA-CO_2-H_2O.

Table 4.4-2. Regressed Parameter Results for MDEA-CO_2-H_2O

Parameter	Component i	Component j	Value (SI units)	Standard deviation
DGAQFM/1	$MDEAH^+$		-2.562E8	0
DHAQFM/1	$MDEAH^+$		-4.985E8	0
CPAQ0/1	$MDEAH^+$		340000	0
CPAQ0/2	$MDEAH^+$		0	0
CPAQ0/3	$MDEAH^+$		0	0
CPAQ0/4	$MDEAH^+$		0	0
GMELCC/1	H_2O	$(MDEAH^+,HCO_3^-)$	9.30	0.202
GMELCC/1	$(MDEAH^+,HCO_3^-)$	H_2O	-4.26	0.090
GMELCC/1	MDEA	$(MDEAH^+,HCO_3^-)$	8.63	0.209
GMELCC/1	$(MDEAH^+,HCO_3^-)$	MDEA	-1.97	0.068
GMELCD/1	H_2O	$(MDEAH^+,HCO_3^-)$	-1.88	0.070
GMELCD/1	$(MDEAH^+,HCO_3^-)$	H_2O	-1.97	0.076
GMELCD/1	MDEA	$(MDEAH^+,HCO_3^-)$	-0.091	0.003
GMELCD/1	$(MDEAH^+,HCO_3^-)$	MDEA	-0.031	0.001
GMELCE/1	H_2O	$(MDEAH^+,HCO_3^-)$	1.57	0.077
GMELCE/1	$(MDEAH^+,HCO_3^-)$	H_2O	0.411	0.022
GMELCE/1	MDEA	$(MDEAH^+,HCO_3^-)$	-2.48	0.107
GMELCE/1	$(MDEAH^+,HCO_3^-)$	MDEA	-0.690	0.046
GMELCC/1	H_2O	$(MDEAH^+,CO_3^{--})$	8.26	0.202
GMELCC/1	$(MDEAH^+,CO_3^{--})$	H_2O	-3.97	0.096
GMELCC/1	MDEA	$(MDEAH^+,CO_3^{--})$	10.74	0.365
GMELCC/1	$(MDEAH^+,CO_3^{--})$	MDEA	-1.93	0.085
GMELCD/1	H_2O	$(MDEAH^+,CO_3^{--})$	-2.04	0.091
GMELCD/1	$(MDEAH^+,CO_3^{--})$	H_2O	-0.034	0.001
GMELCD/1	MDEA	$(MDEAH^+,CO_3^{--})$	0.005	0.001
GMELCD/1	$(MDEAH^+,CO_3^{--})$	MDEA	0.023	0.001
GMELCE/1	H_2O	$(MDEAH^+,CO_3^{--})$	4.47	0.153
GMELCE/1	$(MDEAH^+,CO_3^{--})$	H_2O	0.221	0.013
GMELCE/1	MDEA	$(MDEAH^+,CO_3^{--})$	-2.15	0.109
GMELCE/1	$(MDEAH^+,CO_3^{--})$	MDEA	-2.71	0.157

The regressed parameter results are all statistically significant as the magnitudes of the coefficients are much greater than those of the associated standard deviations. The

correlation matrix for the above 24 parameters, constituting a total of 276 parameter pairs, shows that no two parameters are strongly correlated as all of the correlation factors are below 0.75. All of the above parameters are required to match the variety of data types and sheer volume of data used. Nonetheless, a reduced model with fewer parameters will be presented later. Parameters in the full model having negligible values are zeroed out and again the model was regressed to obtain the reduced case. While the elimination of parameters allows for the development of a simpler model, the ability to fit certain data is compromised to some extent.

The free energy, enthalpy, and heat capacity parameters of the electrolyte $MDEAH^+$ were manually adjusted to simultaneously match: (1) the pKa of the reaction which involves MDEA being protonated to form $MDEAH^+$ and (2) all the rest of the data types. The free energy parameter for this species, DGAQFM, was most crucial for anchoring the pKa and CO_2 solubility predictions at 25 ˚C whereas the enthalpy, DHAQFM, was vital for obtaining the appropriate temperature behaviors of the pKa extrapolation and of the CO_2 solubility and C_p.

Figure 4.4-4 shows predicted pKa for $MDEAH^+$ reaction as obtained by manually adjusting the mentioned parameters. The experimental pKa measurements were obtained by Hamborg and co-workers (2007).

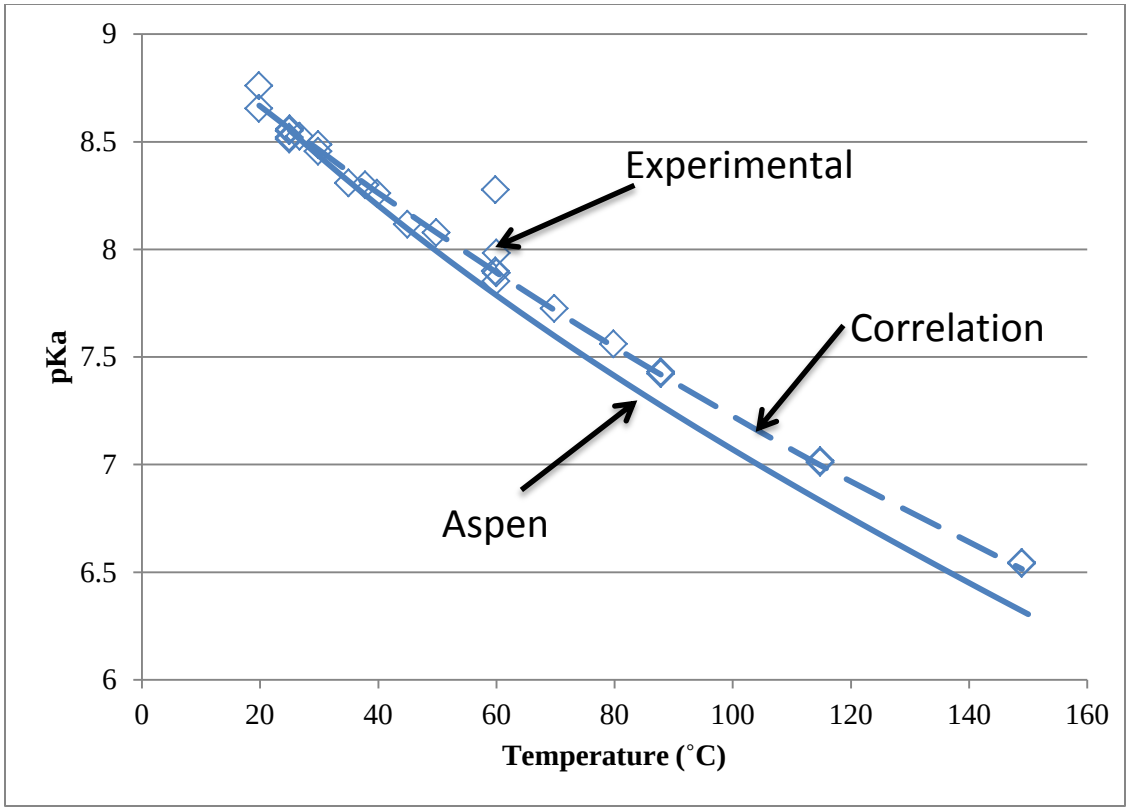

Figure 4.4-4. Comparison of predicted pKa for MDEA protonation to experimental values

The above pKa prediction by Aspen Plus® was the best case scenario obtained by manually adjusting the free energy, enthalpy, and heat capacity of $MDEAH^+$ without compromising the ability to fit the various data types used in the regression. The pKa value predicted at 25 ˚C matched the experimental value exactly which indicated that the free energy parameter for this species was very well approximated. Nevertheless, the slight deviation of the temperature behavior of the pKa curve from the experimental trend suggests that the enthalpy of the species is not adequate for fitting pKa. While this parameter can be adjusted in such a way that the pKa temperature behavior is fitted exactly, this option was not taken because the CO_2 solubility predictions at high temperature, particularly at 120 ˚C, became grossly inaccurate. This tradeoff suggests

that the temperature behavior of the pKa is not consistent with the high temperature VLE. Ultimately, it was decided that it was more important to fit CO_2 solubility more adequately even if it meant compromising the pKa fit to a slight extent as the former data is more crucial to industrial capture process modeling.

In this version of the Fawkes model upgrade, it was decided that the carbonate species (CO_3^{2-}) needed to be introduced into the chemistry set to allow for a better fit of CO_2 solubility at very low loading ($\alpha <= 0.01$ mol CO_2/mol alkalinity). The following reaction was added to the existing chemistry set to incorporate carbonate into the mix as a significant species at low loadings.

$$HCO_3^- + MDEA < \text{--------} > CO_3^{2-} + MDEAH^+ \qquad (4\text{-}12)$$

The addition of the carbonate species proved to be effective as expected in allowing an improved fit of CO_2 solubility at very low loadings. Figures 4.4-5, 6, and 7 show the CO_2 solubility predictions from the full model.

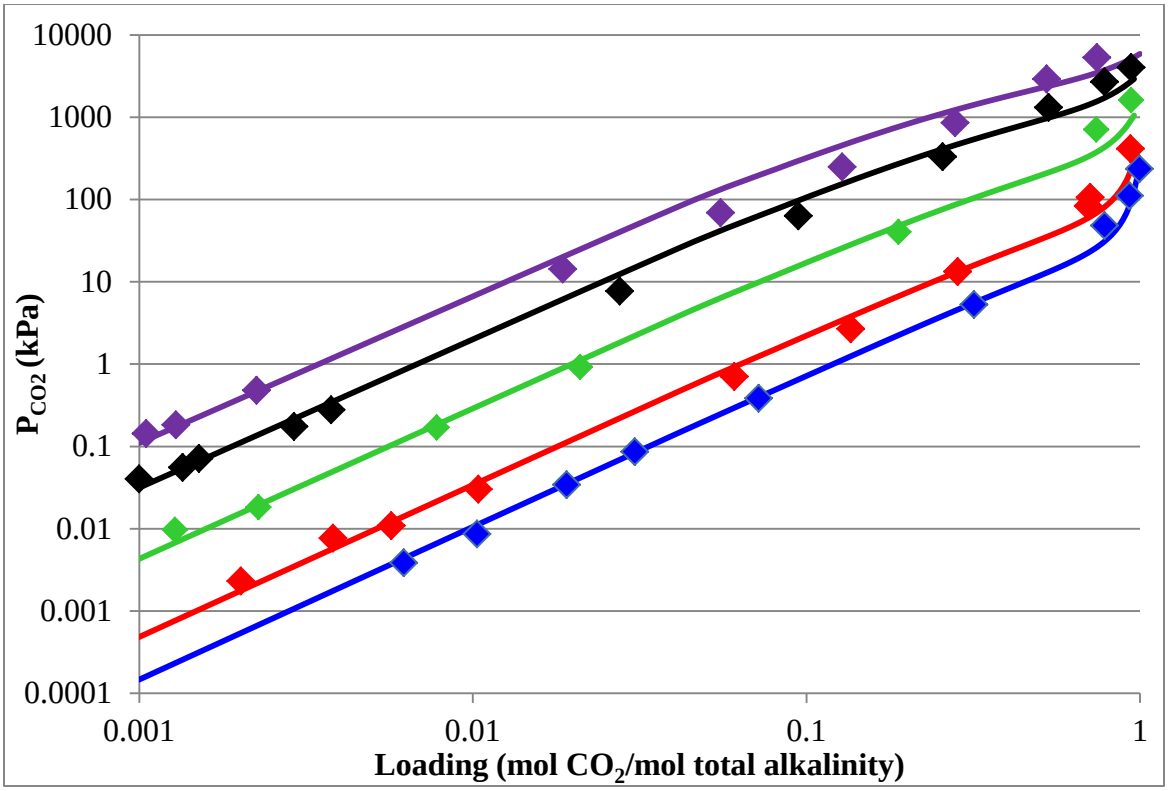

Figure 4.4-5. CO_2 Solubility for 8.4 m MDEA-CO_2-H_2O from 25–120 ˚C (Jou et al., 1982)

The full model captured the experimental CO_2 solubility data well despite a significant offset at 120 ˚C. These results are considered to be the best case prediction which balances the tradeoff discussed earlier between matching the pKa of $MDEAH^+$ reaction and matching the temperature behavior of the data. The enthalpy of $MDEAH^+$ was found to be a highly sensitive parameter which can shift the temperature behavior of the predictions significantly.

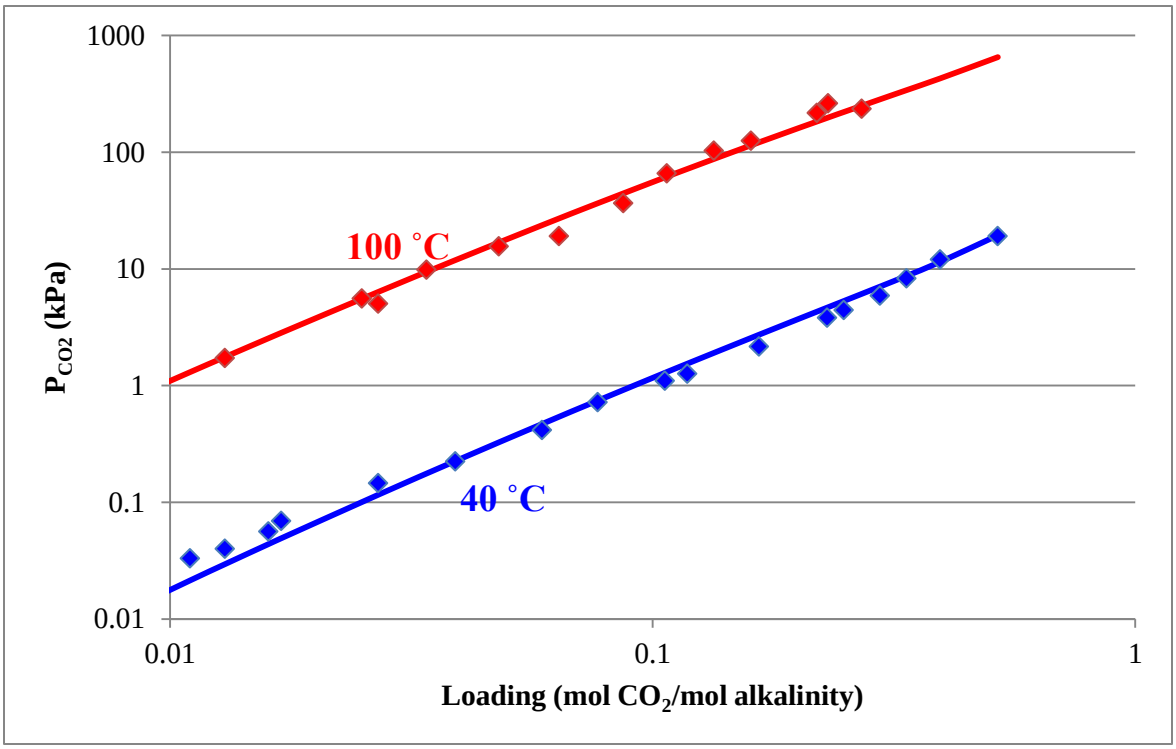

Figure 4.4-6. CO_2 Solubility for 4.5 m MDEA-CO_2-H_2O at 40 and 100 ˚C (Jou et al., 1982)

The full model was able to match the experimental CO_2 solubility well even at low loadings due to the introduction of carbonate species.

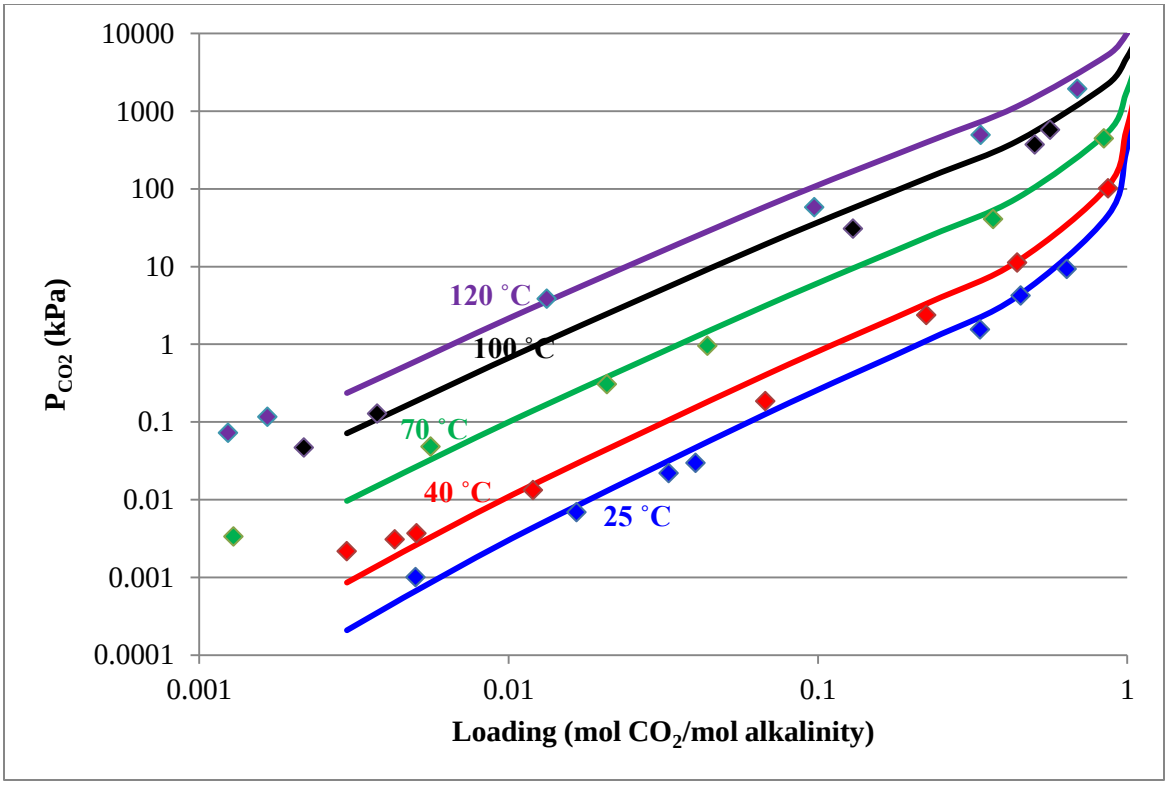

Figure 4.4-7. CO_2 Solubility for 2.8 m MDEA-CO_2-H_2O from 25–120 ˚C (Jou et al., 1982)

The full model was able to adequately represent the CO_2 solubility data at 2.8 m MDEA. It appears that the CO_2 partial pressure at this concentration was even better matched than at higher MDEA as the model is centered on an infinite dilution reference state. Therefore dilute concentration data can be better fitted than concentrated data.

The C_p of MDEA-CO_2-H_2O was also regressed to obtain parameter results. Figure 4.4-8 shows the upgraded Fawkes model predictions of heat capacity at 25 ˚C in loaded MDEA compared to experimental values.

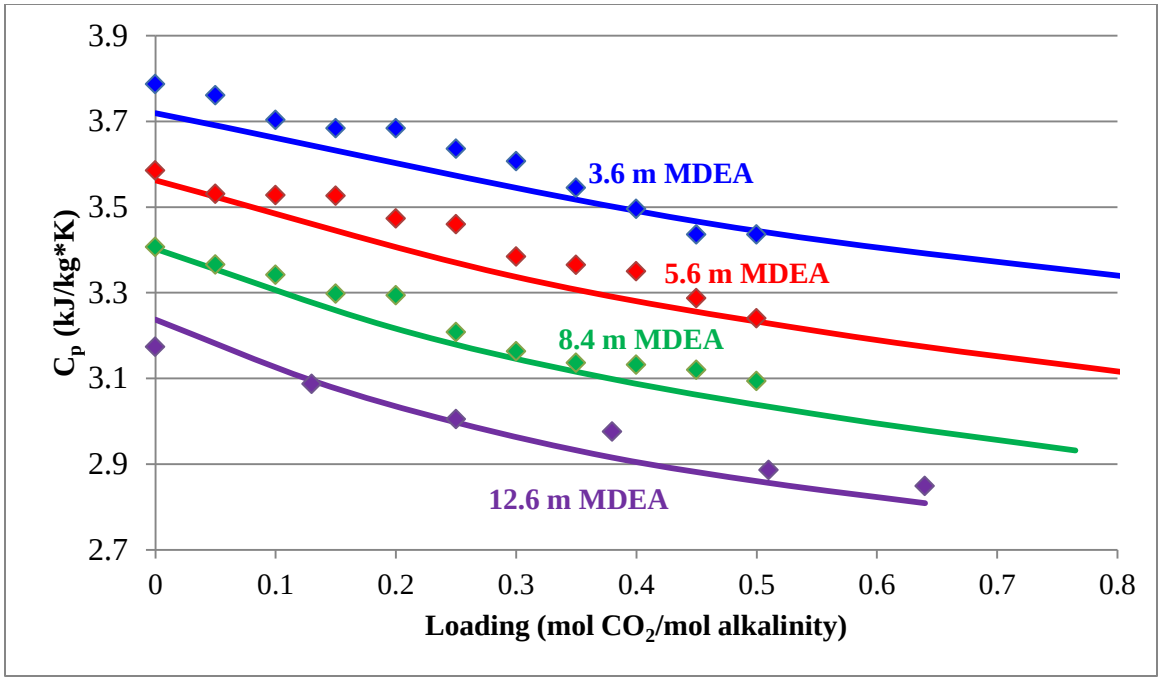

Figure 4.4-8. Heat Capacity for 3.6–12.6 m MDEA-CO_2-H_2O at 25 ˚C (Weiland et al., 1997)

The upgraded Fawkes model captures the both the loading and concentration effects of the experimental C_p fairly well. At a given MDEA concentration, the heat capacity of the solution decreases as loading increases because CO_2 has a negligible specific heat capacity; therefore, adding CO_2 to the solution does not contribute to the total solution heat capacity and even serves to lower the specific C_p of the solution. At a given loading, the solution C_p does not necessarily increase with increasing MDEA either. Since loading is given as moles of CO_2/mol MDEA, a concentrated MDEA solution would have more CO_2 than a less concentrated solution at the same loading. Using the same argument above, the more concentrated MDEA solution (with a greater amount of CO_2) would have lower specific C_p than a less concentrated MDEA solution as CO_2 has negligible C_p as a species and does not contribute to the total C_p of the solution. The total C_p increases solely due to the contribution of MDEA at higher MDEA

concentrations, but this by itself is not enough to offset the increase in CO_2 which does not contribute to the total C_p, and therefore the specific C_p of the solution decreases even as MDEA concentration increases at a given fixed loading.

Figure 4.4-9 shows the above C_p data for MDEA-CO_2-H_2O system in the unit of kJ/(kg amine+H_2O-K) instead of per kg of solution. The heat capacity values are greater on a CO_2-free basis and are rather constant over the loading range examined which suggests that the partial C_p of CO_2 is negligible and possibly even less than zero.

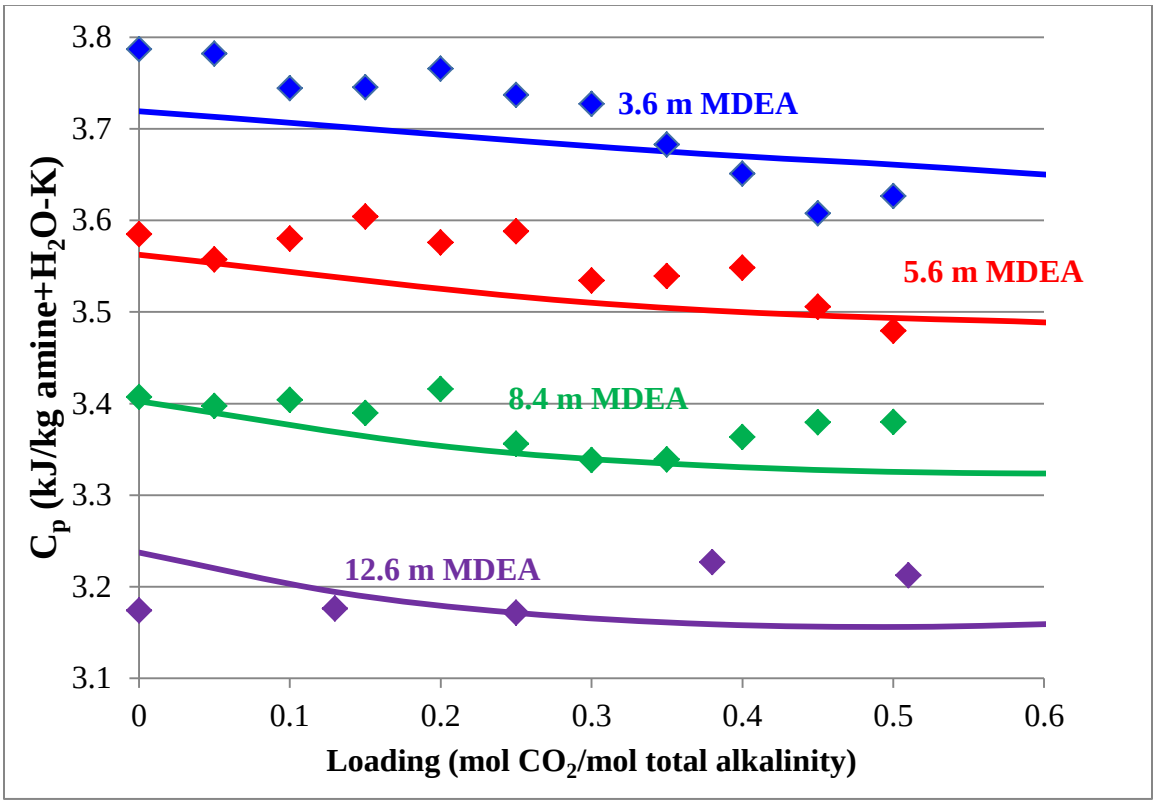

Figure 4.4-9. Heat Capacity for 3.6–12.6 m MDEA-CO_2-H_2O at 25 ˚C on a CO_2-free Basis (Weiland et al., 1997)

Figure 4.4-10 shows the upgraded Fawkes model prediction of 7 m MDEA-CO_2-H_2O C_p for a loading of 0.144 mol CO_2/mol alkalinity from 40–120 ˚C.

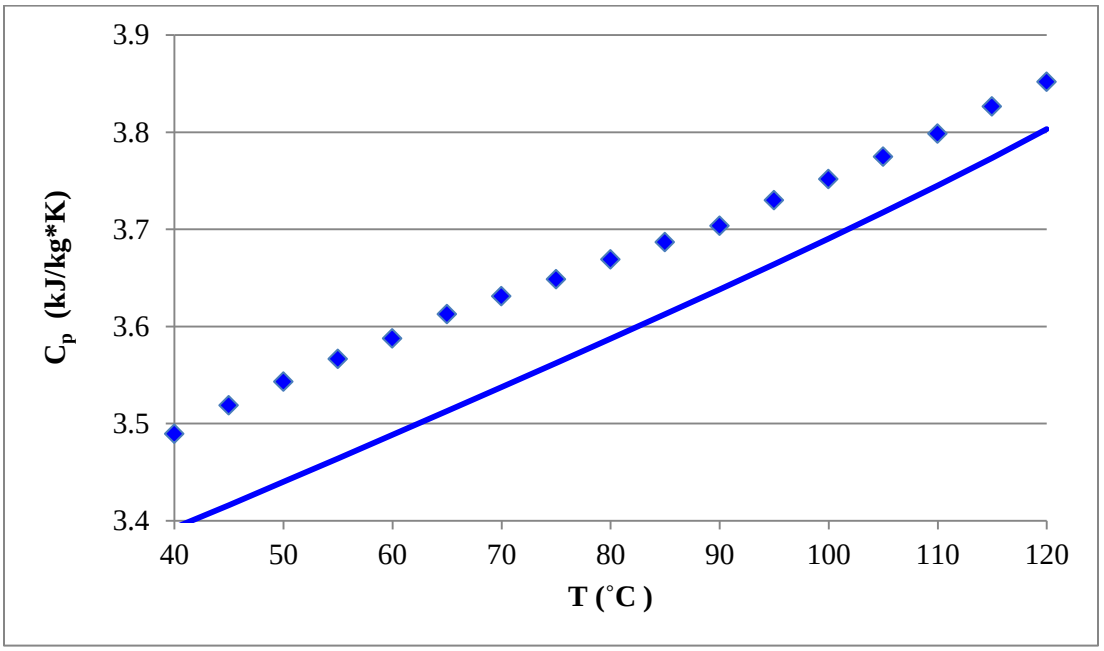

Figure 4.4-10. Fawkes Model Prediction of 7 m MDEA-CO_2-H_2O C_p for Ldg ~0.144

The upgraded Fawkes model is able to match the experimental C_p for loaded 7 m MDEA with only a ±3% error; more importantly, the model is able to capture the temperature behavior of the C_p without the use of any additional constraint or input. This result is rather good given that this specific data was not regressed beforehand with the intention of matching it exactly.

Figure 4.4-11 displays the measured MDEA volatility for 7 m MDEA-CO_2-H_2O and 20 m MDEA-CO_2-H_2O along with the upgraded Fawkes model predictions at 40 ˚ and 60 ˚C.

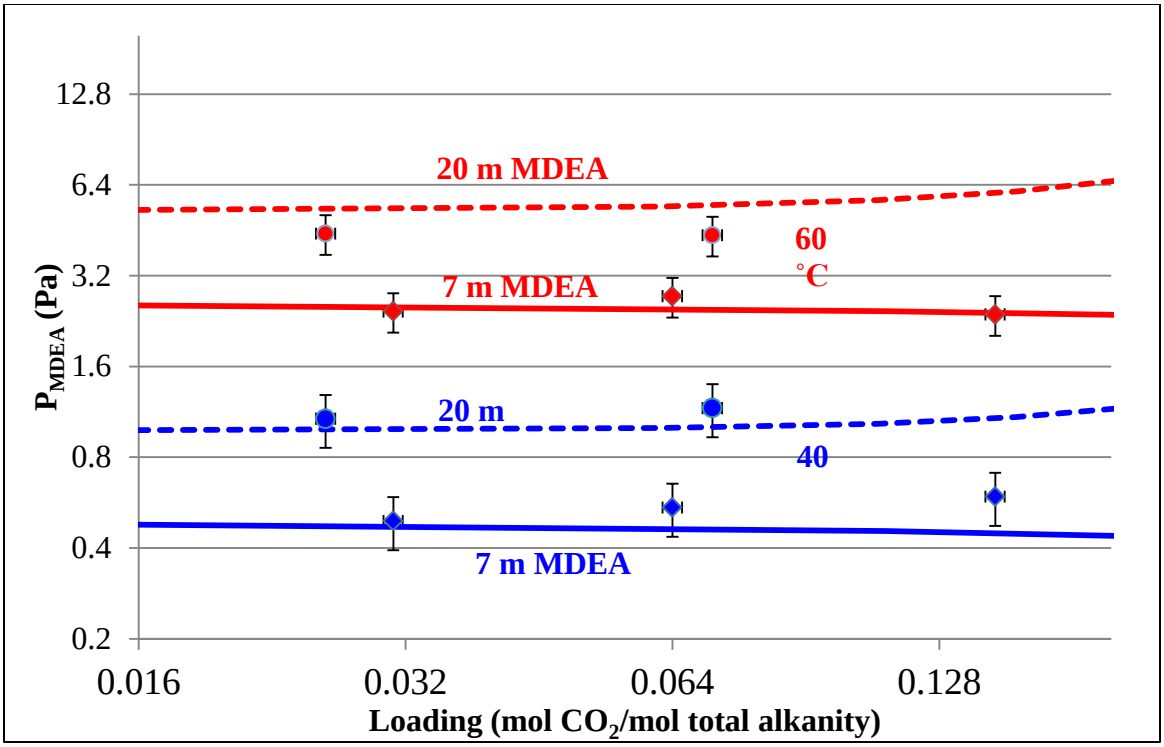

Figure 4.4-11. MDEA Volatility for 7 m and 20 m MDEA-CO_2-H_2O at 40 ˚ and 60 ˚C

Figure 4.4-12 examines the upgraded Fawkes model predictions of activity coefficients for all the key species in an 8.4 m MDEA-CO_2-H_2O solution at 40 ˚C.

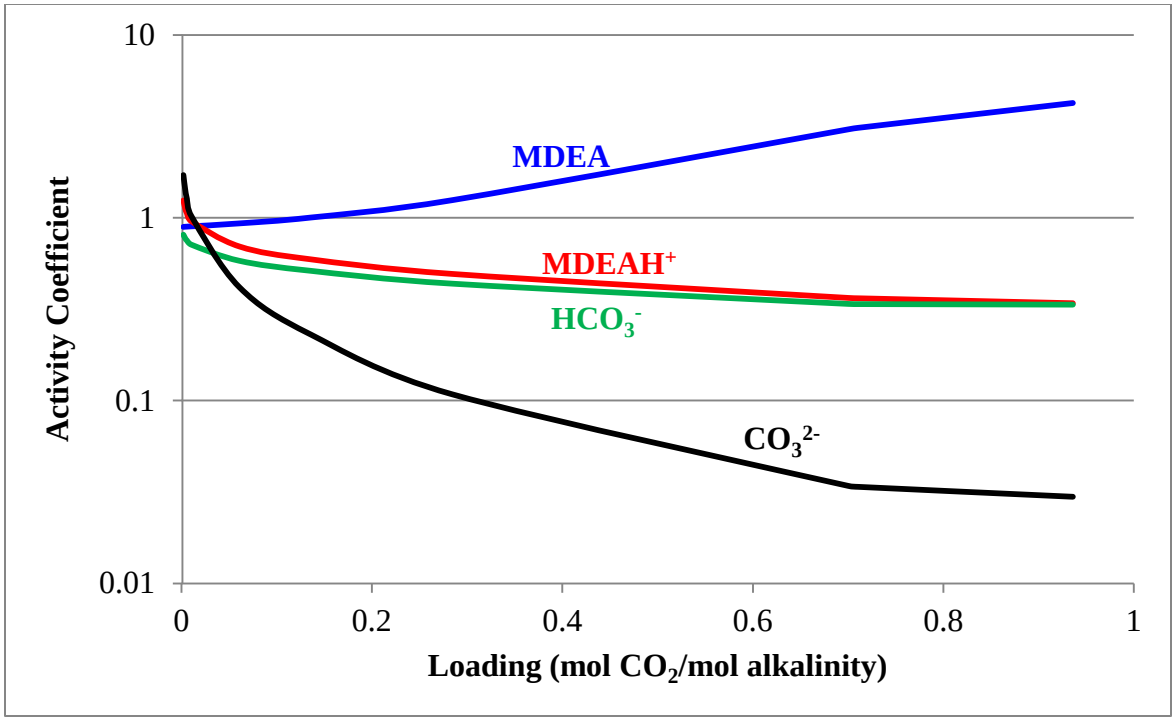

Figure 4.4-12. Species Activity Coefficients for 8.4 m MDEA-CO_2-H_2O at 40 ˚C

MDEA, as a solute, is assigned to have the asymmetric activity coefficient convention in the Fawkes model where its value equals 1, by definition, when present at infinite dilution in the solvent (H_2O). At low loading conditions ($0.001 < \alpha < 0.2$), MDEA maintains an activity coefficient of almost 1 even though it is far from being infinitely dilute in the system (8.4 m MDEA-CO_2-H_2O). For higher loading ($\alpha > 0.2$), the MDEA activity coefficient starts to increase from 1 which indicates that MDEA salts out due to the overwhelming presence of electrolytes generated in solution. Accordingly, MDEA volatility also somewhat increases at higher loading as a consequence of MDEA salting out.

All of the electrolyte species, including $MDEAH^+$, HCO_3^-, and CO_3^{2-}, also share the asymmetric activity coefficient convention. At very lean loading, all of these electrolytes have activity coefficients very close to 1 as their concentrations are

practically negligible, though not infinitely dilute, due to the lack of CO_2. At greater loading, their activity coefficient start to drop due to interactions with increasing amounts of like neighbors being generated with higher amounts of CO_2. In other words, the electrolytes species are salted in with other electrolytes unlike MDEA. In particular, CO_3^{2-} activity coefficient drops significantly with loading as would be expected given increasingly greater concentration of HCO_3^-/CO_3^{2-} being generated.

MDEA-CO_2-H_2O Reduced Model

Certain parameters in the full model whose values were considered negligible were eliminated in an attempt to develop a simpler model for MDEA-CO_2-H_2O. The same data sets were regressed again using fewer parameters to fit the data. Table 4.4-3 summarizes the regressed parameter results for the reduced model.

Table 4.4-3. Regressed Parameter Results for MDEA-CO_2-H_2O Reduced Model

Parameter	Component i	Component j	Value (SI units)	Standard deviation
DGAQFM/1	$MDEAH^+$		-256200000	0
DHAQFM/1	$MDEAH^+$		-498500000	0
CPAQ0/1	$MDEAH^+$		340000	0
CPAQ0/2	$MDEAH^+$		0	0
CPAQ0/3	$MDEAH^+$		0	0
CPAQ0/4	$MDEAH^+$		0	0
GMELCC/1	H_2O	($MDEAH^+$,HCO_3^-)	8.65	0.127
GMELCC/1	($MDEAH^+$,HCO_3^-)	H_2O	-3.96	0.058
GMELCC/1	MDEA	($MDEAH^+$,HCO_3^-)	8.40	0.124
GMELCC/1	($MDEAH^+$,HCO_3^-)	MDEA	-2.08	0.069
GMELCD/1	H_2O	($MDEAH^+$,HCO_3^-)	-1.93	0.044
GMELCD/1	($MDEAH^+$,HCO_3^-)	H_2O	-1.97	0.037
GMELCD/1	MDEA	($MDEAH^+$,HCO_3^-)	0	0
GMELCD/1	($MDEAH^+$,HCO_3^-)	MDEA	0	0
GMELCE/1	H_2O	($MDEAH^+$,HCO_3^-)	0.807	0.027
GMELCE/1	($MDEAH^+$,HCO_3^-)	H_2O	0.119	0.005

GMELCE/1	MDEA	($MDEAH^+$,HCO_3^-)	-0.807	0.044
GMELCE/1	($MDEAH^+$,HCO_3^-)	MDEA	-0.651	0.027
GMELCC/1	H_2O	($MDEAH^+$,CO_3^{--})	8.05	0.226
GMELCC/1	($MDEAH^+$,CO_3^{--})	H_2O	-3.85	0.076
GMELCC/1	MDEA	($MDEAH^+$,CO_3^{--})	9.932	0.234
GMELCC/1	($MDEAH^+$,CO_3^{--})	MDEA	-1.98	0.048
GMELCD/1	H_2O	($MDEAH^+$,CO_3^{--})	-1.96	0.049
GMELCD/1	($MDEAH^+$,CO_3^{--})	H_2O	0	0
GMELCD/1	MDEA	($MDEAH^+$,CO_3^{--})	0	0
GMELCD/1	($MDEAH^+$,CO_3^{--})	MDEA	0	0
GMELCE/1	H_2O	($MDEAH^+$,CO_3^{--})	0.240	0.011
GMELCE/1	($MDEAH^+$,CO_3^{--})	H_2O	0.151	0.007
GMELCE/1	MDEA	($MDEAH^+$,CO_3^{--})	-0.728	0.042
GMELCE/1	($MDEAH^+$,CO_3^{--})	MDEA	-0.360	0.014

The reduced model was able to adequately fit the regressed data almost as well as the full model. The only two pieces of data that were not matched well were the CO_2 solubility for 8.4 m MDEA-CO_2-H_2O at 120 ˚C and the loading effect on the isothermal C_p for various MDEA concentrations at 25 ˚C. Nevertheless, the reduced model proved to be robust overall and serves as a promising alternative to the full model as it allows more flexibility, or more degrees of freedom, when it comes to fitting data for the more complex MDEA-PZ blend. Ultimately the reduced MDEA-CO_2-H_2O model was incorporated into the full model for the blend.

Fawkes Model Upgrade: MDEA-PZ-H_2O

No additional parameter, namely cross parameters for MDEA-PZ interactions, had to be used to match the MDEA/PZ volatility for either 7 m MDEA/2 m PZ or 5 m MDEA/5 m PZ from 40 ˚–60 ˚C. In other words, the cross interaction parameters were set to zero. The reason that this is the case is because the binary MDEA-H_2O parameters

were properly regressed at the earlier stage to where the blend volatilities can be accurately matched accordingly, and also that the MDEA-PZ interactions were not significant. Figures 4.4-13 and 14 show the Flash predictions of the volatilities for 7 m MDEA/2 m PZ and 5 m MDEA/5 m PZ, respectively, in comparison to experimental data.

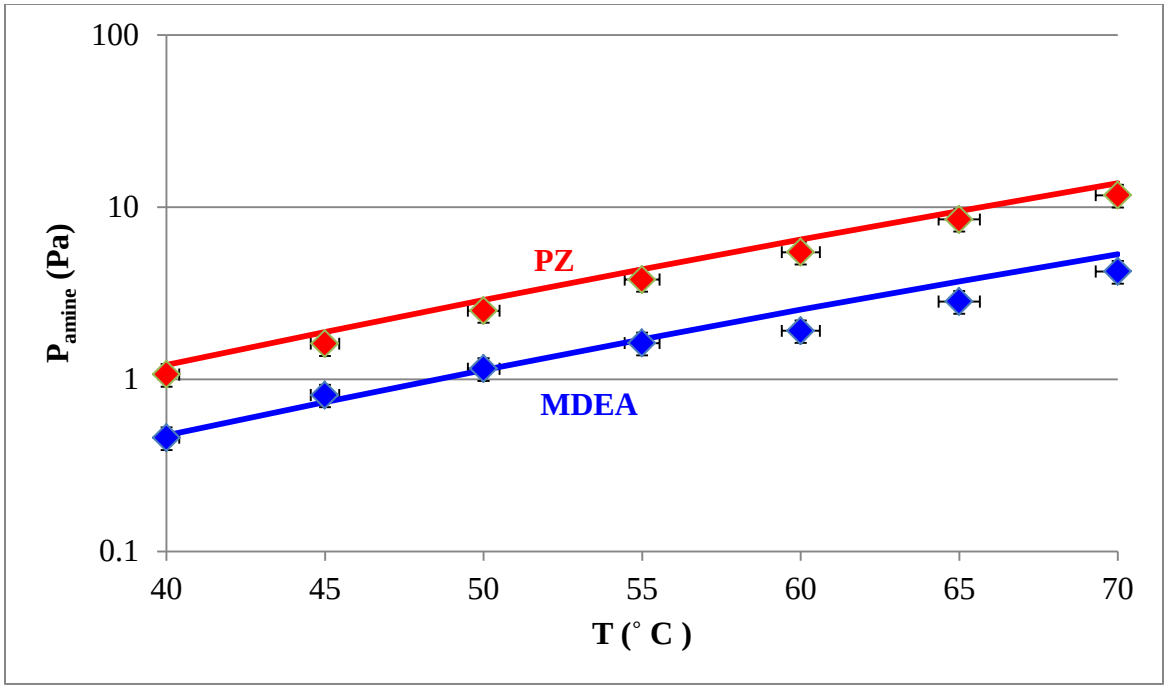

Figure 4.4-13. MDEA and PZ Volatility for 7 m MDEA/2 m PZ for 40 ˚– 70 ˚C

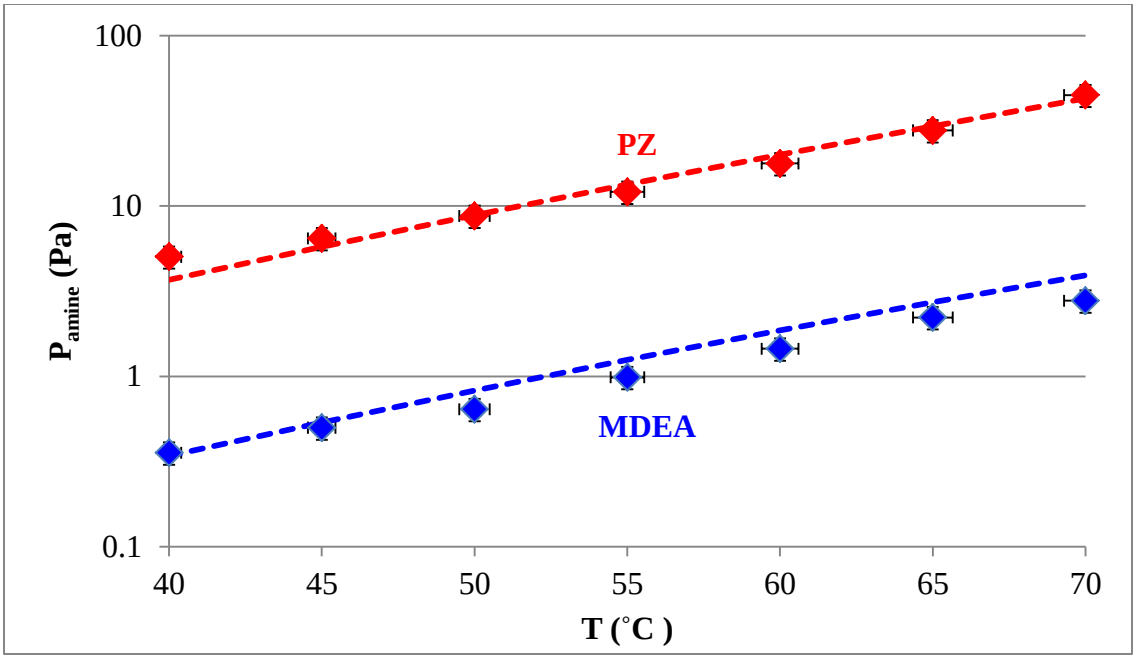

Figure 4.4-14. MDEA and PZ Volatility for 5 m MDEA/5 m PZ for 40 ˚– 70 ˚C

The upgraded Fawkes model now adequately matches experimental volatility data for the two unloaded blends. Recall that matching the blend volatility was an issue with the previous Fawkes model.

Fawkes Model Upgrade: MDEA-PZ-CO_2-H_2O System

CO_2 solubility data for 7 m MDEA/2 m PZ, 5 m MDEA/5 m PZ, and 7.7 m MDEA/1.1 m PZ were used in the regression of MDEA, PZ, and the zwitterion H^+PZCOO^- interactions with ion pairs in solution. The best possible combination of parameters used to match the different types of data includes eNRTL parameters for H_2O interaction with ion pairs, eNRTL default parameter values for molecule to ion interactions to characterize MDEA and PZ interactions with ion pairs (10 for amine to ion pairs, -2 for ion pairs to amine), eNRTL default parameter values to represent the zwitterion H^+PZCOO^- interaction with ion pairs which are set to mimic default water

interaction values (8 for zwitterions to ion pairs, -4 for ion pairs to zwitterion), and the non-randomness factor for zwitterion to MDEA interaction fixed at 0.3. Table 4.4-4 summarizes the values of electrolyte pair interaction parameters for the quaternary MDEA-PZ-CO_2-H_2O regression.

Table 4.4-4. Regressed Parameter Results for MDEA-PZ-CO_2-H_2O Model

Parameter	Component i	Component j	Value (SI units)
GMELCC/1	H_2O	($MDEAH^+$,$PZCOO^-$)	8.45
GMELCC/1	($MDEAH^+$,$PZCOO^-$)	H_2O	-5.60
GMELCC/1	H_2O	($MDEAH^+$,$PZCOO^{-2}$)	7.44
GMELCC/1	($MDEAH^+$,$PZCOO^{-2}$)	H_2O	-4.09
GMELCD/1	H_2O	($MDEAH^+$,$PZCOO^-$)	0
GMELCD/1	($MDEAH^+$, $PZCOO^-$)	H_2O	0
GMELCD/1	H_2O	($MDEAH^+$, $PZCOO^{-2}$)	0
GMELCD/1	($MDEAH^+$, $PZCOO^{-2}$)	H_2O	0
GMELCE/1	H_2O	($MDEAH^+$, $PZCOO^-$)	66.5
GMELCE/1	($MDEAH^+$, $PZCOO^-$)	H_2O	-43.7
GMELCE/1	H_2O	($MDEAH^+$, $PZCOO^{-2}$)	-30.1
GMELCE/1	($MDEAH^+$, $PZCOO^{-2}$)	H_2O	33.4
GMELCC/1	MDEA	($MDEAH^+$, $PZCOO^-$)	21.8
GMELCC/1	($MDEAH^+$, $PZCOO^-$)	MDEA	8.92
GMELCC/1	MDEA	($MDEAH^+$, $PZCOO^{-2}$)	11.1
GMELCC/1	($MDEAH^+$, $PZCOO^{-2}$)	MDEA	1.92
GMELCD/1	MDEA	($MDEAH^+$, $PZCOO^-$)	0
GMELCD/1	($MDEAH^+$, $PZCOO^-$)	MDEA	0
GMELCD/1	MDEA	($MDEAH^+$, $PZCOO^{-2}$)	0
GMELCD/1	($MDEAH^+$, $PZCOO^{-2}$)	MDEA	0
GMELCE/1	MDEA	($MDEAH^+$, $PZCOO^-$)	0
GMELCE/1	($MDEAH^+$, $PZCOO^-$)	MDEA	0
GMELCE/1	MDEA	($MDEAH^+$, $PZCOO^{-2}$)	0
GMELCE/1	($MDEAH^+$, $PZCOO^{-2}$)	MDEA	0
GMELCC/1	MDEA	(PZH^+, $PZCOO^-$)	10
GMELCC/1	(PZH^+, $PZCOO^-$)	MDEA	-2
GMELCC/1	MDEA	(PZH^+, $PZCOO^{-2}$)	10
GMELCC/1	(PZH^+, $PZCOO^{-2}$)	MDEA	-2

GMELCC/1	MDEA	(PZH^+,HCO_3^-)	10
GMELCC/1	(PZH^+, HCO_3^-)	MDEA	-2
GMELCC/1	HPZCOO	($MDEAH^+$, $PZCOO^-$)	8
GMELCC/1	($MDEAH^+$, $PZCOO^-$)	HPZCOO	-4
GMELCC/1	HPZCOO	($MDEAH^+$, $PZCOO^{-2}$)	8
GMELCC/1	($MDEAH^+$, $PZCOO^{-2}$)	HPZCOO	-4
GMELCC/1	HPZCOO	($MDEAH^+$, HCO_3^-)	8
GMELCC/1	($MDEAH^+$, HCO_3^-)	HPZCOO	-4
GMELCD/1	HPZCOO	($MDEAH^+$, $PZCOO^-$)	0
GMELCD/1	($MDEAH^+$, $PZCOO^-$)	HPZCOO	0
GMELCD/1	HPZCOO	($MDEAH^+$, $PZCOO^{-2}$)	0
GMELCD/1	($MDEAH^+$, $PZCOO^{-2}$)	HPZCOO	0
GMELCD/1	HPZCOO	($MDEAH^+$, HCO_3^-)	0
GMELCD/1	($MDEAH^+$, HCO_3^-)	HPZCOO	0
GMELCC/1	PZ	($MDEAH^+$, $PZCOO^-$)	10
GMELCC/1	($MDEAH^+$, $PZCOO^-$)	PZ	-2
GMELCC/1	PZ	($MDEAH^+$, $PZCOO^{-2}$)	10
GMELCC/1	($MDEAH^+$, $PZCOO^{-2}$)	PZ	-2
GMELCC/1	PZ	($MDEAH^+$, HCO_3^-)	10
GMELCC/1	($MDEAH^+$, HCO_3^-)	PZ	-2
NRTL/1	MDEA	HPZCOO	0
NRTL/1	HPZCOO	MDEA	0
NRTL/2	MDEA	HPZCOO	0
NRTL/2	HPZCOO	MDEA	0
NRTL/3	HPZCOO	MDEA	0.3

Figure 4.4-15 shows the upgraded model predictions for CO_2 solubility in comparison to experimental data for 7 m MDEA/2 m PZ from 40 ˚–160 ˚C.

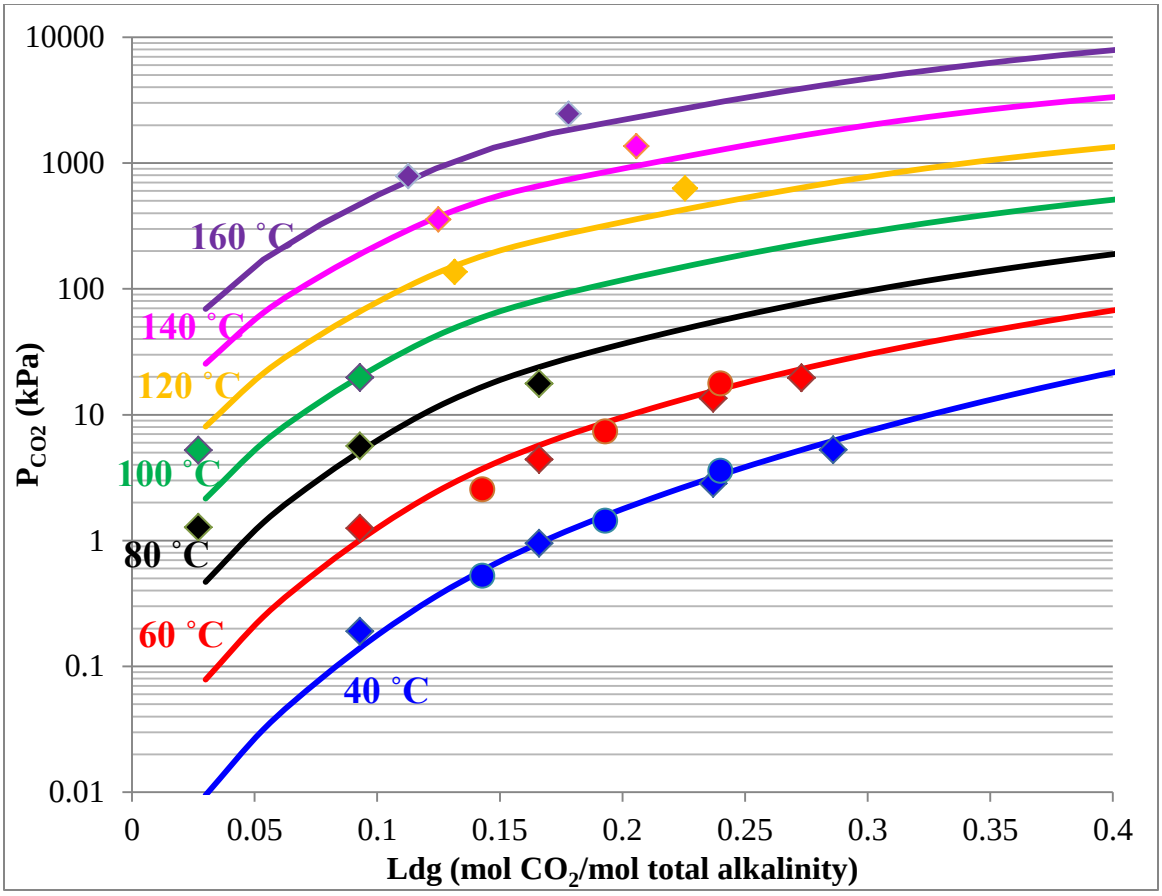

Figure 4.4-15. CO_2 Solubility Predictions for 7 m MDEA/2 m PZ from 40 ˚– 160 ˚C

The upgraded Fawkes model adequately matches CO_2 solubility data for 7 m MDEA/2 m PZ for a wide range of temperature. Experimental data for very lean loadings ($\alpha < 0.05$ mol CO_2/mol total alkalinity) appear to be experimental outliers.

Figure 4.4-16 displays the upgraded model predictions for CO_2 solubility in comparison to experimental data for 5 m MDEA/5 m PZ from 40 ˚– 160 ˚C.

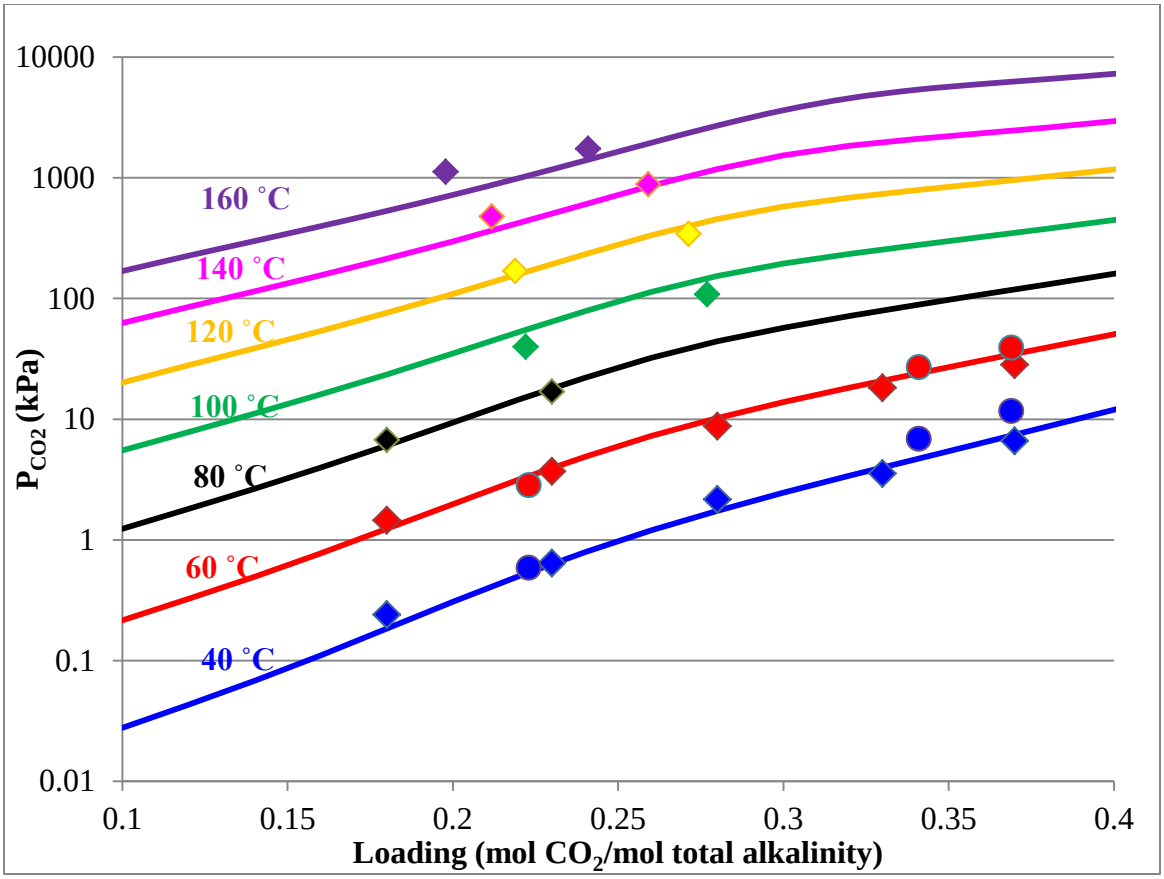

Figure 4.4-16. CO_2 Solubility Predictions for 5 m MDEA/5 m PZ from 40 ˚ – 160 ˚C

The upgraded model sufficiently represents the CO_2 solubility data for 5 m MDEA/5 m PZ for the wide range of temperature shown.

Figure 4.4-17 shows the model predictions for CO_2 solubility for 7.7 m MDEA/1.1 m PZ at 40 ˚ and 70 ˚C. Again, the model extrapolates well in predicting the CO_2 solubility at this blend concentration.

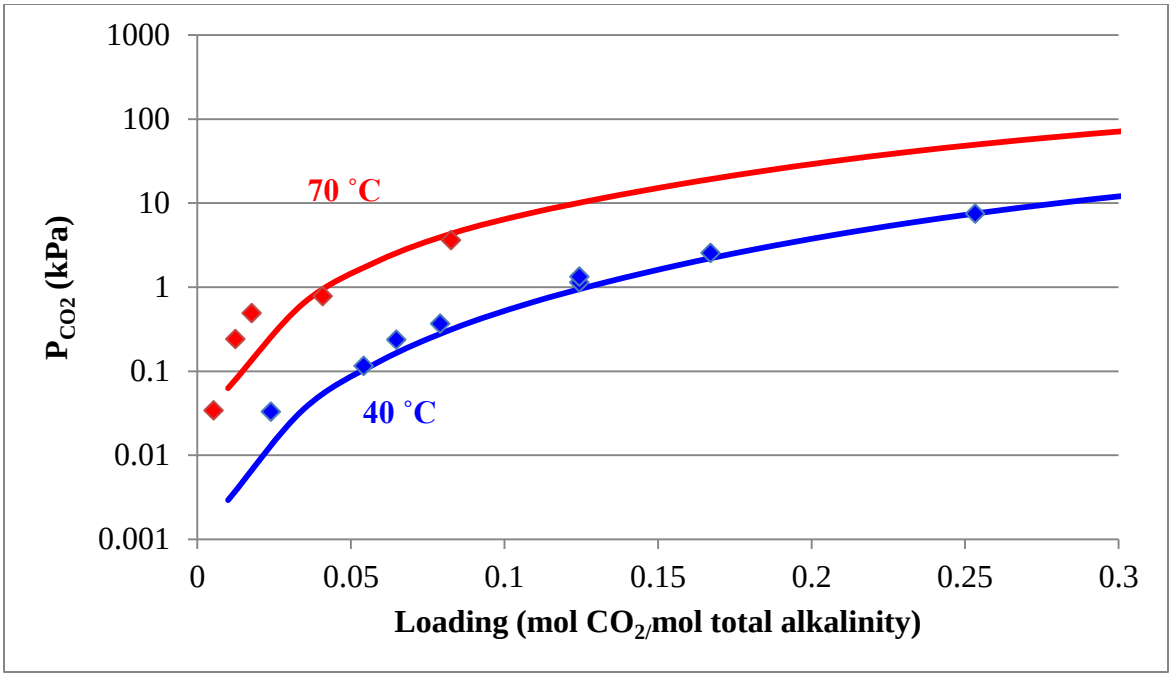

Figure 4.4-17. CO_2 Solubility Predictions for 7.7 m MDEA/1.1 m PZ at 40 ˚– 70 ˚C

Figures 4.4-18 and 19 show the upgraded model prediction of MDEA and PZ volatility for 7 m MDEA/2 m PZ and 5 m MDEA/5 m PZ, respectively, for nominal loadings at 40 ˚ and 60 ˚C.

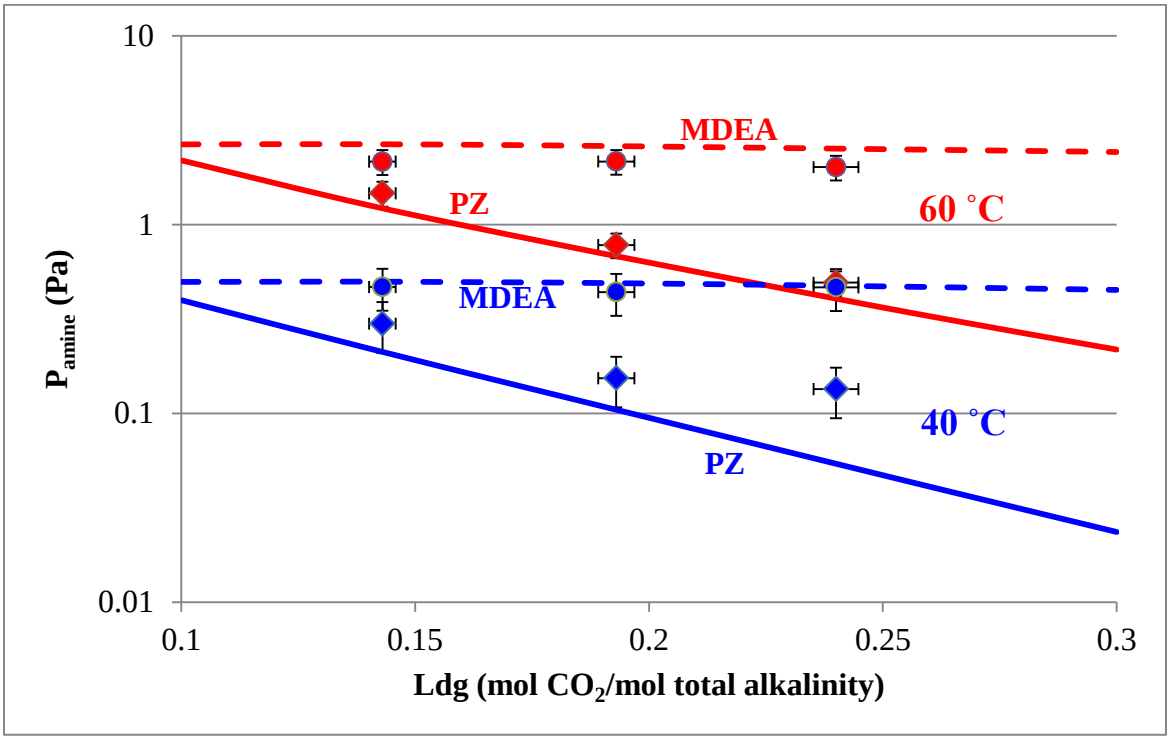

Figure 4.4-18. Amine Volatility Predictions for 7 m MDEA/2 m PZ at 40 ˚ and 60 ˚C

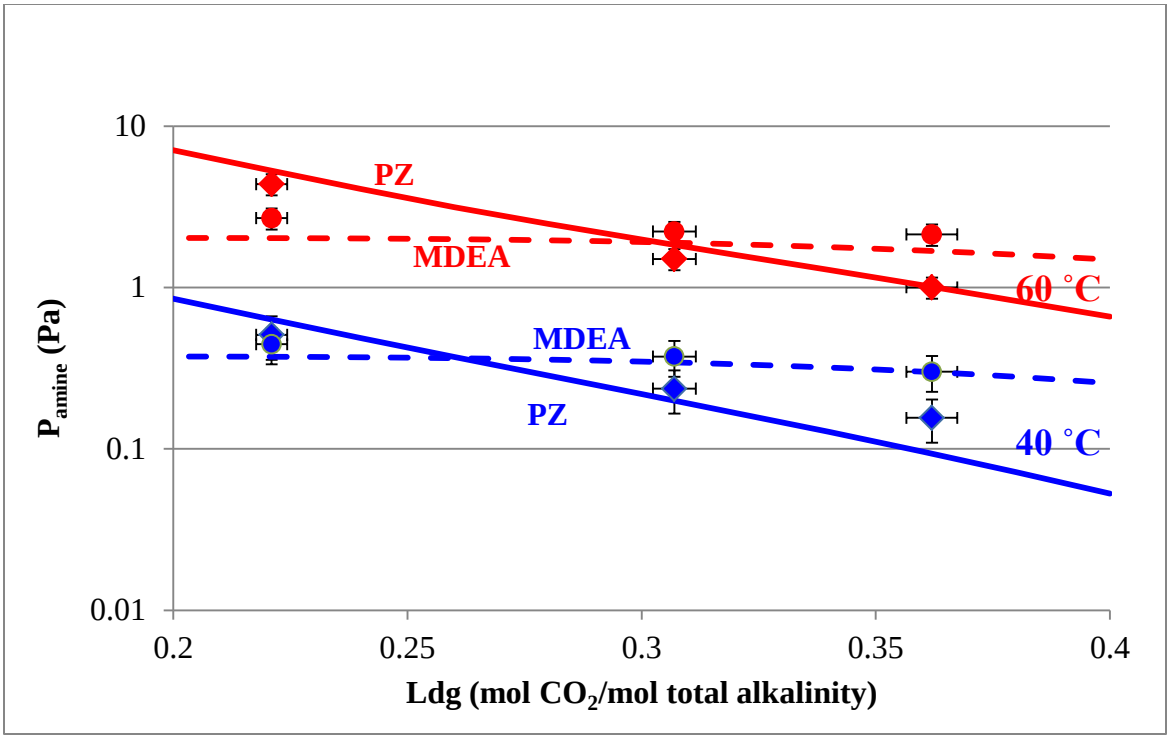

Figure 4.4-19. Amine Volatility Predictions for 5 m MDEA/5 m PZ at 40 ˚and 60 ˚C

The upgraded model successfully captures the volatilities of both MDEA and PZ as a function of loading for both temperatures shown. Much of this success is due to the fact that the H_2O-MDEA and H_2O-CO_2-MDEA parameters were regressed again in this model version to match experimental unloaded MDEA volatility data and CO_2 solubility. Matching volatility data for the blend is a high priority for this model revision. The largest disparity between experimental and model prediction occurs in the case of the 7/2 blend at 40 ˚C, particularly at high loading, where there is a high degree of uncertainty in the accuracy of the data as this condition is at the detection limit of the FTIR apparatus. Because the model represents the data very well at all other conditions shown, it is still considered to be reliable at high loading. The MDEA volatility is not sensitive to changes in loading over the range observed because CO_2 reacts preferentially with PZ,

and not MDEA, due to the fact that the former is the stronger base and has two amine groups that can directly react with CO_2.

Figures 4.4-20 and 21 show the speciation for 7 m MDEA/2 m PZ and 5 m MDEA/5 m PZ, respectively, at 40 ˚C. The experimental NMR data was obtained by using the equipment and procedure described in Chapter 2, Section 3.

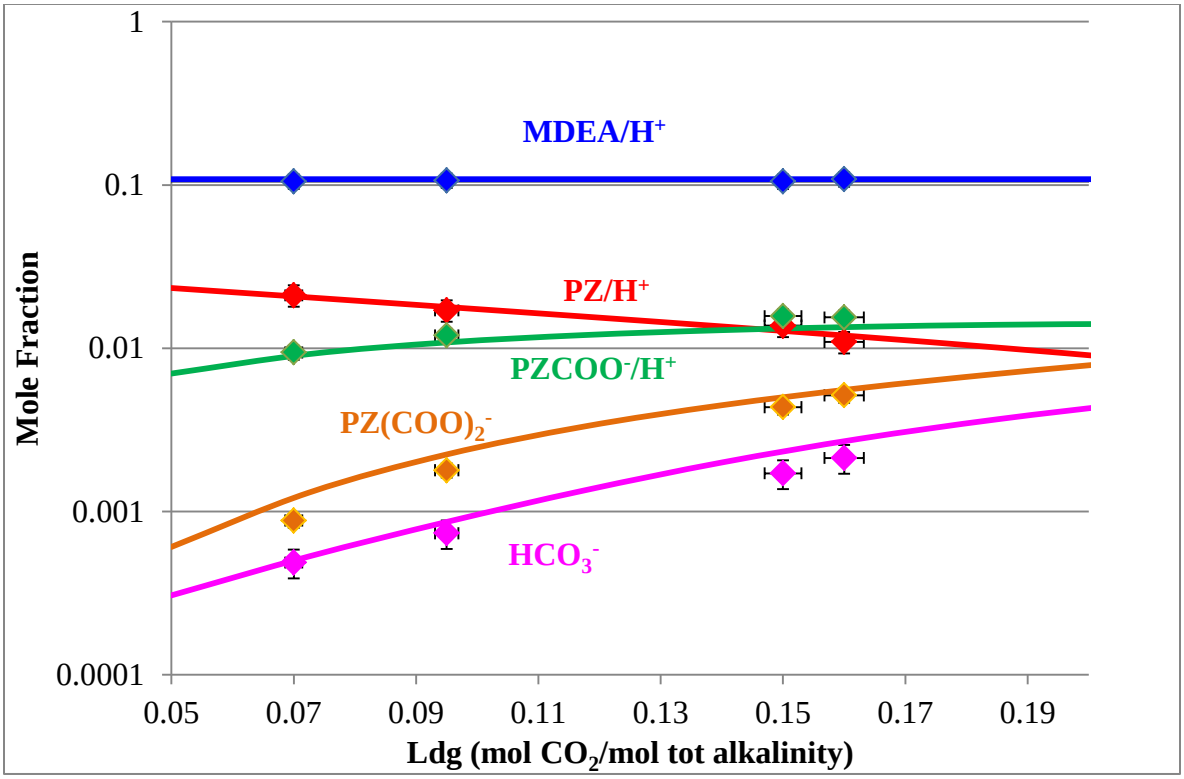

Figure 4.4-20. Speciation for 7 m MDEA/2 m PZ at 40 ˚C

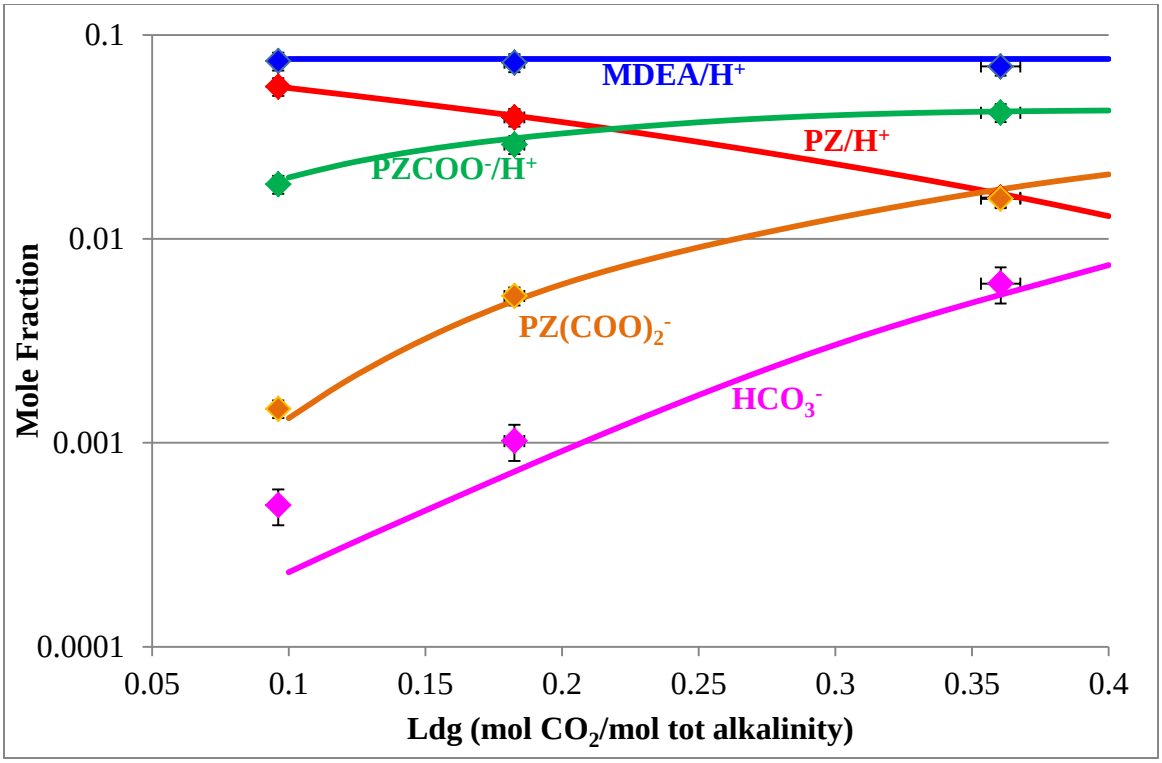

Figure 4.4-21. Speciation for the 5 m MDEA/5 m PZ at 40 ˚C

It was not necessary to regress the experimental speciation data in order for the model to adequately match speciation for both 7 m MDEA/2 m PZ and 5 m MDEA/5 m PZ as shown. Recall that matching the speciation was one of the two key issues in the previous model version. In the previous model, the predictions underestimated the amount of $PZ(COO)_2^-$ formed while overestimating the HCO_3^- amount. In this revision, the H_2O and MDEA interactions with ion pairs involving HCO_3^- were regressed again along with the introduction of CO_3^{2-} species. These changes made it possible to obtain noticeably improved fits of CO_2 solubility and MDEA volatilities, which resulted in accurate speciation predictions. The bicarbonate prediction for the blend at low loading is accurate due to the addition of the carbonate species, whereas the prediction at high

loading is accurate because of the use of appropriate MDEA interaction parameters in the regression of the tertiary MDEA-CO_2-H_2O system. Matching speciation without upsetting CO_2 solubility predictions was a priority for this model upgrade.

Figures 4.4-22 and 23 show the predicted enthalpy of CO_2 absorption for 7 m MDEA/2 m PZ and 5 m MDEA/5 m PZ, respectively, from 60–150 ˚C. These enthalpies were predicted by using the Analysis feature in AspenPlus® V. 7.3. to perform a Flash calculation which estimated the partial pressure of CO_2 as a function of small differential temperature changes (~0.1 ˚C). The Gibbs-Helmholtz relationship was then applied to estimate the enthalpy of CO_2 absorption from the data generated by Aspen.

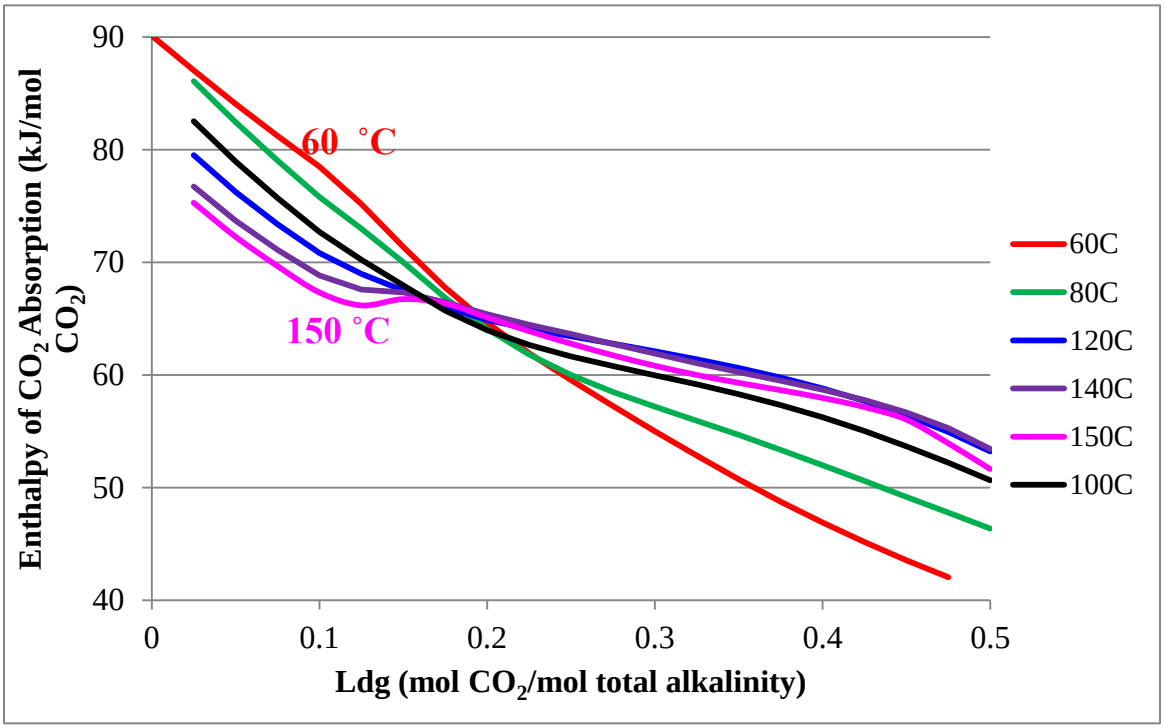

Figure 4.4-22. Enthalpy of CO_2 Absorption for 7 m MDEA/2 m PZ from 60 ˚– 150 ˚C

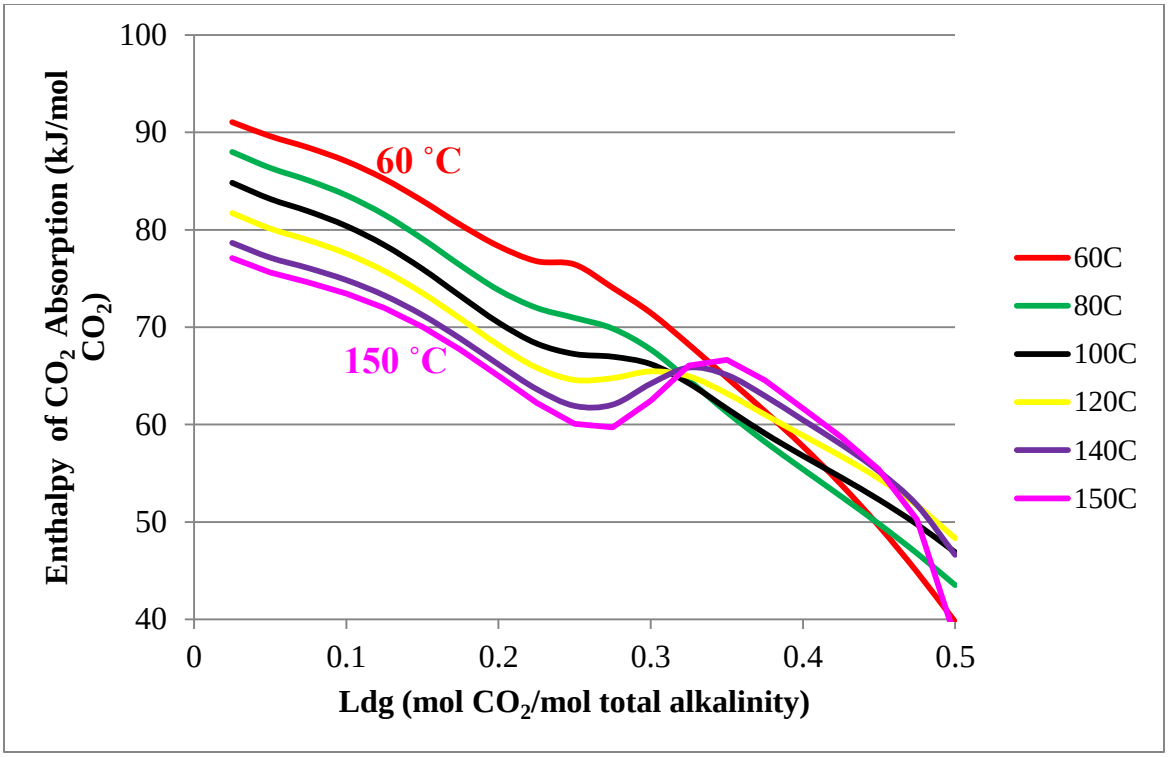

Figure 4.4-23. Enthalpy of CO_2 Absorption for 5 m MDEA/5 m PZ from 60 ˚ – 150 ˚C

There is no experimental data available for the enthalpy of CO_2 absorption in MDEA/PZ system. Nevertheless, the model predicts well-behaved heat of absorption that match expectations and are internally consistent. For both blends, the enthalpy of CO_2 absorption prediction flips temperature behavior at the critical loading where PZ is saturated in both systems by stoichiometry (loading ~ 0.18 for 7/2; ~0.33 for 5/5). Before reaching the critical loading point, CO_2 reacts primarily with PZ, not MDEA, in an exothermic reaction because PZ is a stronger base than MDEA. Since PZ reaction with CO_2 is exothermic, increasing the system temperature would tend to work against this effect and result in a lower drive for the reaction to occur which is reflected in a smaller enthalpy of CO_2 absorption. This is the reason that absorbers require intercooling to reduce the column temperature and thereby improving CO_2 solubility, a process which

manifests in greater values of enthalpy of absorption. After the critical loading where most of the PZ is saturated, CO_2 now reacts with MDEA instead which has a different enthalpy of CO_2 absorption compared to PZ.

At less than 140 ˚C, the enthalpy of CO_2 absorption tends to decrease with loading because there is less free amine available to react with CO_2. At temperature higher than 140 ˚C, there is a competing effect between speciation and temperature on the enthalpy of CO_2 absorption, with the latter overriding the former, particularly for MDEA where the reaction with CO_2 is less exothermic. This behavior is so strong that it compensates for the drop in ΔH_{CO2} due to lack of free amine (PZ); however, if one were to project past a high enough loading (greater than 0.5), the enthalpy of absorption would naturally decline again due to the MDEA running out and not being able to react with CO_2. In other words, speciation would dominate again as it tends to overall. Lastly, it should be noted that predicting the enthalpy of CO_2 absorption is not the primary scope of this work, but is secondary to the needs of matching volatility and speciation. Thus it is acceptable to end up with the enthalpy of CO_2 absorption predictions shown provided that the speciation and volatility are matched rather well.

Figures 4.4-24 and 25 illustrate the heat capacity predictions for 7 m MDEA/2 m PZ and 5 m MDEA/5 m PZ, respectively, from 40 ˚- 120 ˚C. The experimental heat capacity data were obtained by using the equipment and procedure described in Chapter 2 Section 5.

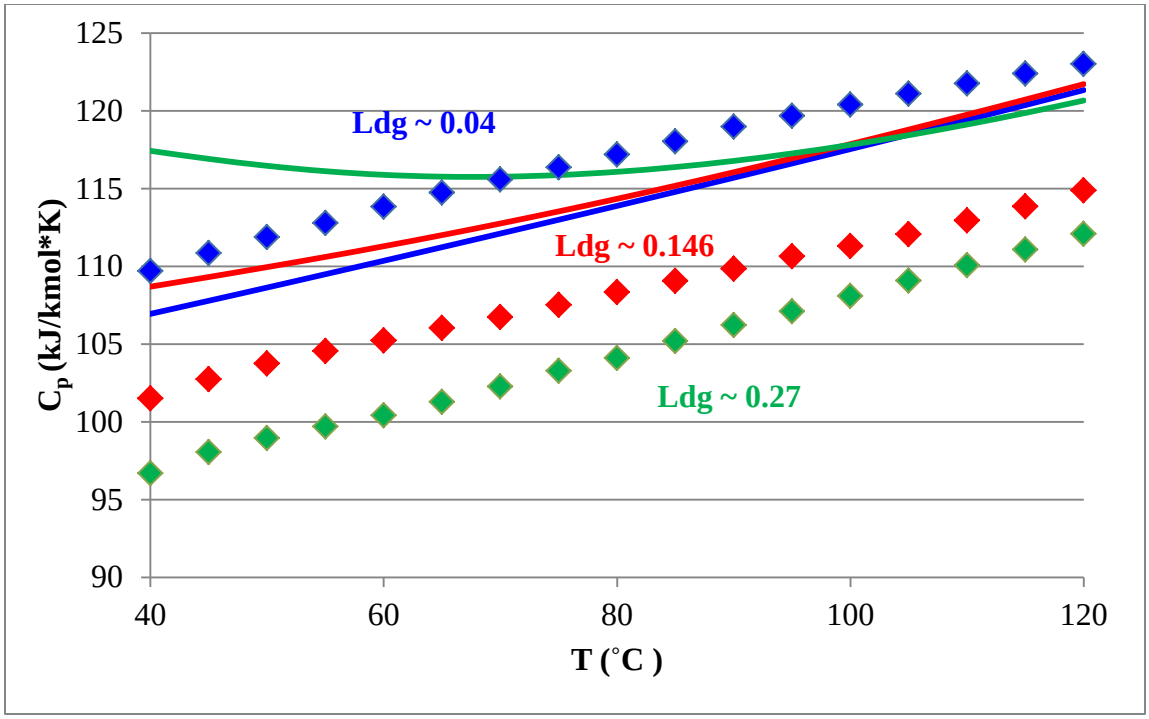

Figure 4.4-24. C_p Predictions for 7 m MDEA/2m PZ from 40 ˚ – 120 ˚C

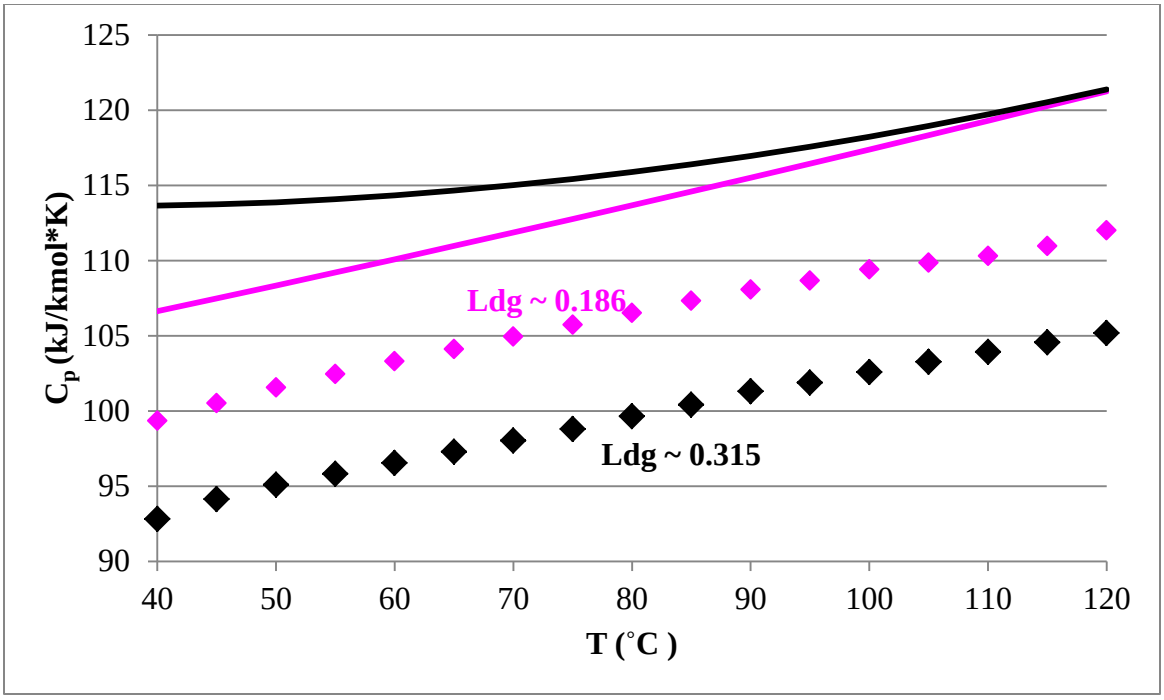

Figure 4.4-25. C_p Predictions for 5 m MDEA/5 m PZ from 40 ˚ – 120 ˚C

The experimental C_p for the blends decreases with loading as the CO_2 heat capacity is believed to be negligible, thus increasing the amount of CO_2 in the system results in a decrease of the total C_p. As seen, the model does not properly match the blend heat capacities. This is because the need to represent experimental C_p was not a priority at the start compared to the needs to match speciation and volatility. It is interesting that the model matches speciation very well but not C_p, which means that at the very least the enthalpy of reaction prediction can be adequately represented but not the total heat. This suggests that the free energies or enthalpies of formation for some of the electrolyte species could use some optimization. Furthermore, it is also important that future regressions use the full set of reactions instead of the reduced set in order to match C_p in addition to speciation. The reduced set may leave out certain reactions

which may be highly relevant to capturing the system heat capacities though they may not be significant enough to impact speciation.

4.5. Conclusions

In order to upgrade the existing Fawkes MDEA-PZ-CO_2-H_2O thermodynamic model, it was necessary to remodel each subsystem within the blend starting with the simplest subsystem and then building up to more complex subsystems.

For MDEA-H_2O, both the MDEA volatility and C_p for 1.7–13.9 m MDEA-H_2O from 5 ˚– 95 ˚C (a total of over 250 points) were adequately fitted using 4 Henry's parameters and 4 binary NRTL parameters. The MDEA-H_2O interaction has a temperature dependence whereas the H_2O-MDEA interaction does not in this regression case.

For MDEA-CO_2-H_2O, the introduction of the carbonate species into the Fawkes MDEA-CO_2-H_2O chemistry set allowed for an improved fit of CO_2 solubility at ultra lean loadings ($0.001 < \alpha < 0.01$). The CO_2 solubility for 2.8 m–8.4 m MDEA-CO_2-H_2O from 25˚ – 120 ˚C, C_p for nominal MDEA concentrations, and loaded MDEA volatility were fitted very well using the free energy and enthalpy of $MDEAH^+$ species along with all of the pair parameters.

For MDEA-PZ-H_2O subsystem, amine volatilities can be represented successfully without the need to regress any additional cross parameter for MDEA-PZ interaction.

For MDEA-PZ-CO_2-H_2O, the best possible combination of parameters used to represent the system includes: NRTL parameters for H_2O interaction with ion pairs,

NRTL default parameter values for molecule to ion interactions to characterize MDEA and PZ interactions with ion pairs (10 for amine to ion pairs, -2 for ion pairs to amine), NRTL default parameter values to represent the zwitterion H^+PZCOO^- interaction with ion pairs which are set to mimic default water interaction parameter values (8 for zwitterions to ion pairs, -4 for ion pairs to zwitterion), and the non-randomness factor for the zwitterion to MDEA interaction fixed at 0.3. Both the amine volatility and speciation for loaded 7/2 and 5/5 MDEA/PZ are successfully matched using the upgraded model.

Finally, it was seen that the upgraded model predicts rather well-behaved enthalpy of CO_2 absorption for the 7/2 blend but not for the 5/5 blend even though the general temperature behaviors are represented as expected. Thus the upgraded model can be used to qualitatively determine the enthalpy of CO_2 absorption behaviors with respect to loading and temperature. In regard to C_p, the new model was not able to capture the effect of loading on C_p for a given temperature range. Recall that the original focus of this work was given to matching volatility and speciation of the blend not so much C_p. In order to improve the C_p fits, it is important to: (1) optimize the Gibbs energy and enthalpies of formation for the electrolyte species and (2) perhaps use a full set of reactions instead of the reduced set in future regression cases because the latter might have possibly omitted certain reactions that maybe highly relevant to C_p even though they may not be that significant to fitting speciation.

Chapter 5: MDEA/PZ Behavior & Generalized Amine Screening

5.1. Introduction

A number of novel amines were screened for amine volatility at nominal lean loading to determine their viabilities for CO_2 capture. Other amine characteristics, including CO_2 capture capacity, reaction rate, and resistance to oxidative and thermal degradation, have been screened by other researchers. In addition to the need to screen for amine volatility, it is also important to explore the VLE of novel amine systems to generalize amine solution behavior in terms of activity coefficients. The trends in amine activity coefficients can be further attributed to speciation, temperature, and the phenomenon where the amine is being "salted out" due to its interactions with surrounding electrolytes.

In this work, detailed analyses of activity coefficient behavior for PZ-CO_2-H_2O (8 – 10 m loaded PZ) and for MDEA-PZ-CO_2-H_2O (loaded 7 m MDEA/2 m PZ and 5 m MDEA/5 m PZ) are used as the basis for interpreting the behavior of novel amines. Other amine systems screened include loaded MEA, MDEA, EDA, AMP, PZ/2-MPZ, and PZ/AMP. MDEA as a tertiary amine is known for its high CO_2 capture capacity. Blending MDEA with PZ serves to avoid PZ precipitation while taking advantage of fast PZ kinetics. EDA, like PZ and any other diamine, was chosen for its high CO_2 capacity with two amine groups to react with CO_2. EDA systems also have a high enthalpy of CO_2 absorption which is considered a favorable characteristic. In theory, a high enthalpy of CO_2 absorption results in high CO_2 partial pressure at stripper conditions to reduce the

work needed for CO_2 compression. Finally, AMP was also chosen for its high CO_2 capture capacity since it is a hindered amine.

5.2. Theory

The amine liquid phase activity coefficient is defined by Henry's Law as follows:

$$\gamma_{amine} = \frac{\phi_{amine} * P_{amine}}{x_{amine} * H_{amine}} \quad (5\text{-}1)$$

where:

Φ_{amine} is the amine fugacity coefficient
P_{amine} is the amine partial pressure (Pa)
x_{amine} is the amine liquid phase mole fraction
H_{amine} is the amine Henry's constant at a given temperature (Pa)
γ_{amine} is the asymmetric amine activity coefficient – defined at a reference state of infinite dilution of amine in water

Since the total system pressure is atmospheric (low pressure), the vapor phase is considered to be ideal; thus, no pressure correction is needed for the vapor phase. The fugacity coefficient is $\phi_{amine} = 1$.

The enthalpy of amine absorption can be estimated from the temperature derivative of the amine partial pressure:

$$\frac{d(\ln P_{amine})}{d(1/T)} = -\frac{\Delta H_{absorption}}{R} \quad (5\text{-}2)$$

where:

P_{amine} is the amine volatility or partial pressure (Pa)
$\Delta H_{absorption}$ is the enthalpy of amine absorption (J/mol amine)

Given that the existing system thermodynamics are anchored on the Henry's constant (referenced to infinite dilution of amine in water), the enthalpy of amine absorption is the sum of three individual enthalpy contributions as follows:

$$\Delta H_{absorption} = \Delta H_{solution} + \Delta H_{reaction} + \Delta H_{excess} \quad (5\text{-}3)$$

where:

$\Delta H_{solution}$ is the enthalpy associated with dissolving amine in water at infinite dilution (J/mol amine)
$\Delta H_{reaction}$ is the enthalpy of reacting amine, water, and CO_2 to form products (J/mol amine)
ΔH_{excess} is the enthalpy associated with the non-ideality of the system (J/mol amine)

Given the enthalpy of amine absorption at different loading and the associated excess enthalpy, one can deduce the enthalpy of reaction by difference. Detailed analysis of these enthalpy contributions will be provided for PZ and MDEA/PZ in the Results & Discussion section.

The enthalpy of amine solution is given by:

$$\frac{d(\ln H_{amine})}{d\,(1/T)} = -\frac{\Delta H_{solution}}{R} \tag{5-4}$$

where:

H_{amine} is the amine Henry's constant (Pa)
R is the universal gas constant, 8.314 J/mol*K

The excess enthalpy of an amine can be determined as follows:

$$\frac{d(\ln \gamma_{amine})}{d\,(1/T)} = \frac{-\Delta H_{excess}}{R} \tag{5-5}$$

where:

γ_{amine} is the asymmetric amine activity coefficient

5.3. Data

Tables 5.3-1 through 5.3-9 show the amine volatility measured in the FTIR apparatus for 7 m MEA-CO_2-H_2O, 7 m MDEA-CO_2-H_2O, 8 m PZ-CO_2-H_2O, 8 m EDA-CO_2-H_2O, 4.8 m AMP-CO_2-H_2O, 7 m MDEA-2 m PZ-CO_2-H_2O, 5 m MDEA-5 m PZ-CO_2-H_2O, 4 m PZ-4 m 2-MPZ-CO_2-H_2O, 2.3 m AMP-5 m PZ-CO_2-H_2O systems at

unloaded and nominal lean loading (mol CO_2/mol alkalinity). The data on MEA were measured by Hilliard (2008) in the identical apparatus.

Table 5.3-1. MEA Volatility for 7 m MEA-CO_2-H_2O (Hilliard 2008)

T (˚C)	Ldg	P_{MEA} (Pa)	P_{CO2} (Pa)	P_{H2O} (kPa)
40	0	10	0	7.50
40	0.47	2.7	574	6.75
60	0	27.1	0	18.3
60	0.39	10	763	16.7

Table 5.3-2. MDEA Volatility for 7 m MDEA-CO_2-H_2O

T (˚C)	Ldg	P_{MDEA} (Pa)	P_{CO2} (Pa)	P_{H2O} (kPa)
40	0	0.485	0	6.50
45	0	0.693	0	8.20
50	0	1.04	0	10.8
55	0	1.49	0	14.1
60	0	1.85	0	17.7
65	0	2.72	0	22.8
70	0	4.06	0	28.7
40	0.03	0.491	520	6.70
46.6	0.03	0.773	816	9.30
50	0.03	1.08	895	11.2
55	0.03	1.74	1225	14.4
60	0.03	2.43	1614	17.9
65	0.03	3.59	2312	22.8
70	0.03	5.17	3096	28.7

Table 5.3-3. PZ Volatility for 8 m PZ-CO_2-H_2O

T (˚C)	Ldg	P_{PZ} (Pa)	P_{CO2} (Pa)	P_{H2O} (kPa)
50	0	17.2	0	8.70
55	0	23.6	0	10.8
60	0	36.8	0	13.7
65	0	57.6	0	17.5
70	0	74.6	0	22.9
40	0.293	0.784	410	5.90
45	0.293	1.30	599	7.50
50	0.293	2.22	944	9.60

55	0.293	3.42	1331	12.4
60	0.293	5.58	1844	15.6
65	0.293	8.07	3031	19.4
70	0.293	11.9	4051	24.6

Table 5.3-4. EDA Volatility for 8 m EDA-CO_2-H_2O

T (˚C)	Ldg	P_{EDA} (Pa)	P_{CO2} (Pa)	P_{H2O} (kPa)
40	0	17.2	0	6.10
45.5	0	26.1	0	7.80
50	0	35.2	0	10.0
55	0	51.5	0	12.7
60	0	69.4	0	15.7
65	0	112	0	18.9
40	0.43	3.41	564	6.30
45	0.43	3.73	786	8.10
50	0.43	4.63	1358	11.0
55	0.43	4.92	2253	13.9
60	0.43	6.45	3295	17.4
65	0.43	7.30	6159	22.8

Table 5.3-5. AMP Volatility for 4.8 m AMP-CO_2-H_2O

T (˚C)	Ldg	P_{AMP} (Pa)	P_{CO2} (Pa)	P_{H2O} (kPa)
40	0	14.2	0	6.80
45	0	19.1	0	8.50
50	0	31.9	0	11.2
55	0	48.0	0	14.2
60	0	64.3	0	17.2
40	0.31	14.8	743	6.60
45	0.31	20.7	988	8.70
50	0.31	33.4	1635	11.6
55	0.31	47.9	2616	14.5
60	0.31	68.7	4561	18.3
65	0.31	102	6722	23.7

Table 5.3-6. MDEA and PZ Volatility for 7 m MDEA-2 m PZ-CO_2-H_2O

T (˚C)	Ldg	P_{PZ} (Pa)	P_{MDEA} (Pa)	P_{CO2} (Pa)	P_{H2O} (kPa)
40	0	1.07	0.457	0	6.40

45	0	1.61	0.810	0	7.90
50	0	2.50	1.15	0	10.3
55	0	3.80	1.62	0	13.2
60	0	5.48	1.91	0	16.7
65	0	8.48	2.83	0	21.1
70	0	11.7	4.23	0	26.8
40	0.143	0.299	0.467	524	6.2
45	0.143	0.404	0.715	750	7.8
50	0.143	0.585	1.10	1145	10.2
55	0.143	0.986	1.63	1596	13.0
60	0.143	1.47	2.16	2537	16.2
65	0.143	2.28	3.44	3586	20.8
70	0.143	3.63	5.62	6003	26.5

Table 5.3-7. MDEA and PZ Volatility for 5 m MDEA-5 m PZ-CO_2-H_2O

T (˚C)	Ldg	P_{PZ} (Pa)	P_{MDEA} (Pa)	P_{CO2} (Pa)	P_{H2O} (kPa)
40	0	5.04	0.356	0	6.40
45	0	6.45	0.499	0	8.00
50	0	8.75	0.642	0	10.2
55	0	12.1	0.988	0	12.9
60	0	17.8	1.45	0	16.3
65	0	27.8	2.22	0	20.7
70	0	44.8	2.78	0	26.6
40	0.221	0.509	0.445	598	6.00
45	0.221	0.723	0.610	1085	7.60
50	0.221	1.22	0.908	1717	10.1
55	0.221	1.81	1.34	2659	12.7
60	0.221	2.85	1.75	4252	16.2
65	0.221	4.37	2.69	7317	20.6
70	0.221	6.78	4.07	10611	26.5

Table 5.3-8. PZ and 2-MPZ Volatilities for 4 m PZ-4 m 2-MPZ-CO_2-H_2O

T (˚C)	Ldg	P_{PZ} (Pa)	$P_{2\text{-}MPZ}$ (Pa)	P_{CO2} (Pa)	P_{H2O} (kPa)
40	0	2.39	8.53	0	5.80
45	0	4.06	12.3	0	7.40
50	0	8.07	15.4	0	9.30
55	0	11.4	22.4	0	11.9

60	0	14.7	38.2	0	15.4
65	0	18.5	47.9	0	19.6
70	0	31.8	71.5	0	24.9
40	0.328	0.100	0.848	652	5.80
45	0.328	0.190	1.62	1051	7.60
50	0.328	0.469	2.32	1464	9.70
55	0.328	1.10	3.64	2453	12.2
60	0.328	2.00	6.28	3569	15.7
66	0.328	3.13	9.74	6021	20.3

Table 5.3-9. PZ and AMP Volatilities for 2.3 m AMP-5 m PZ-CO_2-H_2O

T (˚C)	Ldg	P_{PZ} (Pa)	P_{AMP} (Pa)	P_{CO2} (Pa)	P_{H2O} (kPa)
40	0	4.78	12.2	0	5.90
45	0	5.21	13.8	0	7.10
50	0	8.46	21.1	0	9.40
55	0	13.5	31.1	0	12.2
60	0	15.5	40.2	0	15.4
40	0.3	0.596	5.71	244	5.70
45	0.3	0.650	8.25	407	7.30
50	0.3	1.23	12.6	679	9.80
55	0.3	1.90	17.7	916	12.6
60	0.3	2.69	23.5	1341	15.9
65	0.3	4.15	34.4	2196	20.1

5.4. Results and Discussion

A detailed analysis of the effects of loading, temperature, and amine concentration on amine volatility will first be presented for PZ-CO_2-H_2O and for MDEA-PZ-CO_2-H_2O. The results for these systems will then be used to generalize the volatilities of other amines screened for CO_2 capture.

Amine Volatility: Empirical Modeling

Amine volatility for 8 m PZ-CO_2-H_2O and 7 m MDEA-2 m PZ-CO_2-H_2O is modeled using the following empirical expression:

$$\ln P_{amine}\ (\text{Pa}) = a + \frac{b}{T} + c\alpha + d\left(\frac{\alpha}{T}\right) + e\alpha^2 \qquad (5\text{-}6)$$

where:

T is temperature (K)
α is loading (mol CO_2/mol total alkalinity)

Amine volatility data, estimated from the upgraded Fawkes model, were used to regress the constants in Eq. (5-6) by using the Excel Data Regression feature. Table 5.4-1 summarizes the values of the regressed constants for the two amine systems.

Table 5.4-1. Summary of Regressed Constants for Empirical Models of Amine Volatilities

System	a	b	c	d	e
8 m PZ	29.0 ±1.85	-8466 ± 598	14.8 ± 7.60	-3608 ± 2443	-30.8 ± 1.62
MDEA in 7 m MDEA/2 m PZ	26.5 ± 0.1	-8508 ± 41	4.41 ± 0.43	-1205 ± 139	-2.89 ± 0.09
PZ in 7 m MDEA/2 m PZ	25.6 ± 0.6	-7879 ± 182	25.8 ± 1.90	-12966 ± 616	5.58 ± 0.41

The parameter values are much greater than the magnitudes of their associated standard errors. The R^2 correlations for the fits are ~0.99. Figure 5.4-1 shows how the empirical model matches the experimental data and the upgraded Aspen Fawkes model predictions for 8 m PZ-CO_2-H_2O.

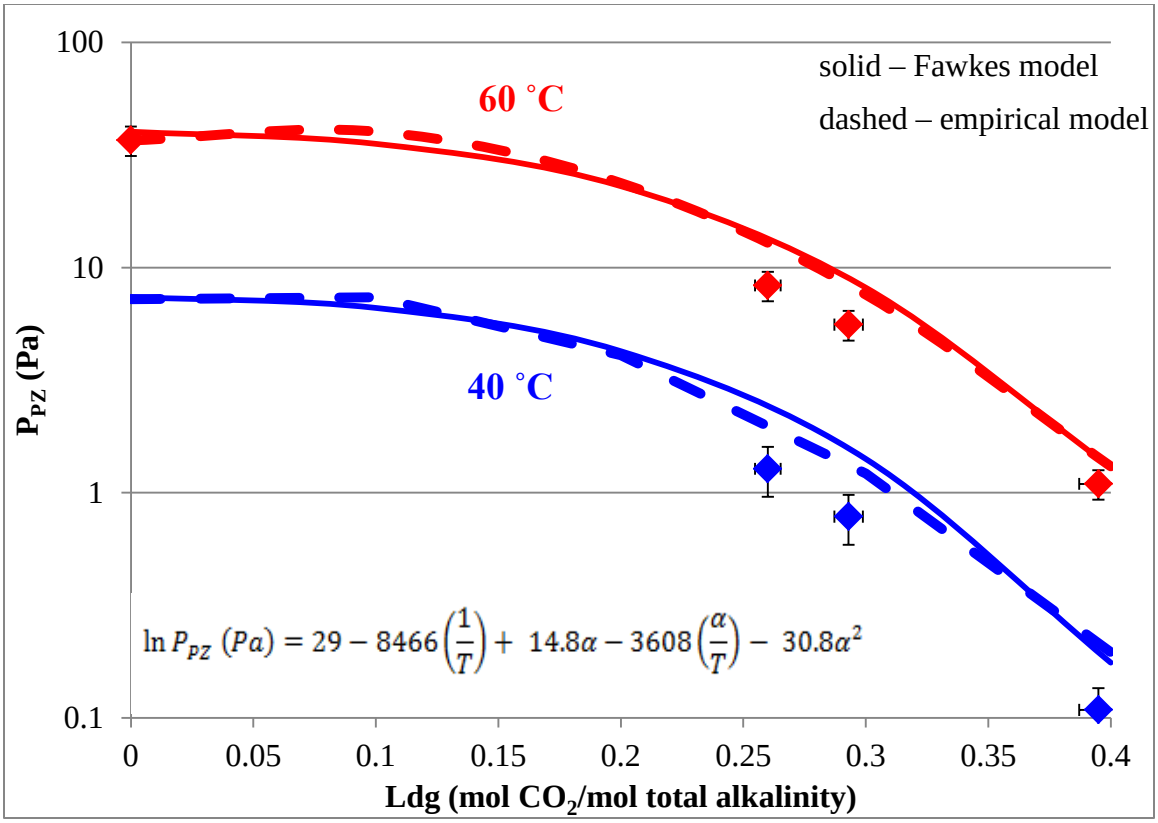

Figure 5.4-1. Model Representation of 8 m PZ-CO_2-H_2O Volatility: Empirical vs. Fawkes Model

There is a slight systematic offset between the experimental data at 40 ˚C and the model predictions. It is believed that there is a fair amount of uncertainty, ~10% -15%, in the measured data at 40 ˚C, especially at high loading, because these conditions result in low amine volatility which challenges the detection capability of the FTIR.

Figure 5.4-2 compares the empirical model prediction to the upgraded Fawkes model prediction for PZ volatility in 7 m MDEA-2 m PZ-CO_2-H_2O.

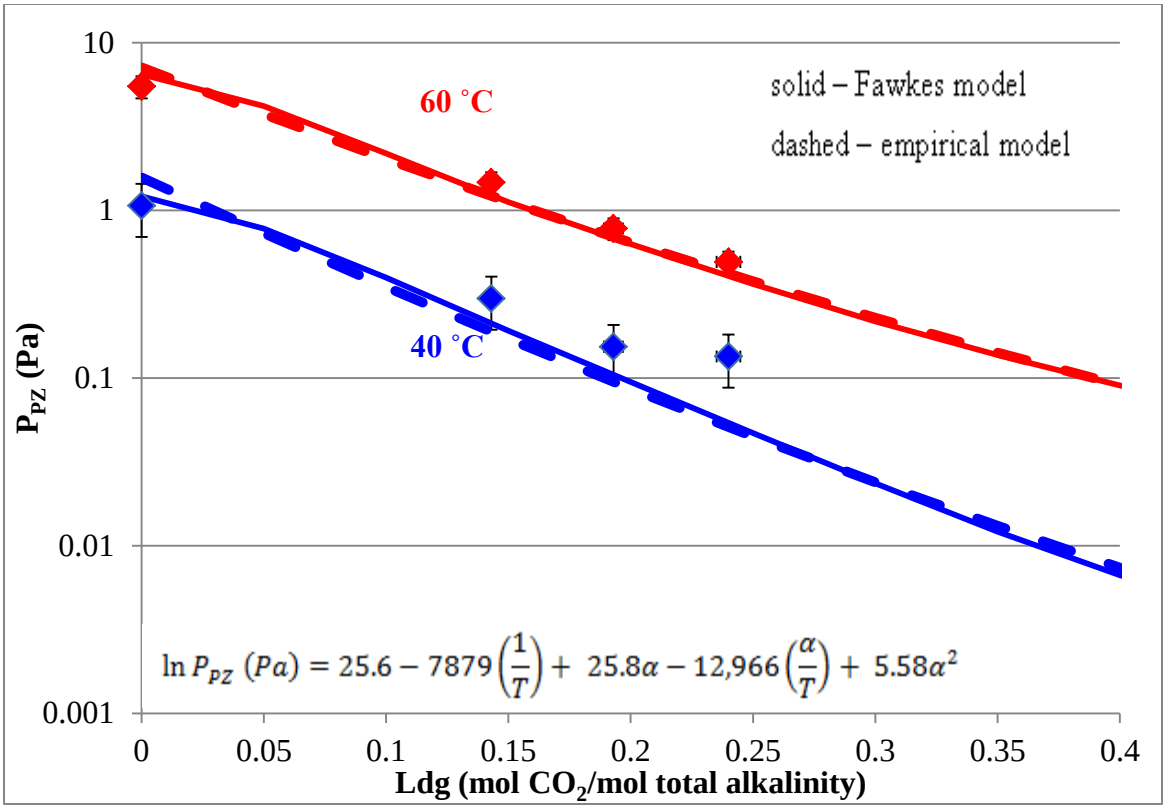

Figure 5.4-2. Model Representation of PZ Volatility in 7 m MDEA/2 m PZ: Empirical vs. Fawkes Model

The empirical model is able to track the upgraded Fawkes model fairly well. Nevertheless, there is a slight offset between the experimental values and the model prediction at 40 ˚C. This is again due to greater experimental uncertainty in the measurements due to system conditions being near the detection limit of the FTIR.

Figure 5.4-3 illustrates how well the empirical model is able to match MDEA volatility in 7 m MDEA-2 m PZ-CO_2-H_2O.

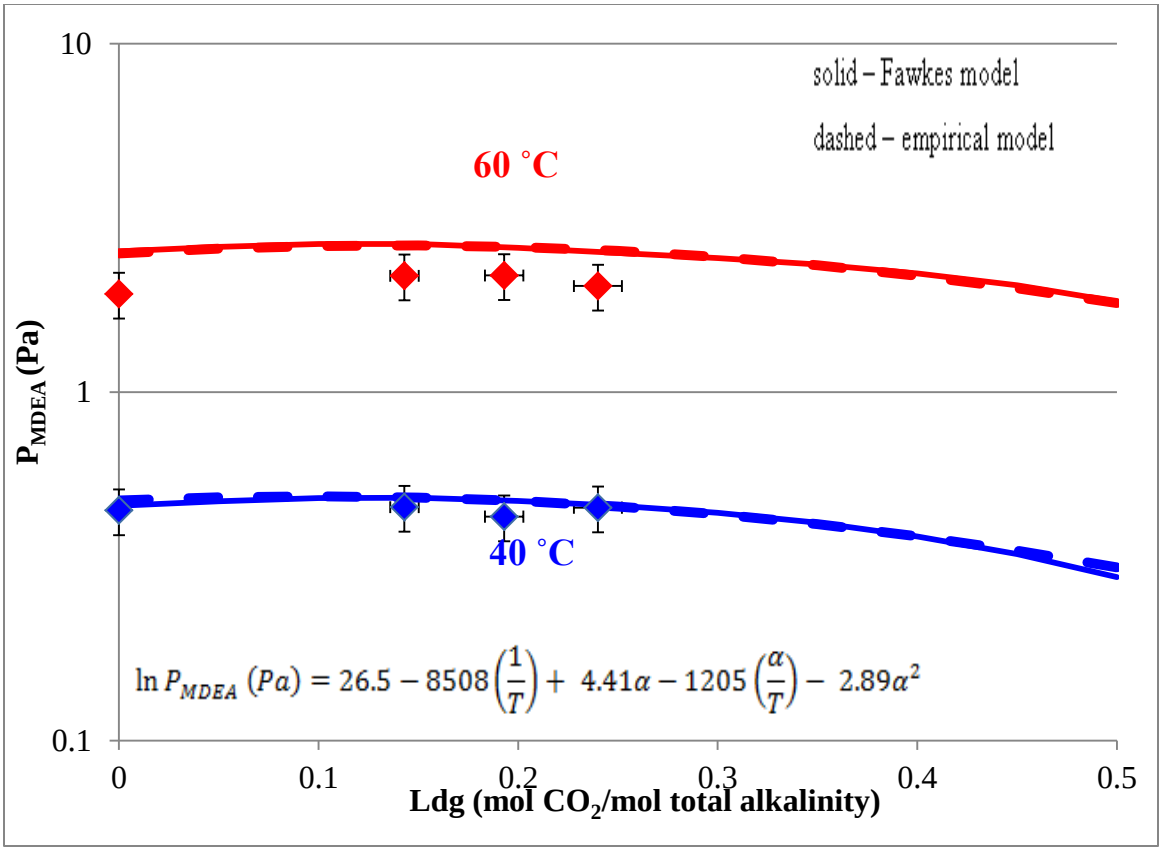

Figure 5.4-3. Model Representation of MDEA Volatility in 7 m MDEA/2 m PZ: Empirical vs. Fawkes Model

The empirical model matches both the experimental data and the Fawkes model prediction. The MDEA volatility is not a strong function of loading compared to PZ since MDEA simply serves as a proton sink and is not able to form carbamates like PZ.

The enthalpy of amine absorption for different systems can be estimated by calculating the change in amine partial pressure, predicted by the upgraded Fawkes model, with respect to a differential change in temperature in accordance with Eq. (5-2). Table 5.4-2 summarizes the enthalpy of absorption for PZ and MDEA/PZ at zero and their respective nominal lean loading.

Table 5.4-2. Summary of Enthalpies of Amine Absorption for MDEA/PZ (40 ˚C)

System	Ldg = 0	Ldg = nom. lean
		(ldg ~ 0.3)
	kJ/mol amine	kJ/mol amine
8 m PZ	74.3	75.9
		(ldg ~ 0.14)
MDEA in 7 m MDEA/2 m PZ	75.2	74.3
PZ in 7 m MDEA/2 m PZ	73.6	74.6

The upgraded Fawkes model can be used to estimate the (asymmetric) amine activity coefficients for PZ and MDEA/PZ. Given the amine activity coefficients at zero and at the nominal lean loading, one can estimate the excess amine enthalpies at the respective loadings for each system in accordance with Eq. (5-5). The enthalpy of amine reaction can be deduced by difference from the enthalpies of absorption, at nominal and zero loadings, and the excess enthalpies in accordance with Eq. (5-3). Table 5.4-3 shows the estimated contributions of the enthalpy of solution, enthalpy of reaction, and excess enthalpy to the total enthalpy of absorption for the systems of interest.

Table 5.4-3. Summary of the Contributions to the Enthalpy of Absorption for PZ and MDEA/PZ

System	$\Delta H_{solution}$	$\Delta H_{excess,\ ldg\ =\ 0}$	$\Delta H_{reaction}$	$\Delta H_{excess,\ ldg\ =\ nom.\ lean}$
	kJ/mol amine	kJ/mol amine	kJ/mol amine	kJ/mol amine
	$\Delta H_{absorption}$ = 74.3		$\Delta H_{absorption}$ = 75.9	
8 m PZ	70.8	3.0	4.9	0.16
	$\Delta H_{absorption}$ = 75.2		$\Delta H_{absorption}$ = 74.3	
MDEA in 7 m MDEA/2 m PZ	74.0	0.42	0.7	-0.40
	$\Delta H_{absorption}$ = 73.6		$\Delta H_{absorption}$ = 74.6	
PZ in 7 m MDEA/2 m PZ	70.8	2.3	3.9	-0.13

The greatest contribution to the total enthalpy of amine absorption is the enthalpy of solution. At zero loading, PZ systems are shown to have greater excess enthalpies

than MDEA. It is speculated that the enthalpy of reaction for these systems should be small because these reactions simply involve a proton exchange as the PZ electrolytes are being interconverted between PZH^+, $PZ(COO)^-$, and $H^+PZ(COO)^-$ at the nominal lean loading. In contrast, with CO_2 absorption by PZ, a more significant enthalpy is expected since chemical bonds are broken to form entirely different product species.

Activity Coefficient Behavior: PZ and MDEA/PZ

PZ-CO_2-H_2O

Figure 5.4-4 shows the effects of loading and temperature on PZ volatility, expressed as partial pressure, for 8 m PZ-CO_2-H_2O.

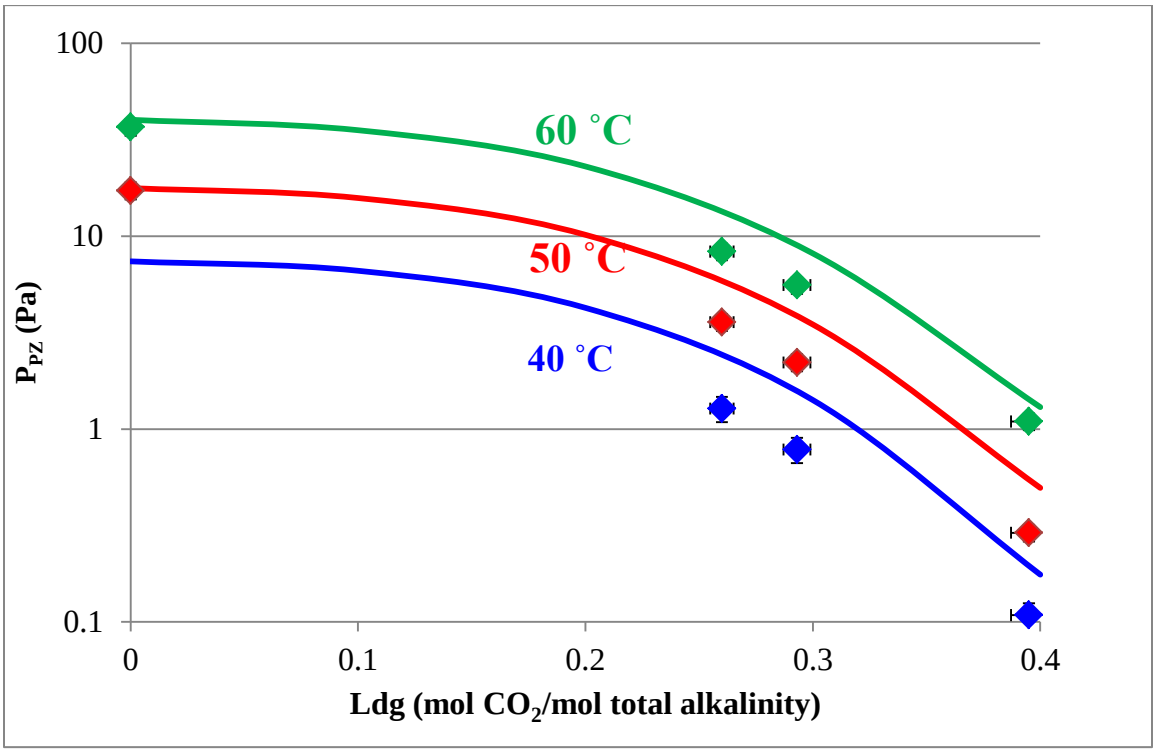

Figure 5.4-4. PZ Volatility in 8 m PZ-CO_2-H_2O, (curves predicted by upgraded Fawkes model)

PZ volatility, or its partial pressure, decreases steadily as loading is increased because there is less free PZ available with greater CO_2 consumption. The majority of the original PZ present is now converted into a number of PZ product species, or electrolytes, such as PZH^+, $PZ(COO)^-$, $PZ(COO)_2^{-2}$.

Figure 5.4-5 illustrates how PZ volatility in PZ-CO_2-H_2O varies with PZ concentration at a constant temperature (40 ˚C).

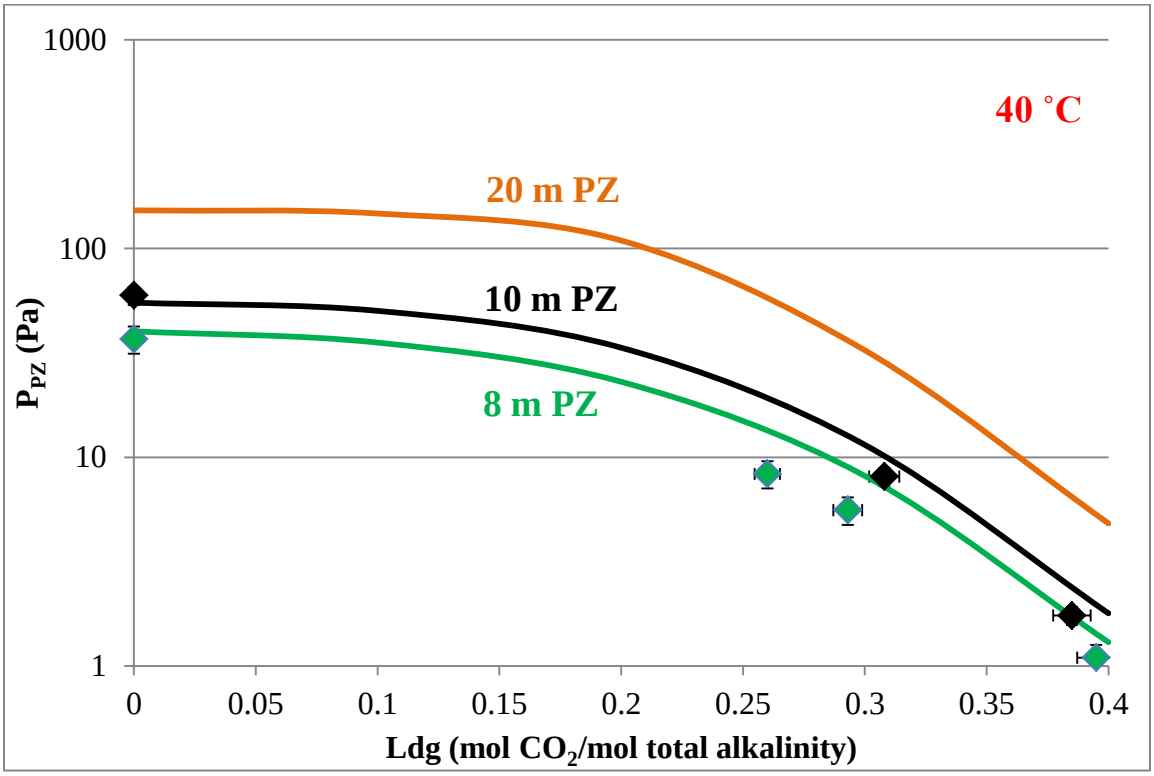

Figure 5.4-5. PZ Volatility for 8 m, 10 m, 20 m PZ-CO_2-H_2O at 40 ˚C (curves predicted by upgraded Fawkes model)

PZ partial pressure increases with increasing PZ due to more free PZ being available. Also, as discussed previously, at a given PZ concentration, PZ volatility decreases with greater loading due to less free PZ available for volatilization.

At a given temperature, PZ volatility in a system is primarily a function of PZ speciation. This is true of amine volatility in all the different amine systems screened. Figure 5.4-6 shows how PZ volatility in 8 m PZ-CO_2-H_2O is driven by PZ speciation as given by the free PZ mole fraction in solution.

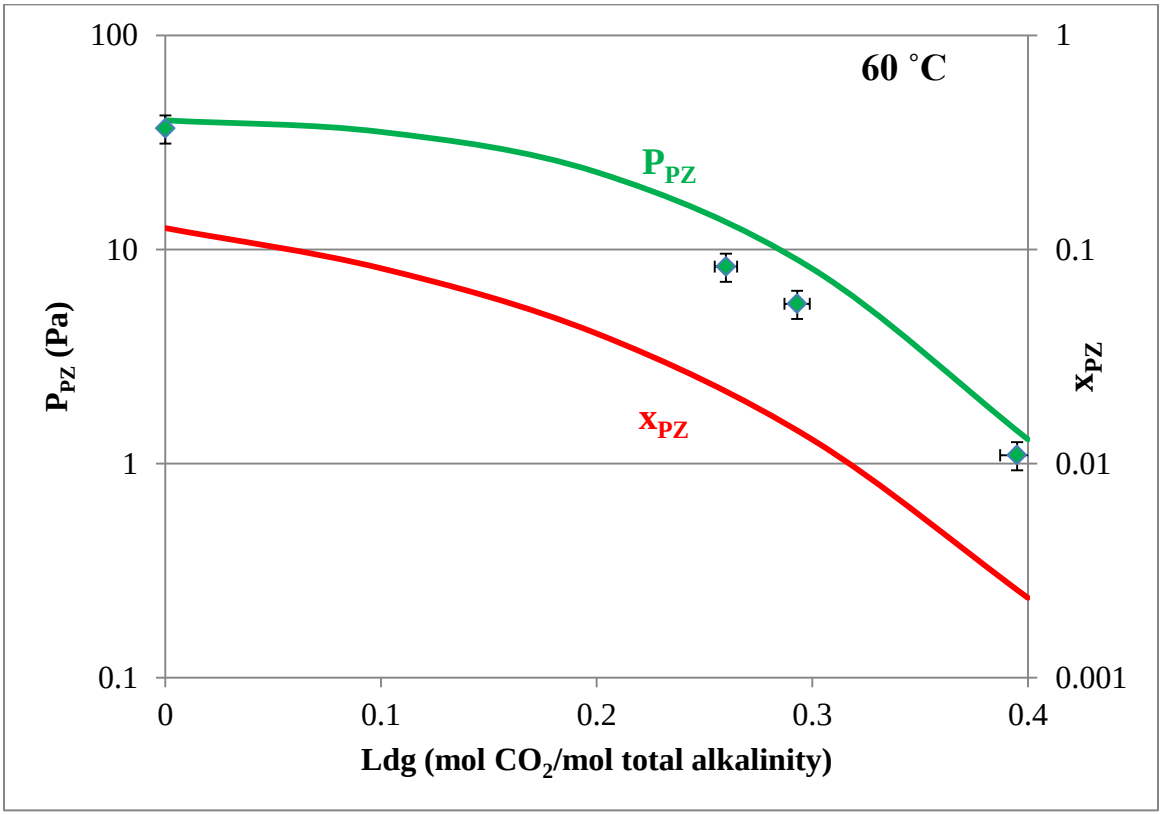

Figure 5.4-6. PZ Volatility and PZ concentration in 8 m PZ-CO_2-H_2O at 60 ˚C (curves predicted by upgraded Fawkes model)

For 8 m PZ-CO_2-H_2O at 60 ˚C, or any other amine system at some given temperature, the amine volatility is primarily driven by speciation as is evident in how the curvature of the free amine profile mirrors the curvature in the amine volatility profile. Other than speciation, the amine volatility is also driven by activity coefficient behavior though to a lesser degree than speciation.

Figure 5.4-7 shows the activity coefficient of PZ in 8 m and 10 m PZ-CO_2-H_2O, as a function of loading, as predicted by the upgraded Fawkes model.

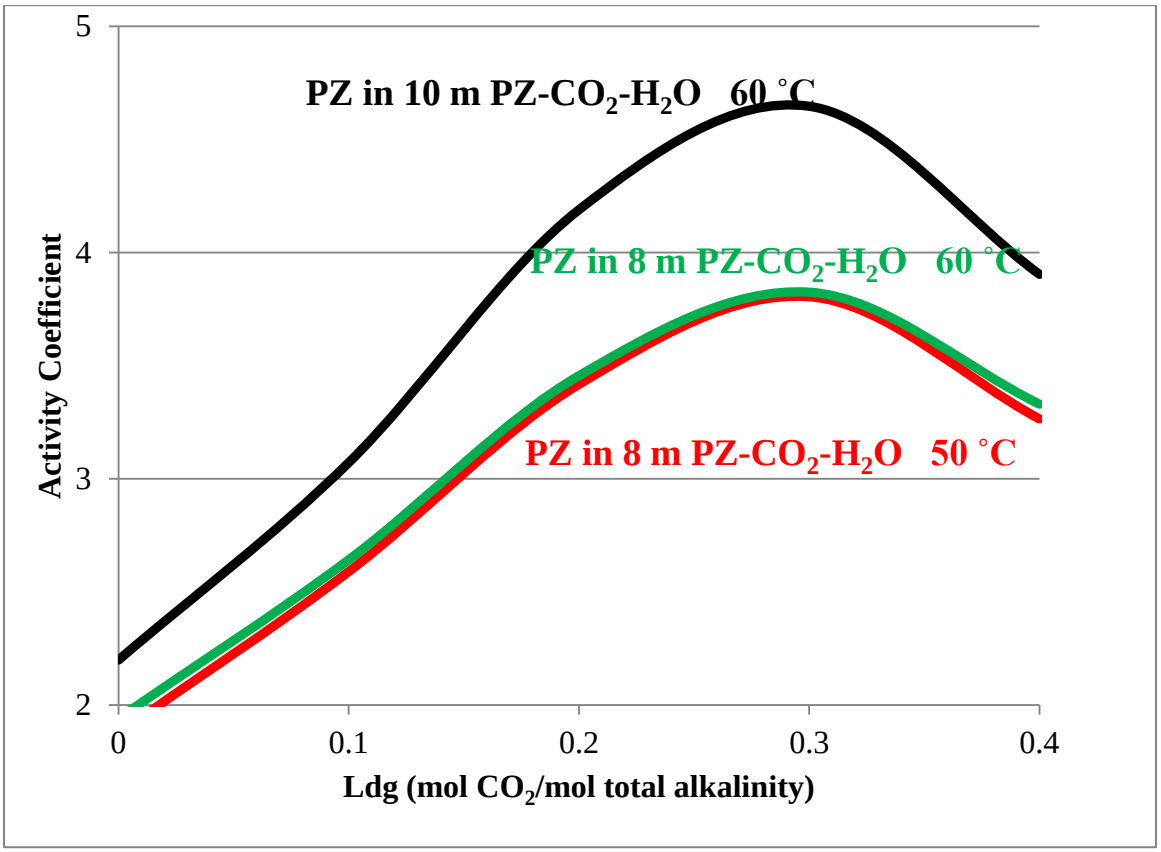

Figure 5.4-7. Activity Coefficients of PZ in 8 m and 10 m PZ-CO_2-H_2O (curves predicted by upgraded Fawkes model)

For both 8 m and 10 m PZ, PZ activity coefficient increases with loading because PZ is being salted out of solution as electrolytes are being increasingly generated. The PZ activity coefficient is greater for 10 m than for 8 m because PZ does not strongly interact with itself as much as it does with water. Because PZ is known to form PZ hexahydrate ($PZ{\cdot}6H_2O$), PZ is salted out at a higher PZ concentration because there is less water in 10 m PZ than in 8 m PZ to hydrate the PZ molecules. The PZ activity coefficient for 8 m PZ-CO_2-H_2O is not seen to vary much going from 50 ˚C to 60 ˚C. Finally, it is not clear

why the estimated PZ activity coefficient would start to decrease past a loading of ~0.3. This is most likely an artifact of the model since it is expected that PZ should continue to salt out at higher loading.

MDEA-PZ-CO_2-H_2O

Figure 5.4-8 shows amine activity coefficient, at 40 ˚C and 70 ˚C (for zero loading), as a function of changing total PZ while keeping MDEA constant at 7 m in the blend.

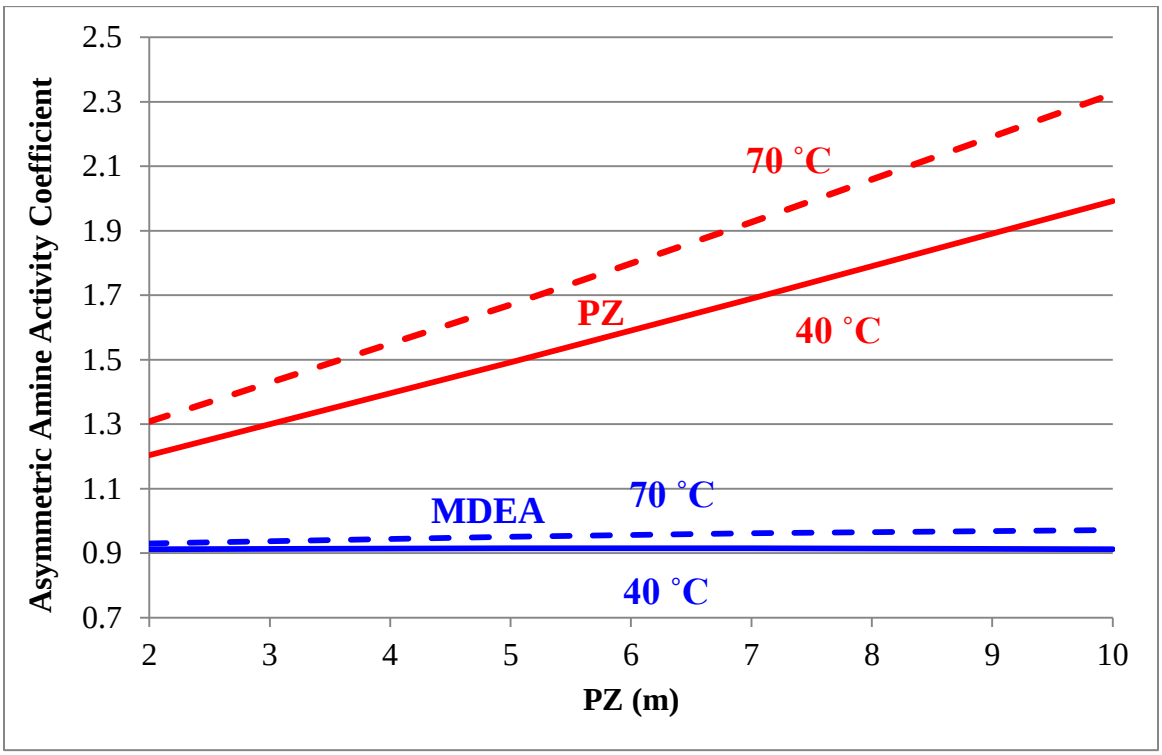

Figure 5.4-8. Amine Activity Coefficient in the Blend with Changing PZ Concentration (Constant MDEA 7 m), Zero loading, (curves predicted by upgraded Fawkes model)

As the PZ concentration is increased in the blend, PZ is increasingly salted out because PZ does not interact favorably with itself. Another reason is because PZ is known to form PZ hexahydrate ($PZ{\cdot}6H_2O$) with water; thus, as the PZ concentration is

increased, there is less water available in the solution to hydrate PZ which leads to PZ salting out. MDEA, on the other hand, does not seem to respond much to the increasing PZ concentration. The MDEA-PZ cross interaction parameter was not needed to model the blend which is further validation of the fact that MDEA does not interact much with PZ. The MDEA activity coefficient is consistently less than that of PZ because MDEA is more polar and therefore has a greater tendency to stay in solution. Finally, the activity coefficients of both MDEA and PZ are slightly greater at higher temperature.

Figure 5.4-9 shows the amine activity coefficient, at 40 ˚C and 70 ˚C (for zero loading), as a function of changing MDEA while keeping the PZ constant at 2 m in the blend.

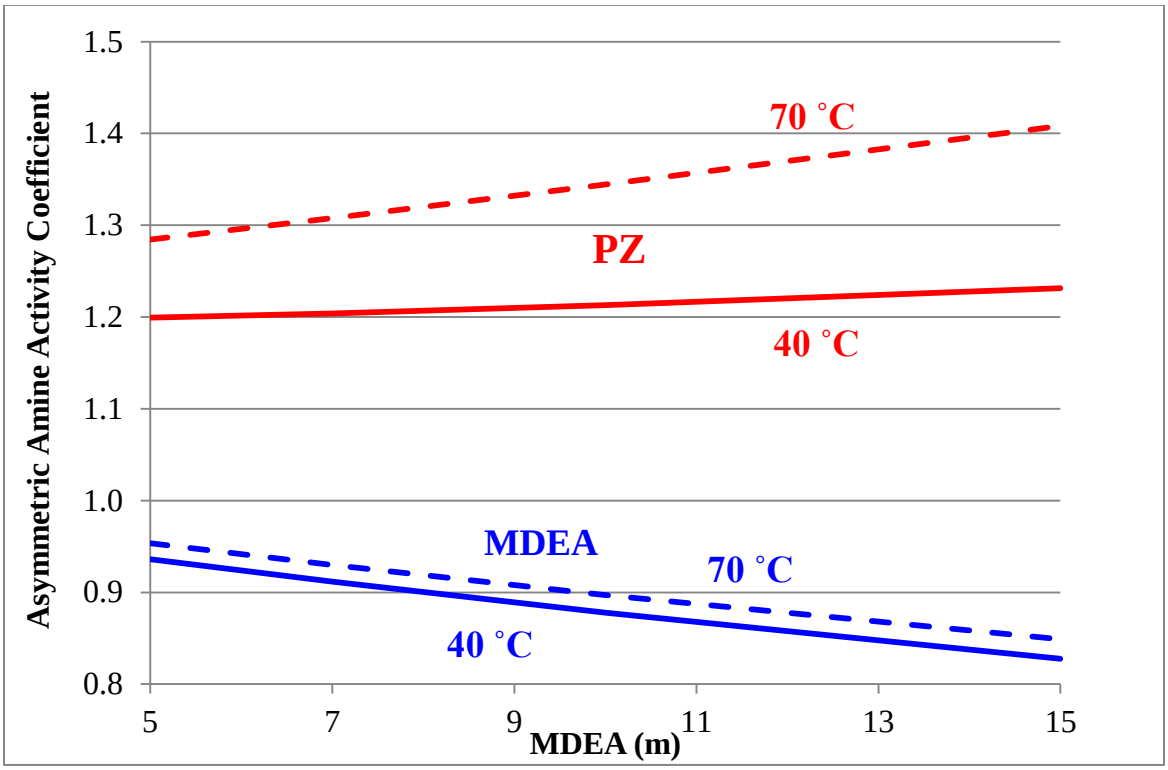

Figure 5.4-9. Amine Activity Coefficient in the Blend with Changing MDEA Concentration (Constant PZ 2 m), Zero loading, (curves predicted by the upgraded Fawkes model)

As the MDEA concentration is increased, MDEA activity coefficient decreases accordingly which suggests that MDEA is salting into the solution. Since MDEA interacts favorably with itself due to hydrogen bonding, there is a greater tendency to stay in solution unlike in the case of PZ. PZ, on the other hand, does not seem to respond much to the changing MDEA concentration which is further confirmation of the understanding that the two amines do not interact very much with each other. Again, the amines interact with their own kinds much more strongly than they do with each other. Lastly, the activity coefficients of both MDEA and PZ are greater at higher temperature as shown previously.

Figure 5.4-10 shows the PZ and H_2O activity coefficients in 7 m MDEA-2 m PZ-CO_2-H_2O as predicted by the upgraded Fawkes model.

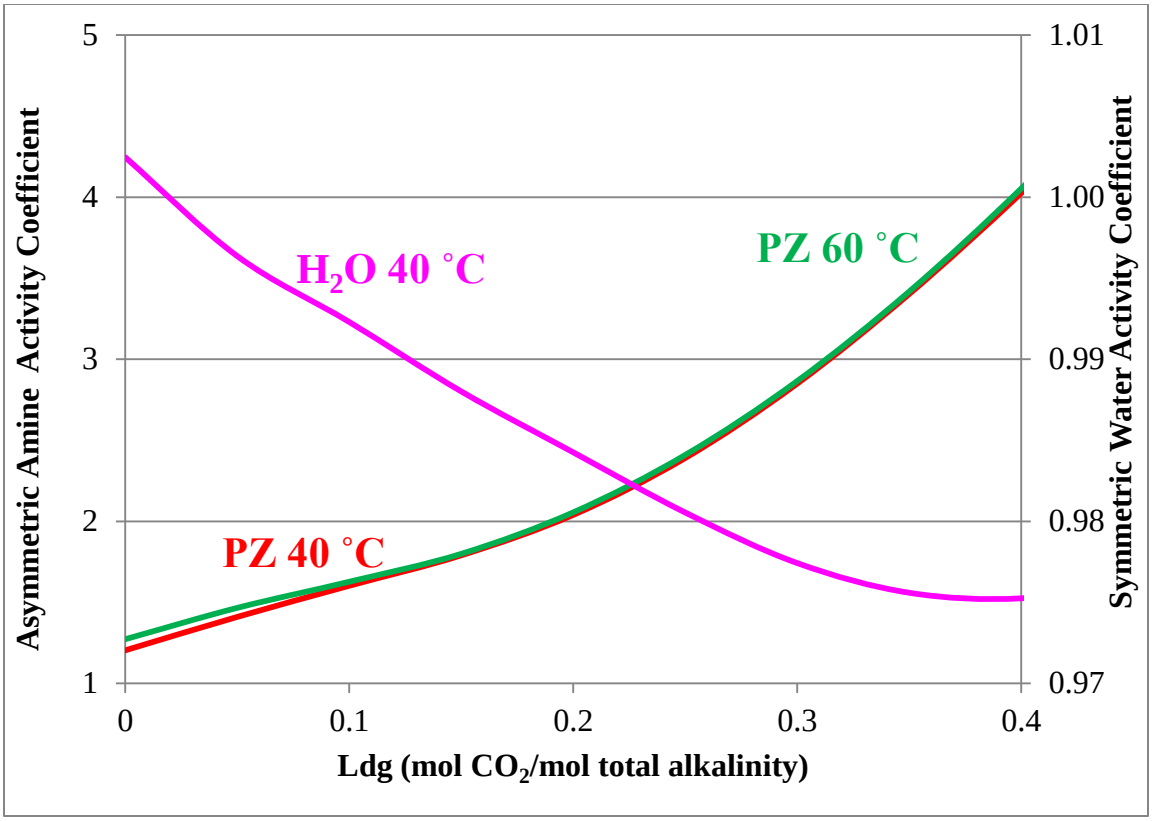

Figure 5.4-10. PZ and H_2O Activity Coefficients in 7 m MDEA/2 m PZ (curves predicted by upgraded Fawkes model)

The activity coefficient curves are generated by the upgraded Fawkes model. As with 8 m PZ-CO_2-H_2O, the PZ activity coefficient in the blend increases with loading as PZ is being salted out of solution by the electrolytes. Also there is little change in PZ activity coefficient with temperature for 7 m MDEA/2 m PZ. Finally, the water activity coefficient in 7 m MDEA/2m PZ at 40 ˚C is close to unity at zero loading. Since water is considered to be the solvent and is defined on the symmetric reference state (pure solvent), its activity coefficient is close to unity since the system is predominantly water. As the solution is loaded up, the water activity coefficient decreases slightly with loading since water interacts favorably with the electrolytes.

Figure 5.4-11 displays MDEA activity coefficient in 7 m MDEA-2 m PZ-CO_2-H_2O as predicted by the upgraded Fawkes model.

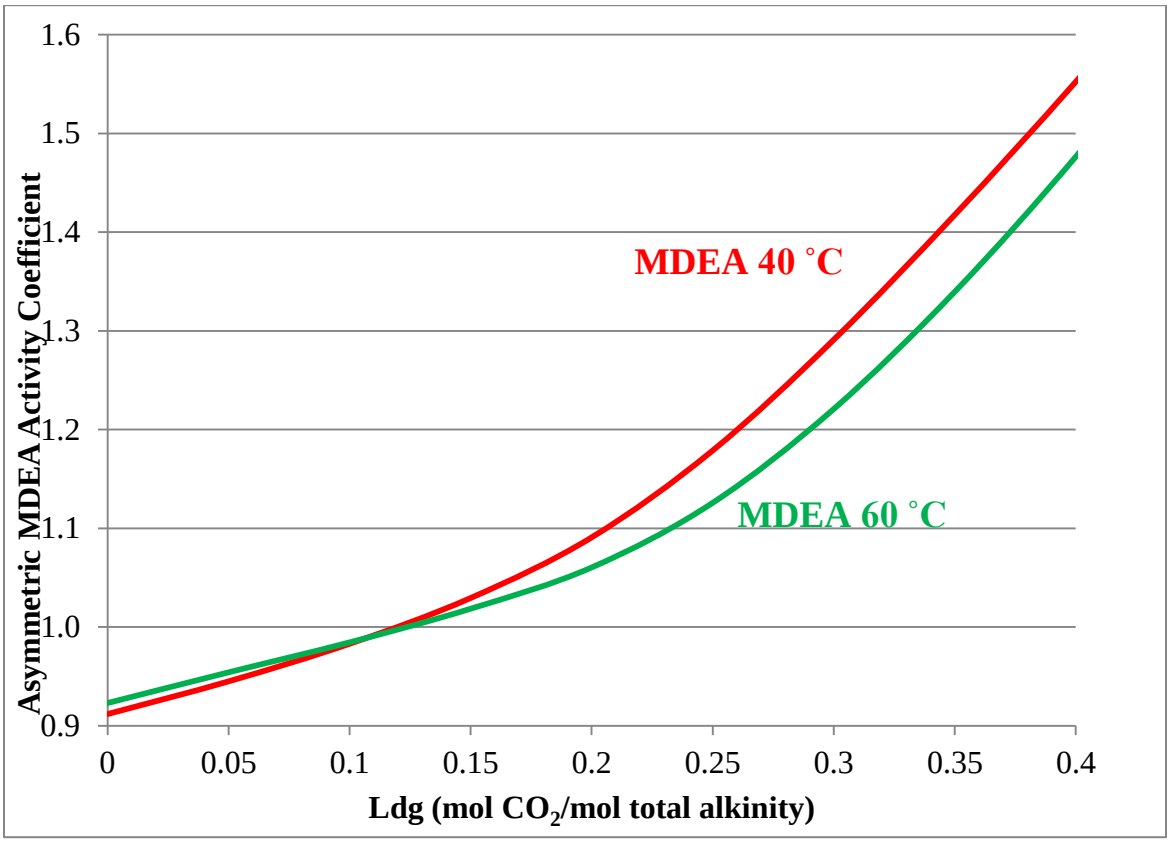

Figure 5.4-11. MDEA Activity Coefficient in 7 m MDEA/2 m PZ (curves predicted by upgraded Fawkes model)

As with PZ, MDEA activity coefficient increases with loading because it is salted out of solution by the electrolytes. Starting at a loading of ~0.18, the MDEA activity coefficient seems to have a slight temperature dependence going from 40 ˚C to 60 ˚C. The loading of ~0.18 is the critical loading for 7 m MDEA/2 m PZ where the PZ is saturated with CO_2; therefore, at a loading higher than 0.18, MDEA is being reacted with CO_2 which could explain why MDEA starts to salt out noticeably since there is less of its own kind available in solution. MDEA interacts favorably with itself which would

suggest that it would salt out if there is less of its own kind present. Since the MDEA activity coefficient has more of a temperature dependence than PZ in this blend, one can conclude that the MDEA excess heat is greater than that of PZ.

Figure 5.4-12 shows both the amine activity coefficients and free amine concentration for 7 m MDEA/2 m PZ at 40 ˚C.

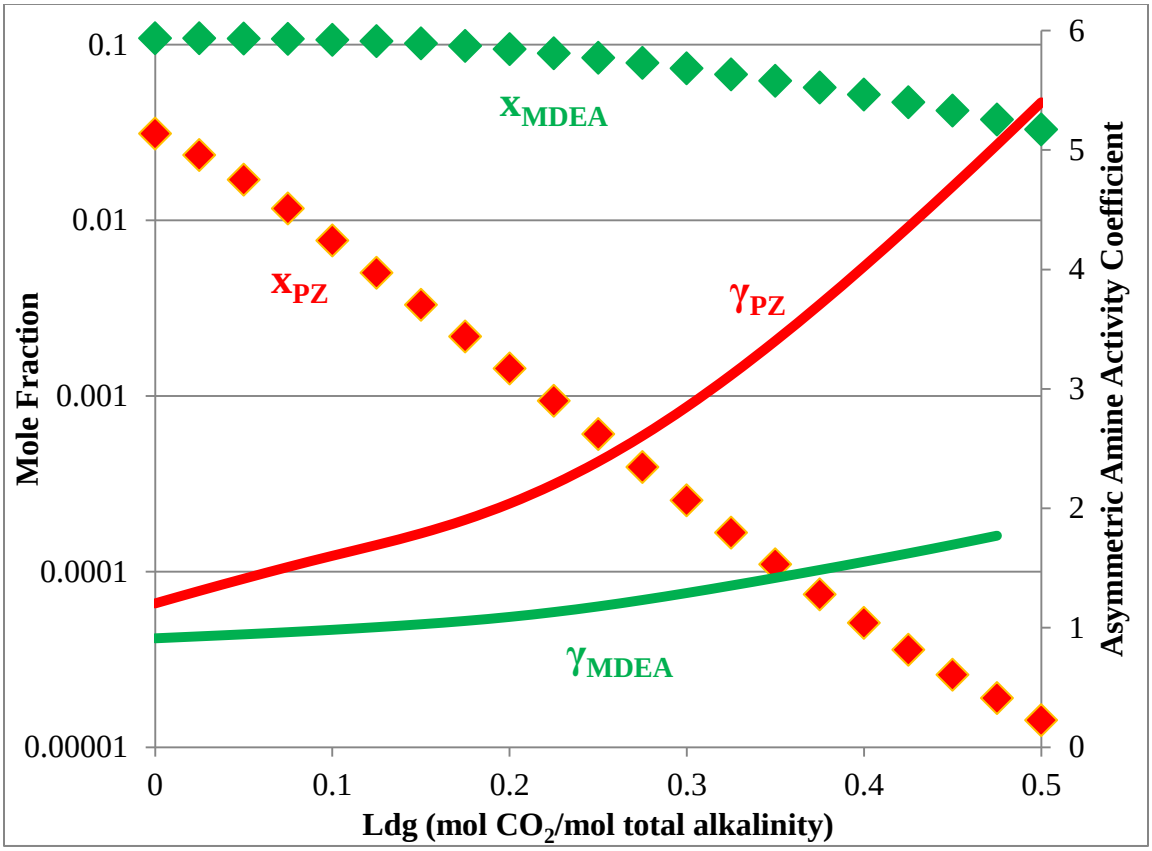

Figure 5.4-12. Amine Concentrations and Activity Coefficients for 7 m MDEA/2 m PZ at 40 ˚C (curves predicted by upgraded Fawkes model)

This plot serves to recap the fundamental speciation and activity coefficient behavior for 7 m MDEA/2 m PZ. As loading is increased, PZ is depleted to a much greater extent than MDEA because PZ reacts more readily with CO_2 as it is the stronger base and is a diamine which can participate in multiple equilibrium reactions with CO_2.

Starting at the critical loading of ~0.18, the total PZ is consumed by CO_2 at which point MDEA now starts reacting; thus, the MDEA concentration can be seen to decrease starting at the critical loading. Finally, the PZ activity coefficient increases more with loading than the MDEA activity coefficient. Again this is because PZ salts out more readily than MDEA in the presence of electrolytes since PZ is not as polar as MDEA.

Figure 5.4-13 shows the PZ activity coefficient for various equi-molal MDEA/PZ blends as a function of ionic strength at 40 ˚C.

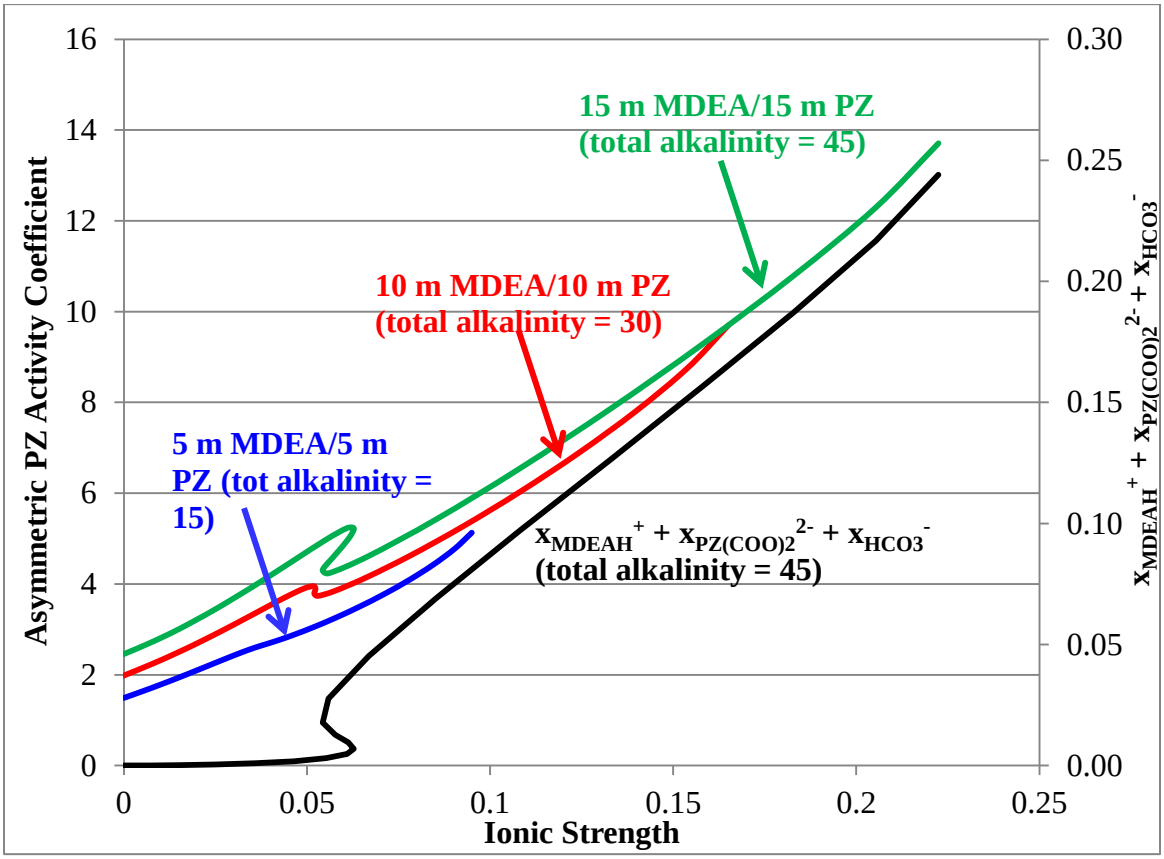

Figure 5.4-13. PZ Activity Coefficient as a Function of Ionic Strength at 40 ˚C

Recall that the ionic strength is calculated as $0.5\sum x_i z_i^2$ where x_i is the liquid mole fraction of an electrolyte species and z_i is its charge. As shown in Figure 5.4-13, blends

with higher total alkalinity can be loaded to higher maximum ionic strengths. Most importantly, the PZ activity coefficient increases with increasing ionic strength as PZ is salted out of solution in the presence of increasing electrolyte generation. Additionally, the PZ activity coefficient is greater with greater PZ concentration in a blend. Recall from earlier that PZ does not interact favorably with its own kind due to competition to bond with water to form PZ hexahydrate complexes; thus, at higher PZ concentration, there is less water available to complex with PZ which results in PZ salting out. The PZ activity coefficient behavior with respect to increasing ionic strength is mirrored by the increasing total production of three key electrolyte species, $x_{MDEAH^+} + x_{PZ(COO)_2^{2-}} + x_{HCO_3^-}$, which drives greater ionic strength (as shown for the 15 m MDEA/15 m PZ case). In light of this profile mirroring, to a first order, one can rationalize that PZ has a greater tendency to salt out as a consequence of the increasing total presence of the electrolytes mentioned.

Figure 5.4-14 displays the MDEA activity coefficient for various equi-molal MDEA/PZ blends as a function of ionic strength at 40 ˚C.

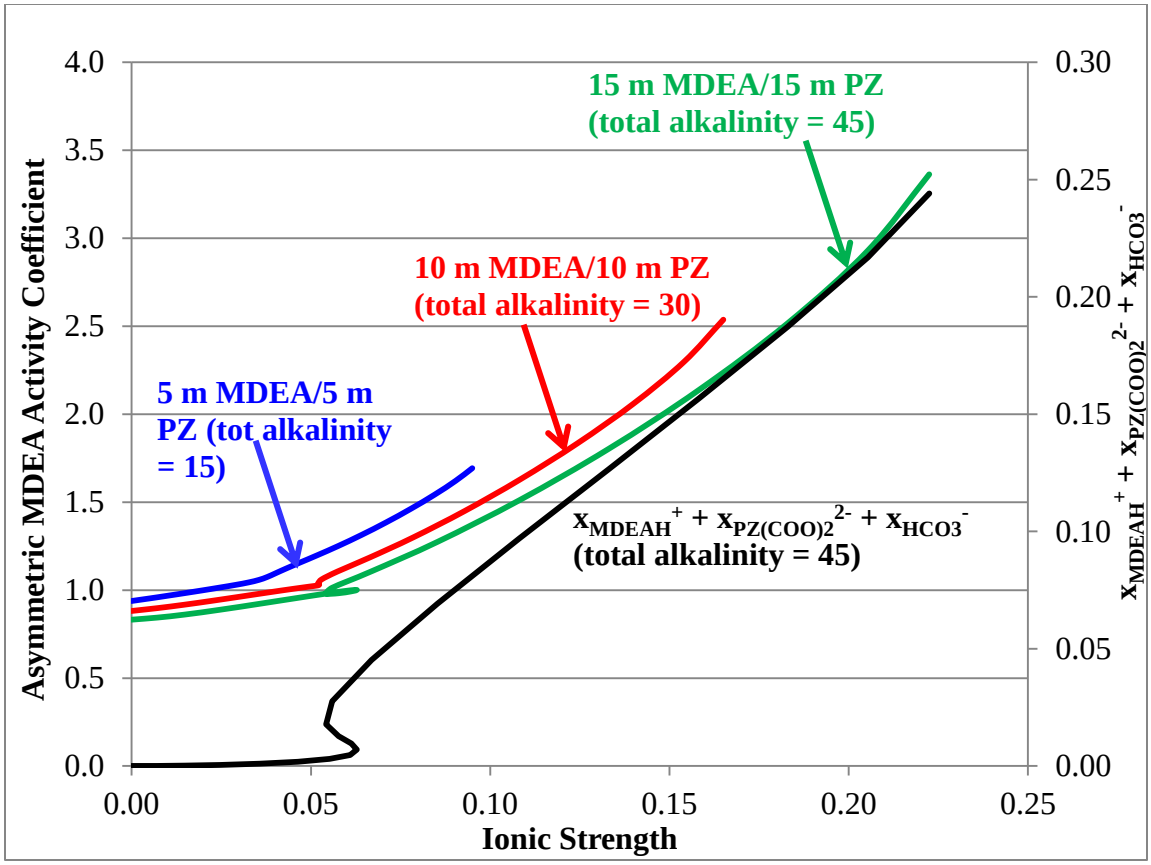

Figure 5.4-14. MDEA Activity Coefficient as a Function of Total Alkalinity and Ionic Strength at 40 ˚C

Again, blends with higher total alkalinity can be loaded to higher maximum ionic strengths. Like PZ, MDEA also salts out of solution with increasing ionic strength. Nevertheless, MDEA salts out to a lesser extent than PZ because it is more polar than PZ and therefore has a stronger affinity to polar electrolytes. Also, the MDEA activity coefficient behavior with respect to ionic strength is mirrored by the increasing total production of $MDEAH^+$, $PZ(COO)_2^{2-}$, and HCO_3^- which drives greater ionic strength. This again suggests, to a first order, that MDEA increasingly salts out of solution in the presence of increasing total production of the key electrolyte species mentioned. Finally, the MDEA activity coefficient decreases with increasing MDEA concentration in the

blend. This phenomenon is a result of MDEA interacting favorably with its own kind due to hydrogen bonding; thus, having more MDEA in solution will result in MDEA salting in to a greater extent.

Figure 5.4-15 shows the activity coefficients of electrolyte species in 7 m MDEA/2 m PZ at 40 ˚C.

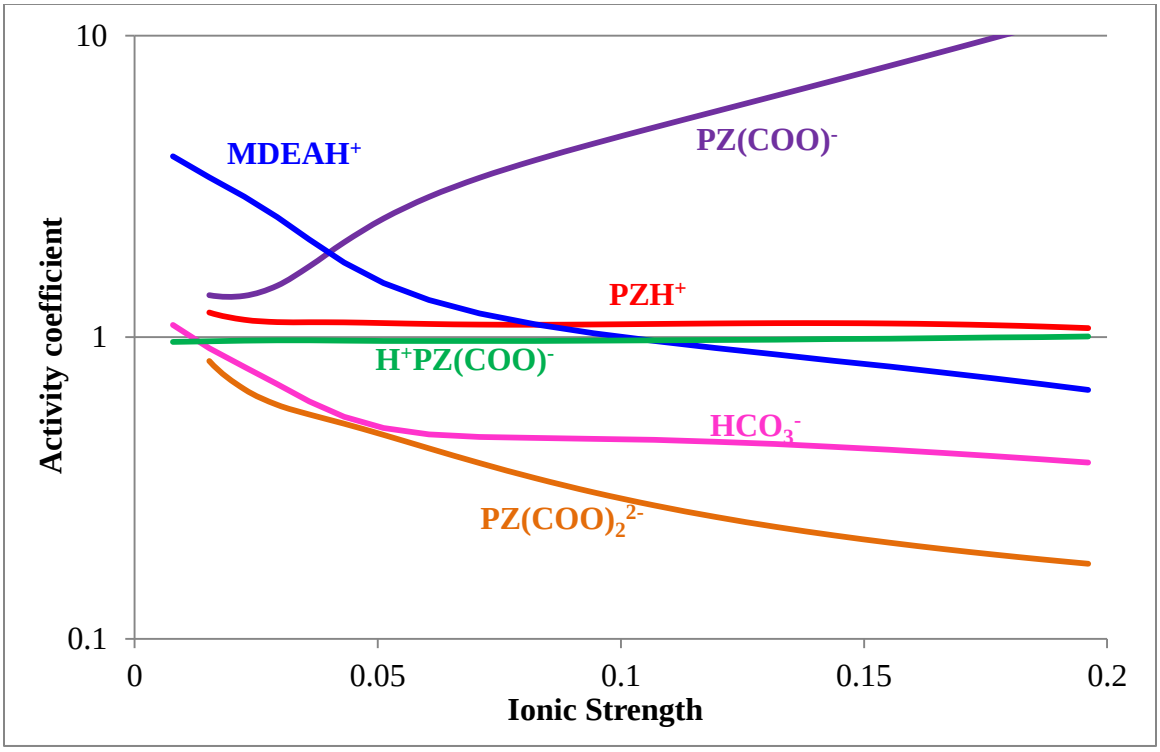

Figure 5.4-15. Activity Coefficients of Electrolytes in 7 m MDEA/2 m PZ at 40 ˚C (curves predicted by upgraded Fawkes model)

The activity coefficients of the majority of electrolytes in 7 m MDEA/2 m PZ are shown to decrease with increasing ionic strength. This result indicates that the electrolytes are salted in with greater ionic strength due to greater concentrations of electrolytes present in solution. Also note that certain electrolytes are seen to salt in more than others such as $PZ(COO)_2^{2-}$ in comparison to $MDEAH^+$. However, $PZ(COO)^-$ seems to salt out with increasing ionic strength. This result maybe an artifact of the model

mathematics; nevertheless, it could be rationalized that $PZ(COO)^-$ is not as ionic as other electrolytes since it possesses an organic PZ group at one end of the molecule. Because of this characteristic, one could speculate that $PZ(COO)^-$ would perhaps tend salt out of solution as opposed to other true electrolytes which salt in.

Amine Screening

Table 5.4-4 summarizes the amine volatility at 40 ˚C for various systems screened for CO_2 capture (with 7 m MEA data taken from Hilliard 2008).

Table 5.4-4. Amine Volatilities for Various Systems Screened at 40 ˚C

	α = 0		α = nominal lean			
Amine System	**P_{amine1} (Pa)**	**P_{amine2} (Pa)**	**P_{amine1} (Pa)**	**P_{amine2} (Pa)**	**Ldg**	**P_{CO2} (Pa)**
7 m MDEA	0.48		0.47		0.03	520
4.8 m AMP	14.2		14.8		0.31	743
7 m MEA	10.0		2.70		0.47	574
8 m PZ	7.41		0.78		0.29	410
8 m EDA	17.2		3.41		0.43	564
7 m MDEA/2 m PZ	0.46	1.07	0.47	0.30	0.14	524
5 m MDEA/5 m PZ	0.36	5.04	0.45	0.51	0.22	598
4 m 2-MPZ/4 m PZ	8.53	2.39	0.85	0.10	0.33	652
2.3 m AMP/5 m PZ	12.2	4.78	5.71	0.61	0.30	244

The volatility of tertiary and hindered amines, such as MDEA and AMP, respectively, does not vary much from zero to the nominal lean loading. This is because tertiary and hindered amines are not able to react directly with CO_2 to form charged carbamates; therefore, the free amine concentrations do not significantly change upon loading, which in turn result in a relatively constant volatility.

Carbamate forming monoamines, such as MEA, can participate in more equilibrium reactions with CO_2, thus resulting in the amine volatility dropping by a factor

of 3 or greater. Diamines, such as PZ and EDA, can participate in multiple equilibrium reactions with CO_2 to form various carbamate and protonated species; as a result, their volatility decreases by a factor of 5, 10, or even more than 20 in some cases.

When PZ is added to make a blend, CO_2 tends to react preferentially with it because it is usually the stronger base of the two amines in the blend and has two amine groups which can undergo extensive speciation. Based on these screening results, it appears that PZ or any blend consisting of diamine promoted by PZ would make a choice solvent for CO_2 capture, at least from a volatility standpoint, given the low volatilities of the amines at nominal loadings. (The PZ volatility for 8 m PZ at zero loading is a value estimated by the upgraded MDEA/PZ Fawkes model. It was not possible to measure PZ volatility at this condition due to solid precipitation.)

Table 5.4-5 displays the estimated (asymmetric) activity coefficients for the different amine systems screened. The activity coefficients of systems forming complex speciation were estimated from the upgraded Fawkes MDEA/PZ thermodynamic model.

Table 5.4-5. Asymmetric Amine Activity Coefficients for Various Systems Screened at 40 ˚C (7 m MEA from Hilliard 2008)

	α = 0		**α = nominal lean**				**Salt Out Factor = $\gamma_{amine,\alpha=lean}/\gamma_{amine,\alpha=0}$**	
System	**γ_{amine1}**	**γ_{amine2}**	**γ_{amine1}**	**γ_{amine2}**	**Ldg**	**P_{CO2}**	**$amine_1$**	**$amine_2$**
7 m MDEA	0.906		0.911		0.03	520	1.01	
4.8 m AMP	0.565		0.862		0.31	743	1.53	
7 m MDEA/ 2 m PZ	0.912	1.21	1.02	1.75	0.14	524	1.12	1.45
5 m MDEA/ 5 m PZ	0.944	1.49	1.07	2.64	0.22	598	1.13	1.77
8 m PZ	1.81		3.8		0.29	410	2.10	
7 m MEA	1.49		6.21		0.47	574	4.17	

The salting out factor is defined as the ratio of the asymmetric amine activity coefficients before and after loading. The degree to which an amine salts out of solution essentially depends upon two factors: (1) the amount of salt or electrolytes generated in a system at a particular loading; (2) how nonpolar the amine is which leads to it salting out in the presence of polar charged electrolytes.

7 m MDEA and 4.8 m AMP show the least salting out. Given that MDEA is a tertiary amine and AMP is a hindered amine, they are not able to react directly with CO_2 to produce a significant amount of electrolytes. With little salt present in the system, MDEA and AMP do not salt out appreciably. AMP salts out to a slightly greater extent than MDEA because it is more nonpolar. In MDEA/PZ, MDEA salts out to a slightly greater extent than in 7 m MDEA because there is more salt generated in the blend coupled with the fact that MDEA has less favorable interactions with PZ. MDEA tends to associate with itself due to hydrogen bonding. In 8 m PZ, a large amount of electrolyte is formed due to PZ being a diamine; thus, PZ salts out noticeably in the presence of high ionic strength. Additionally, the fact that PZ does not interact favorably with its own kind also contributes to greater salting out. 7 m MEA appears to salt out even more than PZ possibly because MEA is more nonpolar than PZ in the presence of all the polar salt in the system.

5.5. Conclusions

The enthalpies of amine absorption, for PZ and for MDEA, at unloaded and nominal lean loading conditions are 73 – 76 kJ/mol amine. The enthalpy of amine solution (71 – 74 kJ/mol) provides the greatest contribution to the enthalpy of absorption,

followed by the enthalpy of reaction (~0.7 – 5 kJ/mol), and finally the amine excess enthalpy (-0.1 - 3 kJ/mol). MDEA has a smaller enthalpy of reaction compared to PZ because: (1) it is a tertiary amine which does not form carbamate and only serves as a proton sink; (2) unlike PZ, it does not react much with CO_2 at the nominal lean loading of interest.

Amine volatility is most strongly a function of speciation, especially in the case of PZ. PZ volatility decreases with increasing loading as proportional to the decrease in free PZ. In 8 m PZ-CO_2-H_2O, as the loading is increased from zero to 0.4 mol CO_2/mol total alkalinity at 60 ˚C, both the PZ volatility and free PZ concentration drop by a factor of 50.

In the case of unloaded MDEA/PZ, as the PZ concentration increases by a factor of 5 (while MDEA concentration is fixed), the PZ activity coefficient increases by a factor of 1.5 – 1.7 because PZ does not interact favorably with its own species, partly due to competition amongst each other to be hydrated in forming PZ hexahydrate. As the MDEA concentration increases by a factor of 3 (while PZ concentration is fixed), the MDEA activity coefficient decreases by a factor of ~1.1-1.2 because MDEA interacts favorably with itself due to hydrogen bonding. As loading is increased from zero to nominal lean loading, both MDEA and PZ activity coefficients increase since the amines are being salted out of solution by the electrolytes; in particular, $MDEAH^+$, $PZ(COO)_2^{2-}$, and HCO_3^- are the species that predominantly drive MDEA and PZ activity coefficient behaviors.

Conversely, the electrolyte products are seen to salt in with increasing ionic strength. $PZ(COO)_2^{2-}$ and HCO_3^- salt in the most. $PZ(COO)^-$ salts in the least, perhaps because PZ carbamate has an organic PZ portion which makes it less polar than the other electrolytes.

The volatilities of tertiary and hindered amines, such as MDEA and AMP, respectively, do not vary much with respect to loading. This is because these amine types are not able to form carbamates by reacting directly with CO_2 like other amines; moreover they tend to serve as proton sinks only. As a result of the limited extent of reaction, their speciation does not change very much with loading which results in seemingly constant volatilities. Mono-amines, such as MEA, show volatilities decreasing by a factor of ~3 or greater upon loading the solutions to the nominal lean loadings. This is because mono-amines can actually form stable carbamates with CO_2 in addition to being proton sinks. Finally, diamines such as EDA and PZ have volatilities that decrease by a factor of 5 to as much as 20 times depending on the system. The volatilities of diamines are very strong functions of loadings because diamines can participate in multiple equilibrium reactions with CO_2 due to having two amine groups.

PZ or any blend consisting of a diamine promoted by PZ would make a choice solvent for CO_2 capture, at least from a volatility standpoint, given the low volatilities of the amines at nominal loadings.

In order of increasing salting out level at nominal lean loading and 40 ˚C: 7 m MDEA < 4.8 m AMP ~ 7 m MDEA/2 m PZ < 8 m PZ < 7 m MEA. Tertiary and hindered amines like MDEA and AMP, respectively, show negligible salting out since not much

salt is generated in these systems. Monoamines and diamines, such as MEA and PZ, salt out more noticeably given higher amount of salt formed in these systems since these amines can react directly with CO_2 to make charged carbamates. Finally MEA salts out more than PZ because it is more nonpolar.

Chapter 6. Conclusions and Recommendations

6.1. Summary of Research Scope and Background

This work investigated the volatilities of amine solvents used for post-combustion CO_2 capture from coal-fired power plants. Amine volatility is one of the key criteria used to screen new solvents for a number of reasons: (1) volatility losses up the stack can react in the atmosphere to form ozone and other toxic compounds; (2) high volatility losses increase the costs spent for solvent make-up; (3) these high amine losses would also require the use of a bigger water wash, and more water, to capture fugitive amines which translate to higher capital and operating costs; (4) amine volatility measurements are needed to construct more accurate and robust thermodynamic models of CO_2 capture systems.

The volatilities of amine solutions, at unloaded and loaded conditions, were measured using the hot gas FTIR apparatus developed by Hilliard (2008). The amine volatility measurements at loaded conditions are first of a kind and have not been made outside the Rochelle group. Also this work is believed to be one of the largest sources of experimental data for amine-water systems available.

The FTIR apparatus used to measure amine volatility is considered to be a fairly novel technique used to determine vapor-liquid equilibrium. Other authors tend to use more traditional experimental methods, such as those that involve a static cell or an Othmer still coupled with Gas Chromatography (GC) analysis. These traditional methods often involve boiling the solution to create a vapor phase for GC analysis, whereas the FTIR method measures amine volatility above a sub-cooled solution. The FTIR method

is believed to be more versatile than existing experimental methods for vapor-liquid equilibrium measurements because: (1) there is much more VLE data can be generated when working with a sub-cooled liquid as opposed to boiling the solution; (2) ease of operation – a definite advantage especially when it comes to working with high boiling solvents. Traditional VLE methods sometime require pulling a vacuum to boil off these high boiling solutions.

With the liquid phase analysis, the solutions are loaded with carbon 13 which enable a Nuclear Magnetic Resonance (NMR) analysis of all the species present in solution. Both the proton (H^1) and carbon (C^{13}) NMR results are used to identify all of the existing product species. These two sets of NMR results are often within ±10% of one another which suggest consistency. Analysis of the liquid phase by NMR is used to understand the speciation in the solution and is used to interpret the gas phase volatility measurements made by the FTIR. For key amine systems such as PZ-CO_2-H_2O and MDEA-PZ-CO_2-H_2O, heat capacity measurements are also made by using a Differential Scanning Calorimeter (DSC). All of the thermodynamic measurements made by this work, including amine volatility, speciation, and heat capacity, are used along with CO_2 solubility measurements to construct rigorous thermodynamic models of the CO_2 capture systems. The thermodynamic models are built using AspenPlus®7.3. These models use the Liquid Activity method to characterize system thermodynamics. The liquid phase is modeled using elecNRTL (Electrolyte NRTL) method whereas the vapor phase is modeled using SRK (Soave-Redlich-Kwong).

There are three key areas of investigation in this work as described in the three individual body chapters (3 – 5). These research areas are: (1) aqueous amine volatility in amine-water systems; (2) thermodynamic modeling of MDEA-PZ-CO_2-H_2O system (with emphasis on upgrading the MDEA thermodynamic portion of the model); (3) generalized amine screening and interpretation (using detailed MDEA-PZ thermodynamics as the basis for interpretation). Note that each of these three areas already comes with detailed conclusions in the individual body chapters; however, this chapter will serve to highlight the key conclusions in each chapter as described in the following sections.

6.2. Key Conclusions by Topic

Aqueous Amine Volatility in Amine-Water Systems

The parameter values for the functional groups used in the model to fit H_{amine} at 40 ˚C are:

Group j	**N**	**NH**	**O**	**NH_2**	**OH**	**N_{cy}**	**O_{cy}**
k_j	-18.9	-15	-13.8	-12.1	-10.8	-7.57	-4.3
Group j	**CH_2-(CH_2)**	**CH_3-(CH)**	**C_{cy}**	**CH_3-(N_{cy})**	**CH_3-(N)**	**CH_2-(OH/N)**	
k_j	0.126	0.16	0.294	1.85	4.48	5.41	

The enthalpy of amine solution is correlated with the entropy of solution at 40 ˚C by $\Delta H_{solution} = 0.74T\Delta S_{solution} + 2256$ (J/mol).

The experimental H_{amine} from this work and those predicted by UNIFAC-DMD theory agree to within an order of magnitude with the exception of PZ and DGA.

H_{amine} estimated by the group contribution method of Hine and Mookerjee (1975) are systematically one to many orders of magnitude less than the experimental data.

At 0.1 to 1 m amine, the concentration range used to measure H_{amine} in this work, the asym- metric activity coefficient of piperazine is 1.02 – 1.10.

The enthalpies of solution of the different aqueous amine systems studied appear to be adequately represented with Arrhenius temperature behavior which assumes a constant enthalpy of solution over a range of temperature.

Upgrading the AspenPlus® v.7.3 Fawkes MDEA-PZ-CO_2-H_2O Thermodynamic Model

In the MDEA-CO_2-H_2O system, carbonate (CO_3^{2-}) is an important species as its introduction into the chemistry set allowed for better fitting of CO_2 solubility at ultra lean loadings ($0.001 < \alpha < 0.01$).

With the MDEA-PZ blend, MDEA-PZ cross interaction parameters were not needed to adequately match the blend volatilities at unloaded condition. This observation suggests that MDEA and PZ interact more strongly with their own species instead of with each other.

Both the blend volatilities, at unloaded and loaded conditions, along with speciation were adequately represented in the upgraded Fawkes model.

MDEA/PZ Behavior & Generalized Amine Screening

The enthalpies of amine absorption, for PZ and for MDEA, at unloaded and nominal lean loading conditions are 73 – 76 kJ/mol amine. The enthalpy of amine solution (71 – 74 kJ/mol) provides the greatest contribution to the enthalpy of absorption,

followed by the enthalpy of reaction (~0.7 – 5 kJ/mol), and finally the amine excess enthalpy (-0.1 - 3 kJ/mol).

The volatilities of tertiary and hindered amines, such as MDEA and AMP, respectively, do not vary significantly with respect to loading since they are unable to form stable carbamates.

Monoamines, such as MEA, show volatilities decreasing by a factor of ~3 or greater upon loading since they can form stable carbamates.

Diamines such as EDA and PZ have volatilities that decrease by a factor of 5 to as much as 20 times depending on the system. The volatilities of diamines are very strong functions of loading because diamines can participate in multiple equilibrium reactions with CO_2 due to having two amine groups.

PZ or a blend consisting of a diamine promoted by PZ would be favorable for CO_2 capture, at least from a volatility standpoint, given the low volatilities of the amines at nominal loadings.

As loading is increased from zero to nominal lean loading, both MDEA and PZ activity coefficients increase since the amines are being salted out of solution by the electrolytes; in particular, $MDEAH^+$, $PZ(COO)_2^{2-}$, and HCO_3^- are the species that predominantly drive MDEA and PZ activity coefficient behaviors.

In order of increasing salting out level at nominal lean loading and 40 ˚C: 7 m MDEA < 4.8 m AMP ~ 7 m MDEA/2 m PZ < 8 m PZ < 7 m MEA. The degree to which an amine is salted out of solution depends on: (1) the amount of salt generated at a given loading; (2) how nonpolar the amine is relative to the charged electrolytes.

6.3. Recommendations and Future Work

Future measurements of aqueous amine volatility, for the purpose of determining the amine Henry's constant, should involve a more rigorous analysis of the error introduced by the asymmetric amine activity coefficient. The experimental deviation from the condition of infinite dilution of amine in water is assumed to be ±10% for all amines studied based on the analysis for PZ alone. In an effort to be more rigorous, future measurements should entail measuring the amine volatilities for a series of dilute amine concentrations in order to quantify the errors associated with experimenting at dilute conditions that are not actually at infinite dilution. Nevertheless, this error should be rather small, and therefore was not rigorously explored for every amine system studied in this work in the interest of time.

Another experimental improvement that can be made to the study of aqueous amine volatility in the future is to perhaps use a more sensitive analytical technique to quantify ultra low volatility measurements. The margin of measurement error already increases by about 15% - 30% for any measurement in the 10-20 ppm's, and can only get worse as one approaches even lower ppm concentrations in the neighborhood of the detection limit (2-5 ppm). One can either upgrade to the next generation of FTIR analysis with higher resolution or somehow use an advanced GC method, such as GC Headspace Chromatography, that can perhaps be customized to the nature of these experiments.

Another key experimental area that also requires optimization is the NMR analysis of speciation. The existing NMR analysis method (using the Varian Inova 500

MHz NMR Spectrometer) is not able to identify between a species and its protonated form due to the rapid exchange of proton involved. Perhaps a different type of NMR spectrometer, or even another liquid analysis method altogether, may have to be utilized in order to be able to make the differentiation between protonated and un-protonated amine species. The ability to analyze liquid speciation at an even more detailed level would allow for a better validation of speciation results from thermodynamic models. Furthermore, the more rigorous and detailed the experimental speciation analysis is, the better one can quantify the exact free amine concentration for diamines and their blends where there is extensive speciation occurring. It follows that having the exact information for the free amine concentration not only helps to validate model speciation results but also to allow for a more rigorous activity coefficient analysis.

For future work, there are a number of thermodynamic studies that are worth pursuing. First, it will be worthwhile to measure and model amine volatilities at the water wash condition (which involves a few ppm of amine volatility in ~15 mol% of water). The water wash topic is important to: (1) controlling amine emission; (2) expanding the range of applicability of the thermodynamic models; (3) sizing proper equipment and costing. In addition to exploring amine volatility at the absorber and water wash condition, it might also be pertinent to investigate amine emission from the stripper for the same reasons. One can even take it a step further and explore amine volatility at all the crucial locations mentioned as applicable to CO_2 capture from natural gas. Finally, it will be very challenging but nonethless insightful to study the volatilities

of amine byproducts, such as nitrosamines, degraded amines, and such, that can also be potentially released into the atmosphere.

Appendix A: H^1 and C^{13} NMR Analysis

1. Introduction

NMR (Nuclear Magnetic Resonance) Spectroscopy is used to study liquid speciation. The analysis is performed by using a Varian Inova 500 MHz NMR Spectrometer. There are two types of NMR analyses that are used to identify liquid speciation: (1) proton (H^1) NMR and (2) C^{13} NMR where the solutions are loaded with C^{13} CO_2 in order for species to be magnetically active and detectable to NMR. All species in solution can be identified with either of the two NMR types; however, the bicarbonate/carbonate species is only detectable with C^{13} NMR, not with H^1 NMR, because there is no hydrogen element in the species to be detected by H^1 NMR.

2. Experimental Procedure

A batch of 5 – 10 g of aqueous amine-water solution is first prepared using analytical grade reagents. The solution is then subsequently mixed with 1 wt % 1,4-dioxane, which serves as an internal standard, and roughly 10 wt % deuterium oxide which keeps the NMR signal of the sample from being swamped out by that of the solvent. The solution is then loaded with C^{13} CO_2 up to the desired loading by using a glass sparging apparatus. The loading process takes place through a few steps: (1) the glass sparging device has to be pre-weighed before it is filled with solution and then weighed again after; (2) the sparging device is now connected to a mini C^{13} CO_2 cylinder (regulators closed); (3) the C^{13} CO_2 is turned on and allowed to flow into the solution for an average of 2-4 minutes; (4) at the end of the loading interval, the entire sparging apparatus is weighed to determine the amount of C^{13} CO_2 that has been loaded; (5) the

loading process is resumed, for several more 2-4 minute intervals with weighing in between, until the desired loading is achieved as reflected by the total CO_2 weight in solution. Next, an aliquot of the loaded solution is transferred into an NMR tube (Wilmad glass, 5 mm OD x 0.77 mm ID). It is recommended that the tube should only be filled up to a height of 1.75 inch from the bottom of the tube to ensure that the solution can be properly heated once inside the 1.75 inch tube holder within the NMR machine chamber. After the NMR tube is filled, it is then sealed thermally by the glass shop prior to being run on the Varian Inova 500 MHz NMR Spectrometer (with variable temperature control). Samples that are to be run at 40 ˚C need to be thermally conditioned for at least an hour before being run.

3. Amine Structural Identification and Peak Assignment

Proton (H^1) Assignment

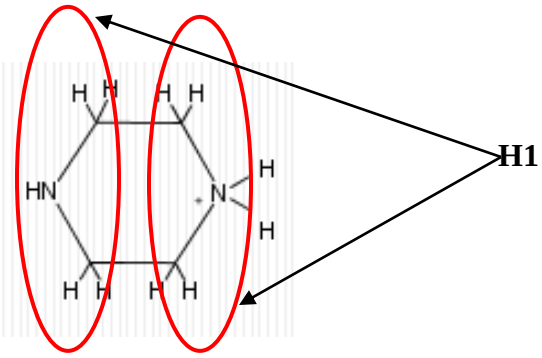

Figure A.1: Molecular Structure and Active Nuclei of Protons associated with PZ/PZH^+

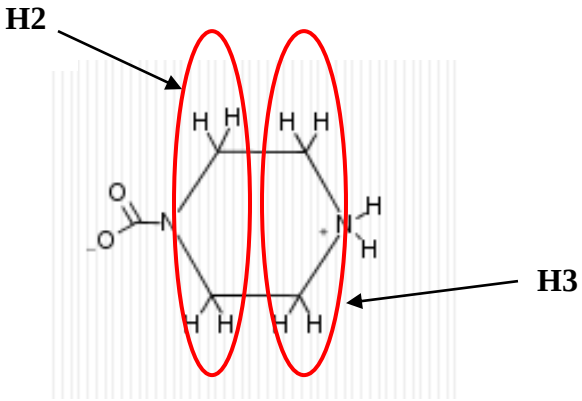

Figure A.2: Molecular Structure and Active Nuclei of Protons associated with $PZ(COO)^-/H^+PZ(COO)^-$

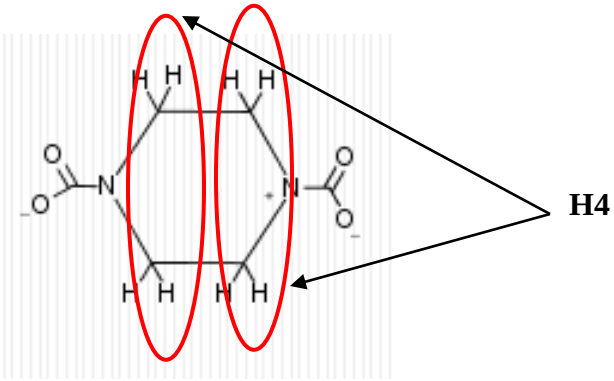

Figure A.3: Molecular Structure and Active Nuclei of Protons associated with $PZ(COO)_2^{2-}$

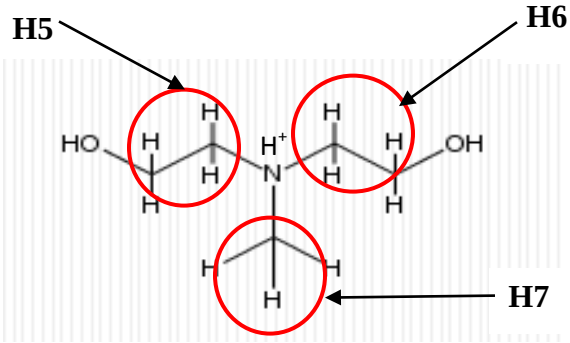

Figure A.4: Molecular Structure and Active Nuclei of Protons associated with $MDEA/MDEAH^+$

C^{13} Assignment

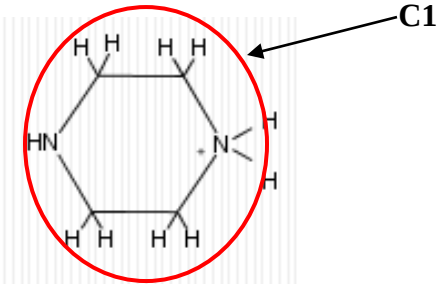

Figure A.5: Molecular Structure and Active Nuclei of Carbons associated with PZ/PZH^{+}

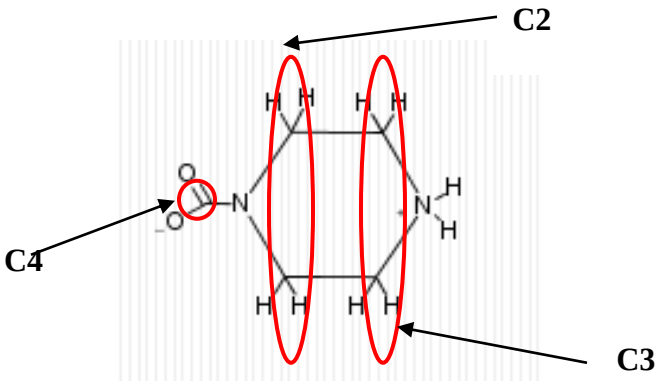

Figure A.6: Molecular Structure and Active Nuclei of Carbons associated with $H^{+}PZ(COO)^{-}/PZ(COO)^{-}$

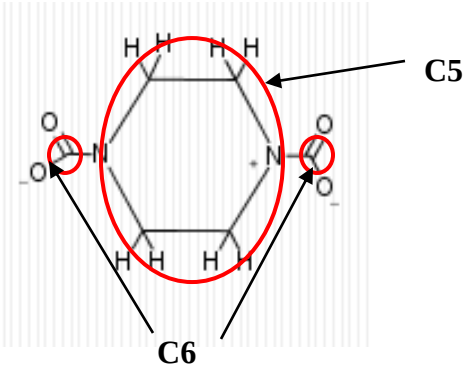

Figure A.7: Molecular Structure and Active Nuclei of Carbons associated with $PZ(COO)_2^{2-}$

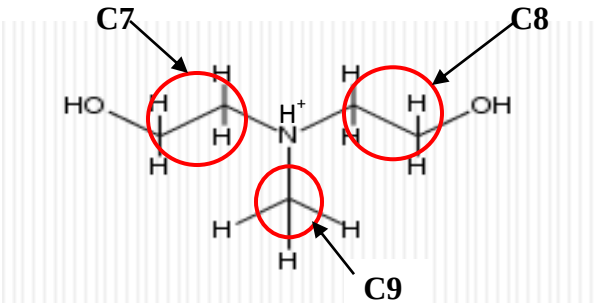

Figure A.8: Molecular Structure and Active Nuclei of Carbons associated with MDEA/MDEAH$^+$

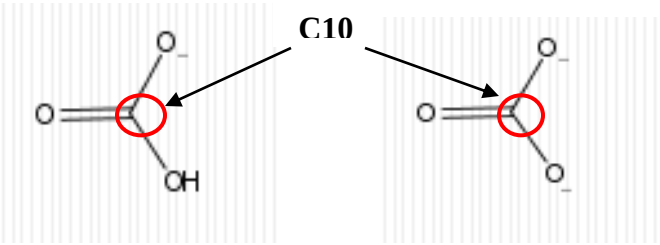

Figure A.9: Molecular Structure and Active Nuclei of Carbons associated with HCO_3^-/CO_3^{2-}

4. NMR Spectra for PZ-CO_2-H_2O and MDEA-PZ-CO_2-H_2O

8 m PZ-CO_2-H_2O

H^1 NMR

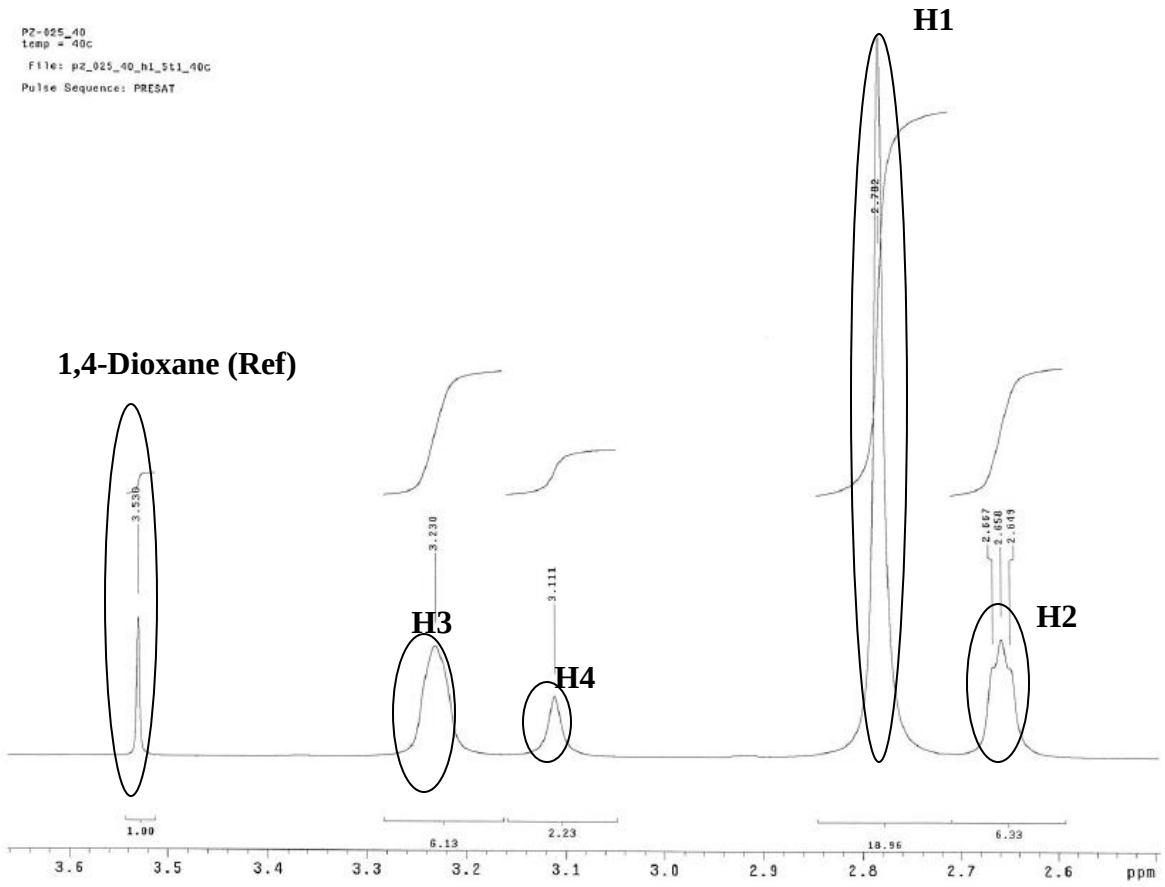

Figure A.10: H^1 NMR Spectrum of 8 m PZ-CO_2-H_2O, α = 0.25 mol CO_2/mol total alkalinity, 40 ˚C

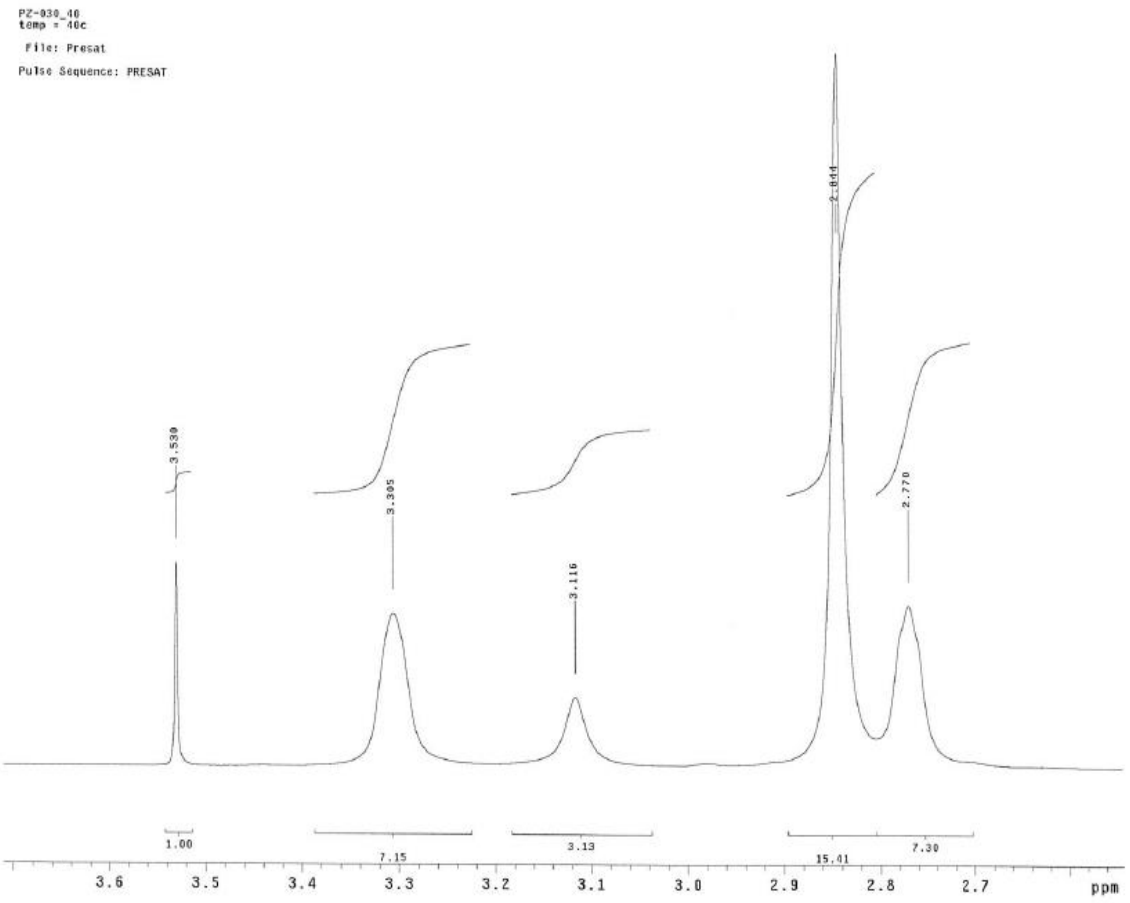

Figure A.11: H^1 NMR Spectrum of 8 m PZ-CO_2-H_2O, α = 0.30 mol CO_2/mol total alkalinity, 40 ˚C

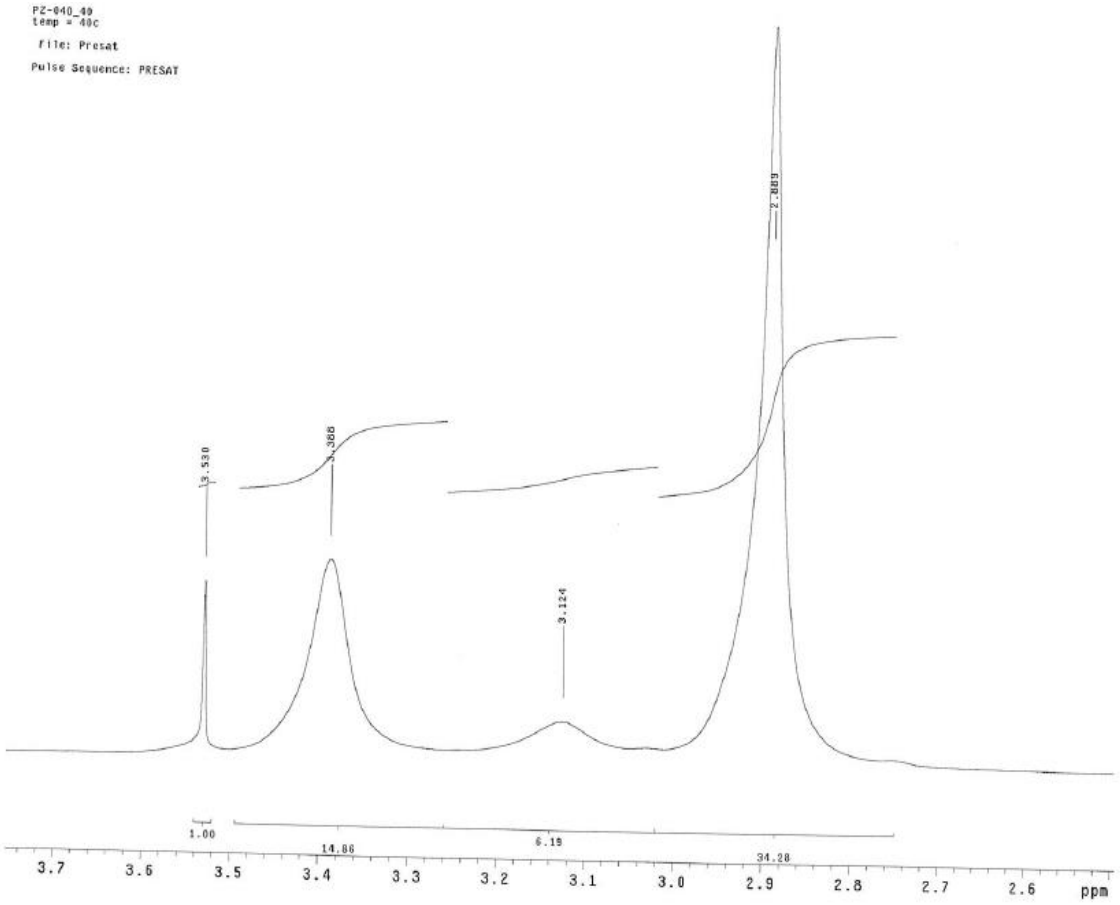

Figure A.12: H^1 NMR Spectrum of 8 m PZ-CO_2-H_2O, α = 0.40 mol CO_2/mol total alkalinity, 40 ˚C

C^{13} NMR

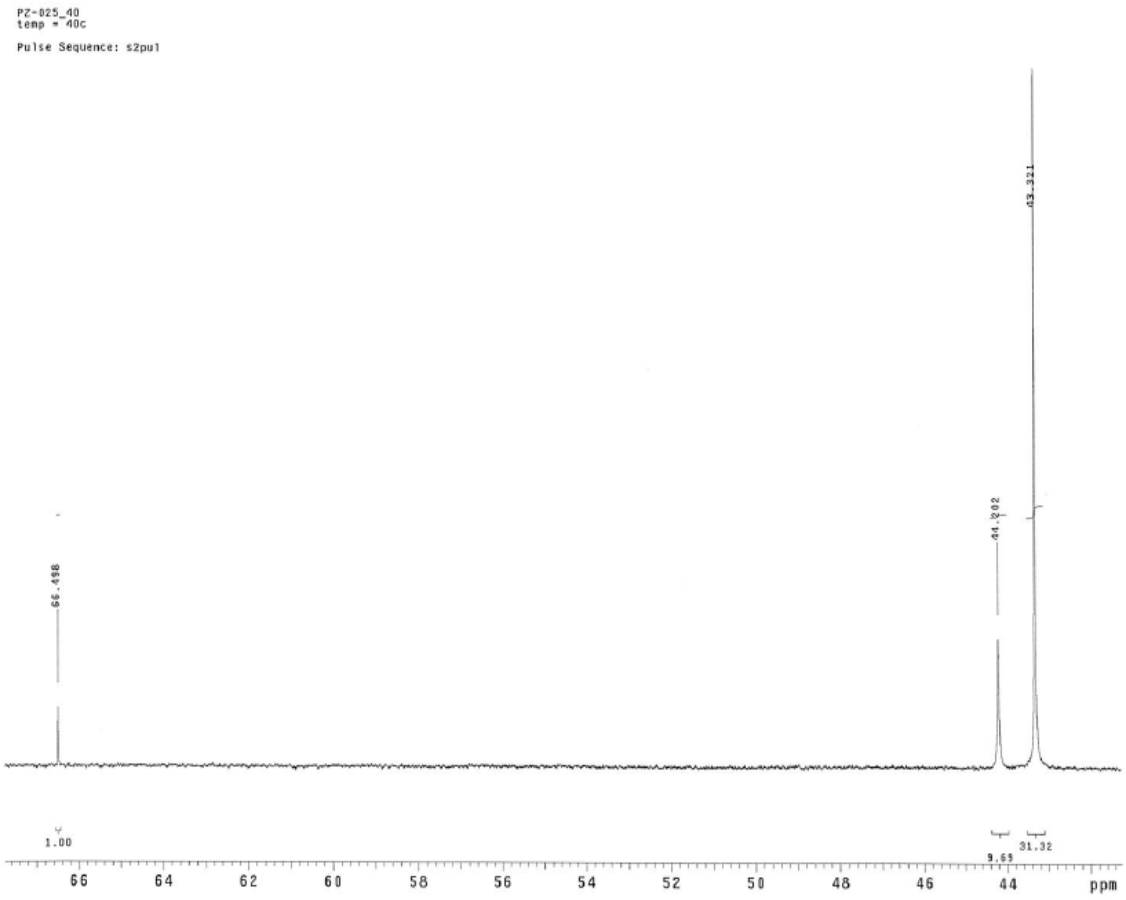

Figure A.13: C^{13} NMR Spectrum of 8 m PZ-CO_2-H_2O, α = 0.25 mol CO_2/mol total alkalinity, 40 ˚C (C^{12} peaks)

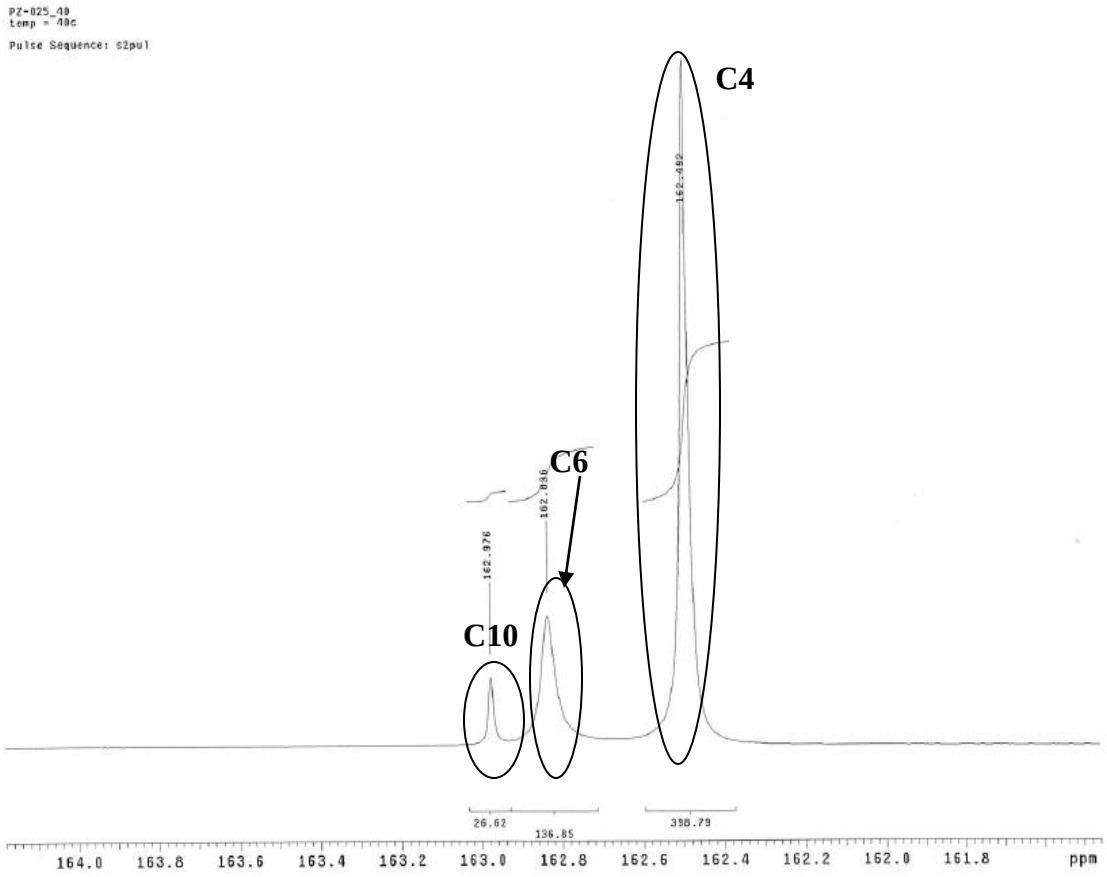

Figure A.14: C^{13} NMR Spectrum of 8 m PZ-CO_2-H_2O, α = 0.25 mol CO_2/mol total alkalinity, 40 ˚C (C^{13} peaks)

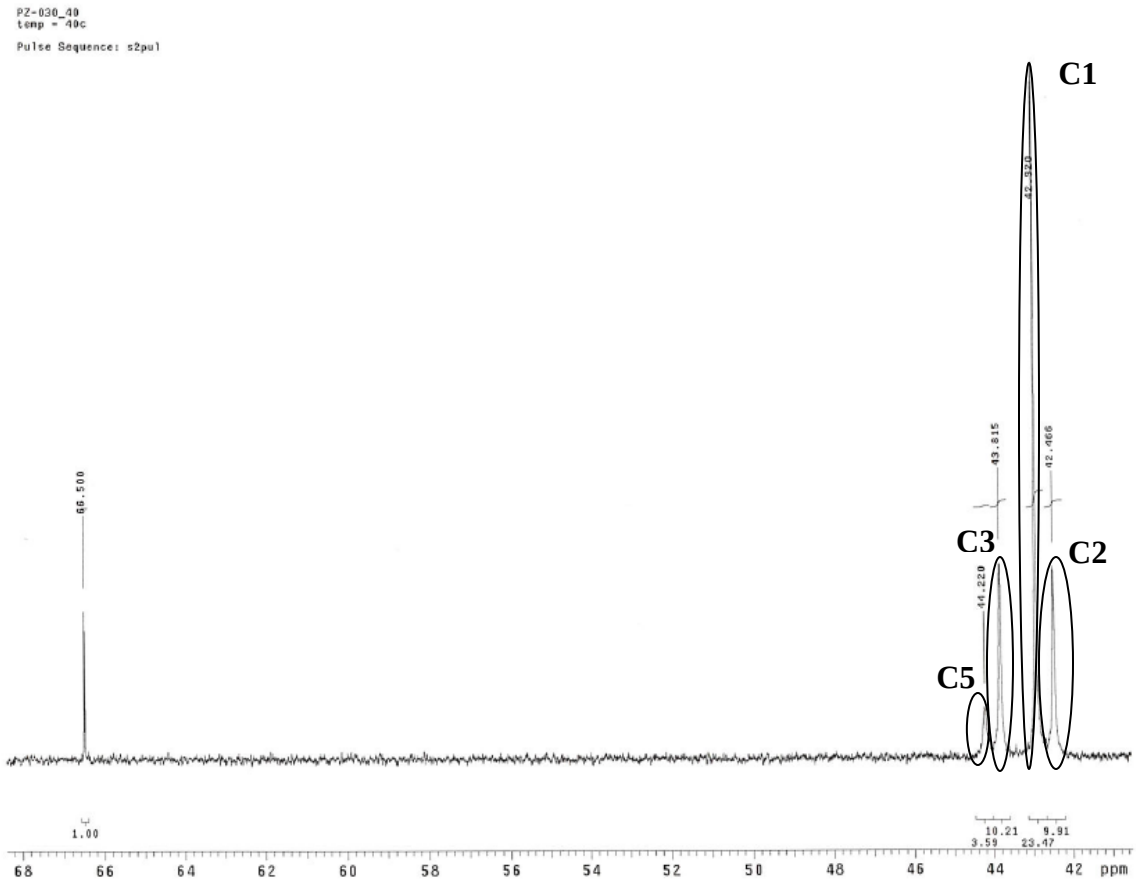

Figure A.15: C^{13} NMR Spectrum of 8 m PZ-CO_2-H_2O, α = 0.30 mol CO_2/mol total alkalinity, 40 ˚C (C^{12} peaks)

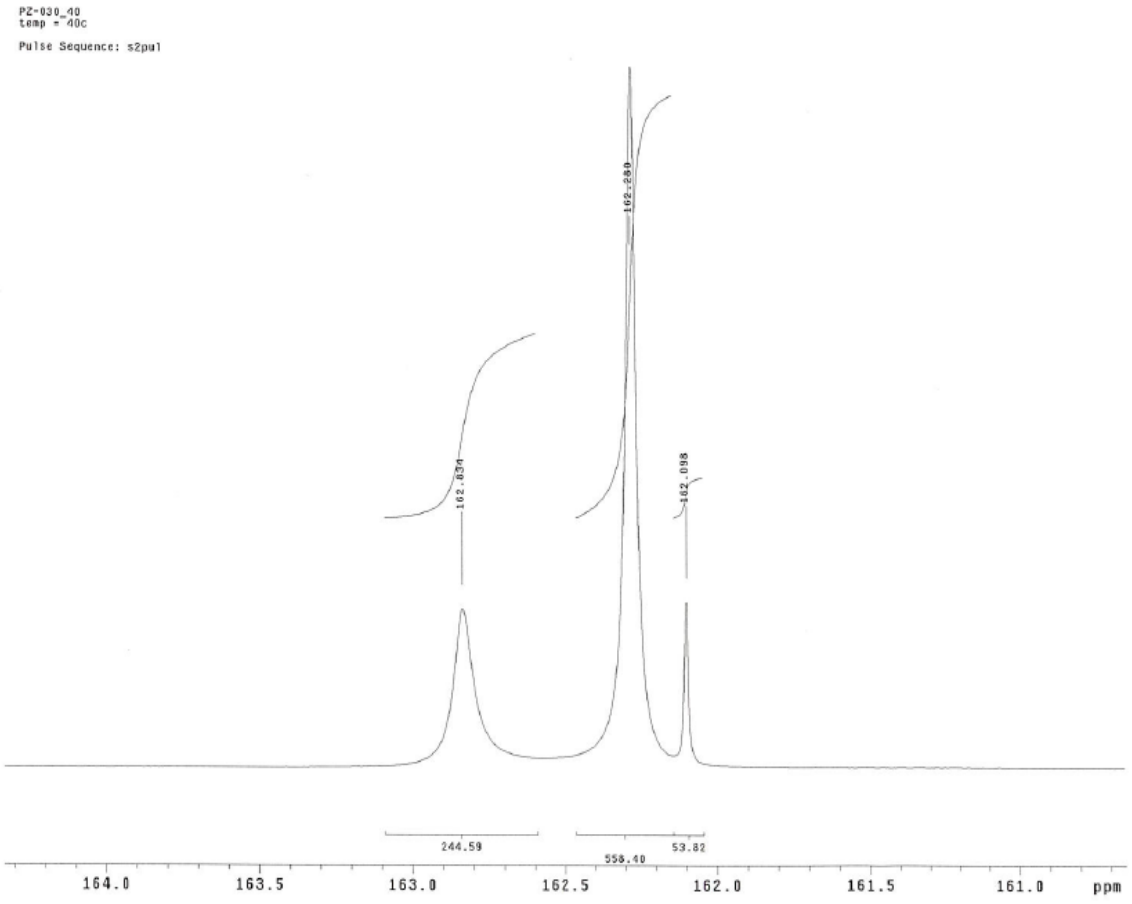

Figure A.16: C^{13} NMR Spectrum of 8 m PZ-CO_2-H_2O, α = 0.30 mol CO_2/mol total alkalinity, 40 ˚C (C^{13} peaks)

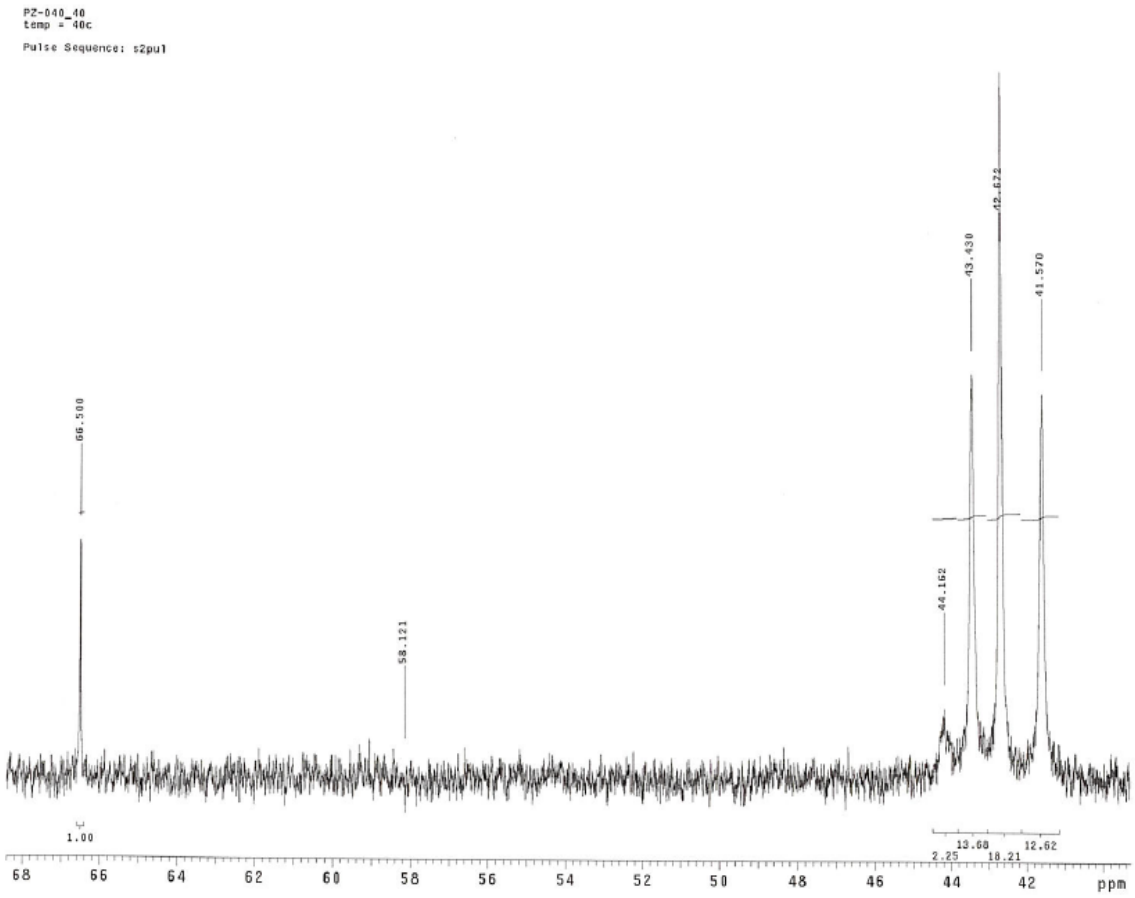

Figure A.17: C^{13} NMR Spectrum of 8 m PZ-CO_2-H_2O, α = 0.40 mol CO_2/mol total alkalinity, 40 ˚C (C^{12} peaks)

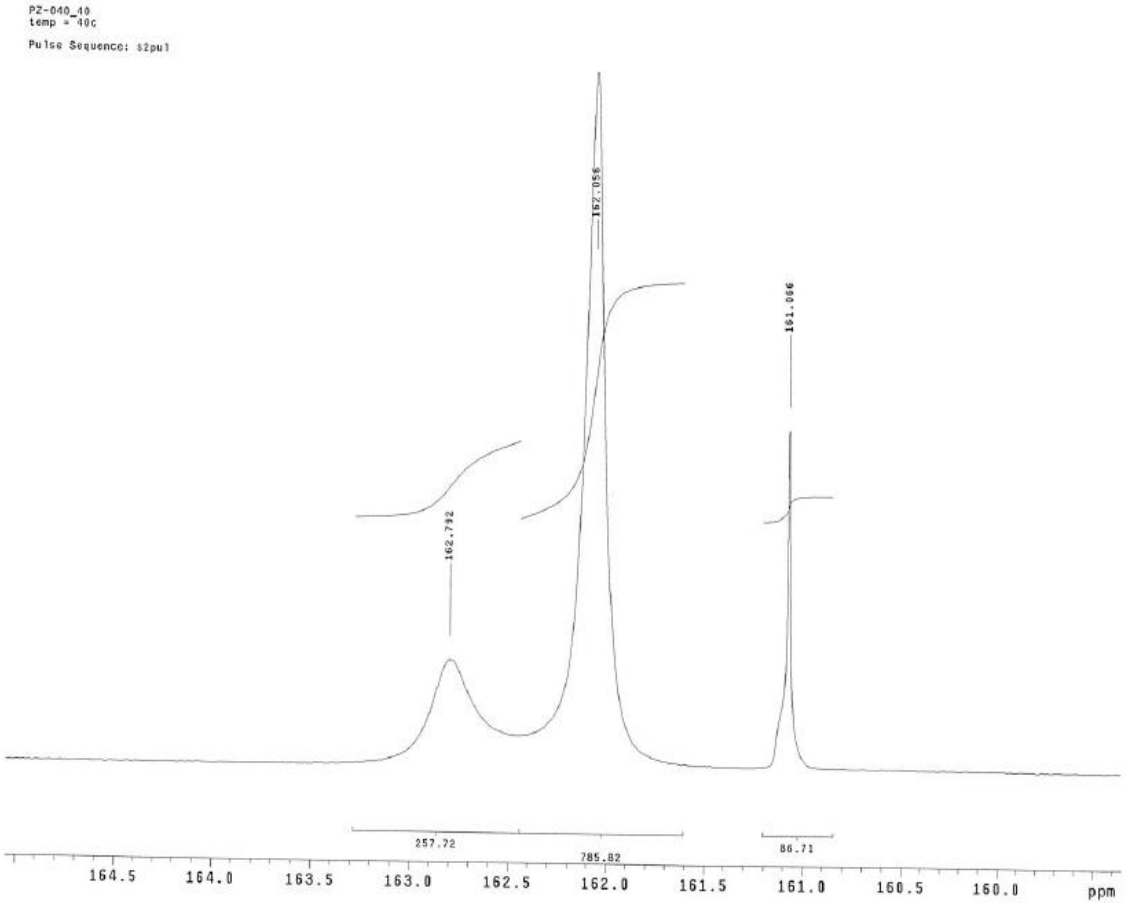

Figure A.18: C^{13} NMR Spectrum of 8 m PZ-CO_2-H_2O, α = 0.40 mol CO_2/mol total alkalinity, 40 ˚C (C^{13} peaks)

7 m MDEA-2 m PZ-CO_2-H_2O

H^1 NMR

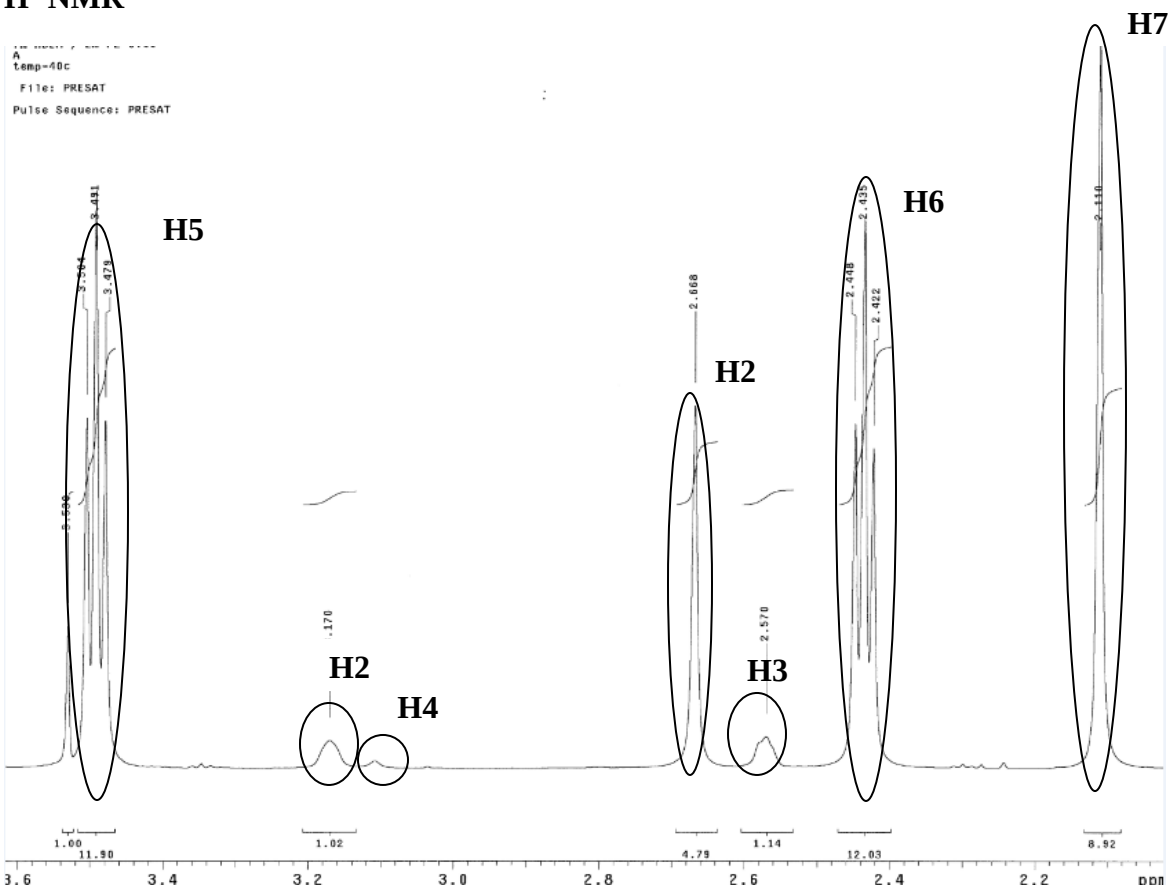

Figure A.19: H^1 NMR Spectrum of 7 m MDEA-2 m PZ-CO_2-H_2O, α = 0.07 mol CO_2/mol total alkalinity, 40 ˚C

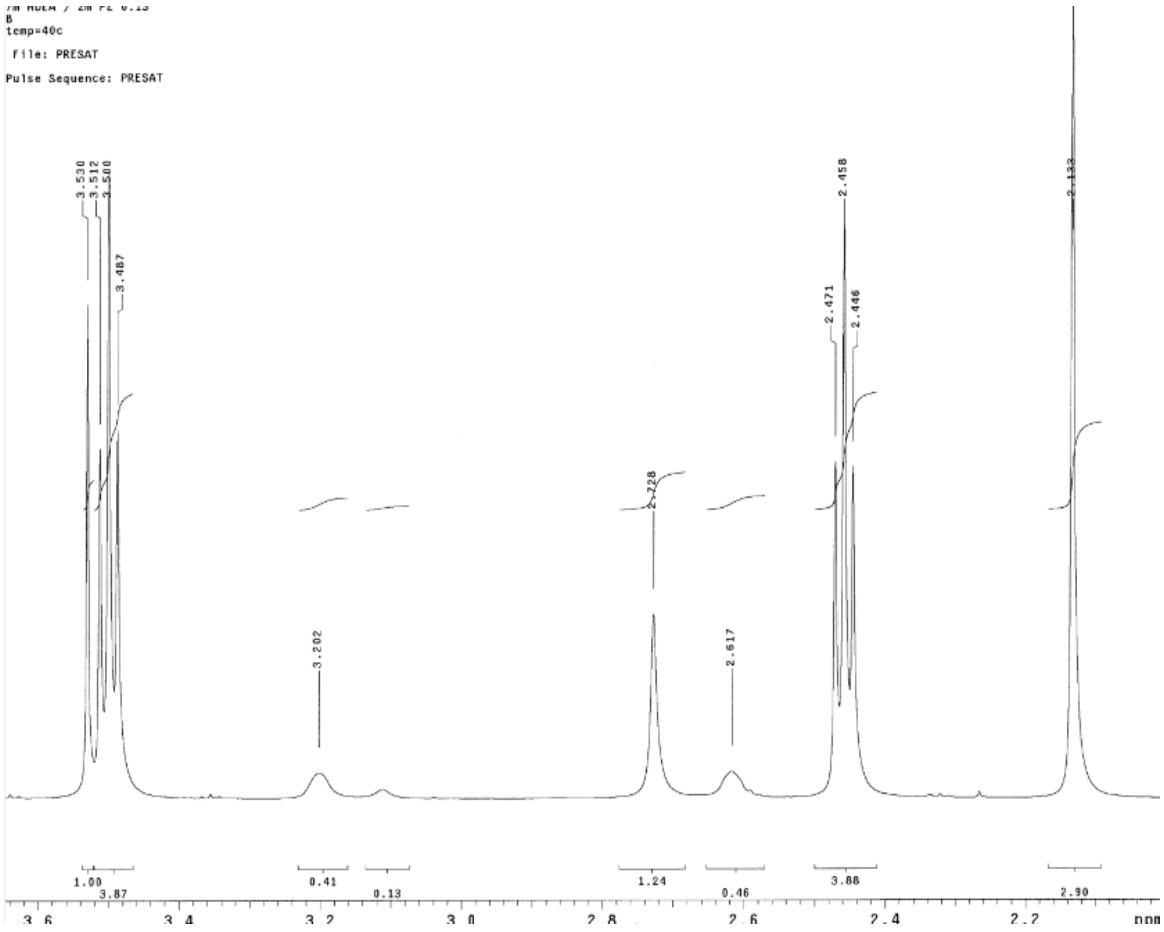

Figure A.20: H^1 NMR Spectrum of 7 m MDEA-2 m PZ-CO_2-H_2O, α = 0.095 mol CO_2/mol total alkalinity, 40 ˚C

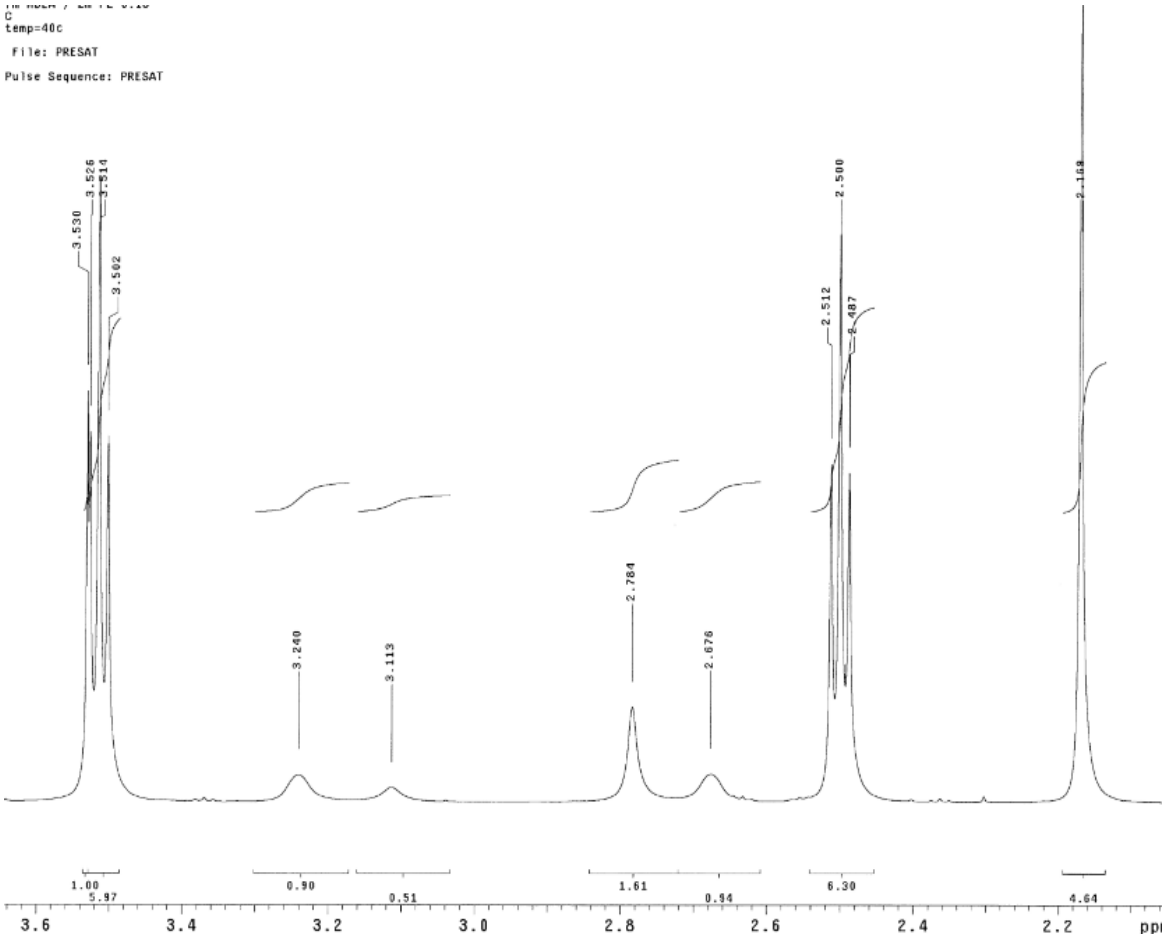

Figure A.21: H^1 NMR Spectrum of 7 m MDEA-2 m PZ-CO_2-H_2O, α = 0.15 mol CO_2/mol total alkalinity, 40 ˚C

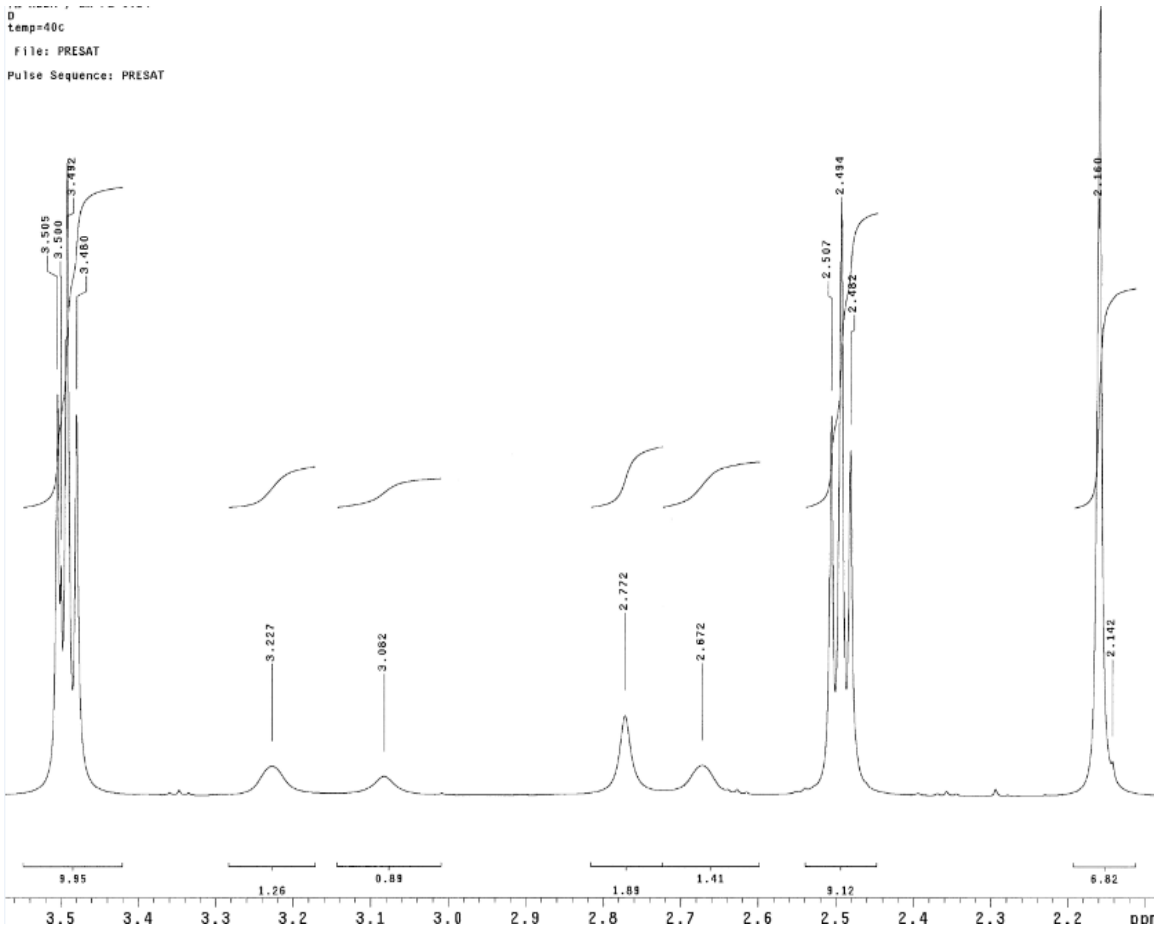

Figure A.22: H^1 NMR Spectrum of 7 m MDEA-2 m PZ-CO_2-H_2O, α = 0.16 mol CO_2/mol total alkalinity, 40 ˚C

C^{13} NMR

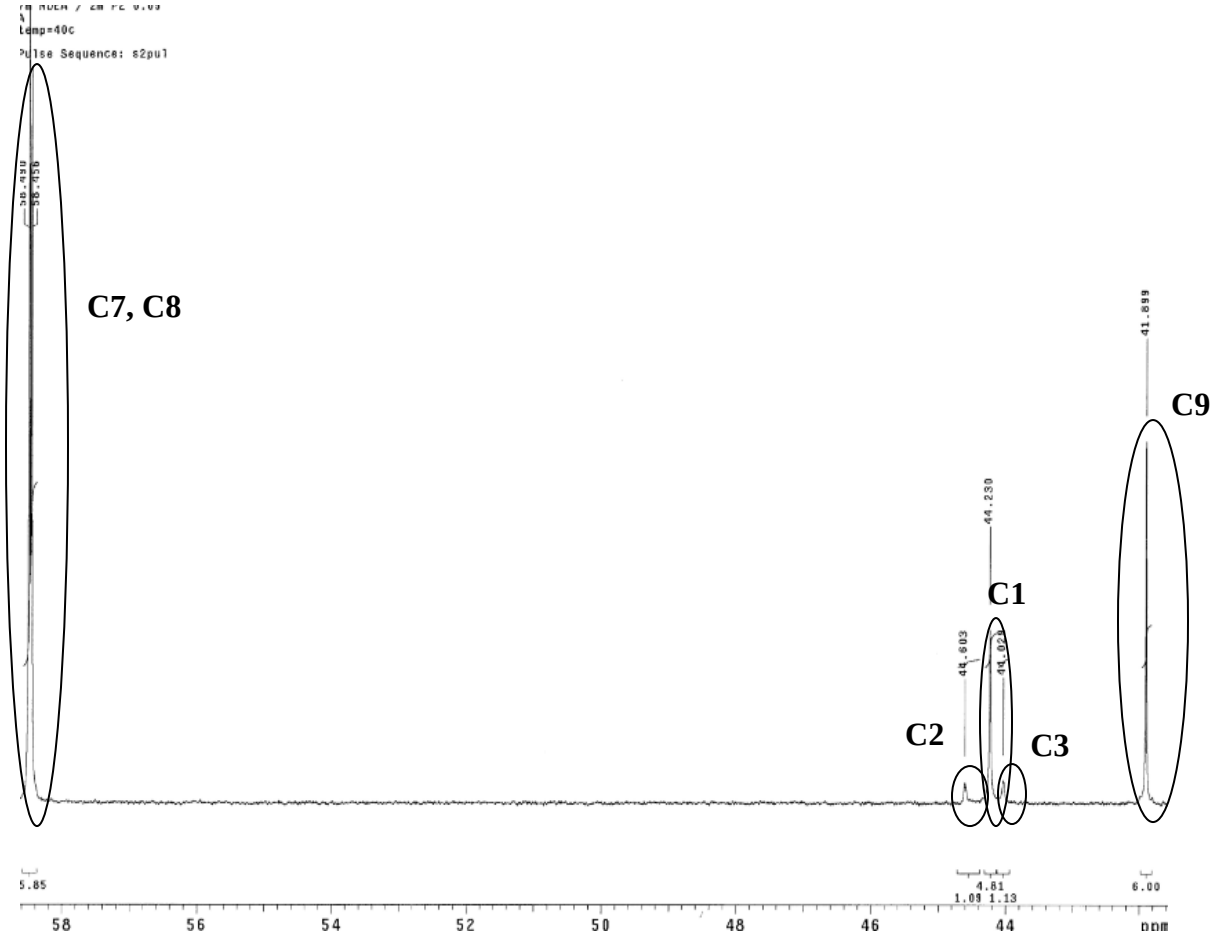

Figure A.23: C^{13} NMR Spectrum of 7 m MDEA-2 m PZ-CO_2-H_2O, α = 0.07 mol CO_2/mol total alkalinity, 40 ˚C (C^{12} peaks)

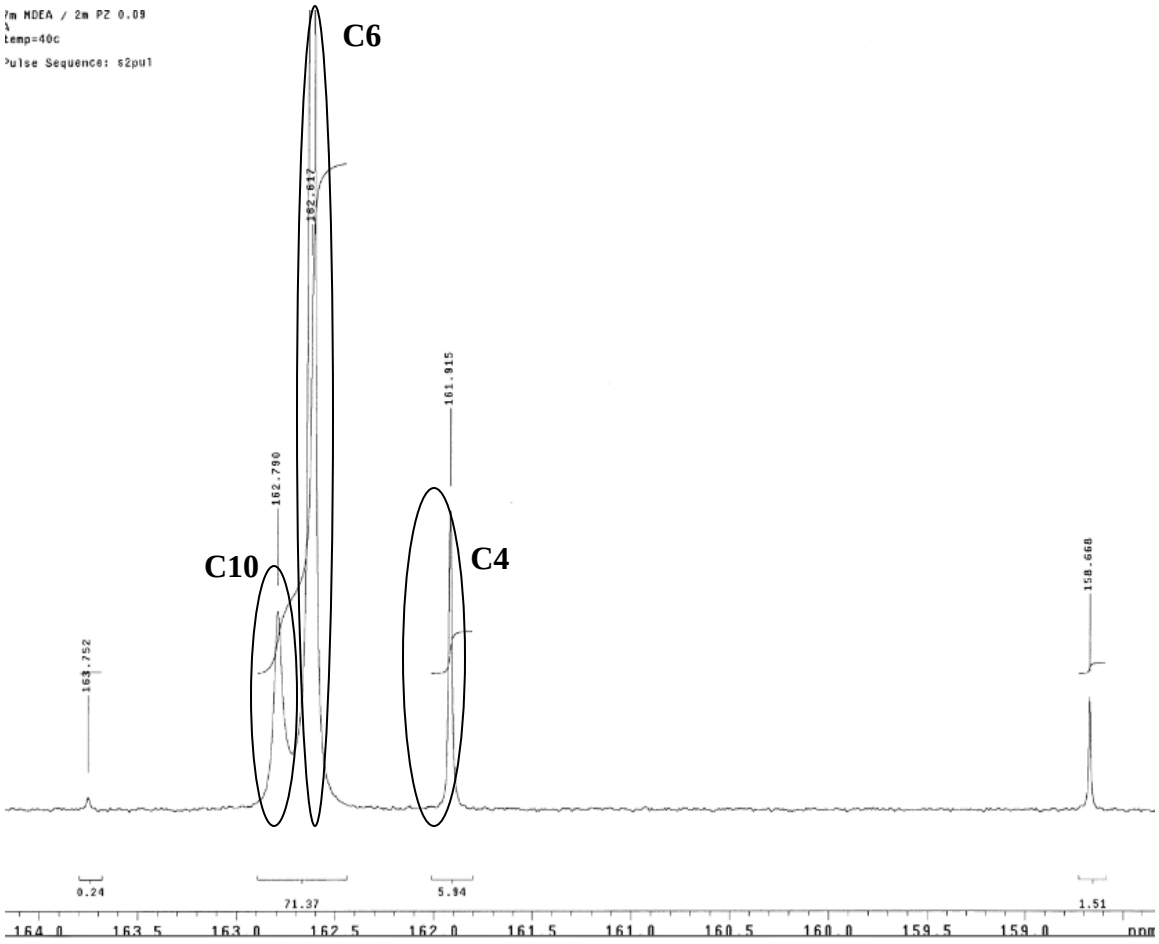

Figure A.24: C^{13} NMR Spectrum of 7 m MDEA-2 m PZ-CO_2-H_2O, α = 0.07 mol CO_2/mol total alkalinity, 40 ˚C (C^{13} peaks)

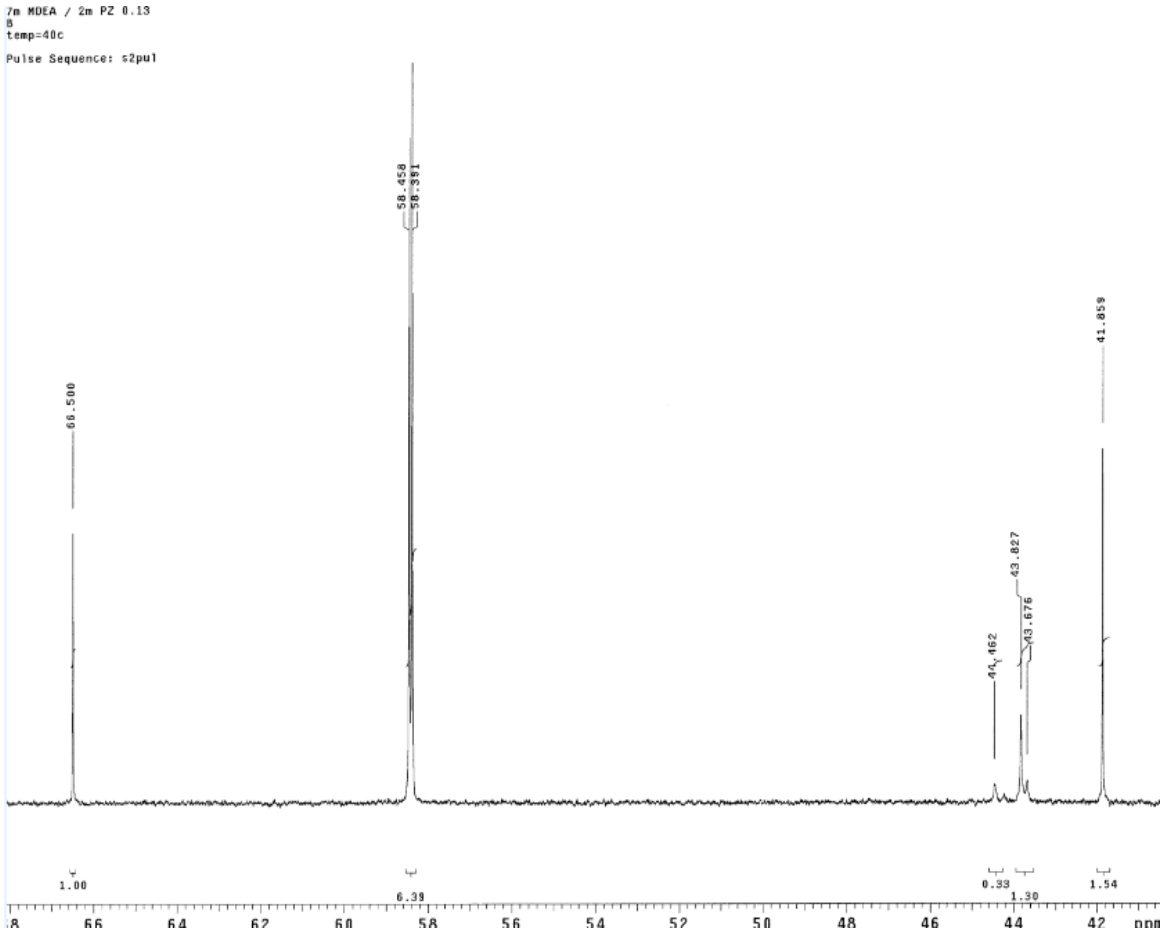

Figure A.25: C^{13} NMR Spectrum of 7 m MDEA-2 m PZ-CO_2-H_2O, α = 0.095 mol CO_2/mol total alkalinity, 40 ˚C (C^{12} peaks)

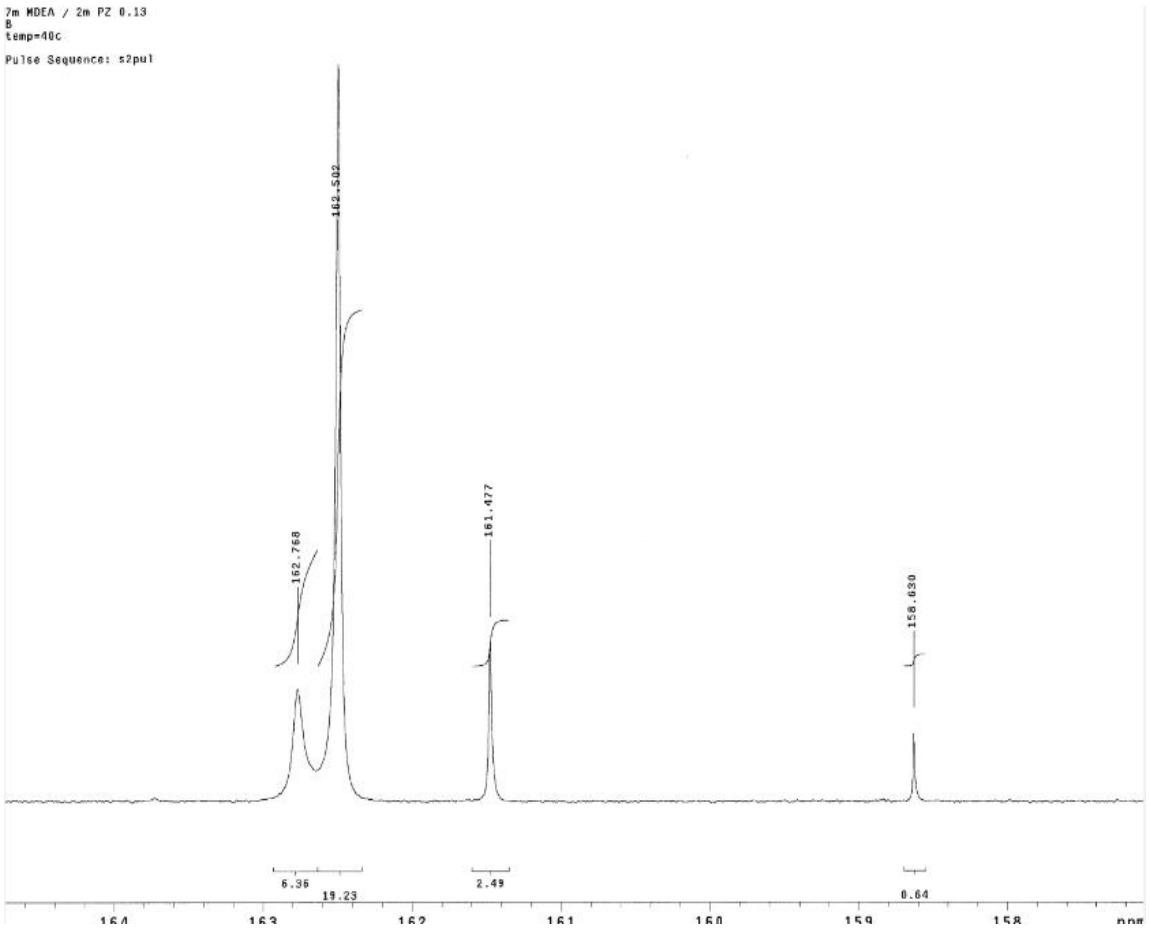

Figure A.26: C^{13} NMR Spectrum of 7 m MDEA-2 m PZ-CO_2-H_2O, α = 0.095 mol CO_2/mol total alkalinity, 40 ˚C (C^{13} peaks)

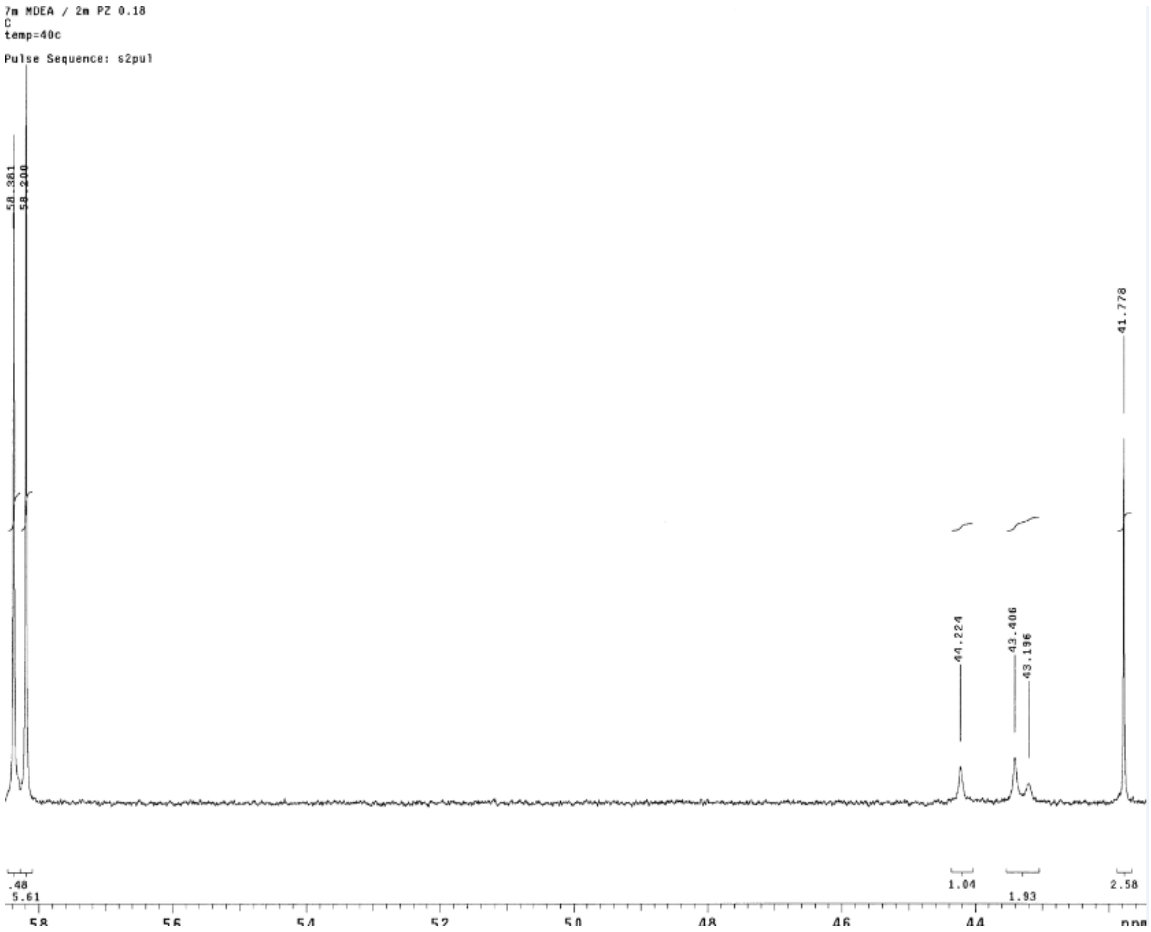

Figure A.27: C^{13} NMR Spectrum of 7 m MDEA-2 m PZ-CO_2-H_2O, α = 0.15 mol CO_2/mol total alkalinity, 40 ˚C (C^{12} peaks)

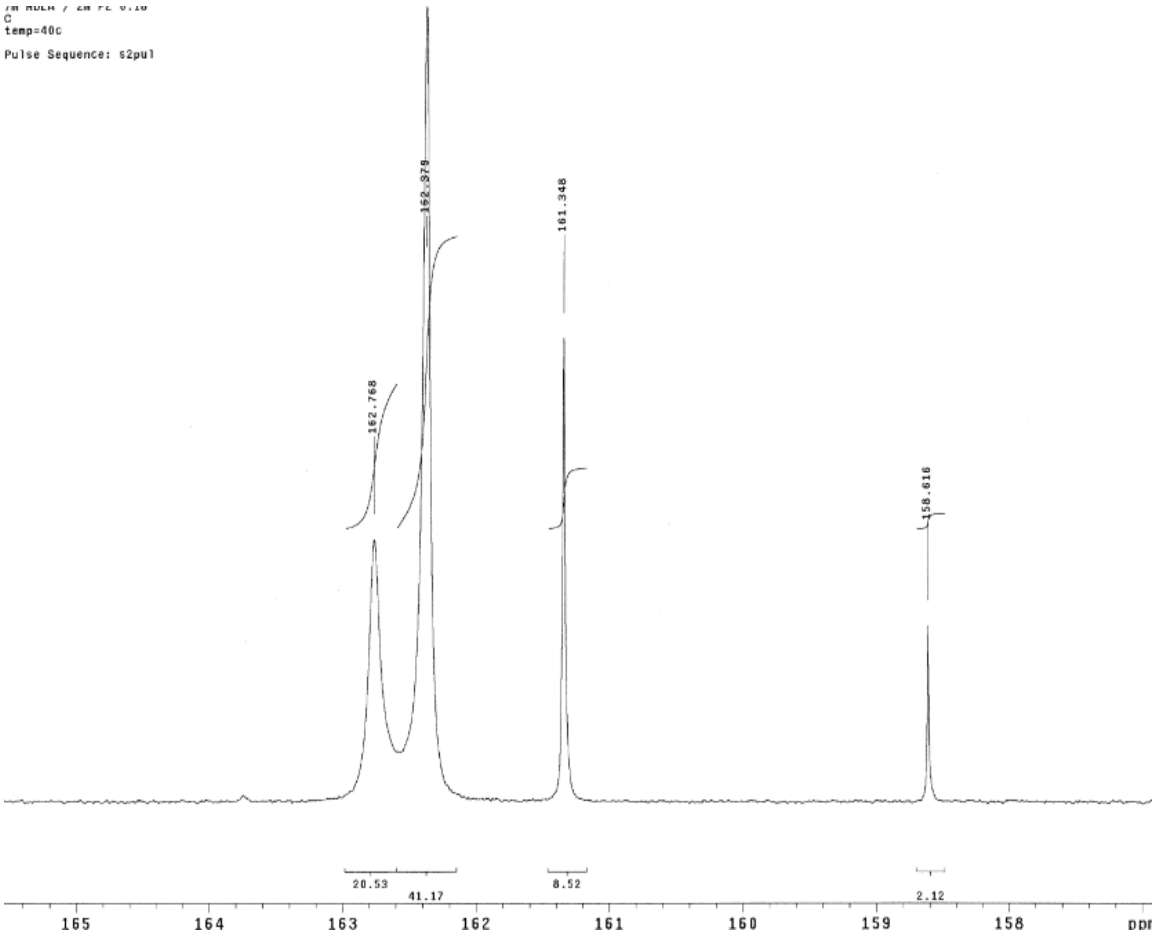

Figure A.28: C^{13} NMR Spectrum of 7 m MDEA-2 m PZ-CO_2-H_2O, α = 0.15 mol CO_2/mol total alkalinity, 40 ˚C (C^{13} peaks)

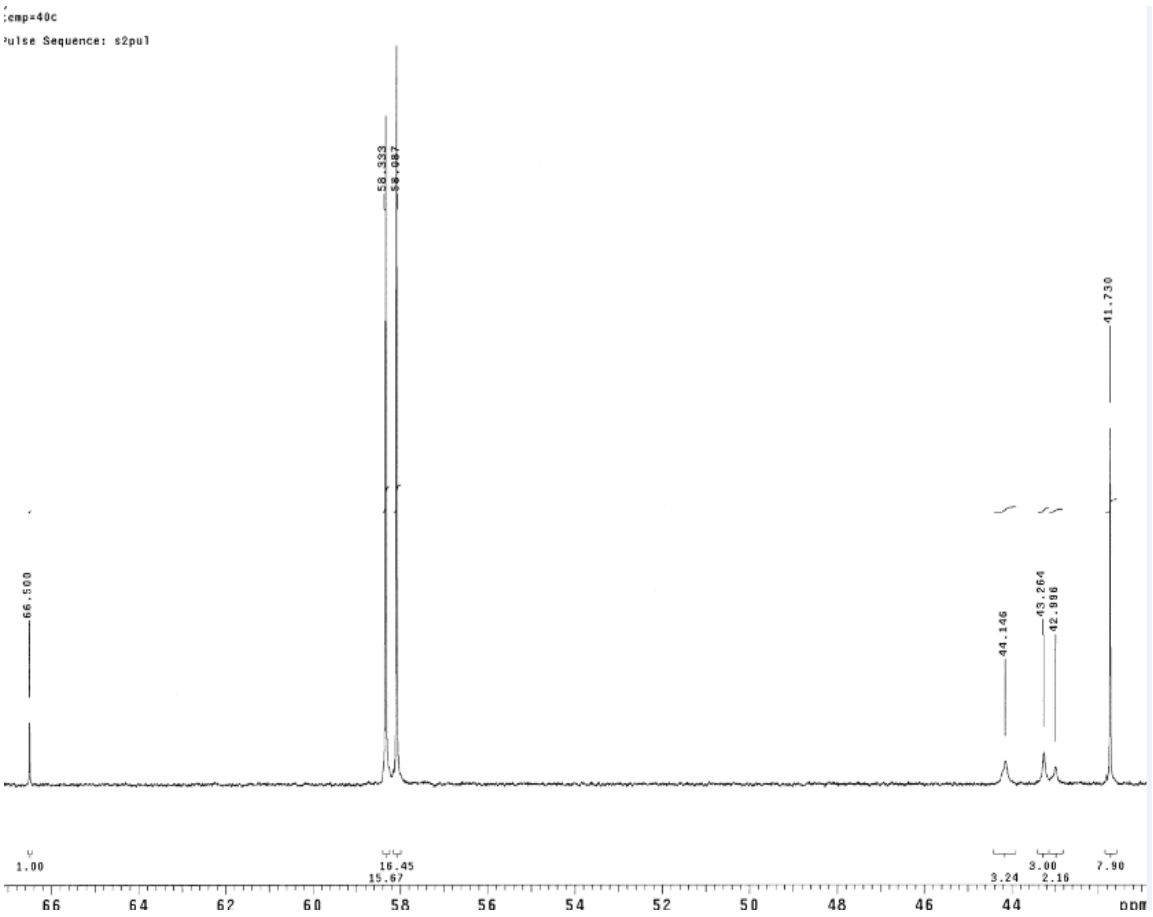

Figure A.29: C^{13} NMR Spectrum of 7 m MDEA-2 m PZ-CO_2-H_2O, α = 0.16 mol CO_2/mol total alkalinity, 40 ˚C (C^{12} peaks)

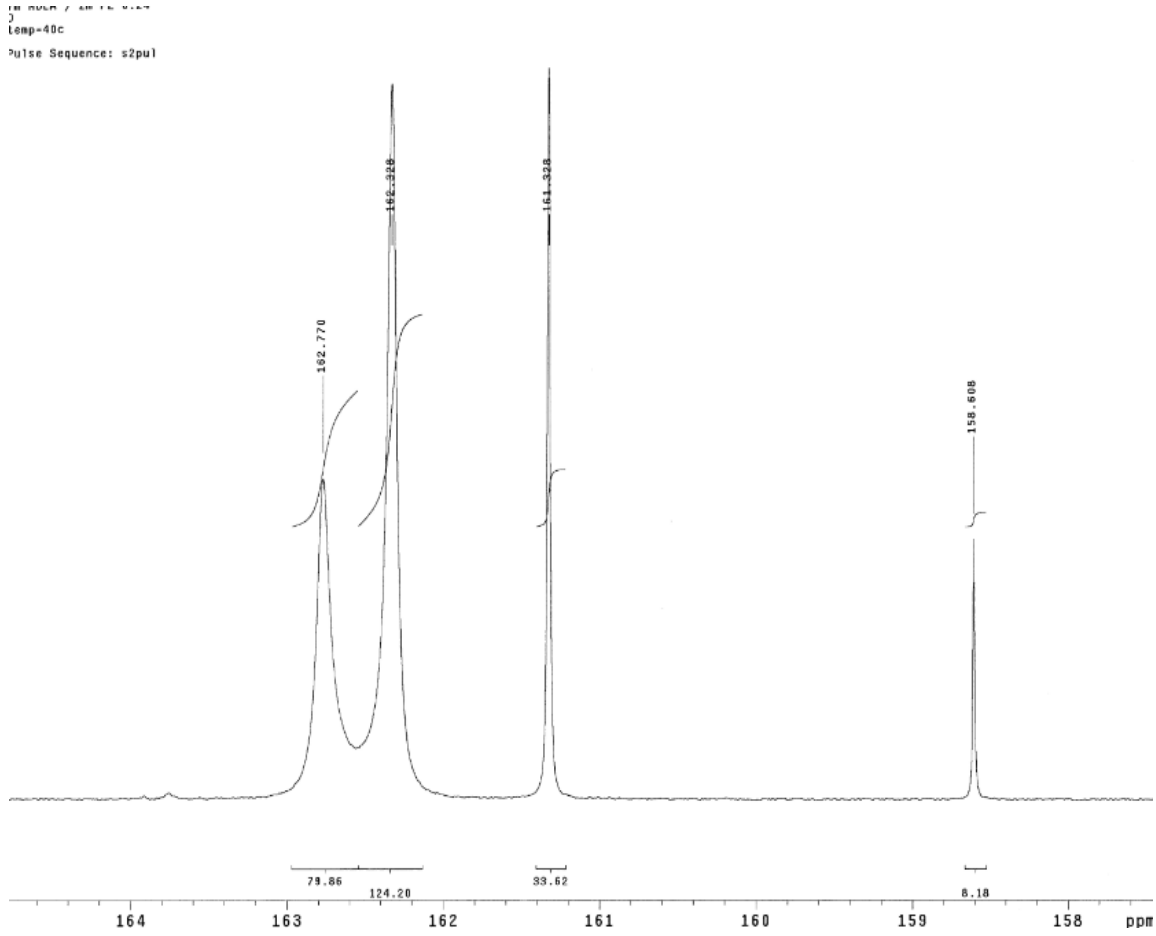

Figure A.30: C^{13} NMR Spectrum of 7 m MDEA-2 m PZ-CO_2-H_2O, α = 0.16 mol CO_2/mol total alkalinity, 40 ˚C (C^{13} peaks)

5 m MDEA-5 m PZ-CO_2-H_2O

H^1 NMR

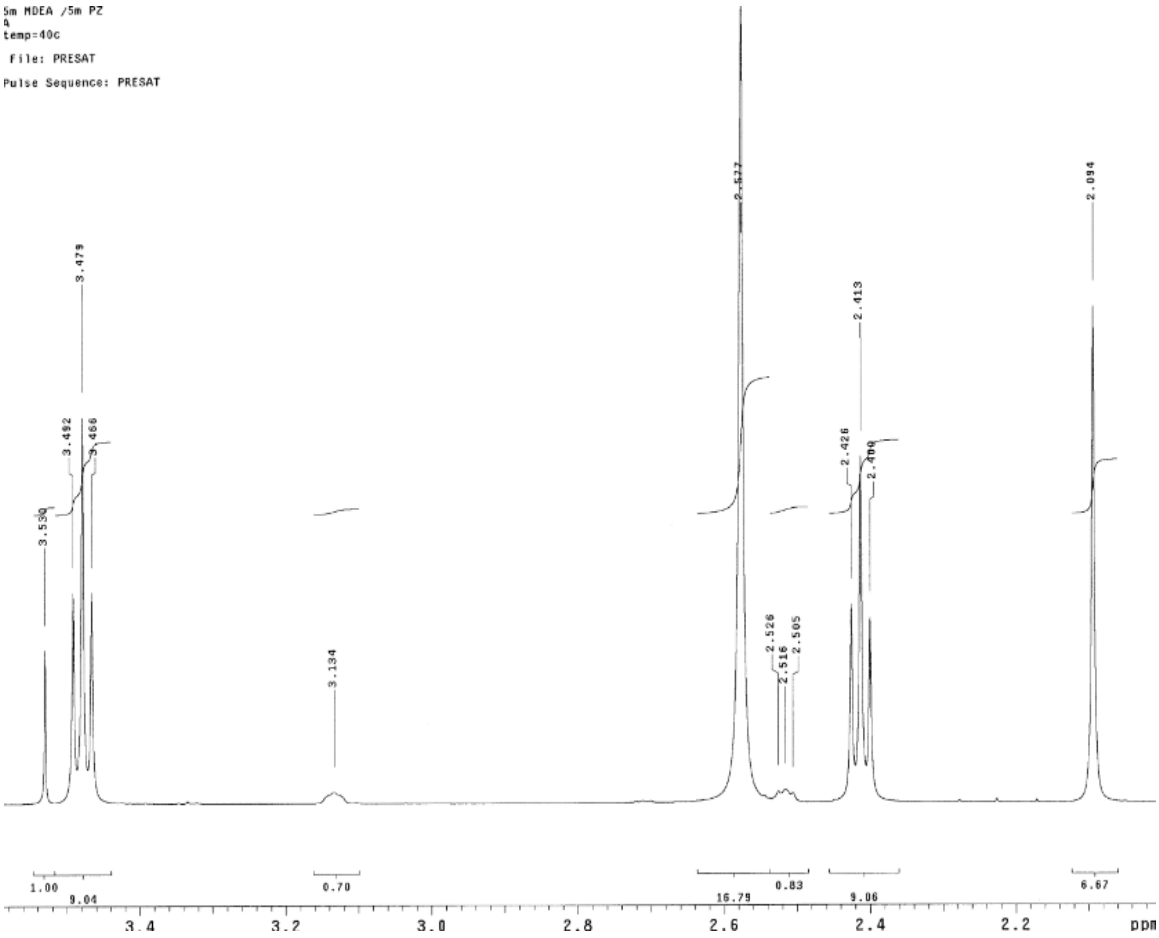

Figure A.31: H^1 NMR Spectrum of 5 m MDEA-5 m PZ-CO_2-H_2O, α = 0.096 mol CO_2/mol total alkalinity, 40 ˚C

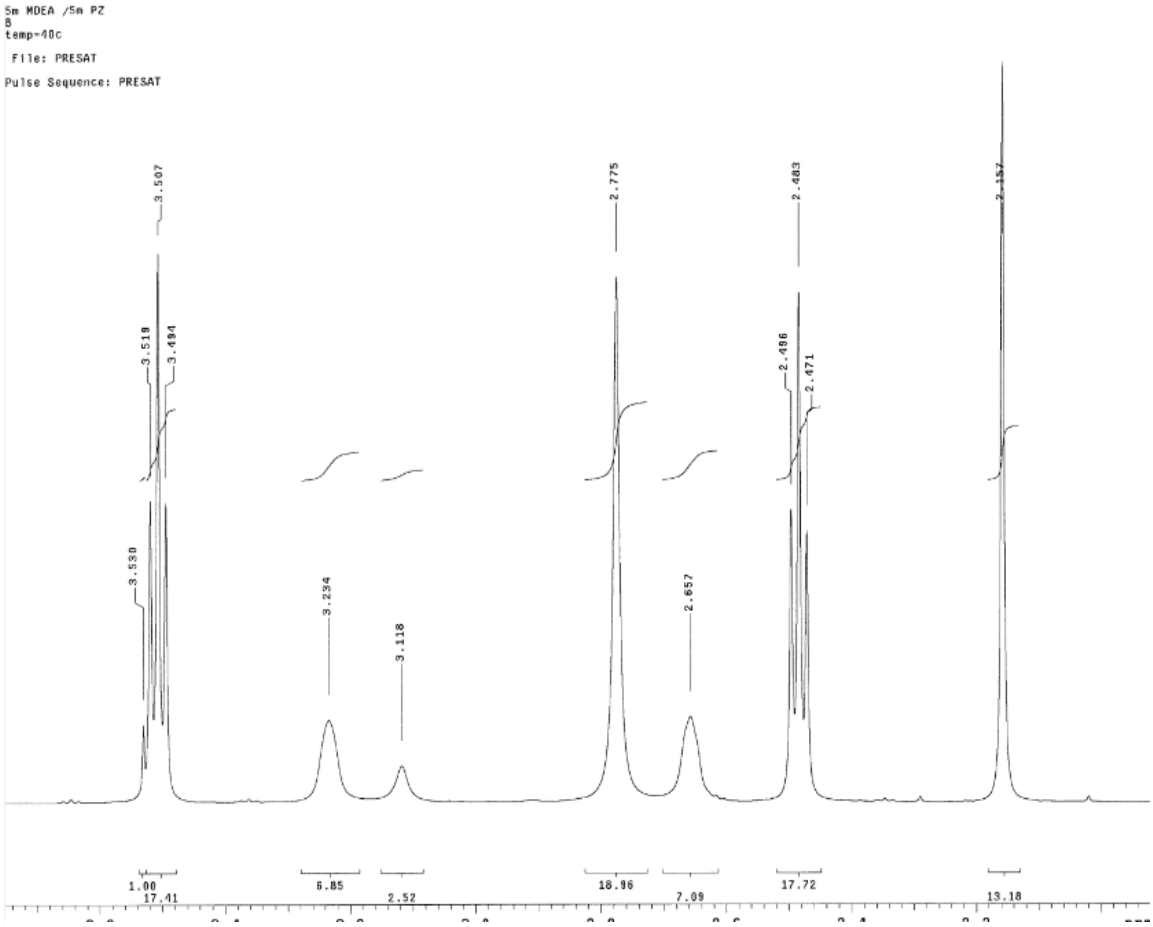

Figure A.32: H^1 NMR Spectrum of 5 m MDEA-5 m PZ-CO_2-H_2O, α = 0.18 mol CO_2/mol total alkalinity, 40 ˚C

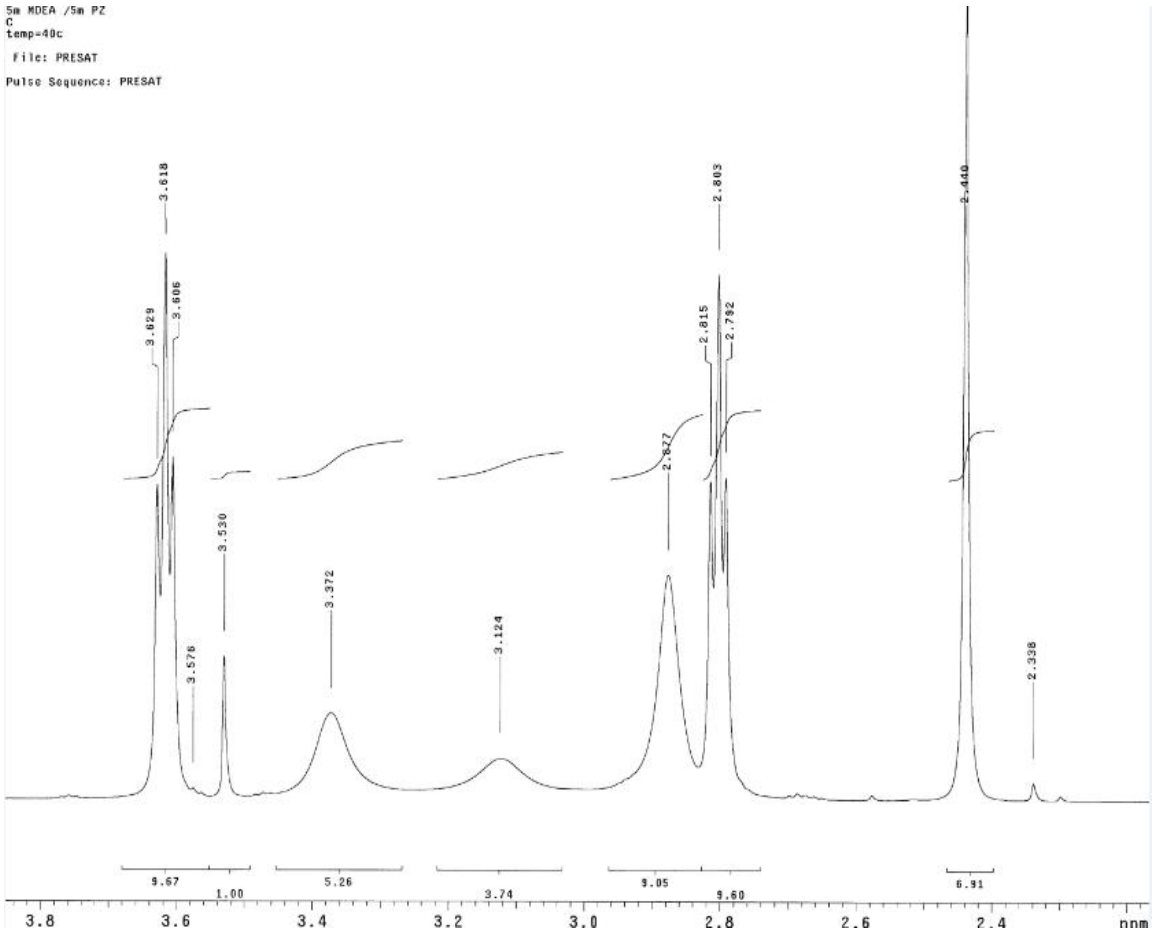

Figure A.33: H^1 NMR Spectrum of 5 m MDEA-5 m PZ-CO_2-H_2O, α = 0.36 mol CO_2/mol total alkalinity, 40 ˚C

C^{13} NMR

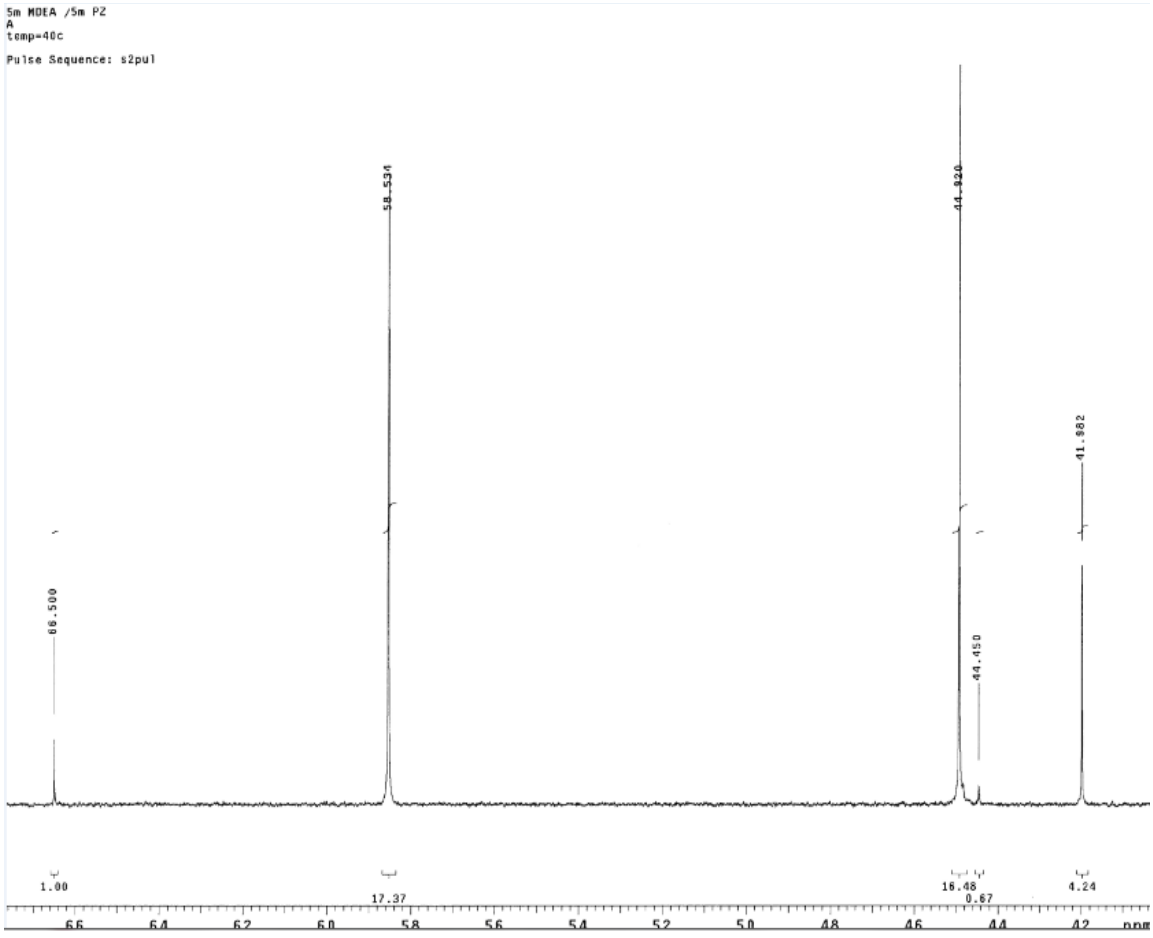

Figure A.34: C^{13} NMR Spectrum of 5 m MDEA-5 m PZ-CO_2-H_2O, α = 0.096 mol CO_2/mol total alkalinity, 40 ˚C (C^{12} peaks)

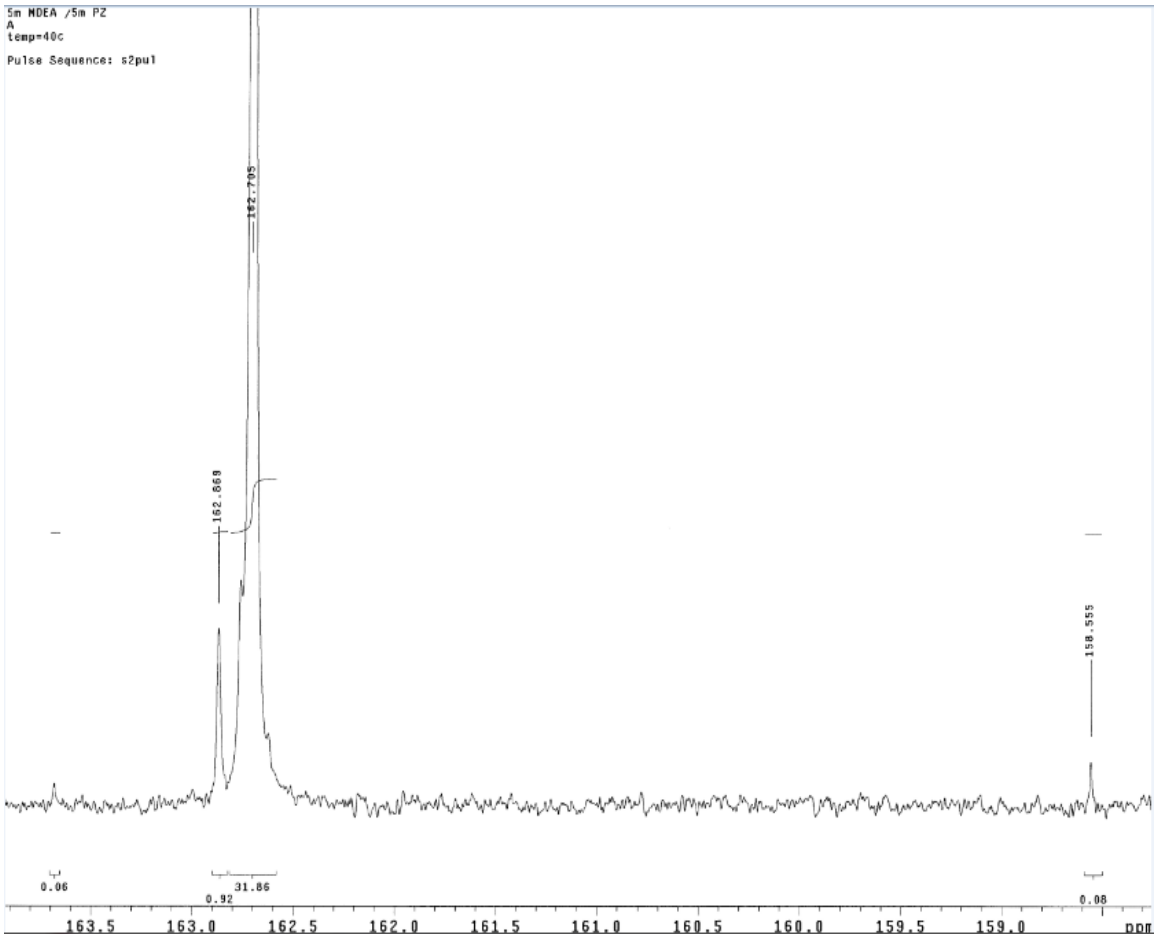

Figure A.35: C^{13} NMR Peaks of 5 m MDEA-5 m PZ-CO_2-H_2O, α = 0.096 mol CO_2/mol total alkalinity, 40 ˚C (C^{13} peaks)

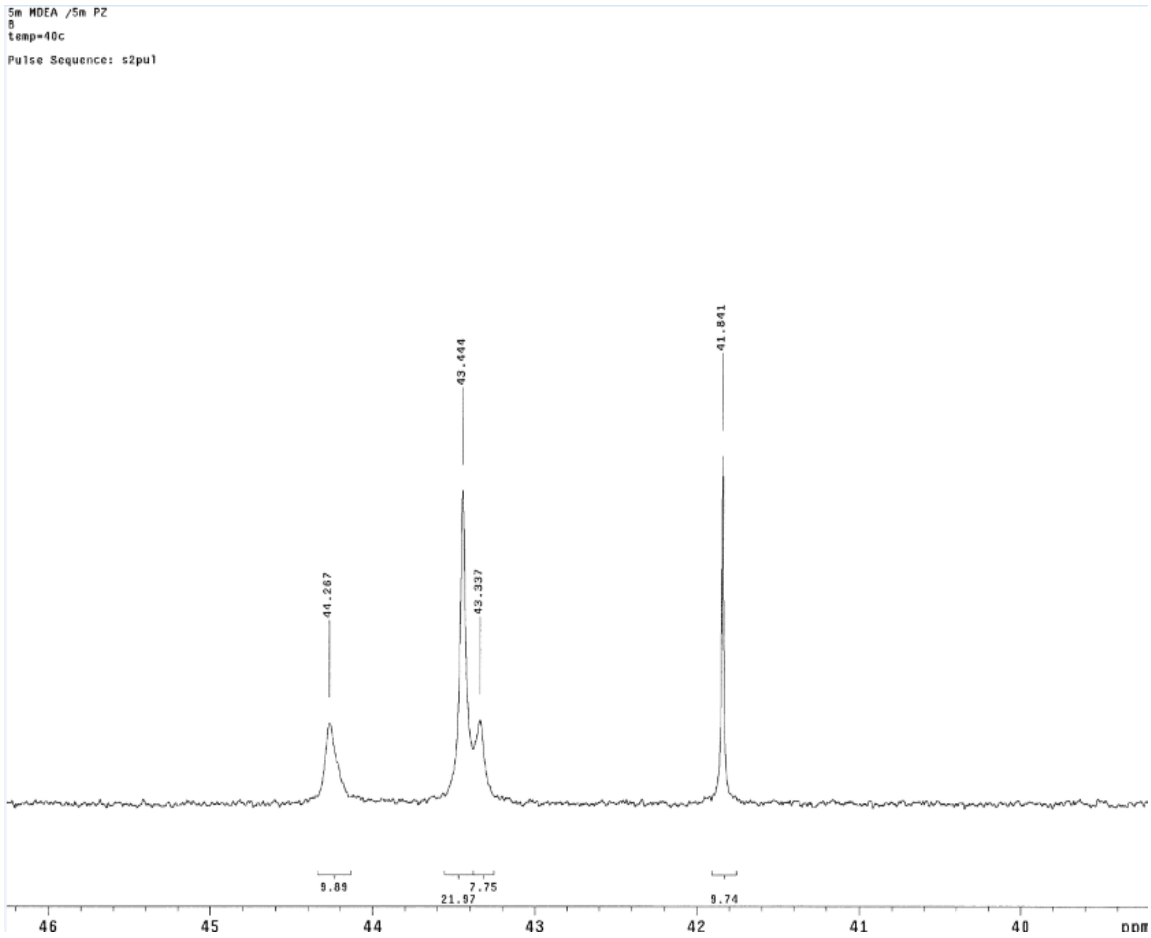

Figure A.36: C^{13} NMR Spectrum of 5 m MDEA-5 m PZ-CO_2-H_2O, α = 0.18 mol CO_2/mol total alkalinity, 40 ˚C (C^{12} Peaks – Part 1)

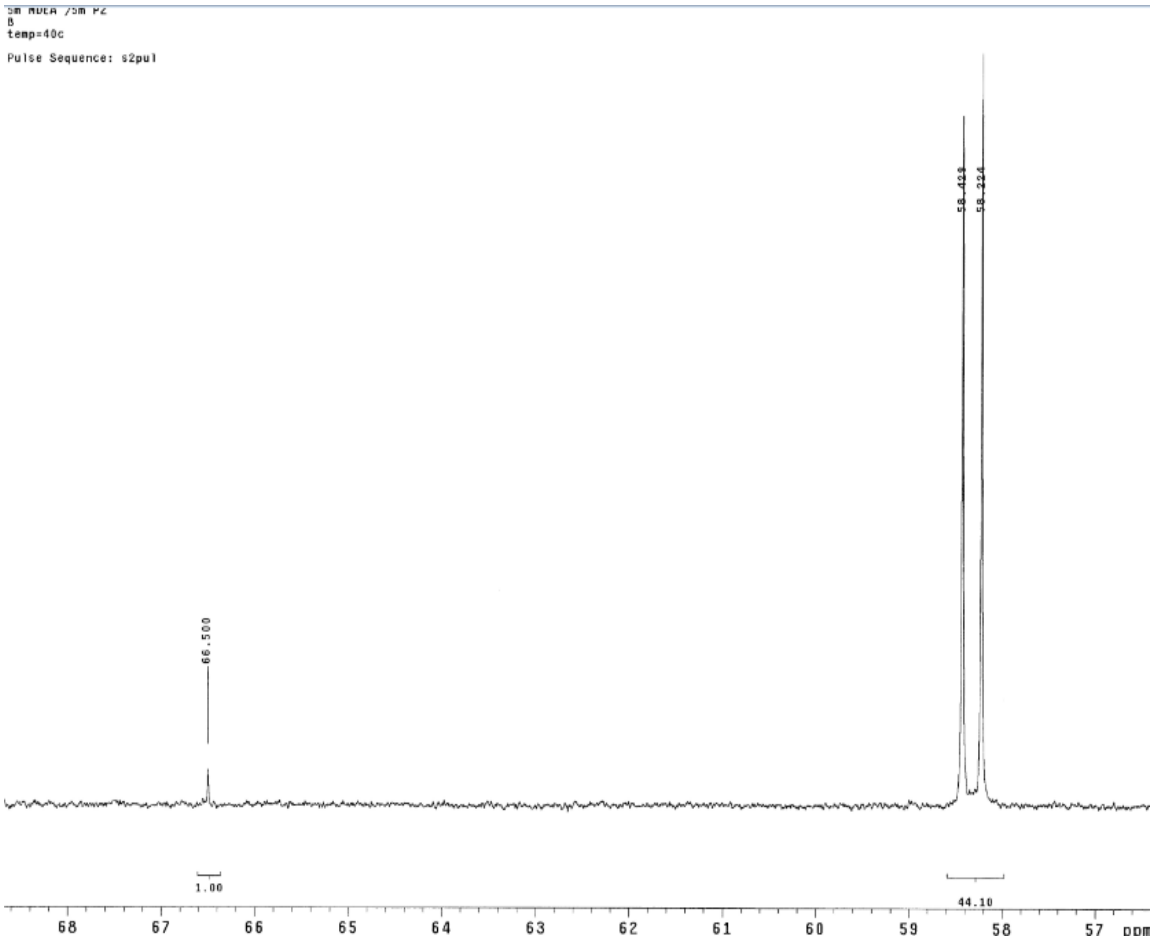

Figure A.37: C^{13} NMR Spectrum of 5 m MDEA-5 m PZ-CO_2-H_2O, α = 0.18 mol CO_2/mol total alkalinity, 40 ˚C (C^{12} Peaks – Part 2)

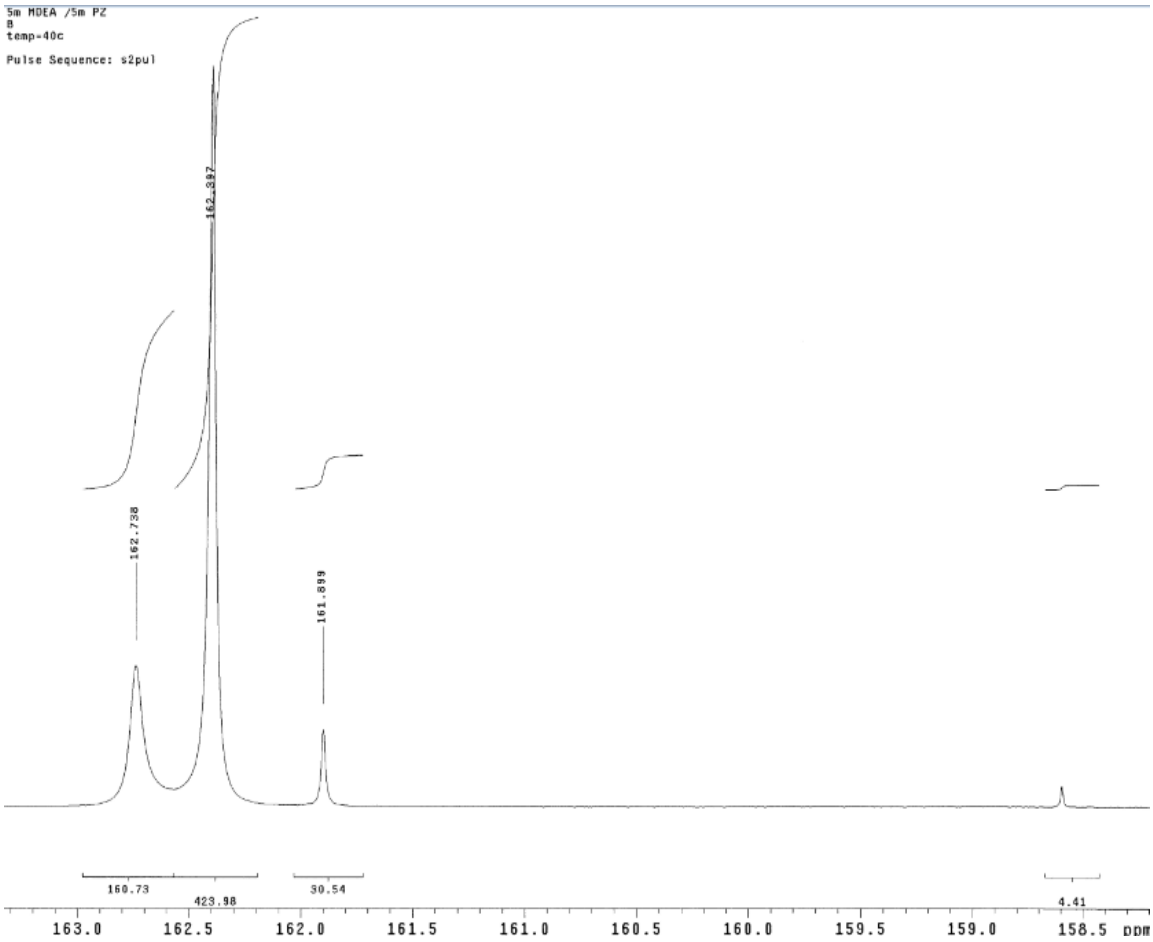

Figure A.38: C^{13} NMR Spectrum of 5 m MDEA-5 m PZ-CO_2-H_2O, α = 0.18 mol CO_2/mol total alkalinity, 40 ˚C (C^{13} peaks)

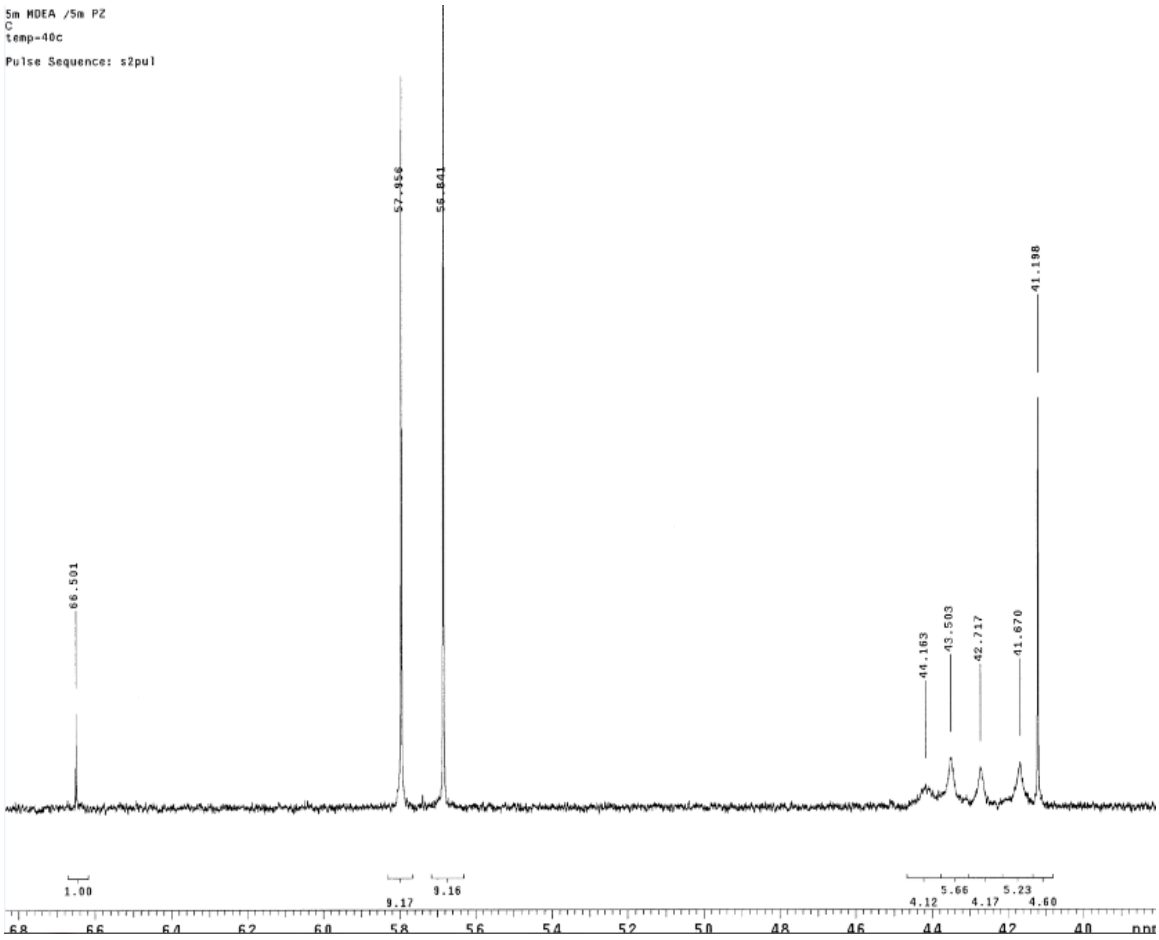

Figure A.39: C^{13} NMR Spectrum of 5 m MDEA-5 m PZ-CO_2-H_2O, α = 0.36 mol CO_2/mol total alkalinity, 40 ˚C (C^{12} peaks)

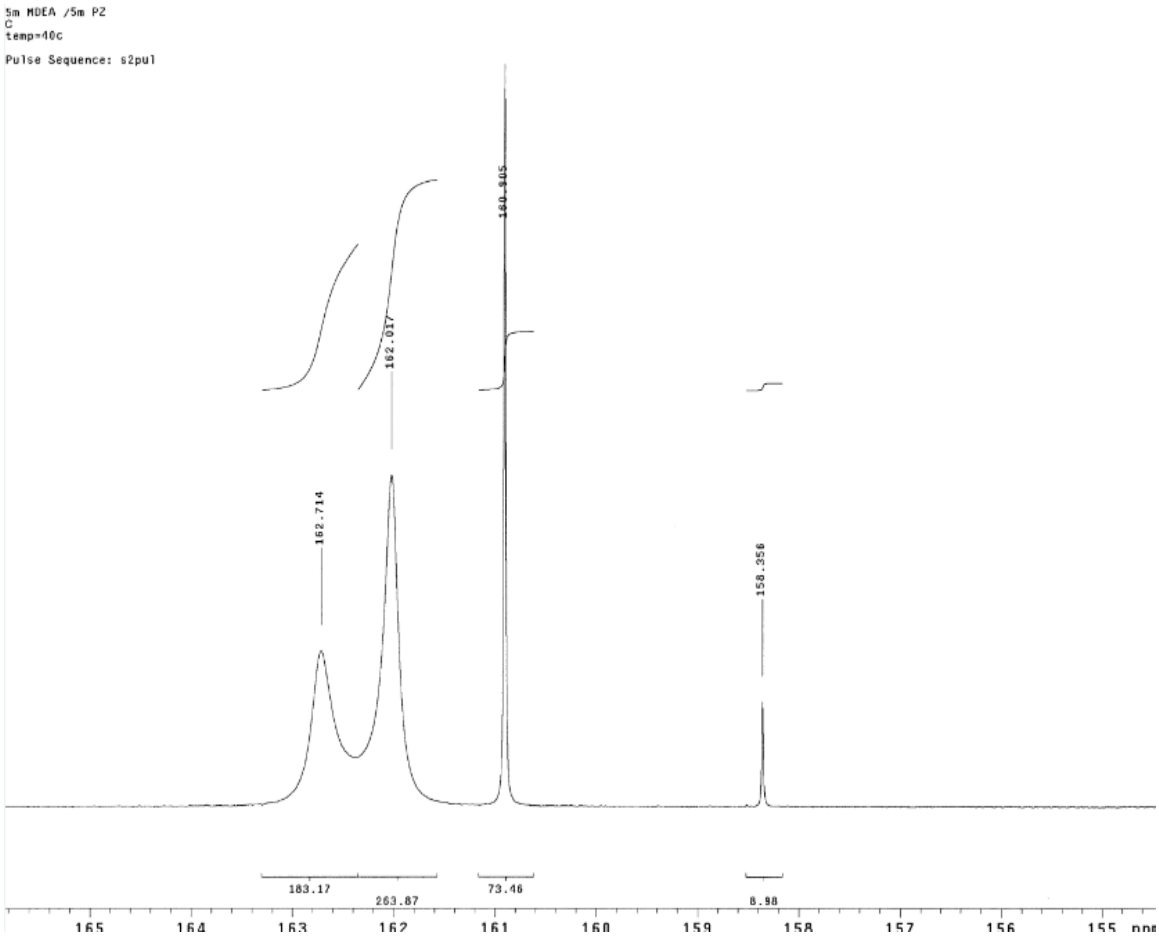

Figure A.40: C^{13} NMR Spectrum of 5 m MDEA-5 m PZ-CO_2-H_2O, α = 0.36 mol CO_2/mol total alkalinity, 40 ˚C (C^{13} peaks)

Appendix B: FTIR Operational Procedure

1. Introduction

The first part of this appendix discusses the procedure for calibrating pure components for FTIR analysis (using the Gasmet DX-4000 analyzer). The latter part describes how to operate the instrument for a standard VLE experimental run.

2. Procedure

Calibration of Pure Components

Pure components that are not already calibrated must be calibrated for FTIR analysis. Calibration must be performed at each desired component concentration (ppm or vol%). The calibration is done by using a Gasmet Calibrator Device that is specially designed to calibrate pure components for Gasmet FTIR analyzers. Figure B.1 shows the Gasmet Calibrator device.

Figure B.1: Gasmet Calibrator

The Gasmet Calibrator setup consists of a syringe pump, manual needle valve, mass flow controller, and a stainless steel injection chamber.

The procedure for setting up the calibrator to work in conjunction with the analyzer is provided below. Note that the FTIR pump module must be disconnected from the analyzer to free up the analyzer inlet and outlet sampling ports. The inlet sampling port of the analyzer is to be connected to one end of the calibrator umbilical line. The outlet sampling port on the analyzer is to be connected to a plastic PTFE vent line which is used to exhaust amines into the hood.

1. Flow N_2 into the calibrator by connecting a PTFE line from the N_2 dispenser on the wall to the designated N_2 port in the calibrator. To begin ensure that the N_2 flow is ~2

SLPM, with as little fluctuation as possible, as indicated by the digital flow indicator in the calibrator.

2. Connect one end of the calibrator umbilical line to the outlet of the heated oven chamber. Connect the other end of the umbilical line to the inlet sampling port of the analyzer.

3. Set the temperature of both the umbilical line and of the heated oven chamber to 180 ˚C. This is to prevent any species from condensing on the internals of the line and apparatus. Do not perform any calibration injection until the setpoint of 180 ˚C is reached.

Figure B.2. shows the internal calibrator setup as it is connected to the FTIR analyzer.

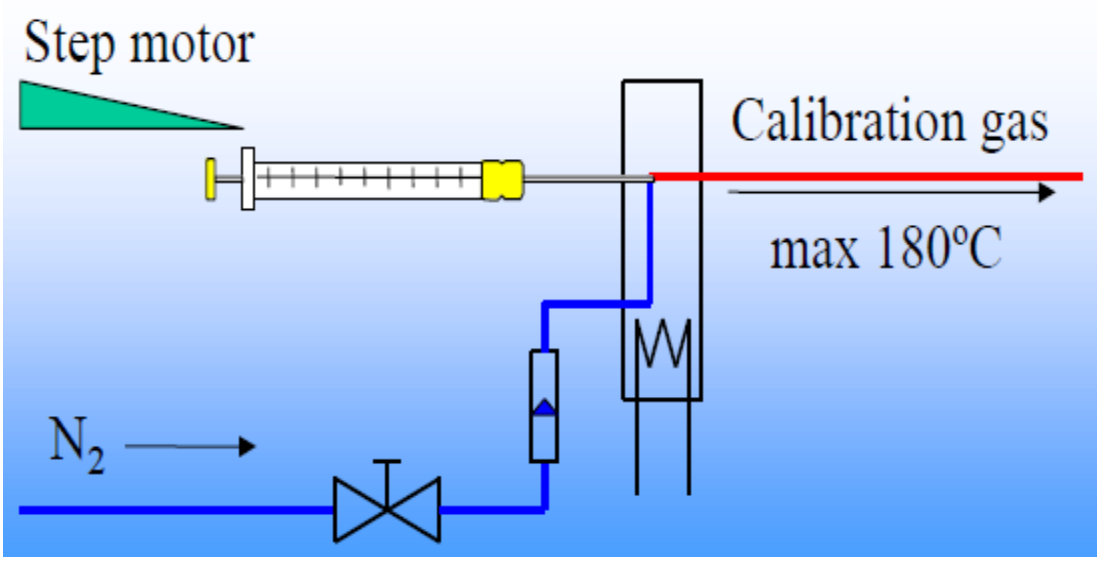

Figure B.2: Internal Gasmet Calibrator Setup

4. Prepare the component to be injected for calibration. Fill up a Hamilton gastight syringe with the component of interest to be calibrated. The concentration at

which the component will be injected into the calibrator will be determined by the rate at which the component is to be injected (μL/hr) relative to the N_2 carrier flow. Calculate the appropriate injection rate relative to the N_2 flow rate to obtain the desired calibration concentration. Note that the N_2 flow rate can be varied from 0.5 up to ~5 SLPM; however, it is not recommended to flow N_2 at too low or too high of a flow rate to avoid frequent flow rate fluctuation.

5. Inject the calibration component into the heated oven inlet of the calibrator at the appropriate injection rate as calculated. The injection rate is set by manually selecting the flow settings in the calibrator flow display. Also ensure that the slider block is properly rested against the syringe to secure the needle.

6. Set the N_2 flow rate to the desired flow to achieve the component flow concentration to be calibrated.

7. Observe the FTIR Calcmet live display of spectrum analysis. The display should be showing no actual spectral feature, but only spectral noise, in the beginning even after the component is injected as only N_2 is flowing through the system at this point. As the component is vaporized inside the heated chamber and is beginning to flow into the analyzer, distinct spectral peaks should visibly emerge on the analysis window. Some components may take longer than others to start showing peaks.

8. The peak signal should increase substantially with time even though it may fluctuate somewhat due to flow irregularity. Ensure that the frequency of FTIR analysis scan is set to every 5 second in order to observe the live changes in spectral peak formation. Let the system equilibrate for as long as it takes, usually 20 – 30 minutes,

until the peak equilibrates to roughly a final constant value (peak height is seen to change on the order of a hundredth or thousandth of a decimal).

9. When the peak height is relatively stable, set the FTIR scan frequency to 3 minutes to do a full peak integration.

10. Once the scan (integration) is completed, a reference spectra would have been generated for the component at the desired concentration to be calibrated. Save this spectra as a calibration spectra type (.REF) to be included in the Calcmet component library. Specify the calibration conditions of the run (temperature and concentration) as exactly as can be determined.

11. Repeat steps 4 – 10 to perform calibration for the same component at a different concentration or for a different component. The reference concentration range should ideally encompass the actual concentration range that is expected to be encountered in an actual experiment.

Operation of the FTIR and Maintenance

The procedure below describes the steps taken to perform a VLE run on the FTIR Gasmet DX-4000. Before any experiment is run, ensure that the umbilical lines, pump modules, and analyzer are heated up to 180 ˚C and that a clean N_2 background spectra (~5 min. scan) is detected. It usually takes about 30 – 45 minutes to heat the lines to 180 ˚C.

1. Prepare about ~525 – 550 g of the solution mixture to be studied. If it is intended to study VLE at a given loading, then the solution needs to be loaded with CO_2 up to the desired loading prior to running the FTIR experiment.

2. Pour the solution mixture into the jacketed glass reactor. Wrap aluminum insulation material around the reactor completely to prevent heat loss. Figure B.3 shows the jacketed glass reactor used for VLE experiments.

Figure B.3: Jacketed 1000 mL Glass Reactor used for VLE Experiments

3. Set the bath temperature to the desired experimental temperature (eg. 40 ˚C). This bath temperature setpoint should ideally be $T_{experiment}$ + 0.3 ˚C to compensate for potential heat loss.

4. Insert a digital thermometer into one of the sealed ports on the reactor. Introduce N_2 from the back wall via the smallest port on the reactor. This N_2 serves to sweep out air from the headspace of the solution. Keep the N_2 off for now. Ensure that the back port is properly connected to the water trap.

5. Connect the plastic line and fittings from the remaining port on the reactor with the FTIR umbilical line. Ensure that both the FTIR pump and line are set to 180 ˚C. Do not run any experiment if these settings are below 180 ˚± 2˚C.

6. Connect the return umbilical line to the reactor outlet. Make sure that this line is set to $T_{reactor}$ + 55 ˚C to prevent the returning gas from experiencing heat loss which could upset equilibrium conditions in the reactor.

7. Turn on the agitator to a mixing speed of 350 ± 5 rpm. Use the tachometer to verify that the mixing speed is as specified.

8. Turn on the FTIR pump. Also start the FTIR analysis scans (on Calcmet software) with the 20 seconds scan for the beginning of the experiment.

9. Turn on N2 flow into the reactor for about 2 – 3 scan duration. This ensures that the headspace of the reactor is fully evacuated.

10. Turn off the N_2. Change the FTIR analysis scan rate to 1 minute for each scan duration. Specify the components that are known to be in solution (eg. water, amine, CO_2). Make sure that there are reference spectra available for each component of interest in the library method.

11. Allow for the experiment to run continuously up until the desired experimental temperature is reached (eg. 40 ˚C). Given the standard heating rate of the temperature bath, it should take ~ 1 hour to reach the desired experimental temperature when starting from room temperature. Make sure that the digital thermometer reads that the solution temperature has reach the desired target.

12. Record the equilibrium component concentrations from Calcmet. These concentrations are the equilibrium concentrations of components in the gas phase. They are used to determine the component volatilities at the experimental temperature.

13. Obtain a reading of the room pressure and record it. The room pressure is the total pressure of the experiment. This number is also used to calculate the equilibrium volatility.

14. Increase the water bath temperature to the next desired experimental temperature. It is recommended to run experiments for every $\Delta T = 5$ ˚C from 40 ˚C – 70 ˚C (represent the absorber operating temperature).

15. Increase the temperature of the return umbilical line by 5 ˚C to match the increase in water bath temperature. Maintain this new temperature for the return line for the duration of this next run.

16. Save the data under a new file and resume the 1 minute analysis scans.

17. Run the experiment continuously until the desired experimental temperature is reached (eg. 45 ˚C). Stop the analysis scan and record the equilibrium concentrations.

18. Repeat steps 13 – 16 until the final desired temperature is reached. On a typical day, about 6 – 7 runs can be performed for temperature 40 ˚, 45 ˚, 50 ˚, 55 ˚, 60 ˚, 65 ˚, 70 ˚C.

19. After the final experiment of the day, drain out the content of the reactor and dispose of properly in designated waste container. Disconnect all the lines from the reactor ports. Make sure that the all the reactor ports are open to dry overnight.

20. Wash the interior of the reactor with ~1 gallon of distilled de-ionized water to properly rinse it.

21. Lower the FTIR analyzer and line setpoints to 25 ˚C. This step is taken for maintenance purposes to extend the life of the line and parts.

Cleaning the Umbilical Lines

It is recommended that the umbilical lines be cleaned every 2 – 3 weeks, or perhaps even more frequently if there is excessive trace contaminants expected to build up in the lines.

1. Disconnect the umbilical line from the inlet of the FTIR analyzer. Also disconnect the return umbilical line from the back of the FTIR pump module. Connect one end of the umbilical line to that of the return umbilical line so that form one long continuous flow path.

2. Set the temperature of the umbilical lines to ~150 ˚C. Hot temperature enhances cleaning and it helps to dry the lines faster after cleaning.

3. Connect a long ptfe line from the lab sink faucet to the free end of the umbilical line. The free end of the return umbilical line should be directed into an empty bucket.

4. Turn on the lab sink water and let flow through the connected umbilical lines. Allow water to flow for ~30 minutes to properly rinse the lines.

5. Turn off the water. Connect the free end of the umbilical line to an air source to blow dry the lines. Ensure that the lines are still heated at 150 ˚C. Let the air blow through the lines for ~1.5 – 2 hours to ensure they are dried thoroughly.

6. Turn off the air and connect the umbilical and return lines to their appropriate ports on the analyzer and the pump module.

Appendix C: Heat Capacity Experimental Procedure & Analysis

1. Introduction

Heat capacity measurements were needed for rigorous thermodynamic modeling of amine systems, which ultimately becomes the key to proper process equipment design. In this work, heat capacity was measured using a Differential Scanning Calorimeter (DSC) from TA Instruments (model Q100) with automated controls provided by TA Explorer DSC software . The following sections describe the experimental procedure for obtaining heat capacity data along with how to analyze them.

2. Procedure

The following heat capacity procedure, which includes sample preparation, is in accordance with standard ASTM Method E 1269-05 for determining heat capacity.

Preparing samples for C_p measurements

Four standard cells (reference, blank, Indium, Aluminum Oxide Al_2O_3) will have to be prepared for any heat capacity experiment. Below is the procedure to prepare these cells.

1. A cell consists of a pan, lid, and O-ring (Perkin Elmer #03190218 – 304 stainless steel with capacity of 60 μL). Weigh the pan, lid, and O-ring separately and record their individual weights for the four cells.

2. Insert the O-ring into the lid of each cell. Make sure that the O-ring is properly tucked inside the lid.

3. With the reference and blank cells, join the lid and pan together to make a cell by using a Perkin Elmer Quick Press #0990-8467 device. When the cell has been

properly sealed, it is guaranteed to be able to withstand up to 150 bars of internal pressure. Record the weights of the reference and blank cells.

4. Fill the Indium pan with ~5 mg of Indium sample. Join the Indium pan and its lid to make the Indium cell. Record the weight of the Indium cell. Subtract this weight from the total initial weight of its parts to determine the exact quantity of Indium in the cell.

5. Fill the Al_2O_3 pan with ~120 mg of Al_2O_3 (Acros Organics, #40 sieve, 99.98 – 99.99% pure). Join the Al_2O_3 pan and its lid to make the Al_2O_3 cell. Record the weight of the Al_2O_3 cell. Subtract this weight from the total initial weight of the parts to determine the exact quantity of Al_2O_3 in the cell.

In regard to the sample cells, it is recommended that 4 sample cells are prepared for each given loading. The need to have as many as 4 replicates of the same sample is to ensure greater data reproducibility which accounts for fluctuations in the machine's calorimetric response.

6. Fill a given sample pan to the top (total capacity ~60 μL) with the sample solution. Join the sample pan and its lid to make the sample cell. Record the weight of the sample cell. Subtract this weight from the total initial weight of the parts to determine the exact quantity of sample in the cell.

7. Repeat step 6 to make as many cells as needed (4 cells for each loading). Place each cell inside a multi-cell container box and label each cell box with a number to distinguish among the samples. Do not contaminate the cell with any type of residue as this will affect the calorimetric measurement of the sample.

Measuring Sample Heat Capacity (on DSC Q100)

1. Start N_2 flow from the cylinder into the DSC instrument. Set the N_2 tank discharge pressure at ~10 psia.

2. On the TA Explorer screen, select the N_2 flow rate to be 50 mL/min. (Navigate to "Notes" tab on the screen ---- > Mass Flow Controller entry field ---- > set to 50)

3. Turn on the Flange Cooler for the DSC and wait for the system to reach ~ -80 ˚C. (Navigate to "Control" ----- > select Event ------ > choose On).

4. When the system is at -80 ˚C or below, calibrate the Indium metal sample. It is recommended that the Indium sample not be used for calibration purposes for more than 4 weeks. A fresh sample should be prepared after the 4 week timeframe to ensure sample integrity. (Navigate to the DSC Calibration Wizard ----- > choose Heat Flow T4 -----> RCS for Cooling Unit ------ > select Cell Constant and Temperature Calibration ------ > fill in Indium for the Standard, sample weight, Other for the Pan Type ------ > select Pre-Melt and specify the heating rate at 5 ˚C/min. Save the calibration under a new file and then choose to Start Experiment. Note that this calibration exercise is used to determine the drift in the machine's calorimetric response and to have the system account for it using an internal Cell Constant factor.

5. Once the Calibration is done, proceed to run the Heat Capacity experiments. First load the sample pan into the DSC (On the instrument operating screen, independent from the TA Explorer screen shown on the computer, select "Control Menu" and choose "Open" Lid. Note that for safety reason it is not recommended to open the internal chamber when the temperature is greater to 40 ˚C). Figure C.1. shows a snapshot of the DSC internal chamber where the samples are stored.

Figure C.1. Snapshot of DSC Internal Chamber: Left (Reference Cell); Right (Sample Cell)

6. Use uncontaminated tweezer to place the empty reference pan and the desired sample plan into appropriate holder platforms (reference pan – left side platform; sample pan – right side platform). Make sure that neither of the two pans will accidentally block the central electrode which is used for heat sensing. Lid will automatically close once the reference pan and sample pan have been properly placed inside the chamber.

7. Load the Heat Capacity Method (or Recipe) to run the experiments (Navigate to the "Summary" tab ------ > select Mode -------- > specify Custom in regard to Standard and Test ----- > Click Green arrow to run the experiment)

The Heat Capacity Method is given below:

Data Storage Off. Ramp at 10 ˚C/min. to 20 ˚C. Isothermal for 10 min. Data Storage On. Ramp at 5 ˚C/min. to 125 ˚C. Date Storage Off. Ramp at 20 ˚C/min. to 25 ˚C. Isothermal for 1 min.

8. Run the cells in this order: Blank, Al_2O_3, then all Samples. Be sure to always place these cells on the right side platform. The reference cell should always be left on the left side platform for each run. A typical run takes approximately 45 minute.

Shutting Down the Instrument

The following steps describe how to shut down the instrument at the end of each day.

1. On the TA Explorer screen, navigate to the "Procedure" tab ----- > Open the Folder icon ------ > Select a program called RCS Off and Open it ------- > Click Green arrow to run it. It should take approximately 15 min. to run the shut down procedure.

2. Navigate to the "Notes" tab ------ > Set the Mass Flow Control to 0 mL/min. to stop N2 flow into the DSC system.

3. Turn off the N2 from the tank.

3. Sample DSC Scans

Sample DSC scans are now provided for the Indium, Blank, Al2O3, and a given sample. Note that all of these scans can be viewed with TA Universal Analysis software (Version 4.2. E). Figure C.2. shows a standard Indium calorimetric scan.

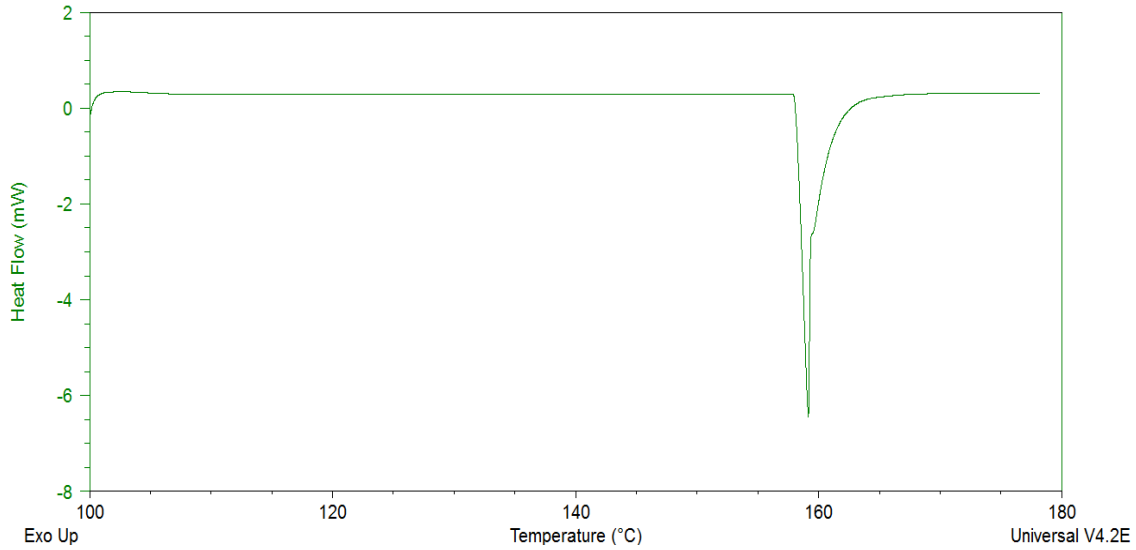

Figure C.2. Calorimetric Scan of Indium Sample (for Calibration of Cell Constant)

The Indium calorimetric profile shows a sharp heating response at ~156.6 which is the reported melting point for Indium metal.

Figure C.3. displays a standard calorimetric scan for Blank sample.

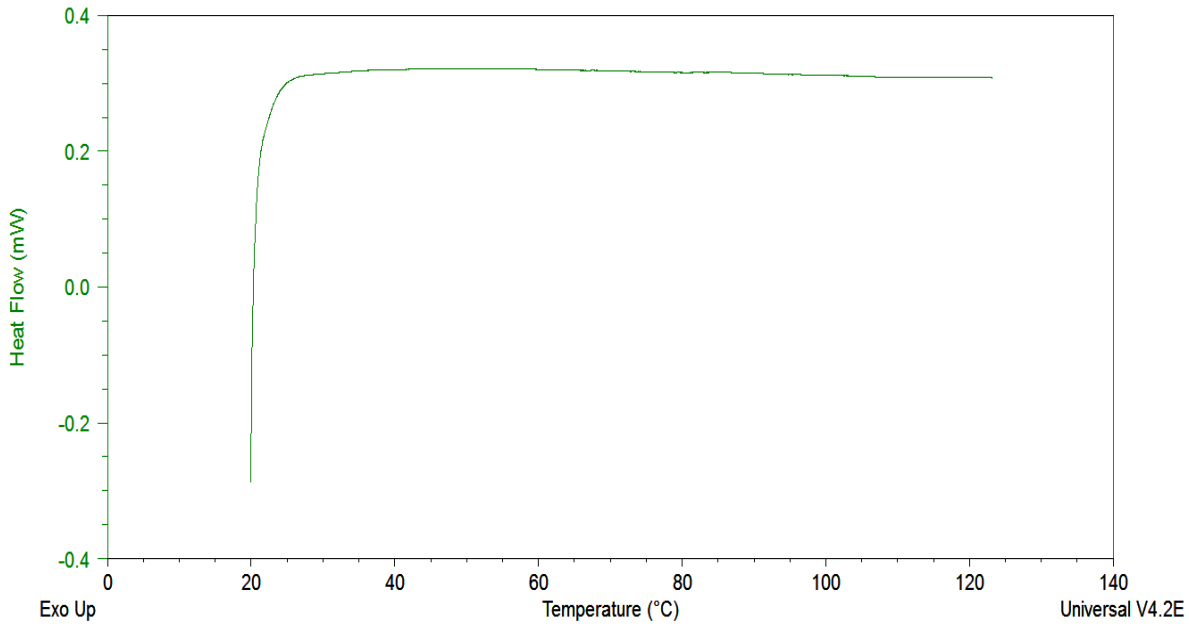

Figure C.3: Calorimetric Scan of Blank Sample

The heat flow of the Blank sample is negligible and remains relatively constant over the temperature range of interest. The negligible heat flow shown is because there is little difference between the amounts of heat absorbed by reference pan vs. a blank pan.

Figure C.4. shows a standard calorimetric scan for the Al_2O3 sample.

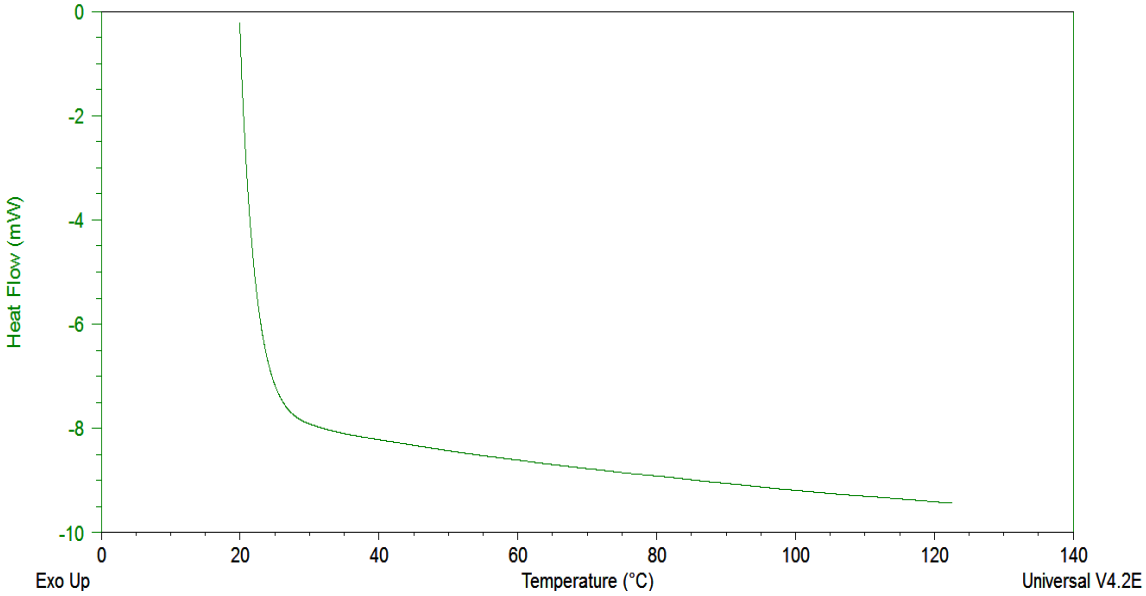

Figure C.4: Calorimetric Scan of Al_2O_3 Sample

Figure C.5 displays a standard calorimetric scan for a loaded amine sample.

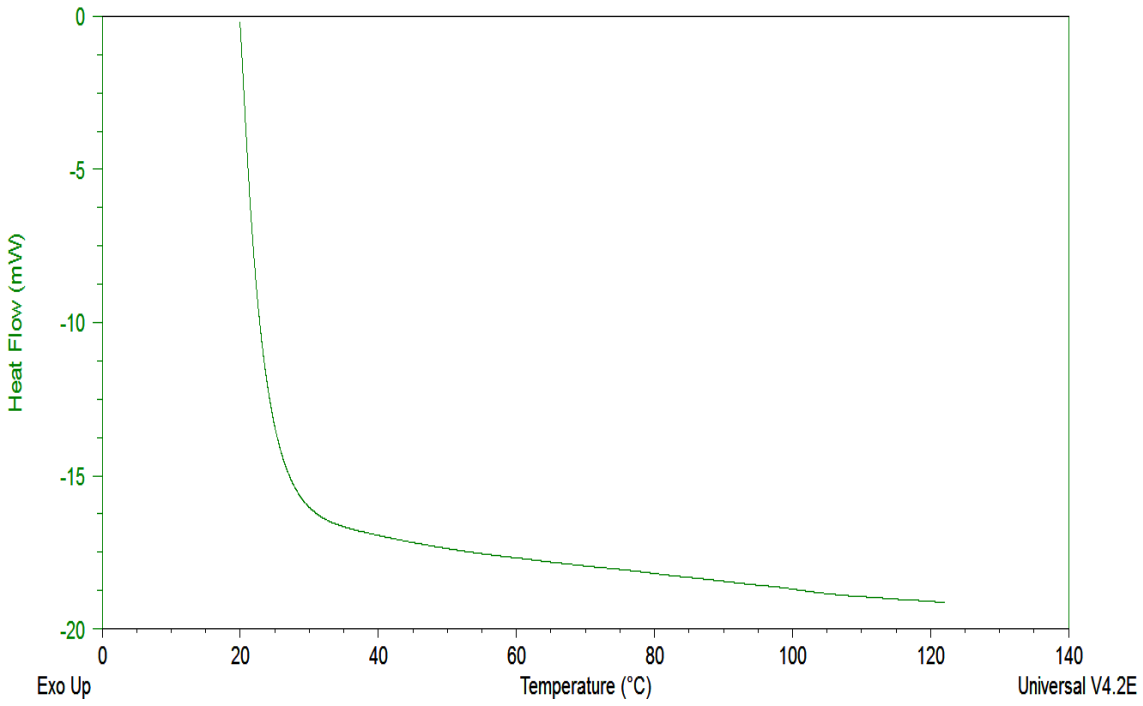

Figure C.5: Calorimetric Scan of an Amine Sample

The following procedure describes how to extract and download the raw calorimetric data from the scans into Excel.

1. Start by opening up the calorimetric scan of the Blank sample in TA Universal Analysis. Zero out the weight of the Blank sample.

2. Open up the calorimetric scan of the Al_2O_3 sample in Universal Analysis. Zero out the weight of the Al_2O_3 sample.

3. Navigate to "Tools". Go to Baseline File and select the Blank sample (already opened) as the baseline. When the pop-up window comes up, make sure to check Heat Flow (mW) for Signals, select Temperature for Base, Subtract for Operations, Name & Units for Match.

4. Navigate to “View”. Go to Data Table and select Spreadsheet as the output format. When the pop-up window comes up, specify the range of temperature for which heat flow measurements are to be reported (40 ˚ - 120 ˚C) with an increment of 5 ˚C. Go to Resolution, click on Temperature, and select round off to 3 significant figures. Choose OK.

These steps will generate an Excel report of the heat flow data over the range of temperature requested. These same steps must be followed to extract the calorimetry data for the samples. The raw data are then used to calculate the sample heat capacity.

Appendix D: FTIR Pure Component Reference Spectra

The reference spectra of pure components used in FTIR analysis are provided below. These spectra were generated by calibrating each pure component using the Gasmet Calibrator device described in Chapter 2. For each component spectrum, the analysis range that provides the optimum analysis is given.

Water (H_2O)

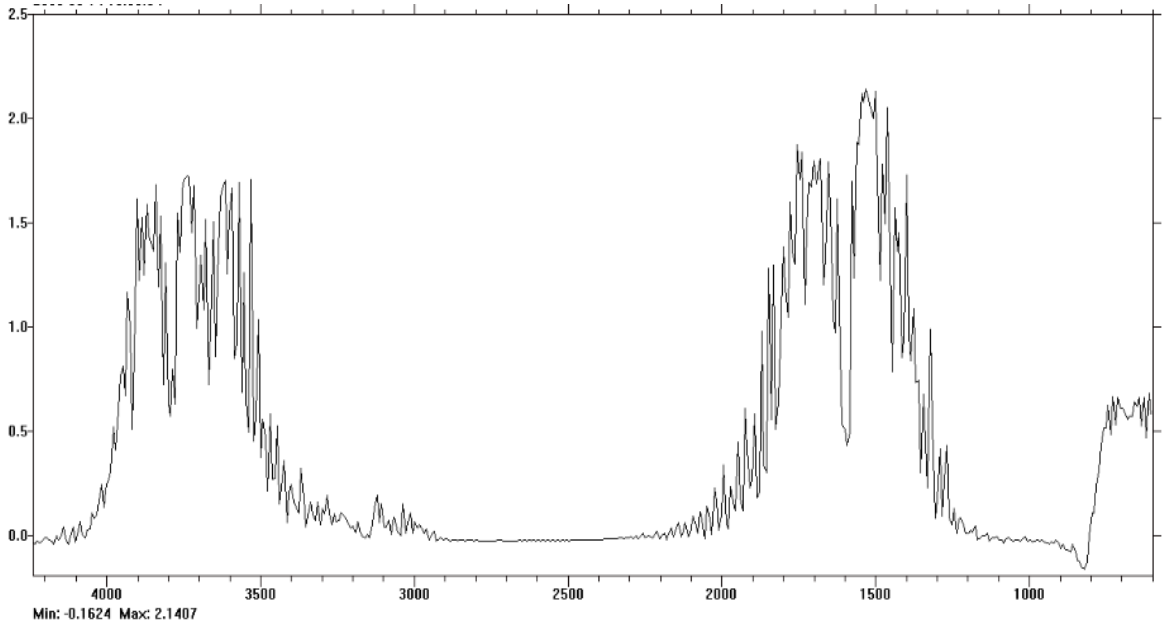

Figure D.1: Water (H_2O) Reference. Optimum Analysis Region: 1980 – 2025

Carbon Dioxide (CO_2)

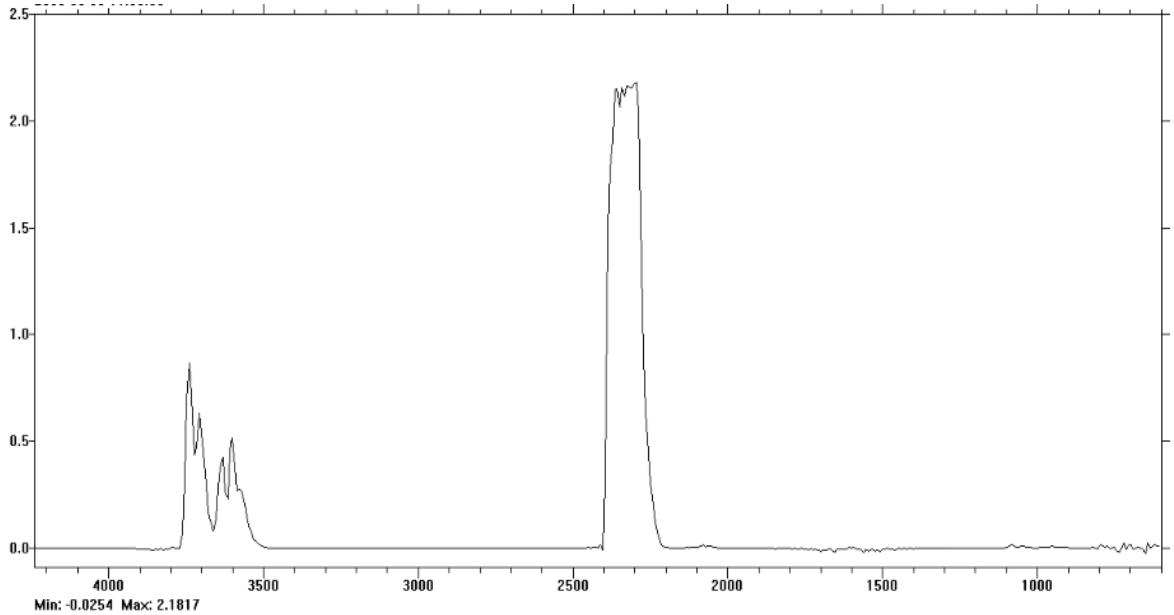

Figure D.2: Carbon Dioxide (CO_2) Reference. Optimum Analysis Region: 2200 – 2240

Monoethanolamine (MEA)

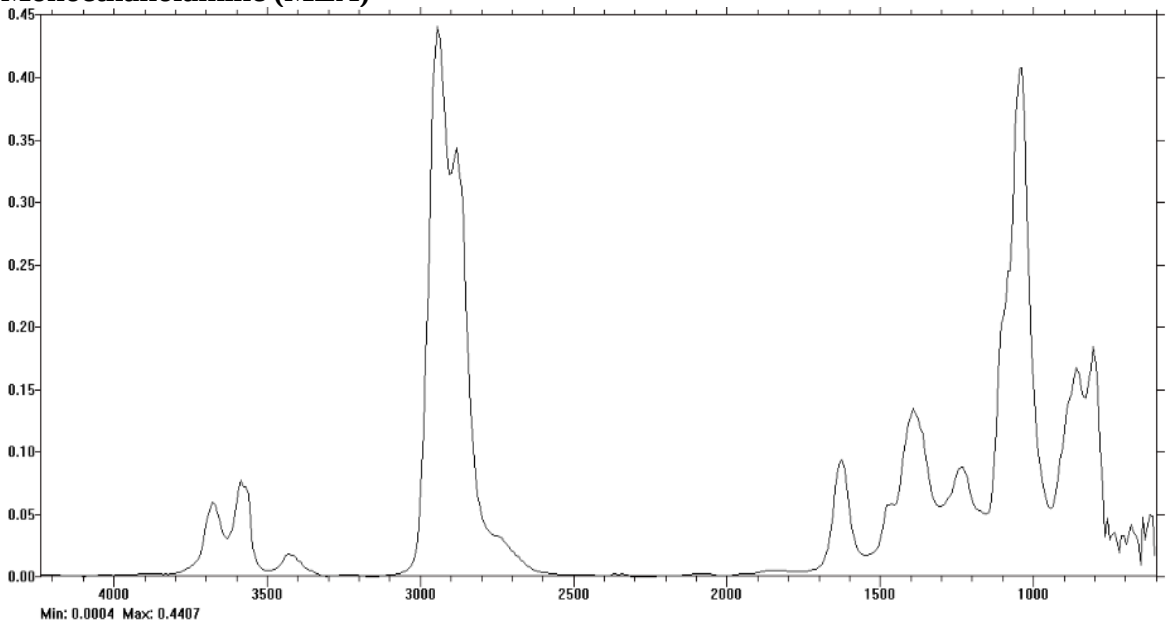

Figure D.3: Monoethanolamine (MEA) Reference. Optimum Analysis Region: 2500 – 3100

Piperazine (PZ)

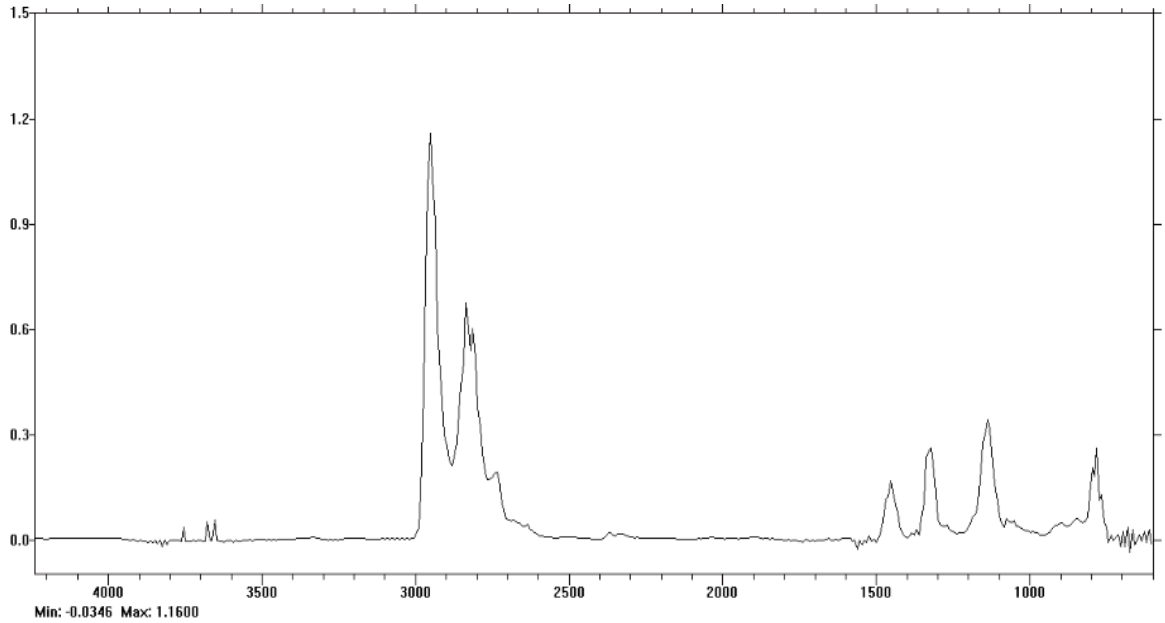

Figure D.4: Piperazine (PZ) Reference. Optimum Analysis Region: 2600 – 3100

N-Methyldiethanolamine (MDEA)

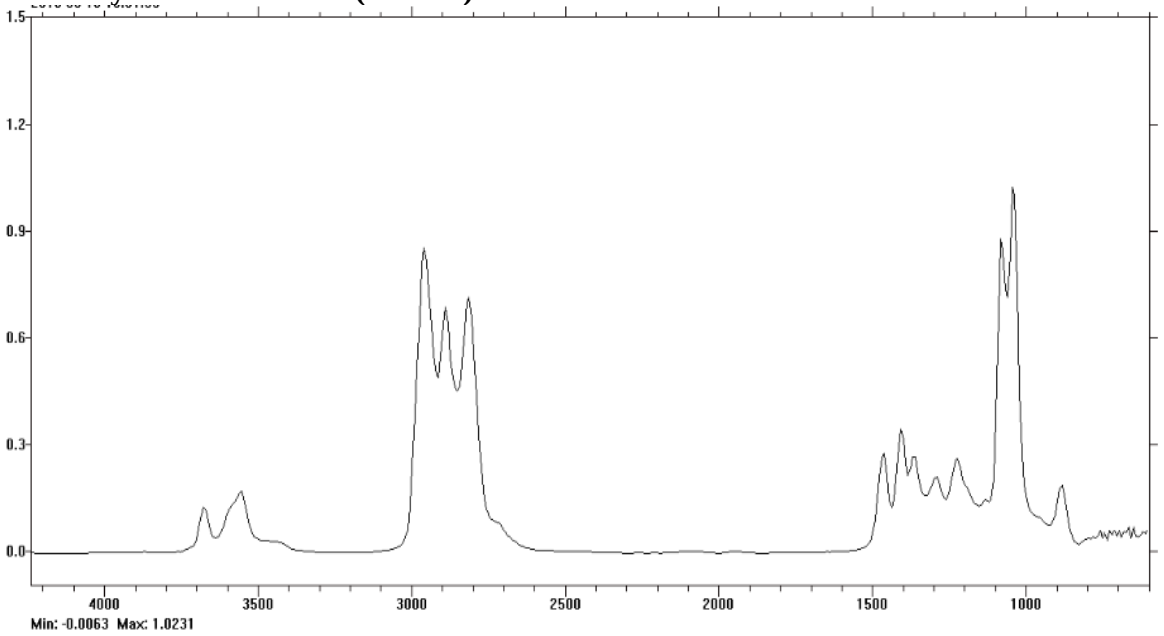

Figure D.5: N-Methyldiethanolamine (MDEA) Reference. Optimum Analysis Region: 2600 - 3050

2-Amino-2-Methyl-1-Propanol (AMP)

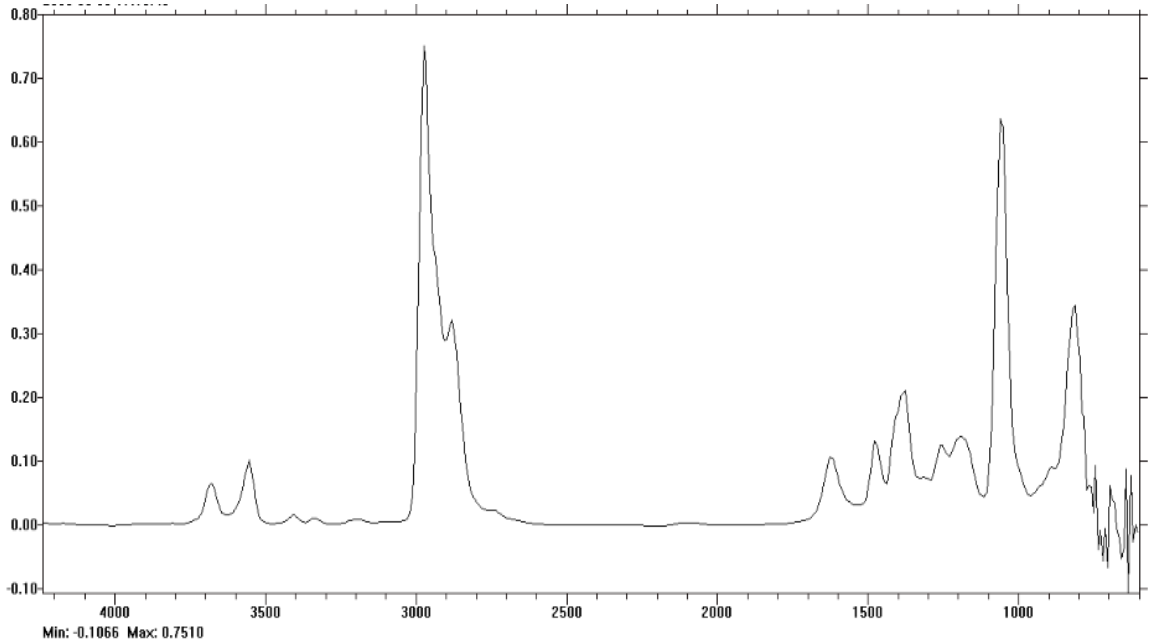

Figure D.6: 2-Amino-2-Methyl-1-Propanol (AMP) Reference. Optimum Analysis Region: 2700 – 3100

Diethanolamine (DEA)

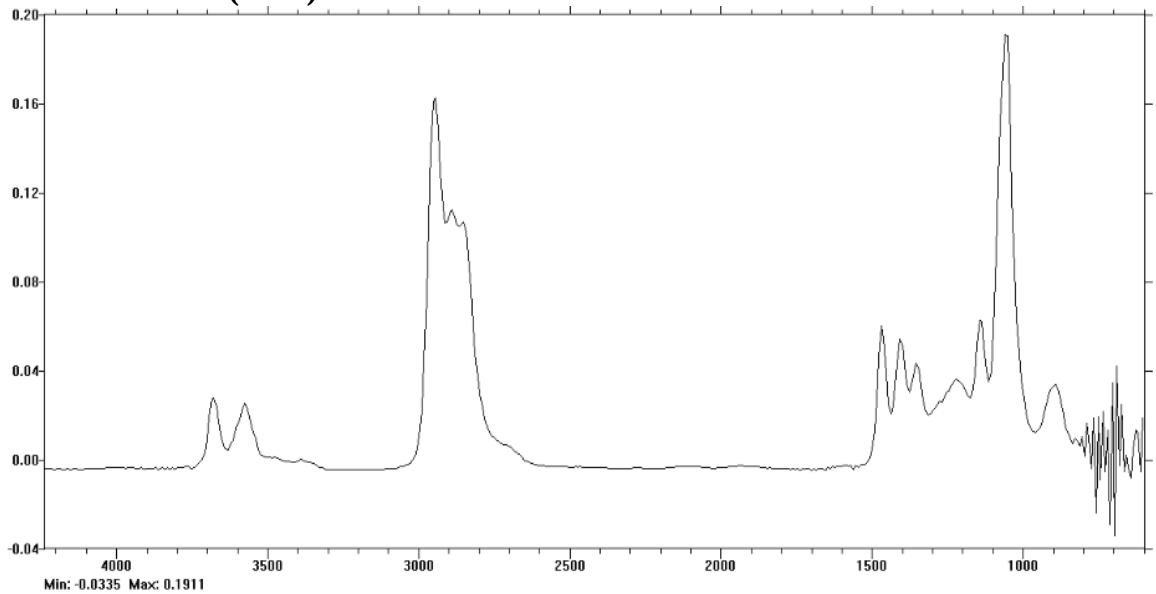

Figure D.7: Diethanolamine (DEA) Reference. Optimum Analysis Region: 2600 – 3100

Ethylenediamine (EDA)

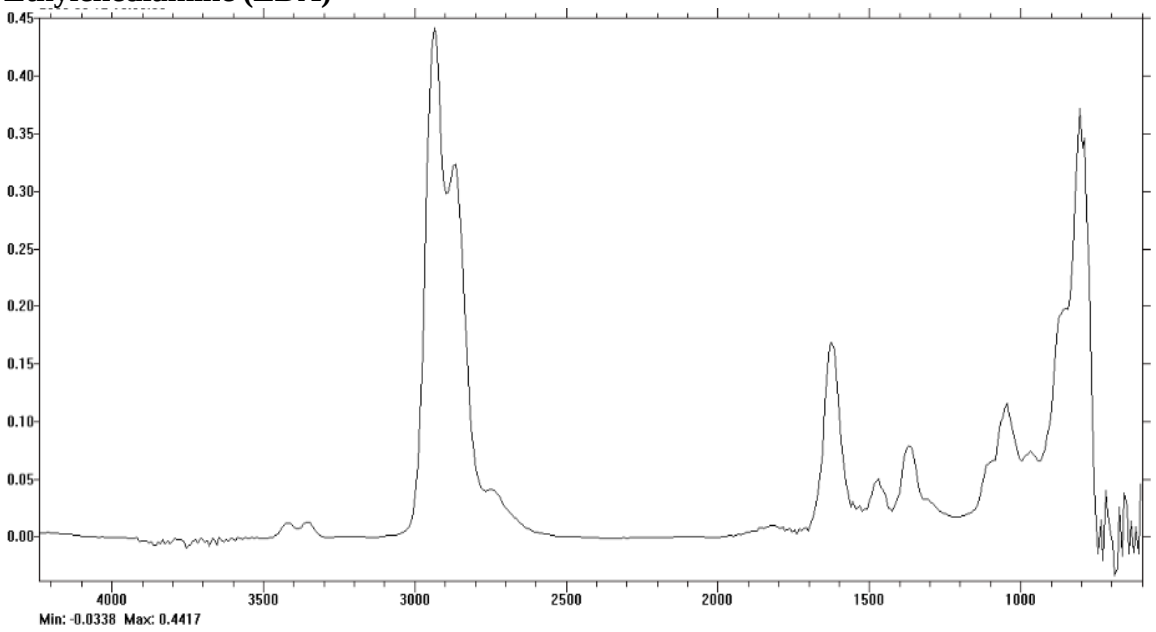

Figure D.8: Ethylenediamine (EDA) Reference. Optimum Analysis Region: 2600 – 3100

Hexamethylenediamine (HMDA)

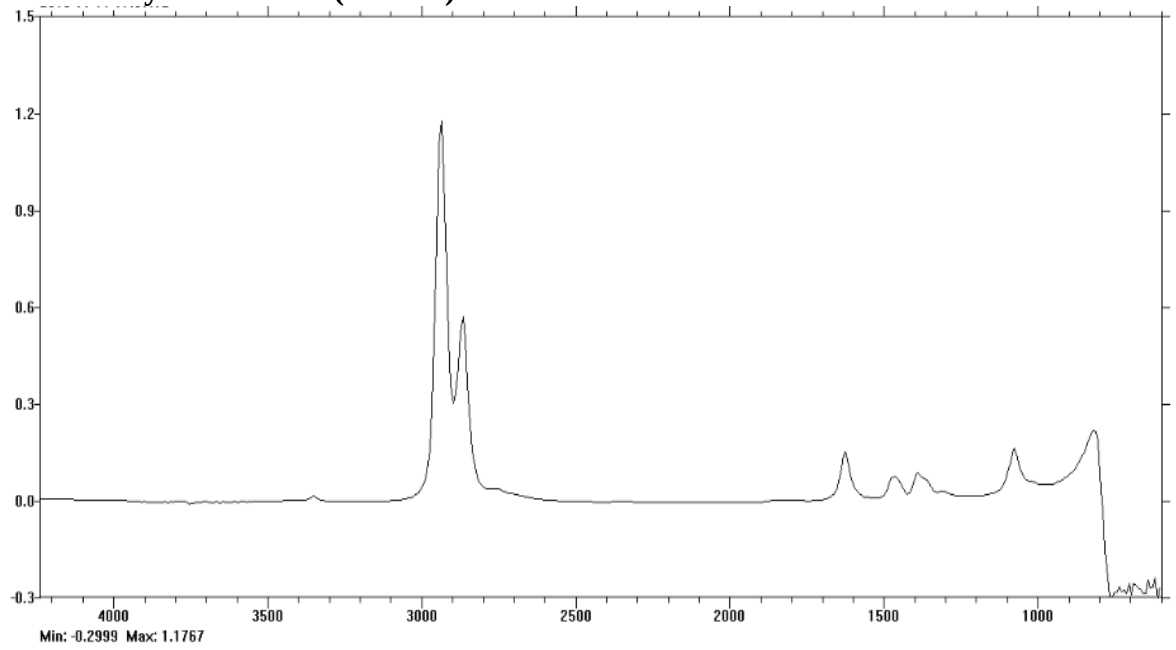

Figure D.9: Hexamethylenediamine (HMDA) Reference. Optimum Analysis Region: 2700 – 3100

2-Methyl Piperazine (2-MPZ)

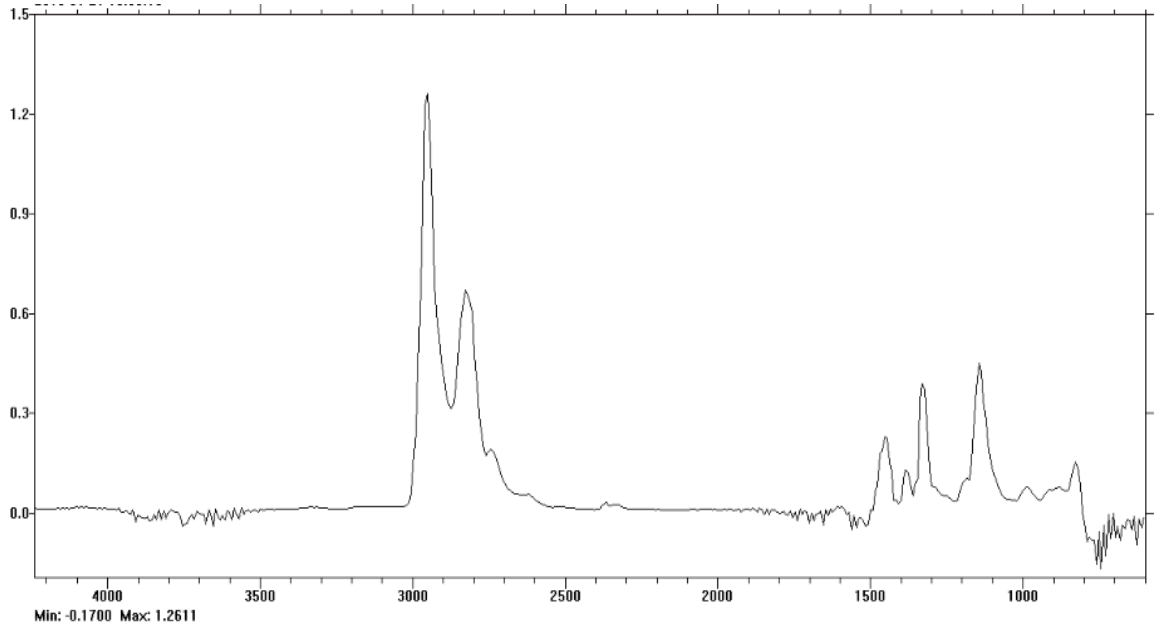

Figure D.10: 2-Methyl Piperazine (2-MPZ) Reference. Optimum Analysis Region: 2600 – 3100

1,4-Dimethyl Piperazine (DMPZ)

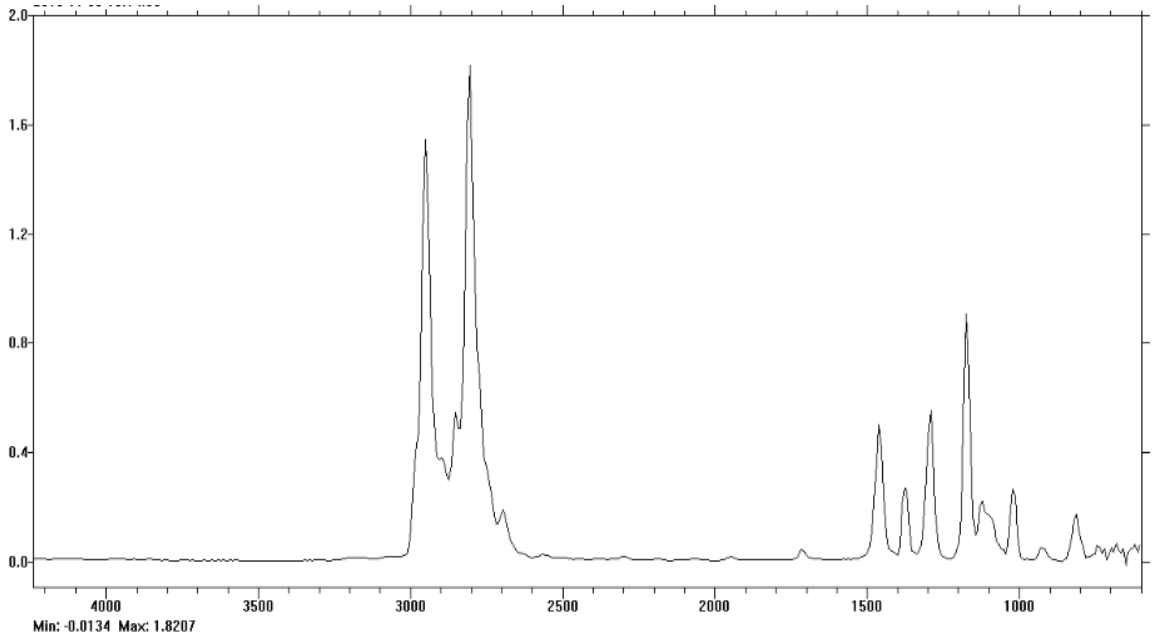

Figure D.11: 1,4-Dimethyl Piperazine (DMPZ) Reference. Optimum Analysis Region: 2500 – 3100

2,2-Dimethylaminoethoxyethanol (2,2-DMAEE)

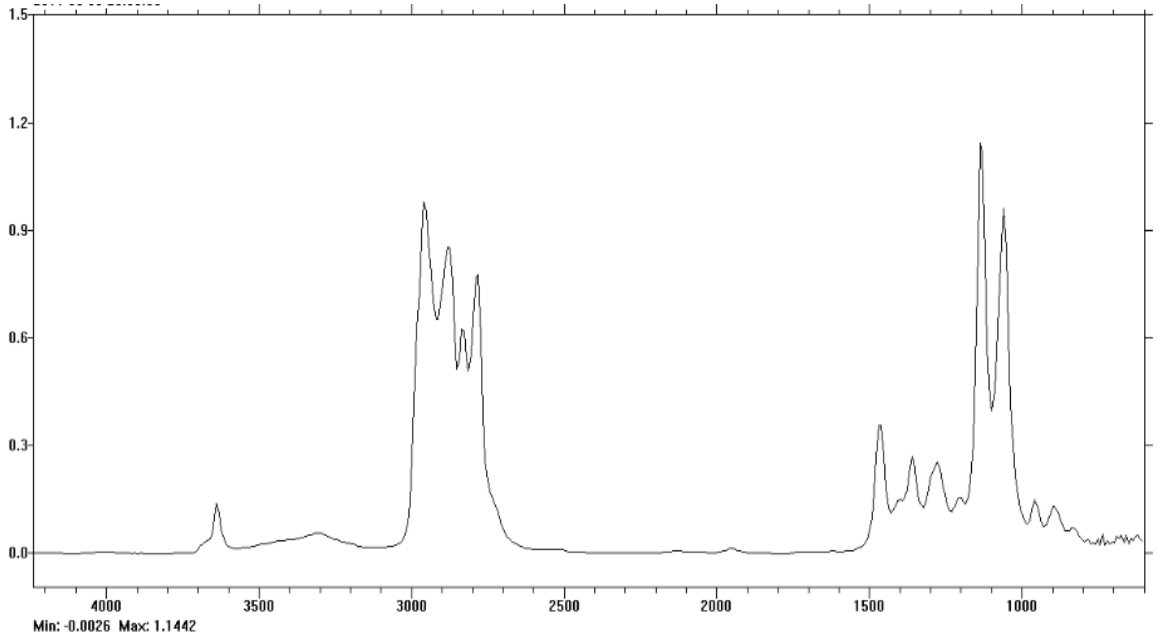

Figure D.12: 2,2-Dimethylaminoethoxyethanol (2,2-DMAEE) Reference. Optimum Analysis Region: 2500 – 3100

Dimethylethanolamine (DMEA)

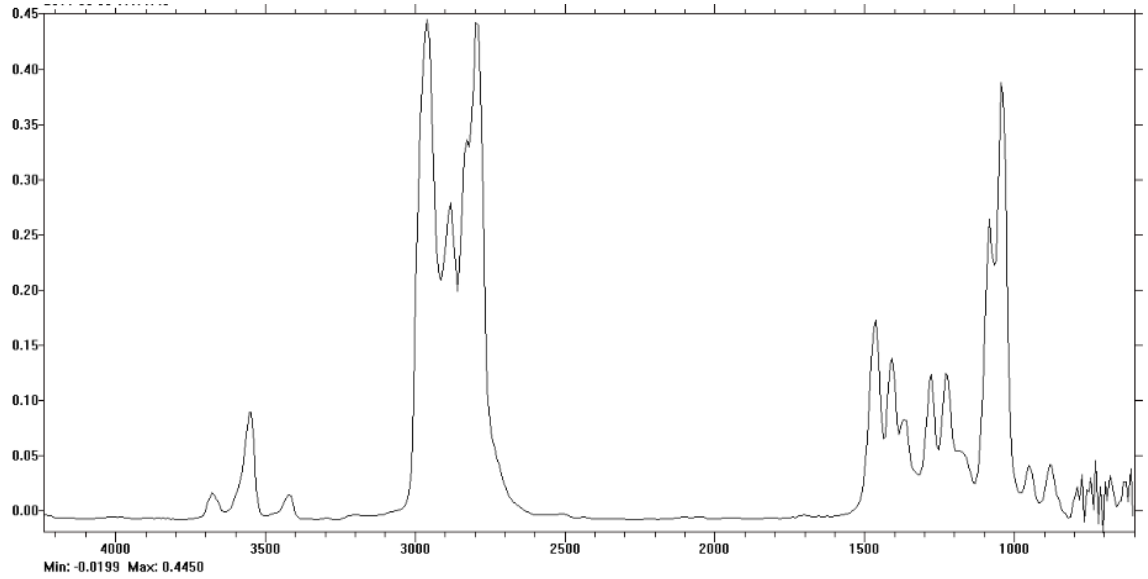

Figure D.13: Dimethylethanolamine (DMEA) Reference. Optimum Analysis Region: 2500 - 3100

DL-Alaninol (ALA)

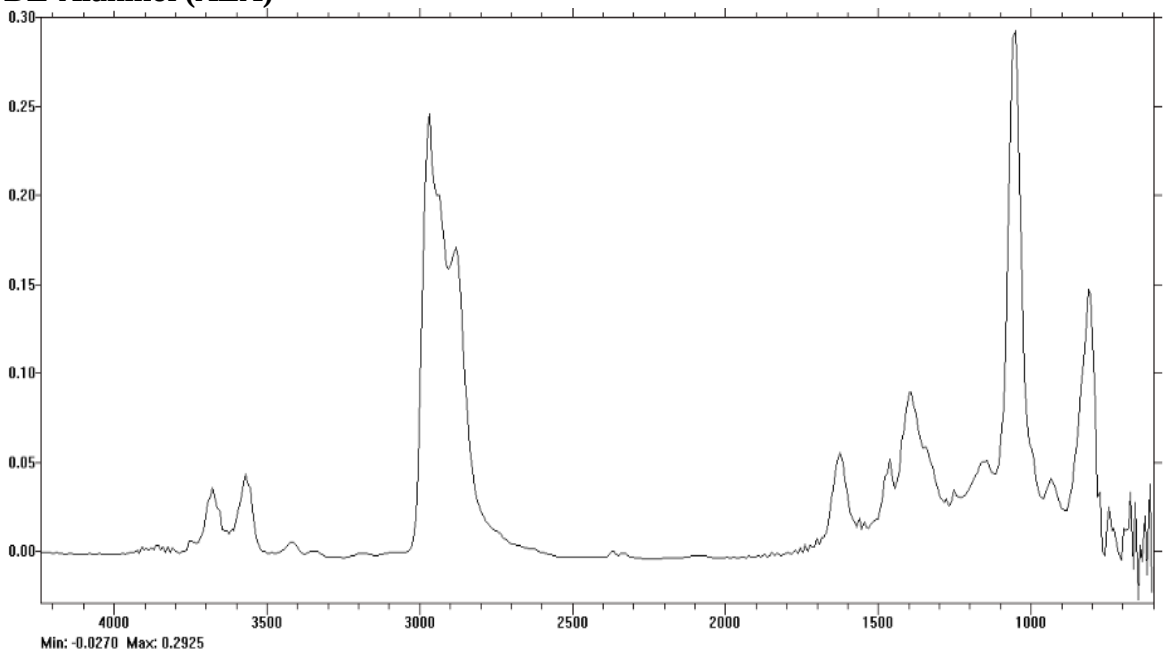

Figure D.14: DL-Alaninol (ALA) Reference. Optimum Analysis Region: 2500 – 3100

2-Hydroxyethyl Piperazine (HEP)

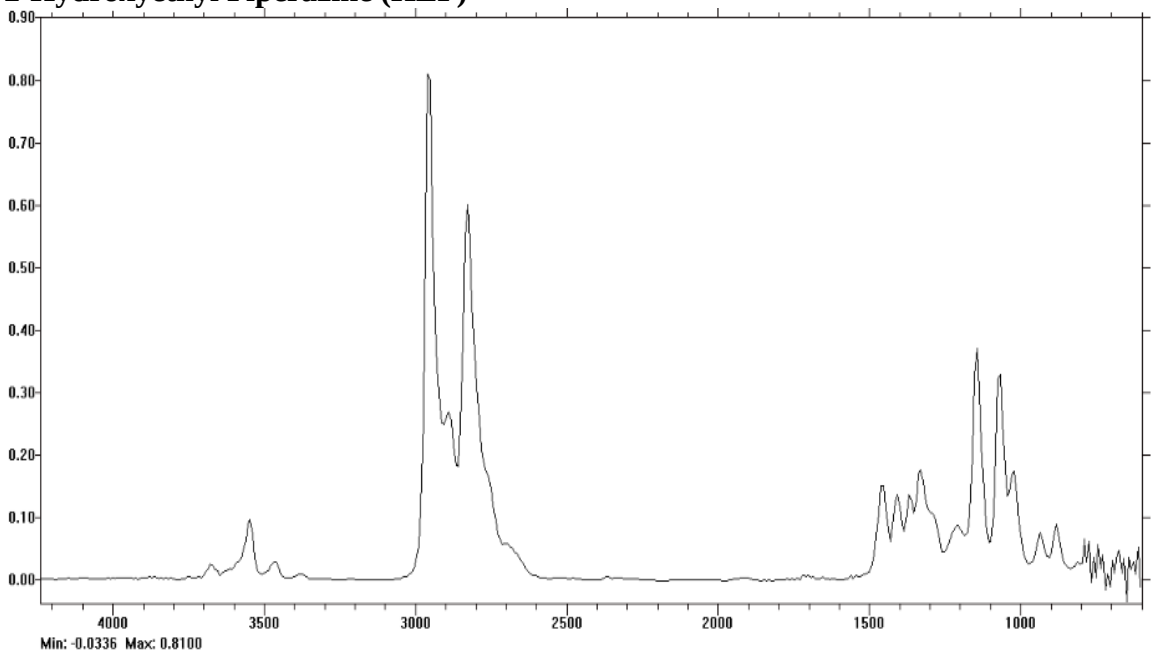

Figure D.15: 2-Hydroxyethyl Piperazine (HEP) Reference. Optimum Analysis Region: 2500 – 3100

1-Methyl Piperazine (1-MPZ)

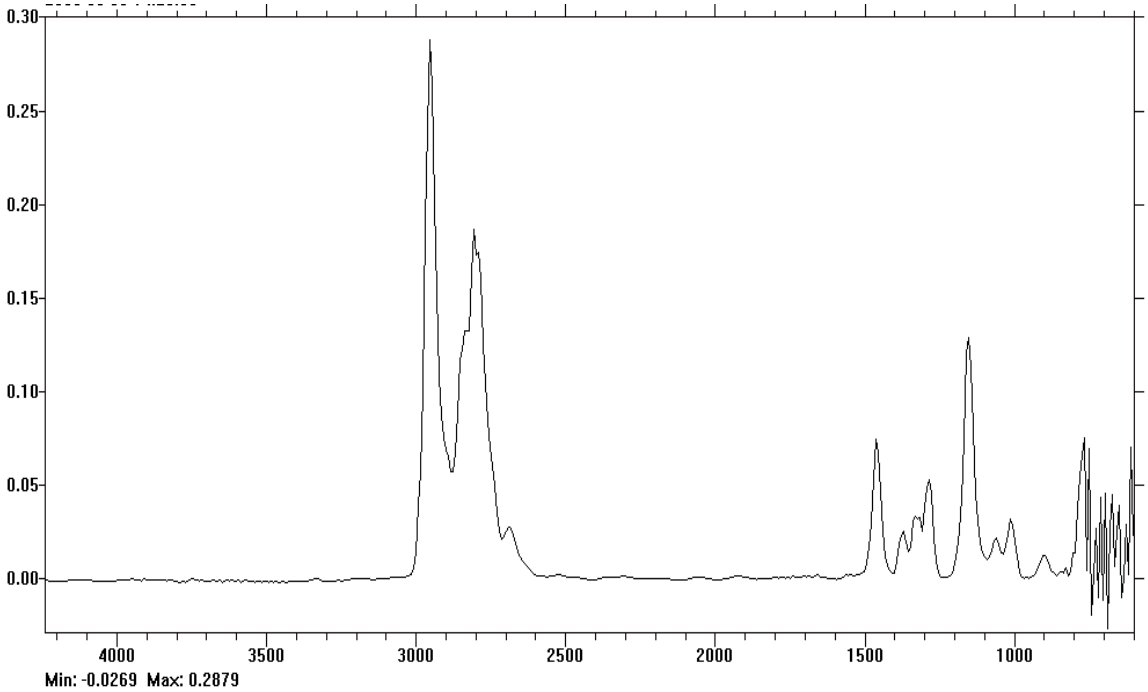

Figure D.16: 1-Methyl Piperazine (1MPZ) Reference. Optimum Analysis Region: 2600 - 3100

1,2-Aminoethyl Piperazine

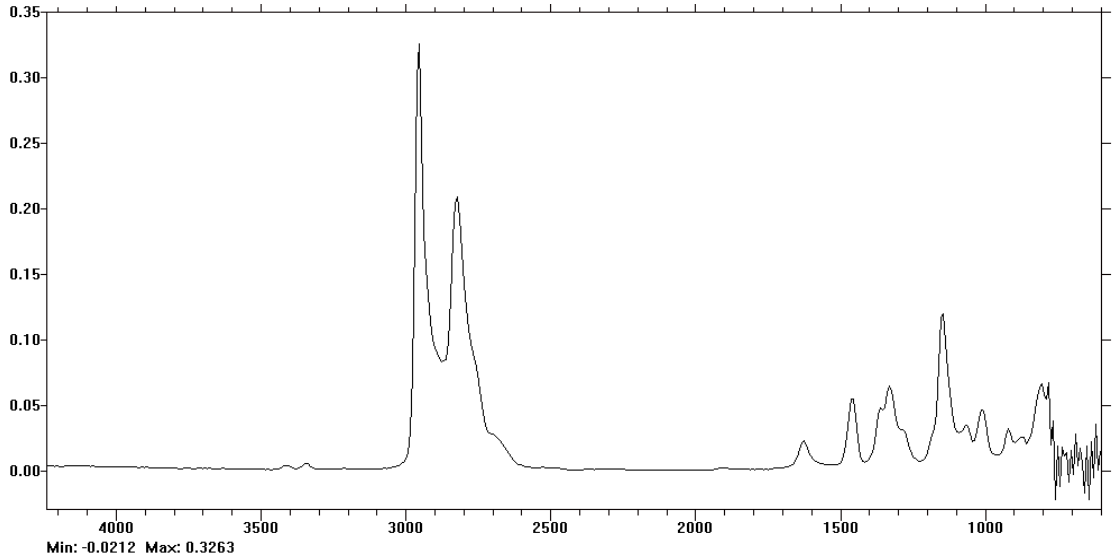

Figure D.17: 1,2-Aminoethyl Piperazine (AEP) Reference. Optimum Analysis Region: 2500 - 3100

Diglycolamine (DGA)

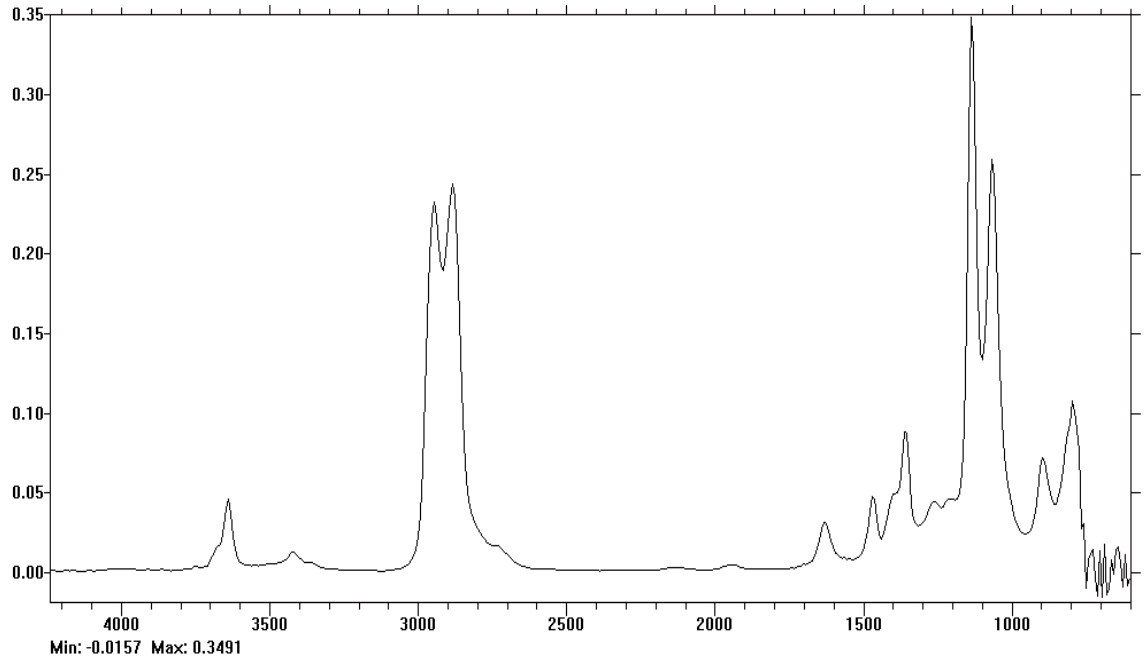

Figure D.18: Diglycolamine (DGA) Reference. Optimum Analysis Region: 2500 - 3100

3-Methylamino Propylamine (MAPA)

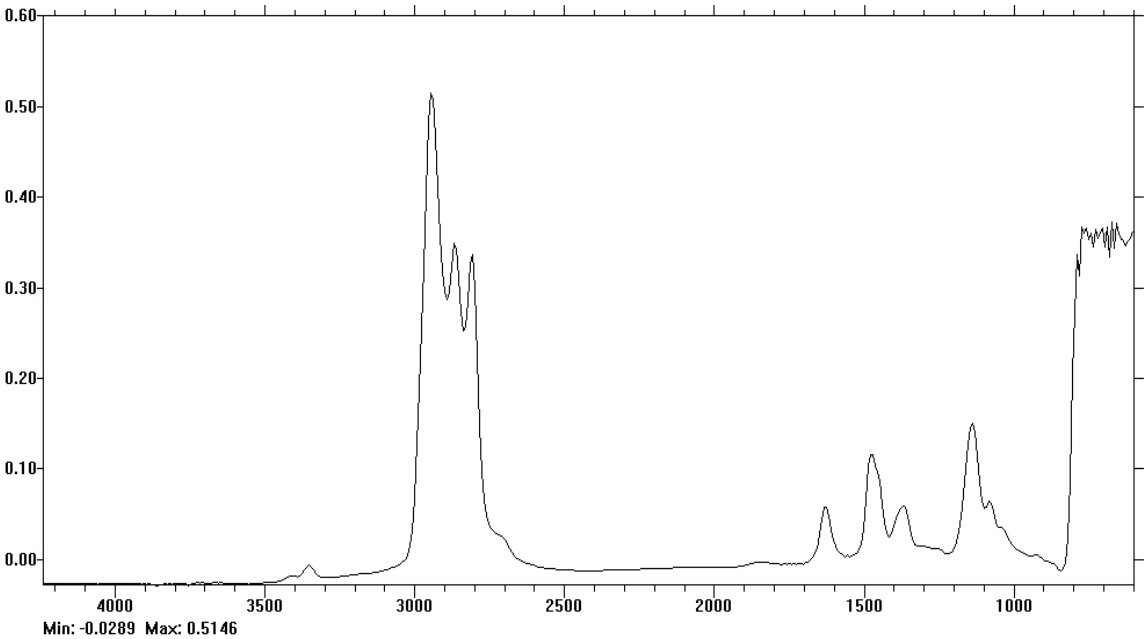

Figure D.19: 3-Methylamino Propylamine (MAPA) Reference. Optimum Analysis Region: 2500 – 3150

1,2-Diaminopropane (DAP)

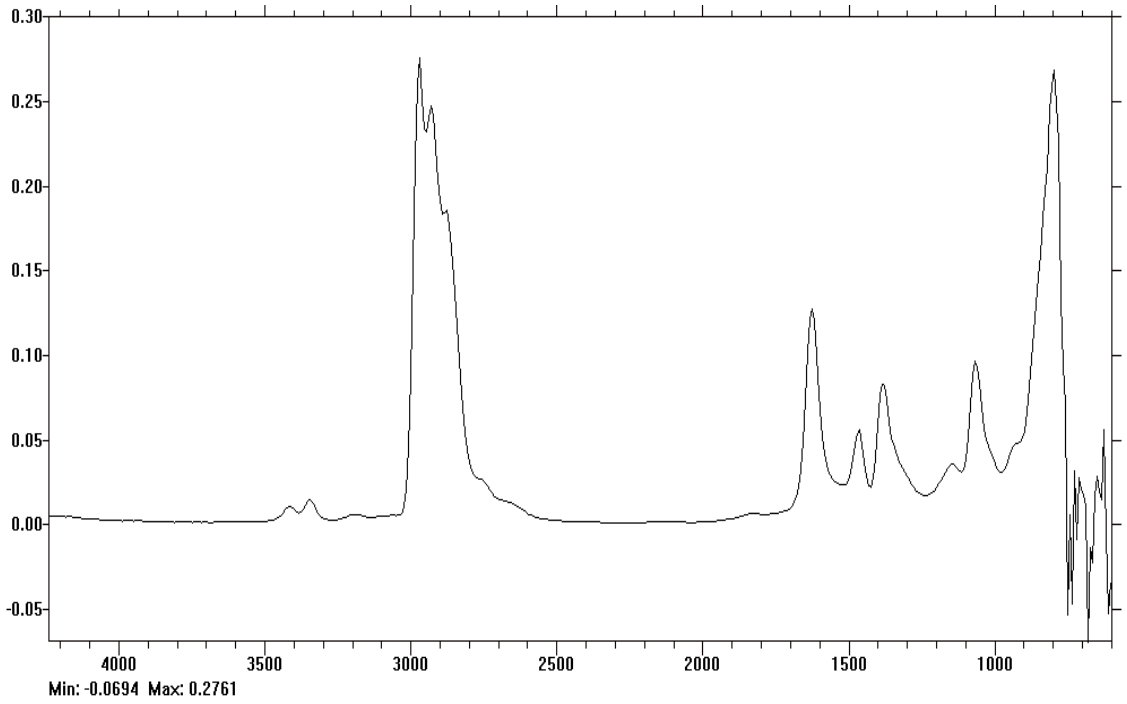

Figure D.20: 1,2-Diaminopropane (DAP) Reference. Optimum Analysis Region: 2500 – 3100

Morpholine (MORPH)

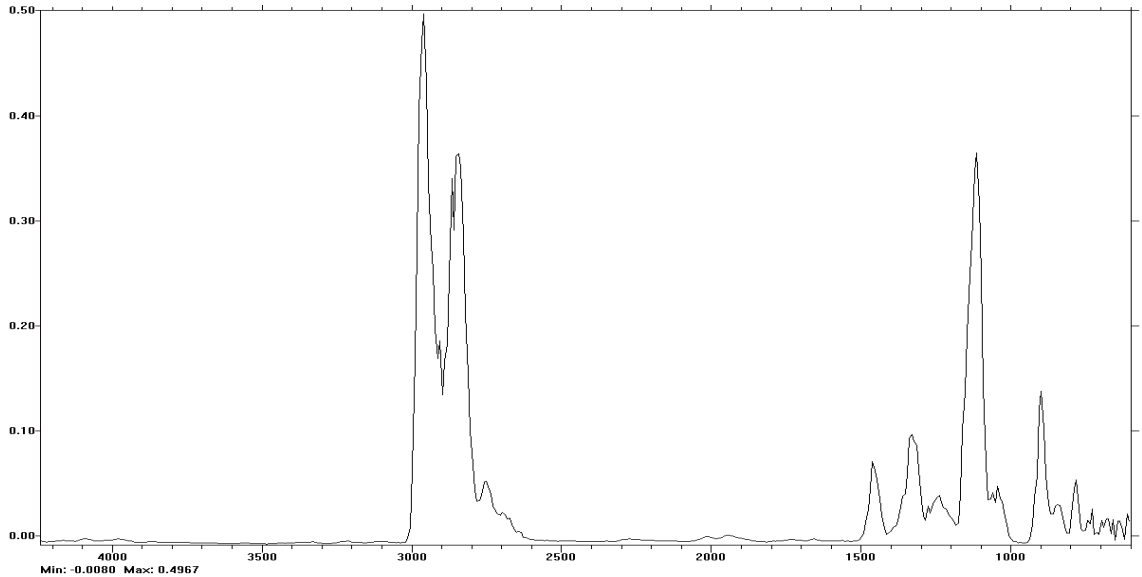

Figure D.21: Morpholine (MORPH) Reference. Optimum Analysis Region: 2500 – 3150

Dimorpholino Diethyl Ether (DMORPH)

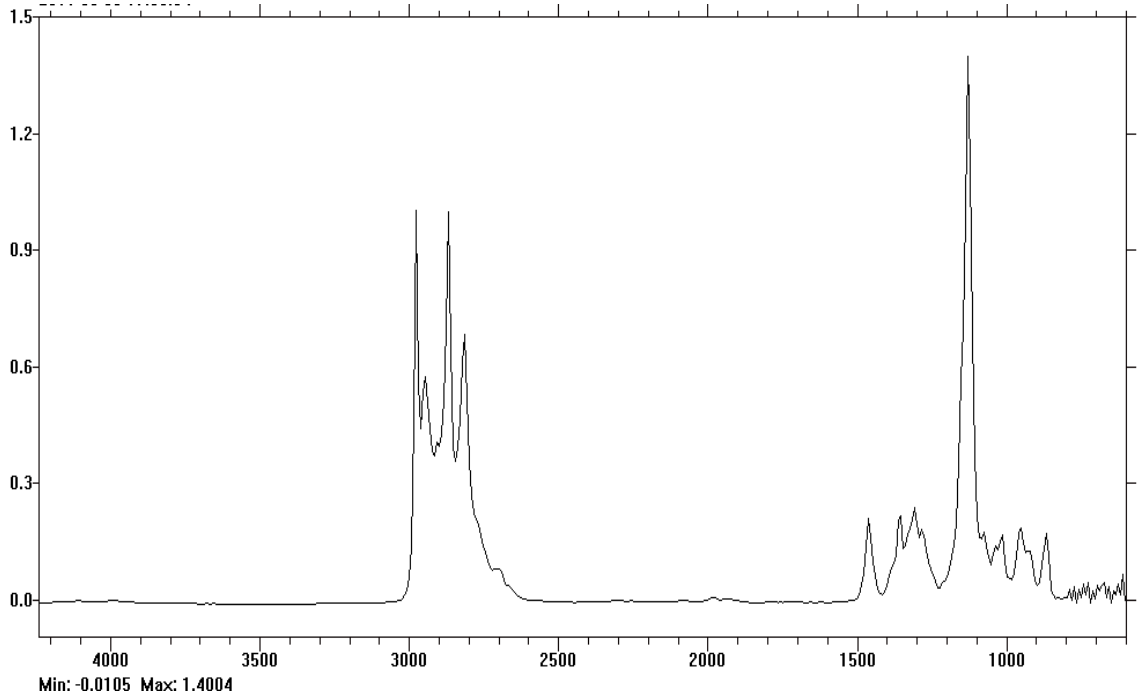

Figure D.22: Dimorpholino Diethyl Ether (DMORPH) Reference. Optimum Analysis Region: 2500 - 3100

Appendix E: Nomenclature

This appendix includes all the shorthand nomenclature used throughout the dissertation. The nomenclature is organized alphabetically. Greek symbols are included at the end.

A_{φ}	Debye Huckel parameter
c_g	Amine concentration in gas phase
C_p	Specific heat capacity of a sample
c_w	Amine concentration in water phase
D_w	Dielectric constant of water
G_{amine}	Gibbs Energy of an amine
$G^{E,\ lc}$	Gibbs energy contribution from the local short range interactions
$G^{E,Born}$	Gibbs energy contribution from Born correction (change in mixed solvent ref.)
$G^{E,PDH}$	Gibbs energy contribution from the Pitzer-Debije-Huckel long range interactions
G^{excess}	Excess Gibbs energy of a system
H_{amine}	Amine Henry's constant
I_x	Ionic strength
K	Amine partition coefficient
k	Boltzmann constant

k_j	Parameter value of molecular group j
M_s	Molecular weight of the solvent
n_j	Number of instances of molecular group j in amine structure
N_o	Avogadro's number
P_{amine}	Amine partial pressure
P_{CO2}	CO_2 partial pressure
P^{sat}_{amine}	Amine saturation (vapor) pressure
R	Universal gas constant
T	Temperature
x_i	Liquid mole fraction of species i
z_i	Charge of species i

Greek Symbols

α	CO_2 loading
γ^*_{amine}	Asymmetric amine activity coefficient - ref state infinite dilution amine in H_2O
γ^{∞}_{amine}	Symmetric Amine activity coefficient at infinite dilution of amine in water
$\Delta H_{solution}$	Change in enthalpy of an amine in solution
ΔG_{amine}	Change in Gibbs energy of an amine in solution
ΔS_{amine}	Change in entropy of an amine in solution

τ_{ij}	Binary interaction parameter between component i and j
G_{ij}	Gibbs interaction energy between component i and j
φ_{amine}	Fugacity coefficient of an amine
$\Delta H_{reaction}$	Change in enthalpy of an amine in a reaction
ΔH_{excess}	Change in excess enthalpy of an amine
ρ_M	Molar density of water

References

Abbott, M.; O'Connell, J.P., Chem. Eng. Educ. 28 (1994) 18 – 23, 77.

Cabani, S., Conti, G., Lepori, L. Thermodynamic Study on Aqueous Dilute Solutions of Organic Compounds. Part 1 – Cyclic Amines. Trans. Faraday Soc. 67 (1971) 1933 – 1942.

Cai, Z.; Xie, R.; Wu, Z., Binary Isobaric Vapor-Liquid Equilibria of Ethanolamines + Water. J. Chem. Eng. Data. 41 (1996) 1101 – 1103.

Chiu, L. F.; Li, M. H., Heat Capacity of Alkanolamine Aqueous Solutions. Journal of Chemical and Engineering Data 1999, 44, (6), 1396-1401.

Closmann, F.B., Oxidation and Thermal Degradation of Methyldiethanolamine/Piperazine in CO_2 Capture. Ph.D. Dissertation. The University of Texas at Austin (2011).

DIPPR 801: Thermophysical Property Database for Pure Chemical Compounds.

Dugas, R.E., Carbon Dioxide Absorption, Desorption, and Diffusion in Aqueous Piperazine and Monoethanolamine. Ph.D. Dissertation. The University of Texas at Austin (2009).

Ermatchkov, V.; Kamps, A. P.-S.; Speyer, D.; Maurer, G., Solubility of Carbon Dioxide in Aqueous Solutions of Piperazine in the Low Gas Loading Region. Journal of Chemical and Engineering Data 2006, 51, (5), 1788-1796.

Ermatchkov, V.; Perez-Salado Kamps, A.; Maurer, G., Chemical Equilibrium Constants for the Formation of Carbamates in (Carbon Dioxide + Piperazine + Water) from 1H NMR-Spectroscopy. Journal of Chemical Thermodynamics 35 (2003) 1277-1289.

Goff, G. S. Oxidative Degradation of Aqueous Monoethanolamine in CO_2 Capture Processes: Iron and Copper Catalysis, Inhibition, and O_2 Mass Transfer. Ph.D. Dissertation. The University of Texas at Austin, Austin, Texas, 2005.

Hamborg E, Niederer J, Versteeg G. "Dissociation Constants and Thermodynamic Properties of Amino Acids used in CO_2 Absorption from 293 to 353 K." J Chem Eng Data. 52 (2007) 2491-2502.

Hilliard, M.D., A Predictive Thermodynamic Model for an Aqueous Blend of Potassium Carbonate, Piperazine, and Monoethanolamine for Carbon Dioxide Capture from Flue Gas. Ph.D. Dissertation. The University of Texas at Austin (2008).

Hine, J; Mookerjee, P., The Intrinsic Hydrophilic Character of Organic Compounds. Correlations in terms of Structural Contributions. J. Org. Chem. 40 (1975) 292 – 298.

Jou, F.-Y.; Mather, A. E.; Otto, F. D., The Solubility of CO_2 in a 30 Mass Percent Monoethanolamine Solution. The Canadian Journal of Chemical Engineering. 73 (1995)
140-146.

Jou, F-Y.; Mather, A.; Otto, F., Solubility of Hydrogen Sulfide and Carbon Dioxide in Aqueous Methyldiethanolamine Solutions. Ind Eng Chem Process Des Dev. 21 (1982) 539-544.

Kell, G. S.; Haar, L.; Gallagher, J. S., NBS/NRC Steam Tables. Thermodynamic and Transport Properties and Computer Programs for Vapor and Liquid States of Water in SI Units. Hemisphere Publishing Corporation: Washington, (1984).

Kim, I.; Svendsen, H.F.; Borresen, E., Ebulliometric Determination of Vapor-Liquid Equilibria for Pure Water, Monoethanolamine, N-Methyldiethanolamine, 3-(Methylamino)-propylamine, and Their Binary and Ternary Solutions. J. Chem. Eng. Data. 53 (2008) 2521-2531.

Larsen, B.; Rasmussen, P; Fredenslund, A., A Modified UNIFAC Group Contribution Model for Prediction of Phase Equilibria and Heats of Mixing. Industrial & Engineering Chemistry Research. 26 (1987) 2274-2286.

Lenard, J.; Rousseau, R.; Teja, A., Vapor-Liquid Equilibria for Mixtures of 2-Aminoethanol + Water. AIChE Symposium Series. 86 (1990) 1-5.

Matthews, E.; Fried, V.; Boublik, T., The Vapour Pressures of Pure Substances. Elsevier: New York, NY, (1973).

Osborne, N. S.; Stimson, H. F.; Ginnings, D. C., Measurements of Heat Capacity and Heat of Vaporization of Water in the Range 0 ^{o}C to 100 ^{o}C. Journal of Research of
the National Bureau of Standards (1939), 23, 197-260.

Pappa, G.; Anastasi, C.; Voutsas, E., Measurement and Thermodynamic Modeling of the Phase Equilibrium of Aqueous 2-Amino-2-Methyl-1-Propanol Solutions. Fluid Phase Equilibria. 243 (2006) 193-197.

Poplsteinova, J.; Krane, J.; Svendsen, H. F., Liquid-Phase Composition Determination in CO_2-H_2O-Alkanolamine Systems: An NMR Study. Ind. Eng. Chem. Res. 2005**,** 44, 9894-9903.

Renon, H.; Prausnitz, J. M., Local Compositions in Thermodynamic Excess Functions for Liquid Mixtures. AICHE J. 1968, 14, (1), 135-44.

Saarinen, P.; Kauppinen, J., Multicomponent Anaylsis of FT-IR Spectra. Applied Spectroscopy. 45, 6 (1991) 953-963.

Sander, R., Compilation of Henry's Law Constants for Inorganic and Organic Species of Potential Importance in Environmental Chemistry. Version 3. (1999). http://www.mpch-mainz.mpg.de/~sander/res/henry.html

Smith, J.; Van Ness, H.; Abbott, M., Introduction to Chemical Engineering Thermodynamics, 6th ed, McGraw-Hill Higher Education. (2001) 644.

Swanson, A. C.; Chueh, C. F., Estimating Liquid Heat Capacity. Chemical Engineering Progress 1973, 69, 83.

U.S. Energy Information Administration (EIA). 2008. http://www.eia.gov/

USEPA. Air and Steam Stripping of Toxic Pollutants. Tech. Rep. EPA-68-03-002, Industrial Environmental Research Laboratory, Cincinnati, OH, USA, 1982.

Van Wagener, D.H. Stripper Modeling for CO_2 Removal Using Monoethanolamine and Piperazine Solvents. Ph.D. Dissertation. The University of Texas at Austin (2011).

Weiland, R.; Dingman, J.; Cronin, B., Heat Capacity of Aqueous Monoethanolamine, Diethanolamine, N-Methyldiethanolamine, and N-Methyldiethanolamine-Based Blends with Carbon Dioxide. J Chem Eng Data. 42 (1997) 1004-1006.

Wilhelm, E., Battino, R., Wilcock, R. Low Pressure Solubility of Gases in Liquid Water. Chem. Rev. 77 (1977) 219 – 262.

Xu, Q. Thermodynamics of CO_2 Loaded Aqueous Amines. Ph.D. Dissertation. The University of Texas at Austin (2011).

Zhang, K.; Hawrylak, B.; Palepu, R.; Tremaine, P., Thermodynamics of Aqueous Amines: Excess Molar Heat Capacities, Volumes, and Expansibilities of {Water + Methyldiethanolamine (MDEA)} and {Water + 2-Amino-2-Methyl-1-Propanol (AMP)}. J Chem Thermodynamics. 34 (2002) 679-710.

Vita

Thu Nguyen was born in Saigon, Vietnam to Dat-Vinh Nguyen and Ngoc-Oanh Pham. After graduating from Lubbock High School in Lubbock, TX in May 1998, she enrolled in The University of Texas at Austin. She received her B.S. in Chemical Engineering in May 2003. After working for a number of years, she enrolled in graduate studies at The University of Texas at Austin in July 2007 working in Dr. Gary Rochelle's group on CO_2 Capture. She has accepted full-time employment with GTC Technology, LLC in Houston, TX.

Permanent Email: tnguyen02_2000@yahoo.com

This dissertation was typed by the author.